An X-ray Spectroscopic Study of the Hot Interstellar Medium in the Milky-Way Galaxy

Toshishige Hagihara

Department of Physics, Graduate School of Science,
The University of Tokyo

Institute of Space and Astronautical Science,
Japan Aerospace Exploration Agency

December, 2009

Abstract

A major fraction of the soft X-ray diffuse background (SXDB) below $\sim$1 keV is considered to be produced by hot interstellar medium (hot ISM) of T$\sim 10^6$ K in and around our Galaxy. Yao et al. (2009) constrained the physical properties of the hot ISM along the LMC X–3 sight line with combined analysis of the emission and absorption data. However, it is not confirmed whether those values are common to the hot ISM in all direction or only localized in this direction. Moreover LMC located only 50 kpc away and they can not exclude the possibility that the emission comes from behind LMC.

In this thesis, we investigated the physical properties and spatial distribution of the hot ISM along two sight lines with combined analysis. The one direction are selected to clarify the ambiguity of the results of LMC X-3 and we choose bright blazer PKS 2155-304 (z =0.117). We observed PKS 2155-304 with *Chandra* grating for absorption induced from the hot ISM and adjacent field with *Suzaku* CCD for emission induced from the hot ISM. To investigate hot ISM in the Galactic center region, we observed 4U 1820-303 located 7.6 kpc away in the Galactic bulge. *Chandra* grating and *Suzaku* CCD are also used for observation.

The local O VII and O VIII absorption lines are clearly measured in the PKS 2155-304 absorption spectra , and the O VII, O VIII and Ne IX emission lines are clearly detected in the adjacent fields. Then assuming vertically exponential distributions of the gas temperature and the density, we perform a combined analysis of the absorption and emission data. The gas temperature and density at the Galactic plane are determined to be $3.2(+0.7, -0.6)\times10^6$ K and $1.3(+9.7, -0.7)\times10^{-3}$ cm^{-3} and the scale heights of the gas temperature and density are 2.2(+13, −2.1) kpc and 5.1(+3.9, −4.7) kpc, respectively.

As for 4U 1820-303 direction, the O VII, O VIII and Ne IX absorption lines are measured in the absorption spectra. In the emission spectra the O VII, O VIII, Ne IX, Ne X and Fe complex emission lines are clearly detected with higher intensities. Then we compare the absorption and emission data with the best fitted exponential disk model in PKS 2155-304 direction with plane parallel assumption. Though the absorption lines are explained only by the model, the emission lines in 0.5–1.1 keV are clearly insufficient. This suggest that additional hot ISM exist behind 4U 1820-303. The temperature of the additional components are 4.0 (+0.4, -0.4)$\times10^6$ K and 1.0(+0.8,-0.5)$\times10^6$ K. Then we perform a combined analysis with two simple models. The first is that two uniform plasma exist in front of 4U 1820-303 and no plasma exist behind. The temperature of the plasmas are 3.2 (+0.2,-0.2) $\times10^6$ K and 1.0 (+0.2,-0.2) $\times10^6$ K. The second is that one uniform plasma exist in front of 4U 1820-303 and the other exist behind. The temperature of the front plasma is 1.7 (+0.2,-0.2) $\times10^6$ K and the temperature of the behind plasma is 3.9 (+0.4,-0.3) $\times10^6$ K.

The comparable value of the exponential disk in the PKS 2155-304 and LMC X-3 direction suggest that global hot ISM surrounding our Galaxy has common structure. However in the Galactic center direction, this model failed to explain the emission spectra and this suggest hotter dense ISM exist in the Galactic center. The metal abundance, pressure at the mid-plane and the energy loss rate suggest that the hot ISM originate SNe.

Acknowledgment

In the five years for this work, I have been supported by many people. I could not become what I am without their cordial help.

Firstly I am very grateful for my supervisor associate professor N. Y. Yamasaki who has always guided and encouraged me to write this doctor thesis. When I was confused and went to her room, she always said to me "calm down Toshi, think it yourself!" strictly and kindly. I feel myself fortunate to meet such a great adviser.

And I would like to thank professor K. Mitsuda. I have learned a lot of things from his strict attitude for deriving and treating scientific result.

Assistant professor Y. Takei who gave me many advices and much vigor. When I went to his room, he looked at me and said "Oh, you are coming again!" with laughter. He is one of the most reliable person in my life.

I can not help to say thanks again and again to Dr. Yangsen Yao, who is my co-researcher and teacher of absorption analysis. When I went to USA, he helped me not only research but life in Boulder Colorado. With he and his family, I went many places and made priceless memories. After backing Japan, he also helped and encouraged me. I'd like to appreciate he and his family.

Professor Dan Mccammon has great knowledge and experience about interstellarmedium research, I would thank for useful discussion with him.

Professor Daniel Q. Wang gave a lot of advice and insight to me.

I also wish to thank S. Ito who is a secretary of our laboratory. I always feel comfortable with her tasty tea and sweet cake.

I thank colleagues and friends at ISAS: K. Shinozaki, T. Yoshino, H. Kawahara, K. Mukai, H. Yoshitake, I. Mitsuishi, N. Sekiya, W. Hirakoso. A little discussion and a lot of trivial talk with them is precious memory for my life.

And my fellows, M. Koshiishi, S. Kimura, T. Miyakawa, R. Nakamura, M. Ushio, A. Sekiguchi, J. Katsuta who shares so much with me. We have come long way together, and I want to say "Thank you all".

Finally, I would acknowledge my father, mother and sister for their great help. The support of my mind when I seem to fail is always their kindness and tenderness. And I am very grateful to Y. Mihoko who always make me relaxed and give a lot of happiness.

Contents

Chapter 1

Introduction

In the diffuse background emission from radio to gamma ray bands, early rockets observations followed by the *SAS-3*, *HEAO-1*, and *ROSAT* all sky surveys (RASS) showed that the whole sky is shining much more brightly in the 0.1 – 1 keV X-ray band than could be explained by the extragalactic background seen at higher energies. The nature of the soft X-ray emission was solved by a high resolution X-ray microcalorimeter experiment by a sounding rocket (McCammon et al. (2002)). Many emission lines from Oxygen, Neon, Iron etc. were clearly detected and proved that the origin of the soft X-ray emission is hot interstellar medium (hot ISM) with T$\sim 10^6$K. It was gradually realized that these hot ISM prevail our galaxy and play important roles in feedback control of star formation and circulation of the elements not only within our galaxy but with intergalactic mediums. It is of great importance to investigate the physical properties and spatial distribution of the hot ISM in revealing the history of our galaxy.

Recently, *Suzaku* , *Chandra* and *XMM-Newton* offer new approaches to investigate hot ISM. Absorption analysis using high-resolution grating instruments onboard *Chandra* and *XMM-Newton* are enable to detect the X-ray absorption lines by hot plasma. Indeed absorption lines of z=0 are detected in spectra of many galactic and extragalactic sources (e.g. Bregman & Lloyd-Davies (2007), Fang et al. (2006)). Also, X-ray CCDs onboard *Suzaku* have high energy resolution enough to distinguish O VII Kα and O VIII Kα lines from plasma of T$\sim 10^6$ K. Yoshino et al. (2009) used 14 blank sky observation by *Suzaku* and analyzed surface brightness ratio of O VII and O VIII lines in each direction. They revealed that the temperature of the hot ISN distributed very narrow range as $\sim$ 0.2 keV. However, the physical properties of the hot ISM such as density, length, and scale height were still poorly understood, because only the integrated physical quantities along the line of sight are obtained by emission or absorption observation alone.

Yao et al. (2009) constrained the physical properties of the hot ISM along the LMC X–3 sight line with new approach; combined analysis of the emission and absorption data. This method based on simple fact that the absorption intensity is proportional to the column density of ions, while the emission line intensity is proportional to the integration of the density square. Thus we can solve the density and the length of the hot ISM. They estimated gas temperature and density at the Galactic plane and their scale heights as 3.6 (+0.8, -0.7) $\times 10^6$ K and 1.4 (+2.0, -1.0) $\times 10^{-3}$ cm^{-3} and 1.4 (+3.8, -1.2) kpc and 2.8 (+3.6, -1.8) kpc, respectively. However, there are still possibilities that this parameters are caused by local structure. Moreover LMC located only 50 kpc away and they can not exclude the possibility

that the emission comes from behind LMC.

In this thesis, we investigated the hot ISM along two sight lines to exclude the ambiguity of the LMC X-3 results and reveal the global structure of the hot ISM. We analyzed absorption and emission spectra separately to estimate the contribution of the hot ISM steadily. Then we perform combined analysis along two sight lines and present the physical properties and spatial distribution of the hot ISM. The global structure and origins of the hot ISM are also discussed.

This thesis consists of the following structure. Past observation of hot ISM are reviewed in Chapter 2. Chapter 3 describe the instrumentation. In Chapter 4 we explain the data reduction as well as the observed fields. The results of spectral analysis are presented in 5 and 6. The discussion and conclusion are given in Chapter 7 and 8.

In this thesis, errors are quoted at 90% confidence level in the text and tables, unless otherwise described. The solar abundance means the abundance given in Anders & Grevesse (1989).

Chapter 2

Review

2.1 the Soft X-ray Diffuse Background and Hot Interstellar Medium

In this thesis we use the word, the soft X-ray diffuse background (SXDB), for the X-ray emission below $\sim$ 1 keV which is spatially unresolved to individual sources. A certain fraction of the SXDB comes from extragalactic faint sources which is just an extension of the cosmic X-ray background (CXB) in hard X-ray band to the lower energy range.

However, the SXDB cannot be explained only by the extension and the remaining emission is considered to consist of emission from highly ionized ions, such as C V, O VII, O VIII, Fe XVII, and Ne IX, in solar neighborhoods, in our Galaxy, and possibly in the intergalactic space. We will search the nature and origin of this soft X-ray emission from the ionized plasma.

2.1.1 Brief history; early observations to Rosat all sky survey

A sounding rocket experiment, which gave a birth to X-ray astronomy, also discovered the existence of diffuse X-ray background (Giacconi et al. (1962)). The Geiger-counters onboard this rocket were sensitive to X-rays in 2-6 keV (2-8Å) range and the Galaxy is nearly transparent for X-rays in this energy range (Figure 2.1). The isotropic nature of this background emission suggests that its origin is extragalactic. Now, the X-ray background in this energy range is believed to originate active galactic nuclei (AGN) and with the deep observations of the *Chandra* and *XMM-Newton* observatories, about 80 % of the background has been actually resolved into point sources. We call this unresolved X-ray emission above 2 keV, the cosmic X-ray background (CXB).

How is the X-ray background below 2 keV? Extrapolation of the CXB spectrum below 2 keV cannot explain the total intensity. Existence of this discrepancy was first noted by sounding rockets experiments in 1970s. The observations were conducted by using proportional counters with thin entrance windows and slats collimators. From these early observations, it was noted that the intensity in the carbon band (C band), the energy band below the C K edge (284 eV) is anti-correlated with Galactic neutral hydrogen column density of the direction. Since the X-rays in the C band are not transparent to the Galactic neutral medium of 10^{21} cm^{-2} (Figure 2.1), the anti-correlation cannot be explained by the absorption of

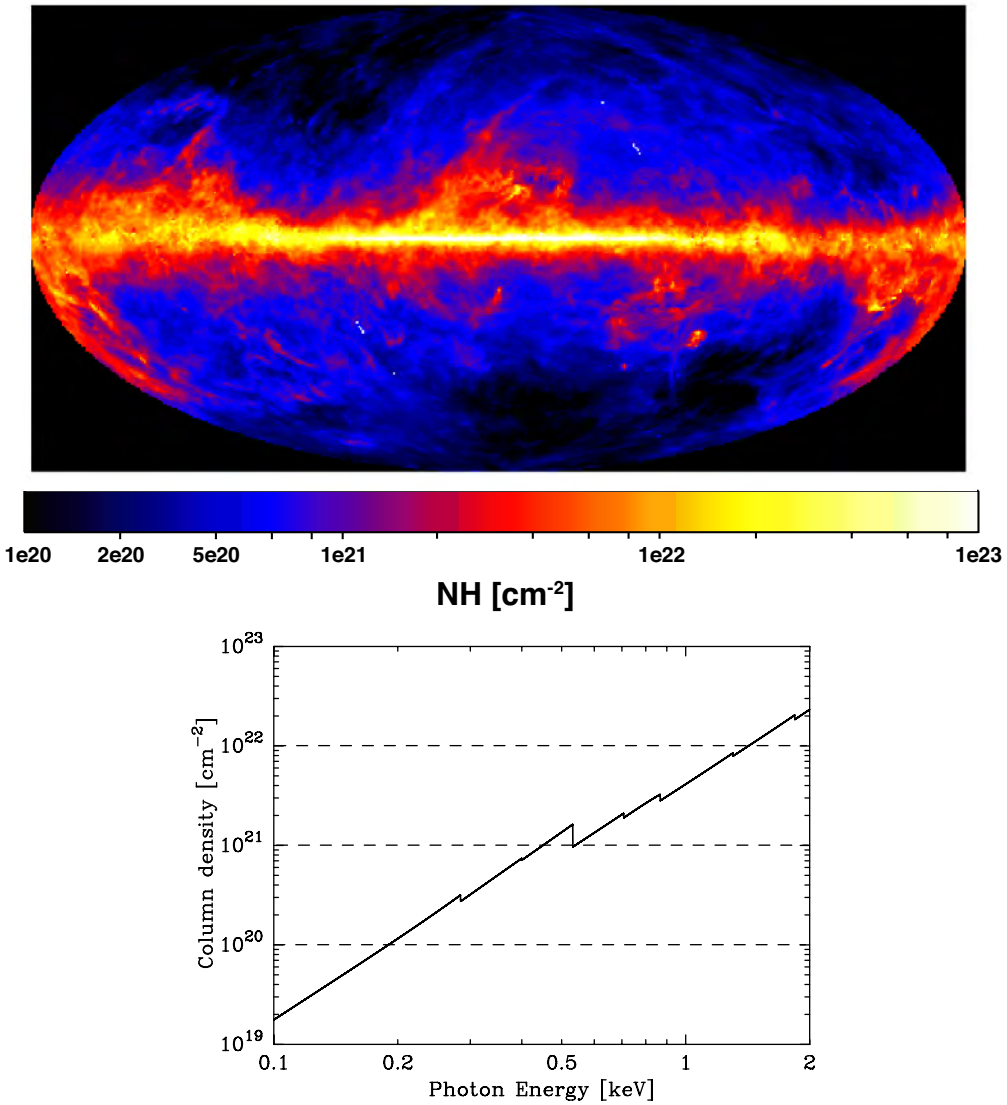

Figure 2.1: (top): Column density of the neutral hydrogen in the ISM. This map is derived from IRAS 100 μm survey. Intensity of 100 μm ($I_{\rm IR}$) is converted to neutral hydrogen column density($N_{\rm H}$) by the following equation; $N_{\rm H} = A_1 \times I_{\rm IR} + A_2$. Here $A_1 = 1.4 \times 10^{20}$ [cm^{-2} MJy^{-1} sr^{-1}], $A_2 = 0.15 \times 10^{20}$ [cm^{-2}] (bottom): Energy dependence of column density at which the optical depth is equal to unity assumed the ISM of solar abundance of metals. For 0.2 keV photons our galaxy is opaque, while for photons with energy larger than 2 keV our galaxy is almost transparent.

emission outside the bulk of Galactic neutral medium. It was interpreted as a displacement of the neutral matter by hot plasma close to the solar neighborhood; the solar system is surrounded by a hot plasma of $T \sim 10^6$ K, and in the directions in which the hot plasma is more extended, the column density of the neutral matter is smaller (Tanaka & Bleeker, 1977). The cavity of neutral medium was called the Local Bubble. NaI (λ5890Å) is also a good tracer for cold (T<1000 K) gas and Lallement et al. (2003) made 3D absorption maps of the local distribution of neutral gas using 1005 sight-lines with Hipparcos. This map

clearly show the local cavity of $\sim$ 100 pc radius. If 1×10^6 K plasma fill in this cavity at a thermal pressure approximately equal to the total pressure of the surrounding ISM, it can well reproduce the observed X-ray excess in C band. This is the idea of Local Hot Bubble (LHB), but the temperature and emission measure of the LHB is not evaluated. Detection of the O VI absorption line towards several OB stars located within the solar neighborhood by the *Copernicus* strongly support this idea that Local Cavity was filled with a highly ionized and low density hot plasma (Jenkins (1978)). However, recently as discussed in Lallement et al. (2003) and Welsh & Shelton (2009) the temperature of the gas filling the LHB is controversial because some observation results support the order of lower temperature $\sim 10^{4-5}$ K plasma instead of 1×10^6 K plasma model. Using ultra violet of 90–256Å, Hurwitz et al. (2005) gave an upper limit of the emission measure of 4×10^{-4} cm^{-6} pc for the plasma with temperature of $10^{5.6-6.4}$ K. Emission measure of a few $\times 10^{-3}$ cm^{-6} pc is required to reproduce the observed emission and modifications to the LHB are needed.

In 1996, surprising X-ray emission was found by Lisse et al. (1996). The origin of this emission was a comet which is considered to be too cold to produce X-ray. The mechanism to produce such X-ray emission was argued, and now it is believed to be the dominant mechanism that charge transfer from cometary neutrals to heavy ions in the solar wind (Cravens (1997)). The discovery of X-rays induced from the charge exchange process between the neutral medium and ions in the solar wind (Solar Wind Charge eXchange: SWCX) can contribute to the SXDB instead the LHB. This process can occur everywhere in the heliosphere and Cox (1998) and Cravens (2000) suggested that a significant fraction of the SXDB can be explained by the SWCX in the interplanetary space.

X-rays induced from the LHB and/or the SWCX arise within a few hundred pc from the sun. Shadowing observations using molecular cloud revealed that almost all the emission in C band originate such foreground sources (Snowden et al. (1993), Kuntz et al. (1997)). However, they also discovered that in energy range larger than 0.5 keV, dominant fraction of the X-rays come from behind such cloud.

2.1.2 ROSAT all sky map in 3/4 keV band

The *ROSAT* all sky survey (*RASS*) carried out in 1990 to 1991 by the *ROSAT* improved the angular resolution of the SXDB by using an X-ray focusing mirror and the Position Sensitive Proportional Counter (PSPC). Because of the high spatial resolution of the system ($\sim 1'$), point sources up to 4×10^{-13} erg s^{-1} cm^{-2} had been removed from the map. Figure 2.2 shows the soft X-ray diffuse background maps by *RASS* in the 3/4 keV band (the R45 band), which are approximately 0.47–1.21 keV (effective area of *ROSAT* PSPC is shown in Figure 2.3). The contribution of X-ray point sources, geocoronal solar wind charge exchange, solar scattered X-ray and particle background are excluded from the map as far as possible.

There is a large enhancement in the Galactic center region expanding to $\pm 30^\circ$ in longitude and latitude. Snowden et al. (1997) suggest that hot ISM confined in the Galactic center region could reproduce the enhancement. Molecular cloud of $\sim 10^{21}$ cm^{-2} hydrogen column density is opaque to the soft X-rays lower than 1 keV. Shadowing observations using such molecular cloud located few kpc away give us important clues(Park et al. (1997), Almy et al. (2000)). The foreground emission certainly exist, however a large fraction of the enhancement comes from behind the clouds.

In the high b direction, there still comes weak and isotropic emission. If |b| is larger than

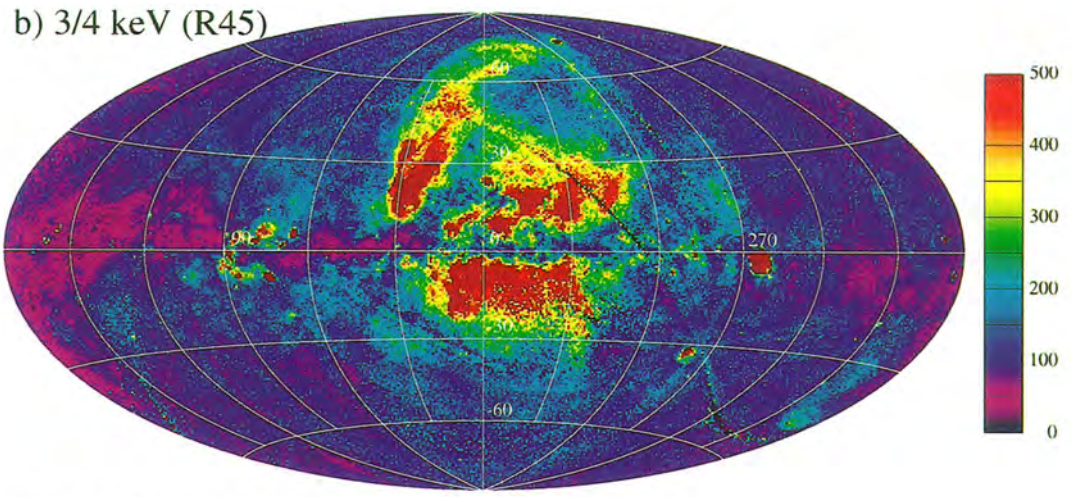

Figure 2.2: *ROSAT* all sky survey (RASS) map of the R45 (3/4 keV) band diffuse background in Galactic coordinates by Snowden et al. (1997). *ROSAT* intensity units are 10^{-6} counts s^{-1} arcmin^{-2}. Nearly isotropic emissions can be seen in middle to high latitude and large mission feature exist toward Galactic center.

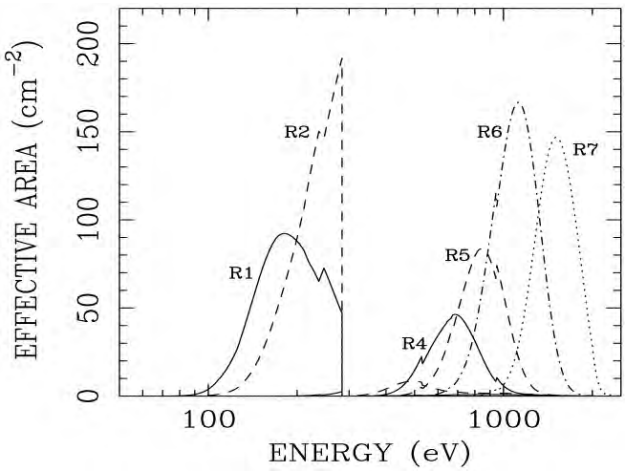

Figure 2.3: Effective area of the *ROSAT* position sensitive proportional counter (PSPC). R1–R7 correspond to the each energy band. R1; 0.11–0.284 keV, R2; 0.14–0.284 keV, R4; 0.44-1.01 keV, R5; 0.56–1.21 keV, R6; 0.73–1.56 keV, R7; 1.05–2.04 keV.

30° the galaxy become transparent to the X-rays of 0.5 keV and higher energy and photons can reach the Earth through the neutral medium in the disk. Shadowing observations (Snowden et al. (1993), Kuntz et al. (1997)) revealed a large fraction comes from behind the clouds and indicate that the origin expand beyond the Galactic disk.

2.1.3 Hot ISM in the high galactic latitude

2.1.3.1 Hints from the shadowing observations

The MBM-12 molecular cloud is located in the direction well outside the local Galactic structures and in a reasonably high latitude $(\ell, b) = (159°.2, -34°.5)$. The distance is about 100 pc, although there is uncertainty from 60 ± 30 to 275 ± 65 pc (Smith et al., 2005). The column density of the cloud itself is high enough($N_{\rm H}$= 4×10^{21}cm^{-2}) to block X-rays below 1 keV in dens region . Thus this cloud is very useful to distinguish the emission within $\sim$ 100 pc. Snowden et al. (1993) observed MBM 12 with *ROSAT* and compare X-ray ($I_{\rm X}$) and 100 μm IR intensity (I_{100}). The IR emission originate dust grains in the neutral ISM and its intensity is proportional to the column density of the neutral medium ($N_{\rm H} + N_{\rm H_2}$). To investigate the origin of the emission, they construct a simple emission model as following equation,

$$I_X = I_{Local} + I_{Distant} \times \exp(-\sigma\alpha I_{100}) \tag{2.1}$$

where I_{Local}, $I_{Distant}$, σ and α are X-ray intensity arise in front of the cloud, X-ray intensity arise behind the cloud, absorption cross section averaged in the energy range of the band and coefficient to convert I_{100} to the $N_{\rm H} + N_{\rm H_2}$. They fitted R12, R45 and R67 band data with this model. The $I_{\rm X}$ and I_{100} show clear correlation and the model fitted the data well (Figure 2.4). Figure 2.4 clearly indicates significant fraction of R45 and R67 emission come from distant part beyond MBM 12 and almost all R12 emission originate within 100 pc. Kuntz et al. (1997) perform same shadowing analysis against high latitude molecular clouds and obtained same results.

The shadowing experiments using these clouds clearly shows that a significant fraction of the SXDB in R45 band arises behind the cloud. It is likely to arise from distant part of the galaxy; mostly above or beyond the bulk of absorption in the Galactic disk. Kuntz & Snowden (2000) separated this component in the *ROSAT* all sky map utilizing the directional dependence of the absorption column density. They argued that the emission spectrum can be described by a two-temperature thermal emission model of temperatures $\sim$ 1.2 and 2.9×10^6 K (k$T \sim 0.10$ and 0.25 keV). However there is no constraint on distance other than absorption. Moreover *ROSAT* did not have sufficient energy resolution to distinguish emission lines which characterize plasma of T $\sim 10^6$ K and it is hard to constrain the origins conclusively.

2.1.3.2 Discovery of hot ISM by high resolution spectroscopy

Hot ionized gas of a temperature about 10^6 K is characterized by X-ray Kα lines such as O VII ($\sim$ 560 eV), O VIII ($\sim$ 650 eV), Ne IX ($\sim$ 920 eV)and Ne X ($\sim$ 1020 eV). The energy range of these lines are from 0.3 to 1 keV. Left panel of Figure 2.5 shows emissivity (Λ) of these representative lines for a gas in collisional ionization equilibrium state adopting the solar abundance , which are calculated by using publicly available software SPEX[1]. The intensity (I) of a line emission is calculated as

$$I = \frac{1}{4\pi} \int \Lambda(T) n_{\rm e} n_{\rm H} {\rm d}l \tag{2.2}$$

[1]http://www.sron.nl/index.php?option=com_content&task=view&id=125&Itemid=279

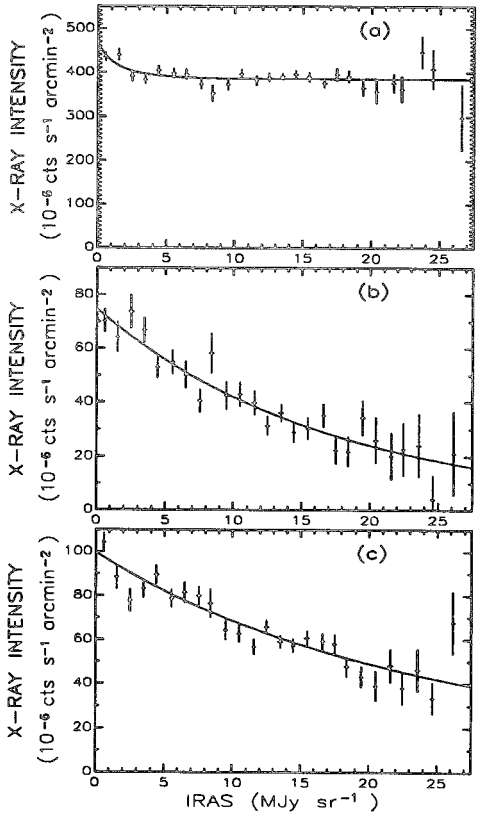

Figure 2.4: Plot of averaged X-ray intensity vs. IRAS 100 μm intensity with the best fit models displayed as solid curved for (a) 1/4 keV = R12 band , (b) 3/4 keV = R45 band and (c) 1.5 keV = R67 band.

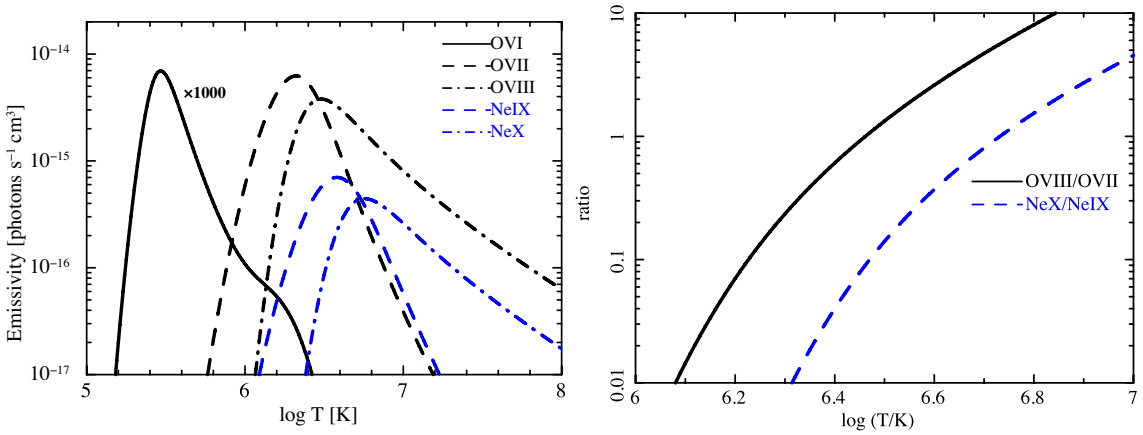

Figure 2.5: (left): The emissivity of O VI, O VII, O VIII, Ne IX and Ne X line as a function of temperature for a gas in the collisional ionization equilibrium state. The emissivity of O VI is scale down by a factor of 1000 for demonstration purpose. (right): The line intensity ratio of O VIII to O VII and Ne X to Ne IX as a function of temperature.

where $n_{\rm e}$ and $n_{\rm H}$ are number density of electron and hydrogen of the plasma and the integration is done along the line of sight. Assuming isothermal plasma, this equation could be modified as

$$I = \frac{1}{4\pi}\Lambda(T)\int n_{\rm e}n_{\rm H}{\rm d}l \tag{2.3}$$

$$= \frac{1}{4\pi}\Lambda(T)EM \tag{2.4}$$

where the emission measure (EM) is defined as

$$EM = \int n_{\rm e}n_{\rm H}{\rm d}l \tag{2.5}$$

For instance, the emission measure of a plasma of which $n_{\rm H}$ is 1.0×10^{-3} and length along the sight line is 100 pc is calculated as $1.2\cdot1.0\times10^{-3}\cdot1.0\times10^{-3}\cdot3.1\times10^{20}\sim3.7\times10^{14}{\rm cm}^{-5}$ where the ratio of hydrogen to electron is 1.2. Assuming the temperature as $2\times10^6=10^{6.3}$ K, the intensity of the O VII line in line unit (LU=photons ${\rm s}^{-1}$ ${\rm cm}^{-2}$ ${\rm str}^{-1}$) is estimated as $1/4\pi\times\Lambda(10^{6.3})EM\sim0.2$ LU. As shown in right panel of Figure 2.5, the intensity ratio of O VIII to O VII and Ne X to Ne IX are sensitive to the temperature in the range from 10^6 K to 10^7 K. As the oxygen and neon is abundant elements, spectroscopic study of oxygen and neon lines are the powerful tracer and tool to reveal the distribution and nature of hot plasma in and around our galaxy.

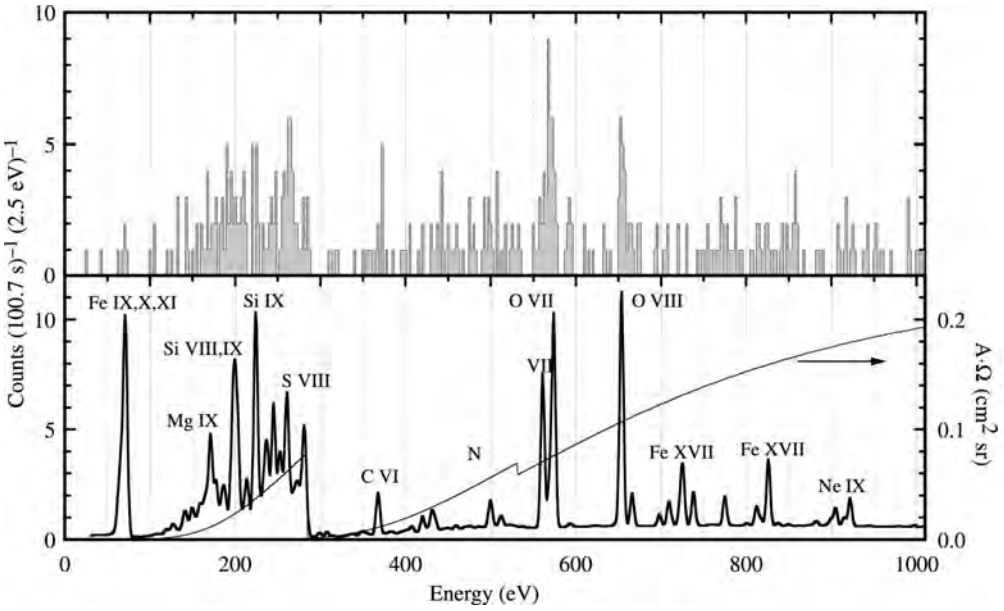

Figure 2.6: Observed spectrum from high latitude region with X-ray microcalorimeter (top) and the normal abundance two-temperature thin thermal model (bottom). Figure is taken from McCammon et al. (2002).

Finally, the SXDB in this direction was clearly resolved into line emissions with the sounding rocket experiment conducted by the Wisconsin and NASA/GSFC group (McCammon

et al., 2002). The rocket carried an X-ray microcalorimeter array operated at the cryogenic temperature of 60 mK. The field of view of the detector was confined by a collimator to the sky area of $\sim$ 1 str. By virtue of high energy resolution, the X-ray spectrum was resolved into number of emission lines (Figure 2.6). With spectroscopic analysis they conclude that these lines originate thin thermal plasmas of T $\sim 10^6$ K i.e. hot ISM. Here after we use hot ISM to mean hot components of the interstellar medium of T $\sim 10^6$ K. Though these hot ISM could not be confined in the Galactic disk, we use this word to mean the hot plasma belongs to Milky-Way Galaxy. Comparing the line intensities and the previous SXDB and CXB observations, McCammon et al. (2002) estimated that about 40 % of the emission in the *ROSAT* R45 band are the extragalactic continuum emission, i.e. the CXB.

2.1.3.3 The hot ISM at the several direction observed with *Suzaku*

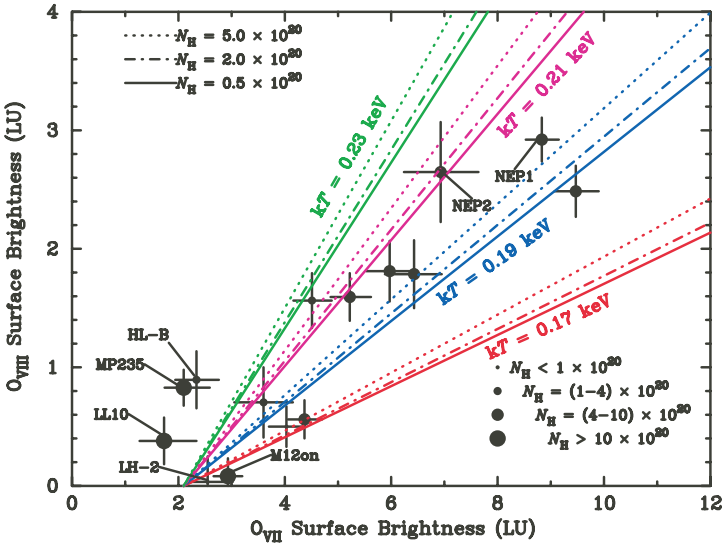

Figure 2.7: Relation between O VII and O VIII surface brightnesses for the 14 sky fields observed with *Suzaku* . The horizontal and vertical bars of data points show the 1 σ errors of the estimation. The contribution of O VII Kβ emission in the Gaussian function for O VIII Kα is subtracted . The diagonal lines show the relation between O VII and O VIII , assuming an offset O VII emission of 2.1 LU and emission from a hot plasma of the temperature and the absorption column density shown in the figure. The Galactic absorption column density of the observation fields are indicated by the maker size of the data points. The short names of five data points on the intensity floor of O VII emission are also shown. from Yoshino et al. (2009)

Suzaku , launched in 2005, also have enough energy resolution ($\sim$ 100 eV at 1 keV) to distinguish dominant lines. Using *Suzaku* data of 14 blank sky at $65° < l < 295°$, Yoshino et al. (2009) revealed that the surface brightness of O VII and O VIII lines in these directions could be understood in a scheme; constant foreground emission + distant emission with almost constant ratio of O VIII to O VII (Figure 2.7). As shown in Figure 2.5, the ratio of

O VII to O VIII is very sensitive to the temperature and Yoshino et al. (2009) revealed that the temperature of the hot ISM deduced from O VII and O VIII ratio distributed very narrow range as 0.19-0.23 keV (2.2-2.7$\times 10^6$ K). The mechanism to maintain the plasma in this narrow temperature range is not understood. In addition to the constraint to the temperature of the hot ISM, they also found that the foreground components can be described as ~ 2 photons s^{-1} cm^{-2} str^{-1} (LU) and ~ 0 LU respectively. The constant foreground emission can be considered to originate from the SWCX + LHB emission.

2.1.3.4 The hot ISM through absorption line observation

Absorption observation is also useful to investigate hot ISM. As shown in Figure 2.8, ionization fraction is sensitive to the temperature and can be a good tracer. The intensity of the radiation is reduced by absorption as

$$I(\nu)/I_0(\nu) = \exp(-\sigma(\nu)CD_{\rm ion}) \tag{2.6}$$

where $\sigma(\nu)$ and $CD_{\rm ion}$ are absorption cross section and column density of the absorbing ion. Column density is defined as

$$CD = \int n_{\rm ion} dl \tag{2.7}$$

where $n_{\rm ion}$ is number density of ion and the integration is done along the line of sight. Actually, the absorption depth intricately depends on the velocity dispersion (v_b) of the plasma with line broadening mechanism and it is indispensable to determine the velocity dispersion to derive column density. However, for now X-ray detectors do not have enough energy resolution to determine v_b only by a line shape and alternatively invariant quantity, equivalent width (EW), is used to determine the column density. EW measures the net flux removed from the incident beam by the absorption line. The EW induced from the column density with a constant velocity dispersion is plotted as a curve of growth (Figure 2.9) and it is used to estimate the column density with EW.

Absorption observations also succeeded to detect the X-ray absorption lines at $z = 0$, in particular the helium- and hydrogen-like O VII and O VIII lines, in spectra of many galactic and extragalactic sources (e.g. Yao et al. (2005), Williams et al. (2007)). Recently, Fang et al. (2006) and Bregman & Lloyd-Davies (2007) find that the O VII absorption line can always be detected in an AGN spectrum as long as the spectrum is of high signal-to-noise ratio. Column density of O VII ions induced by these observations are similar values of $\sim 10^{16}$ cm^{-2}. However it is difficult to conclude that these absorptions lines originate hot ISM around our galaxy only by the absorption observations because the energy resolution of the detectors are not enough to distinguish the redshift of the local group.

2.1.4 Hot ISM in the galactic bulge region

All sky survey in radio band identified several large loop structures in the Galaxy (Berkhuijsen (1971)). Their morphology and size suggest that they are old super nova remnants or super bubbles and actually surface brightness (Σ) and diameter (D) of the Loops are well consistent with Σ-D relation of the SNRs (Urošević (2003)). Among these radio loops, Radio Loop I (Loop I) is a giant one of 58°±4° radius centered at $(\ell, b) = (329.0°\pm1°, 17.5°\pm3.0°)$ (Berkhuijsen (1971)). Distance to the North Polar Spur (NPS), the brightest part of the

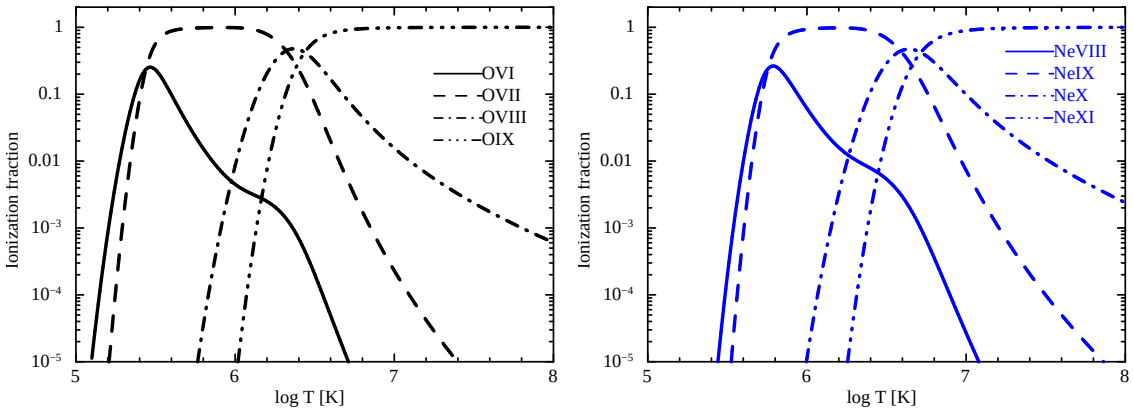

Figure 2.8: (left): Ionization fraction of O VI, O VII, O VIII and O IX as a function of temperature. (right): Ionization fraction of Ne VIII Ne IX Ne X and Ne XI as a function of temperature.

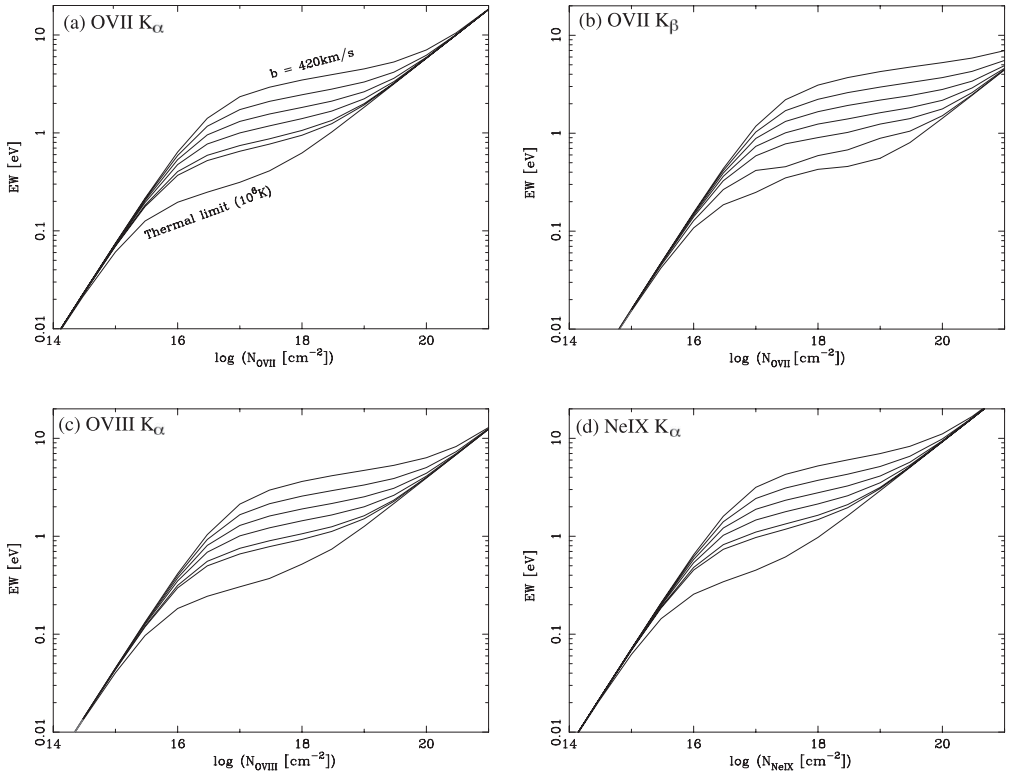

Figure 2.9: Curve of growth for (a) O VII K_α, (b) O VII K_β (c) O VIII K_α , and (d) Ne IX K_α absorption lines. The different curves correspond to different values of velocity dispersion parameter, v_b = 32 (for O) or 29 (for Ne), 60, 100, 140, 200, 280, and 420 km s^{-1} . The minimum value of b corresponds to thermal motion with T=10^6 K, and the maximum, 420 km s^{-1}, to the upper limit of the intrinsic line width of the O VII K_α line.

Loop I and aligned with the ℓ=30° contour, was determined by the optical polarization to be 100±20 pc away. From the morphology and distance, Scorpio-Centaurus OB association

is considered to be the origin of Loop I and therefore the distance to the center of the shell would be close to Sco-Cen association at a distance of $\sim$ 170 pc. Loop I well lap the enhanced region and this can easily lead the conclusion that all enhancement could be due to Loop I.

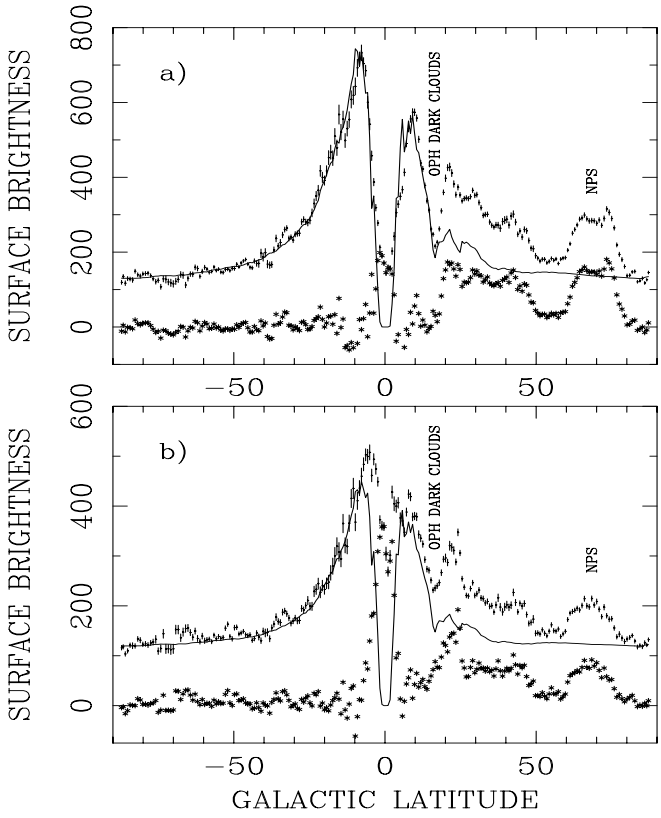

Figure 2.10: Cuts across the Galactic plane at l=335°±5° in the (a) 3/4 kev (0.4–1.2 keV) band and (b) 1.5 keV (0.7–2.0 keV) band. The upper points (with error bars) are the data, the curve is the prediction of the hot plasma model and the lower points are the residuals. Surface brightness is in units of 10^{-6} counts s^{-1} $arcmin^{-2}$. Emission from Loop I including the NPS is not modeled. (from Snowden et al. (1997))

To confirm this possibility, Snowden et al. (1997) summed 3/4 keV (0.4–1.2 keV) and 1.5 keV (0.7–2.0 keV) RASS data with 10° wide centered on $\ell = 353°$ and check the latitude profile of the surface brightness (Figure 2.10). They found that the intensity distribution of the enhancement in $b > 0°$ region and $b < 0°$ significantly different. They construct an isothermal ($T=10^{6.6}$ K) cylinder plasma model with an exponential fall-off in density with height above the plane and showed that the enhancement in $b < 0°$ can be well explained by this model. The hot gas cylinder is located at galactic center and its required radius is 5.6 kpc, with a electron density of 3.5 10^{-3} cm^{-3} in the disk and scale height of 1.9 kpc. And they also suggest that in $b > 0°$ region, this model always produce less intensity than the data and this implies additional component such as Loop I. The total luminosity of plasma cylinder was 1.9×10^{39} erg s^{-1} and mass was $\sim 3 \times 10^7 M_\odot$.

This X-ray Bulge model was supported by shadowing observations using molecular cloud at a distance of few kpc. Park et al. (1997) observed (ℓ, b)=($\sim$10°,0°) direction using

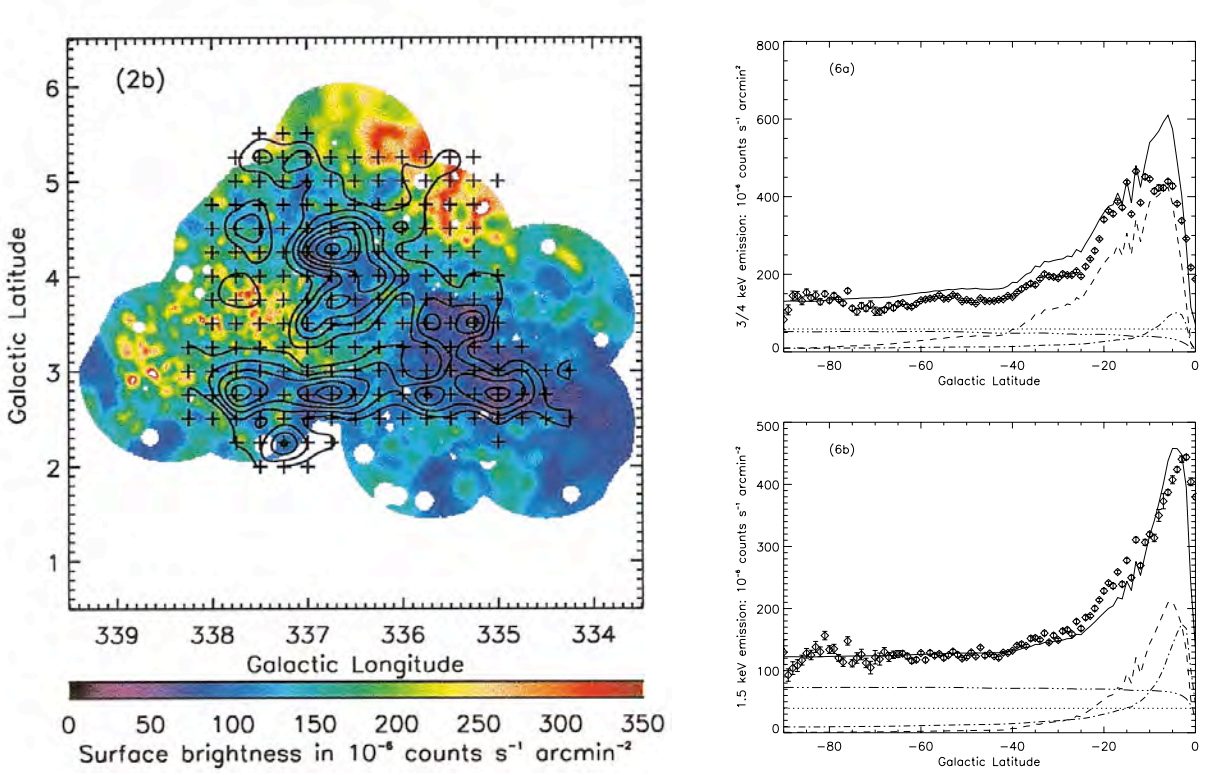

Figure 2.11: (left): CO data (contours) and 3/4 keV X-ray data (color scale) used for the shadowing study in Almy et al. (2000). The X-ray data have been smoothed for display purposes only, using the adaptive smoothing algorithm described by Snowden (1994). Locations of CO observations are indicated by plus symbols. (right): (a) Emission in the 3/4 keV band (R4+R5) averaged over longitude $| l | \leq 30°$ in 1° high-latitude strips. Diamonds show the data from the ROSAT all sky survey. The solid line shows total modeled emission, consists of polytrope emission, emission from normal stars, CXB, unabsorbed foreground emission. (b) The same except showing the emission in the 1.5 keV band (R6+R7). (from Almy et al. (2000))

ROSAT in which molecular cloud located at $\sim$ 3 kpc away shows correlation with the X-ray shadows. They compare X-ray intensity in on-cloud and off-cloud direction to find that almost 40% of the emission in both 3/4 and 1.5 keV band come from behind the cloud. This number is derived without taking into account the absorption. Almy et al. (2000) also carried shadowing analysis using *ROSAT* PSPC data in (ℓ, b)=($\sim$337°,4°) (Figure 2.11). They construct emission model like Equation 2.1 and revealed more than 70% of the emission is due to X-ray source behind the cloud. Then they constructed polytrope model in which the force due to the gravitational potential gradient is balanced by a thermal pressure gradient, and unique solution is obtained once determining two from the parameter set; temperature, density and pressure at the Galactic center and polytrope coefficient. This model is physically self-consistent and can explain how the gas is confined at the Galactic center. They fit the polytrope pressure and polytrope coefficient parameters to the region of $| \ell | <\sim 50°$ and $-50° < b < 0$ of the *ROSAT* 3/4 keV map, where the enhanced region was included

and confusion from Loop I was excluded. They also include the CXB emission, emission from the stars and isotropic unabsorbed component to the model. The best fit results are as following; pressure at the Galactic center of $P_0/k_B = 1.8 \times 10^5$ cm^{-3} K, temperature of 8.2×10^6 K and electron density of 1.1×10^{-2} cm^{-3}. The total mass, thermal energy and bolometric luminosity are $\sim 1.3 \times 10^8 M_\odot$, $\sim 8.9 \times 10^{55}$ erg and $\sim 8.9 \times 10^{39}$ erg s^{-1}. Though this model certainly reproduce the total intensity of the RASS map, it is difficult to confirm the origin only by the RASS because of the poor energy resolution. The hot ISM model is only a possibility.

Absorption observation toward the enhancement region was also carried. X-ray binary 4U 1820-303 is located at (ℓ,b)=(2.8°,−7.9°), 7.6±0.4 kpc away and was observed by high resolution grating detector onboard *Chandra* and absorption line by O VII, O VIII and Ne IX were reported (Futamoto et al. (2004), Yao & Wang (2006a)). Futamoto et al. (2004) analyzed data using curve of growth and constrained the column density of each ion as log $N_{O\ \mathrm{VII}} = 16.2 - 16.7$, log $N_{O\ \mathrm{VIII}} = 15.9 - 16.5$ and log $N_{Ne\ \mathrm{IX}} = 15.7 - 16.1$. Velocity dispersion ($v_b$) was derived using joint analysis of O VII Kα and O VII Kβ to $v_b >$ 200 km s^{-1} and column density of O VIII and Ne IX are derived assuming same velocity dispersion constraint as O VII. Meanwhile Yao & Wang (2006a) used their *absline* absorption model and reported the column density as log $N_{O\ \mathrm{VII}} = 16.3(+0.2, -0.2)$, log $N_{O\ \mathrm{VIII}} = 16.4(+0.2, -0.2)$ and log $N_{Ne\ \mathrm{IX}} = 16.0(+0.1, -0.1)$ and velocitiy dispersion was 255 (+114,-90) km s^{-1}.

2.2 Combined Analysis: A New Approach to the Hot ISM

As shown in previous sections, hot ISM could be an absorber and emitter simultaneously. A combined analysis of high resolution absorption and emission data provides us with a powerful diagnostic of properties of the absorbing/emitting plasma (Figure 2.12). If the temperatue of the plasma can be determined with line ratio, as shown in Equation 2.2 and 2.6, emission measure (EM) and column density (CD) are derived from the emission and absorption data.

$$CD = \int n_{\mathrm{ion}} \mathrm{d}l \tag{2.8}$$

$$EM = \int n_{\mathrm{e}} n_{\mathrm{H}} \mathrm{d}l \tag{2.9}$$

This equation can be modified as

$$CD = \int A_{\mathrm{element}} f_{\mathrm{ion}}(T) n_{\mathrm{H}} \mathrm{d}l \tag{2.10}$$

$$EM = \int (1 + 2A_{\mathrm{He}}) n_{\mathrm{H}}^2 \mathrm{d}l \tag{2.11}$$

where A_{element}, A_{He} and $f_{\mathrm{ion}}(T)$ are the abundance ratio of the element to H, the abundance ratio of He to H and ionization fraction. In T$\sim 10^6$ K plasma, H and He are fully ionized and number density ratio of the H to electron can be described as $n_{\mathrm{e}}/n_{\mathrm{H}} = (1 + 2A_{\mathrm{He}})$. Assuming solar abundance and density distribution, this equation can be solved easily. Thus,

a combination of the emission and absorption data naturally yields the density and the size of the responding absorbing/emitting gas.

To perform this powerful analysis, absorption observation toward a point source and emission observation toward off field are needed (Figure 2.12). Since the ion fractions and emissivities are very sensitive to gas temperature at $\sim 10^6$ K, a combined analysis of these emission and absorption lines will also constrain the gas temperature and its distribution without the complexity of relative chemical abundances of metal elements.

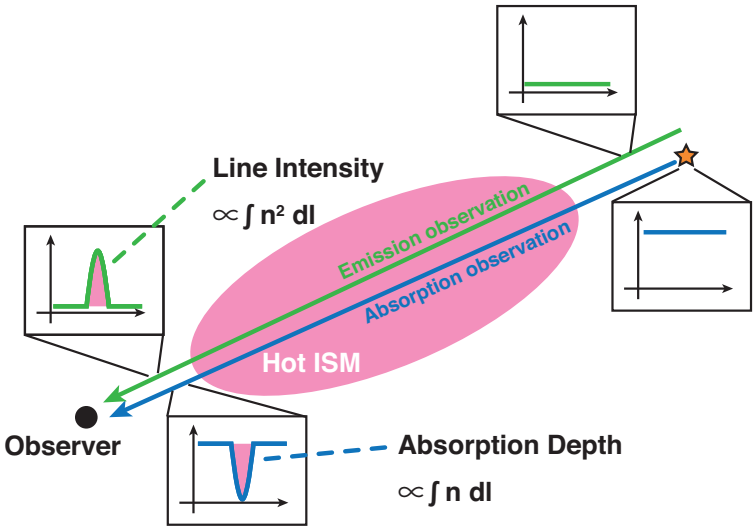

Figure 2.12: Schematic view of the observations to preform combined analysis.

Although this combined analysis method has long been applied in the ultraviolet wavelength band (Shull & Slavin, 1994), its application in the X-ray band just began. Complementing the high resolution absorption data observed with *Chandra* with the broadband emission data obtained with RASS, Yao & Wang (2007) firstly attempted to conduct the combined analysis in the X-ray band to infer the hot gas properties in our Galaxy. They also proposed a model for the Galactic disk assuming the temperature and density of the hot gas fading off exponentially along the vertical direction (exponential disk model). They concluded that the O VII and O VIII absorption lines observed along the Mrk 421 sight line are consistent with the Galactic disk origin. However it is difficult for RASS to distinguish emission lines, and emission spectra obtained with detectors of much higher energy resolution are needed for further analysis.

In Yao et al. (2009), we analyzed the absorption spectra of LMC X-3 obtained with the transmission grating (HETG) on board *Chandra* , and the emission spectra from the blank fields about 30' away from LMC X-3 observed with the CCD camera (XIS) on board *Suzaku* . There is a discrepancy of between temperature induced by the emission and absorption data alone. This indicate that the hot gas can not be isothermal. Instead, the exponential disk model can consistently explain the observations. We obtained scale heights of $1.4\xi^{-1}$ and $2.8\xi^{-1}$ kpc, and the mid-plane values of 0.31 keV and 1.4×10^{-3}cm^{-3} for the temperature and the density, respectively. Here, ξ is the volume filling factor of the hot gas. The scale height and temperature obtained by these analysis is surprisingly consistent with hot ISM observed in other galaxies.

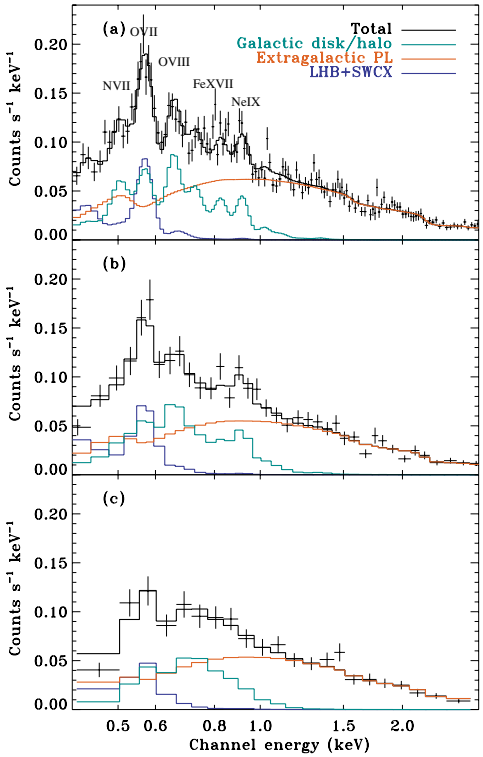

Figure 2.13: The emission spectra in the off-fields of the LMC X-3 sight line obtained with Suzaku XIS1. Three plot shows different observations. O VII, O VII and Ne IX emission lines are clearly detected. (Yao et al. (2009))

2.3 Observations of Other Galaxies

Edge-on spiral galaxies such as our own are also observed in X-ray band. Observation with high spatial and energy resolution detector revealed that some of spiral galaxies have hot ISM of $\sim 10^6$ K expanding a few kpc beyond the disk (hot halo).

Strickland et al. (2004) analyzed *Chandra* X-ray and optical Hα imaging data of 10 edge-on star-forming disk galaxies (seven starburst and three normal spiral galaxies) and found that eight of ten galaxies have X-ray halos besides two low mass normal spiral galaxy. The vertical distribution of X-ray intensities in these X-ray halos is well described by an exponential with scale height of few kpc. The total luminosity of X-ray halos in 0.3-2.0 keV are from $1.3 \times 10^{38} - 8.3 \times 10^{39}$ erg s^{-1}. They discussed the origin of such halo and raised a scenario, galactic superwind (see Section 2.4).

Also using *Chandra* X-ray and multi-wavelength data, Li et al. (2008) analyzed NGC 5775 in which starformation is spread out across the galactic disk, not only nuclear region. In the left panel of Figure 2.14, the X-ray, R band and Hα image and X-ray intensity contours are shown. X-ray image clearly shows clumpy structure of the hot halo. In right panel of Figure 2.14, the vertical diffuse X-ray intensity profiles are shown as a function of the distance from the galaxy's major axis. A dip in $\sim +0.5$ arcmin is due to the X-ray absorption by the tilted disk. They fit the profiles with an exponential law plus constant only in the negative side with z $<\sim$-0.2 arcmin to minimize the residual absorption effect of the

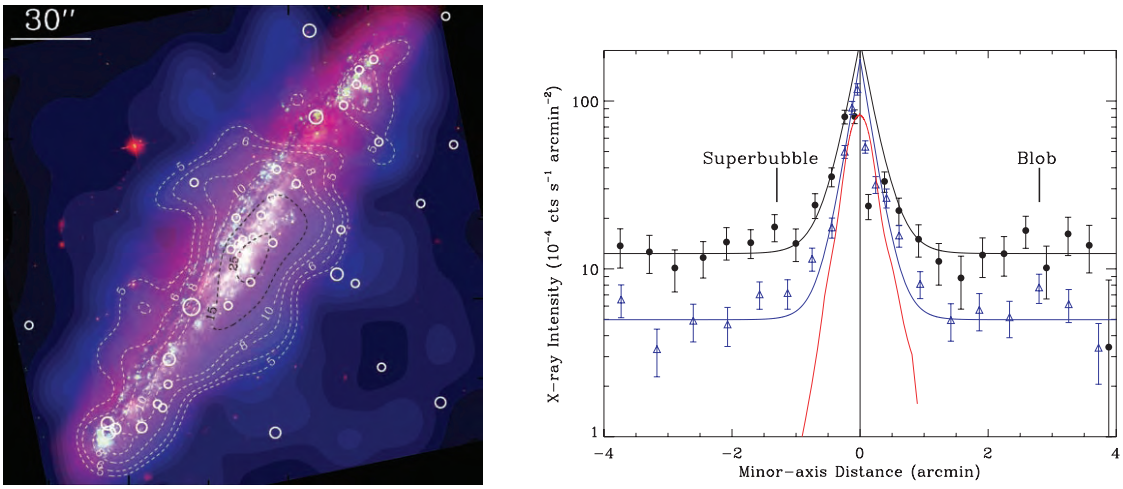

Figure 2.14: (left): Diffuse X-ray intensity and the HST/ACS images of NGC 5775 (in this figure 30" corresponds to 3.6 kpc): R band (red), Hα (green) and 0.3-1.5 keV (blue). The white circles mark the discrete sources detected. (right): Chandra ACIS-S intensity distributions of the diffuse emission as a function of the distance off the major axis of NGC 5775. The data are extracted in the 0.3–0.7 keV (black-filled circles) and 0.7-1.5 keV (blue triangles) bands (southwest as negative). The full width along the major axis of the disc used for averaging the intensity is 200 arcsec. The black and blue curves on the negative side show the best fit exponential law plus a local background, while on the positive side, the fitted curves have the same parameters and are only plotted for comparison. from Li et al. (2008)

disk and obtained the scale heights of 1.5 and 1.3 kpc for 0.3-0.7 and 0.7-1.5 keV respectively. The halo spectrum is well fitted with two thin thermal plasma model of 2.0×10^6 K and 6.6×10^6 K and the total luminosity of X-ray halo is 3.5×10^{39} erg s^{-1}. They suggested the relationships between star formation rate in the disk and soft X-ray intensity of the halo and described as a function $I_{0.3-2.0keV}(10^{38}\mathrm{ergs}^{-1}kpc^{-2}) \sim (2-8)I_{SF}(M_{\odot}yr^{-1}kpc^{-2})$.

From the point of metal abundance, Yamasaki et al. (2009) analyzed NGC 4631 data observed by *Suzaku* with its high energy resolution CCD camera. They clearly detected oxygen, neon, iron and other metal lines from the $\sim 10^6$ K plasma in halo and revealed the metal abundance, Z/O ratio, is explained well by type II SNe ejecta. However, as they discussed these estimation can be biased by several effect. One is charge exchange between galactic wind and gas in the halo, Another is metal depletion to the dust. The existence of temperature gradient can lead over- or underestimate of the metal abundance.

2.4 Possible Origin of the Hot ISM and Its Implications

How are the hot ISM maintained to be such high temperature? The most plausible origins of the energy and the mass in the hot ISM are SNe and infall primordial gases. Firstly, we will review the concept of the hot ISM in the global picture of galaxies and the roles of SNe.

The fundamental ISM model was first suggested by Spitzer (1968). Then Field et al. (1969) investigated the thermal process in the ISM, namely heating by cosmic rays and cooling by radiation. Assuming thermal balance and pressure equilibrium, two thermally stable phases are arisen. One is the cold cloud phase with the temperature of 30 K and the density of 100 cm^{-3}, and the other is a warm, partially ionized phase with the temperature of 8×10^3 K and the density of 0.4 atoms cm^{-3}. This picture was modified by the discovery of the hot gas component with the X-ray and UV observations. Several ideas were proposed to explain these hot components and McKee & Ostriker (1977) presented a revolutionary dynamic ISM model, in which the hot gas component with temperature of 5×10^5 K and the density of 3×10^{-3} atoms cm^{-3} occupies about 75% of the volume, and the surrounding warm ionized gas are distributed within the pervasive hot gas. The structure of this three phase ISM model is determined by SN rate and the total gas density. Because in the low SN rate and/or high density environment, the two-phase structure arises by the thermal balance and in high SN rate and low density environment, the three-phase structure arises. Norman & Ikeuchi (1989) presented "Chimney" model, in which the SN rate is not too high to fill the ISM with hot components and the density is enough low not to be cooled too much. If a number of SNe occurs in small regions like OB association, it make a large bubble which likely to expand upward to the halo and blow up the hot gases to the halo region like "Chimney". This mechanism can produce the hot ISM with newly synthesized metals exist high above the disk. Another idea to convey hot gases to the halo region is "Galactic fountain" (Shapiro & Marchant (1976)). In this model, the hot gases produced by SNe float above by the buoyant force and cooled in the halo. Finally these gases re-fall into the disk and this upward-downward motion seems like a "fountain". "Galactic superwind" (Strickland (2002)) is the idea to explain hot gases expanding a few kpc above the disk discovered by the observation of other galaxies. This wind is triggered by starburst activity in the galactic core region. O and B stars born in the starburst eject large amounts of kinetic energy through stellar wind and SNe and blow out ISM with a velocity more than 100 km s^{-1}. In any case, SNe produce hot gases and the hot ISM can transport metals within galaxies and/or toward the intergalactic space. In this sense, the hot ISM is important to understand the material circulation and chemical evolution in galaxies. In our Galaxy, quantitative study of this hot ISM is still underway.

Next, we introduce the primordial gas infall briefly. It is well known that a large fraction ($\sim$ 50%) of the baryon in present universe exist as intergalactic medium (Cen & Ostriker (1999)). However it is difficult to investigate these tenuous gas with recent detectors and the physical properties of these primordial gases are not well understood. Some of these gases are in self-gravitational state and the other are falling into galaxies and clusters. From numerical simulation and analytic method, the infall rate is calculated (e.g. White & Frenk (1991)) and also our galaxy is considered to be evolving through such accretion even now.

2.5 Summary of the Review

Understanding of the SXDB and evaluation of the hot ISM has been gradually increased since early observations in 1970's. So far, the SXDB is considered to consist of various components; solar wind charge exchange (SWCX) occurred in the geocorona and the heliosphere, supernova remnants (SNR), unresolved stars, hot ISM etc. Scale of these components are

from $\sim$ Earth's radius to $\sim$ kpc or more. In these components, hot ISM could produce most emissions ($\sim$ 50%) below 1 keV and it is gradually revealed that they prevail our galaxy and dominate large unignoreble of its X-ray luminosity. The hot ISM plays an important role in galactic evolution through chemical circulation and interaction between galaxies and intergalactic medium and itself contains the structure of the Galaxy as its physical properties and spatial distribution. However, still only little is known about hot ISM.

Now *Suzaku* and *Chandra* are bringing another great step in the research of hot ISM, with good energy resolution to separate the emission/absorption lines. The present status may be summarized as below.

- The SXDB in 3/4 keV band was dominated by emission from further (>1kpc) part of the Galaxy or beyond. These emission consist of many emission lines from highly ionized elements such as O, Ne and Fe. A thin thermal plasma of T $\geq 10^6$ K (the hot ISM) is the most possible origin of these emissions.

- In the high galactic latitude, The temperature of the hot ISM is distributed 2.2-2.7$\times 10^6$ K. The absorption observations detected O VII absorption lines in many directions with high S/N ratio data.

- In the galactic center direction, a large enhancement region exist. Hot ISM model confined in the Galactic center could reproduce this enhancement well. The nature and origins of this emission has not been understood well.

- Hot ISM along the LMC X-3 sight line can be explained with the exponential disk model with the combined analysis of the emission and absorption X-ray spectra.. However the global structure of the hot ISM is still unknown and the relation between the hot ISM in the high galactic latitude and the bulge region is also unknown.

The emission components of the SXDB and the neutral (cool) ISM are schematically illustrated in Figure 2.15 with arbitrary scale and the hot ISM image induced only from LMC X-3 direction is also included. Confirmation of the existence and scale of the widely spreading hot ISM and evaluation of their physical properties shall be studied quantitatively through this thesis.

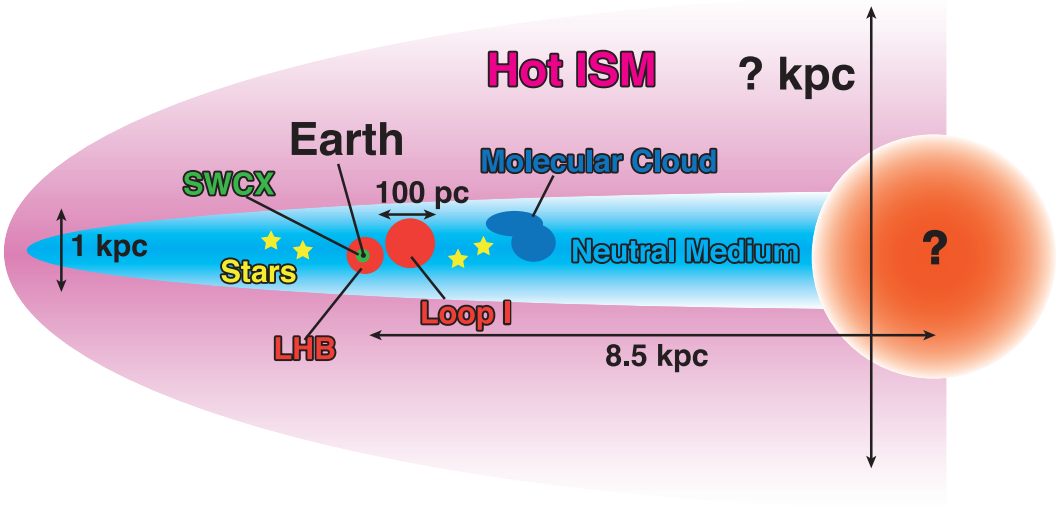

Figure 2.15: Schematic drawing of the possible components of the SXDB and cool absorbing materials in the Galaxy. Scale of each component is arbitrary.

Chapter 3

Instruments

This thesis deals with emission and absorption induced from hot ISM and we utilize a satellite *Suzaku* and *Chandra* . *Suzaku* is most suitable for investigating superposed emission on soft X-ray diffuse background because of its unprecedented energy resolution below $\sim$ 1 keV for spatially extended source. While *Chandra* is most suitable to detect absorption lines because its grating detector have intriguing energy resolution below $\sim$ 1 keV for point source.

The first section in this chapter outlines the *Suzaku* instrumentation. The second section, outlines the *Chandra* instrumentation.

3.1 The *Suzaku* satellite

3.1.1 Mission Description

Suzaku is placed in a near-circular orbit with an apogee of 568 km, an inclination of 31.9 degrees, and an orbital period of about 96 minutes. The maximum slew rate of the spacecraft is 6 degrees/min, and settling to the final attitude takes $\sim$ 10 minutes, using the star trackers.

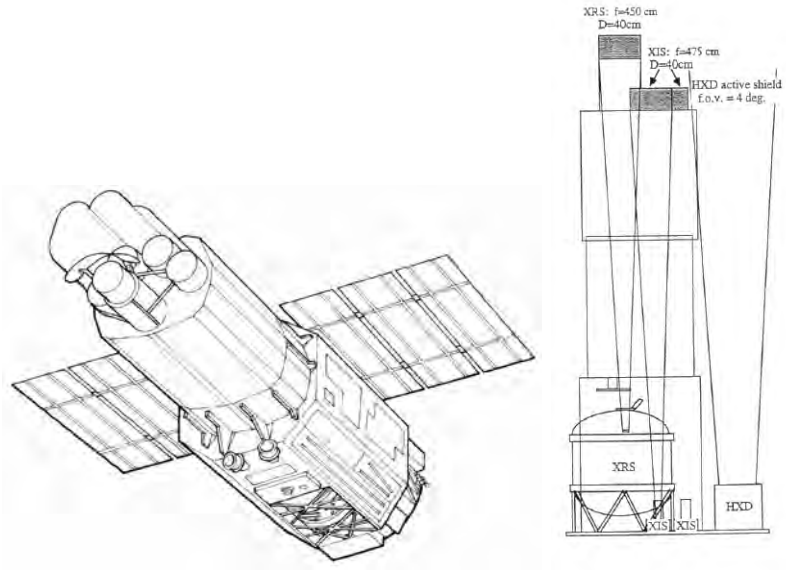

Figure 3.1: [Left] Schematic picture of the bottom of the *Suzaku* satellite. [Right] A side view of the instrument and telescopes on *Suzaku* .

The scientific payload of *Suzaku* (Fig. 3.1) initially consisted of three distinct co-aligned scientific instruments. There are four X–ray sensitive imaging CCD cameras (X–ray Imaging Spectrometers, or XISs), three front-illuminated (FI; energy range 0.4-12 keV) and one back-illuminated (BI; energy range 0.2-12 keV), capable of moderate energy resolution. Each XIS is located in the focal plane of a dedicated X–ray telescope. The second instrument is the non-imaging, collimated Hard X–ray Detector (HXD), which extends the bandpass of the observatory to much higher energies with its 10–600 keV pointed bandpass. The X–Ray Spectrometer (XRS) is no longer operational. And one of the X–ray Imaging sensor XIS-S2 became disabled. XRT–XIS modules and HXD operate simultaneously. In the study of this thesis, only XRT/XIS were used. The description of the HXD is hence omitted.

Table 3.2 summarizes the calibration items of XRT and XIS, the current status, and their expected accuracy. These values are the 90% limits, equivalent to 1.6σ. Note that the values listed are those required from the scientific purpose and ultimate goals which are possible to be realized on the basis of the instrument design, and are not measurement results.

3.1.2 X–Ray Telescopes (XRTs)

Suzaku has five light-weight thin-foil X–Ray Telescopes (XRTs). These are grazing-incidence reflective optics consisting of compactly nested, thin conical elements. Because of the reflectors' small thickness, they permit high density nesting and thus provide large collecting

Table 3.1: Overview of *Suzaku* capabilities

S/C	Orbit Apogee	568 km
	Orbital Period	96 minutes
	Observing Efficiency	$\sim 45\%$
XRT	Focal length	4.75 m
	Field of View	$17'$ at 1.5 keV
		$13'$ at 8 keV
	Plate scale	0.724 arcmin/mm
	Effective Area	440 cm^2 at 1.5 keV
		250 cm^2 at 8 keV
	Angular Resolution	$2'$ (HPD)
XIS	Field of View	$17.8' \times 17.8'$
	Bandpass	0.2–12 keV
	Pixel grid	1024×1024
	Pixel size	24 μm× 24 μm
	Energy Resolution	~ 130 eV at 6 keV
	Effective Area	340 cm^2 (FI), 390 cm^2 (BI) at 1.5 keV
	(incl XRT-I)	150 cm^2 (FI), 100 cm^2 (BI) at 8 keV
	Time Resolution	8 s (Normal mode), 7.8 ms (P-Sum mode)

Table 3.2: Error Budgets of Scientific Instrument Calibrations

	Calibration Item	October 2005	Requirement	Goal
XRT−I/XIS	On-axis effective area [a]	∼10%	5%	5%
	Vignetting	∼50%	5%	2%
	On-axis EEF [b]	∼20%	5%	1%
	Off-axis EEF [c]	∼30%	20%	2%
	Optical axis position in XIS	$\sim 0.5'$	$< 0.2'$	$<0.2'$
	Energy scale	0.3%	0.1%	0.1%
	Energy resolution (FWHM) at 5.9 keV	5%	1%	1%

Note ··· All the values quoted are preliminary.

a: Valid in the 1–8 keV band. Calibration uncertainty may become larger outside this energy range, especially below 0.3 keV (BI chip) and above 10 keV.

b: For all integration radii from $1'$-$6'$. No error on attitude control is included.

c: As on-axis but for all XIS f.o.v. No calibration is currently scheduled.

efficiency with a moderate imaging capability in the energy range of 0.2-12 keV, all accomplished in telescope units under 20 kg each.

Four XRTs on-board *Suzaku* (XRT-I) are used on the XIS, and the other XRT (XRT-S) is for the XRS. XRT-S is no more functional. The XRTs are arranged on the Extensible Optical Bench (EOB) on the spacecraft in the manner shown in Figure 3.2. The external dimensions of the 4 XRT-Is, however, are the same (See Table 3.3).

The angular resolutions of the XRTs range from $1.8'$ to $2.3'$, expressed in terms of half-power diameter, which is the diameter within which half of the focused X–ray is enclosed.

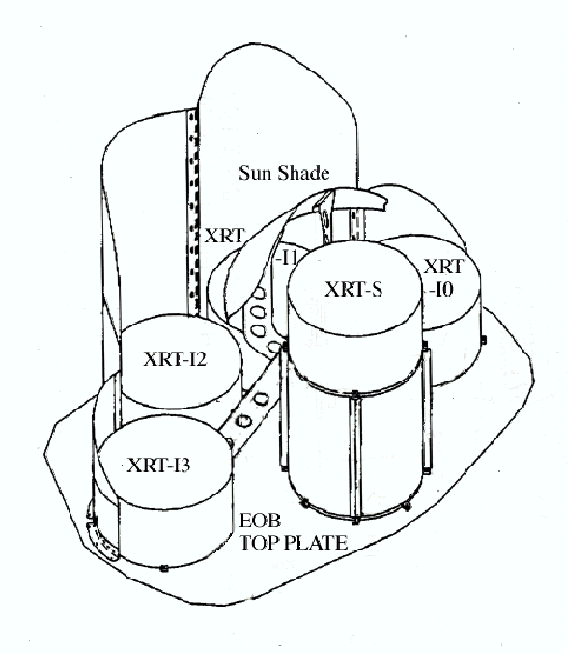

Figure 3.2: Layout of the XRTs on the *Suzaku* spacecraft.

Figure 3.3: A *Suzaku* X–Ray Telescope

Table 3.3: Telescope Dimensions and Parameters of XRT-I

Number of telescopes	4
Focal length	4.75 m
Inner Diameter	118 mm
Outer Diameter	399 mm
Height	279 mm
Mass/Telescope	19.5 kg
Number of nested shells	175
Reflectors/Telescope	1400
Geometric area/Telescope	873 cm^2
Reflecting surface	Gold
Substrate material	Aluminum
Substrate thickness	155 μm
Reflector slant height	101.6 mm

The angular resolution does not significantly depend on the energy of the incident X–ray in the energy range of *Suzaku* , 0.2-12 keV. The effective areas are typically 440 cm^2 at 1.5 keV and 250 cm^2 at 8 keV. The focal lengths are 4.75 m for the XRT-I. Individual XRT quadrants have their component focal lengths deviated from the design values by a few cm. The optical axes of the quadrants of each XRT are aligned within $2'$ from the mechanical axis. The field of view for XRT-Is is about $17'$ at 1.5 keV and $13'$ at 8 keV. (see also Table 3.1)

3.1.2.1 Basic Components of XRT

The *Suzaku* X–Ray Telescopes (XRTs) consist of closely nested thin-foil reflectors, reflecting X–ray at small grazing angles. An XRT is a cylindrical structure, having the following layered components: a thermal shield at the entrance aperture to help maintain a uniform temperature; a pre-collimator mounted on metal rings for stray light elimination; a primary stage for the first X–ray reflection; a secondary stage for the second X–ray reflection; a base ring for structural integrity and interface with the EOB of the spacecraft. All these components, except the base rings, are constructed in 90° segments. Four of these quadrants are coupled together by interconnect-couplers and also by the top and base rings (Figure 3.3). The telescope housings are made of aluminum for an optimal strength to mass ratio. Each reflector consists of a substrate also made of aluminum and an epoxy layer that couples the reflecting gold surface to the substrate.

3.1.2.2 Reflectors

In shape, each reflector is a 90° segment of a section of a cone. The cone angle is designed to be the angle of on-axis incidence for the primary stage and 3 times that for the secondary stage. They are 101.6 mm in slant length and with radii extending approximately from 60 mm at the inner part to 200 mm at the outer part. The reflectors are nominally 178 μm in thickness. All reflectors are positioned with grooved alignment bars, which hold the foils at their circular edges. There are 13 alignment bars at each face of each quadrant, separated at approximately 6.4° apart.

To properly reflect and focus X–ray at grazing incidence, the precision of the reflector figure and the smoothness of the reflector surface are important aspects. Since polishing of thin reflectors is both impractical and expensive, reflectors in *Suzaku* XRTs acquire their surface smoothness by a replication technique and their shape by thermo-forming of aluminum. In the replication method, metallic gold is deposited on extrusion glass mandrel ("replication mandrel"), of which the surface has sub-nanometer smoothness over a wide spatial frequency, and the substrate is subsequently bonded with the metallic film with a layer of epoxy. After the epoxy is hardened, the substrate-epoxy-gold film composite can be removed from the glass mandrel and the replica acquires the smoothness of the glass. The replica typically has $\sim$0.5 nm rms roughness in the mm or smaller spatial scale, which is sufficient for excellent reflectivity at incident angle less than the critical angle. The *Suzaku* XRTs are designed with on-axis reflection at less than critical angle, which is approximately inversely proportional to X–ray energy.

In the thermo-forming of the substrate, pre-cut, mechanically rolled aluminum foils are pressed onto a precisely shaped "forming mandrel", which is not the same as the replication mandrel. The combination is then heated until the aluminum softened. The aluminum foils acquire the figure of the properly shaped mandrel after cooling and release of pressure. In

Table 3.4: Design Parameters for Pre-collimator

	XRT-I
Number of Collimators	4
Height	32 mm
Blade Substrate	Aluminum
Blade Thickness	120 μm
Blade Height	22 mm
Height from Blade Top to Reflector Top	30 mm
Number of nested shells	175
Blade/Telescope	700
Mass/Collimator	2.7 kg

the *Suzaku* XRTs, the conical approximation of the Wolter-I type geometry is used. This approximation fundamentally limits the angle resolution achievable. More significantly, the combination of the figure error in the replication mandrels and the imperfection in the thermo-forming process (to about 4 micrometers in the low frequency components of the figure error in the axial direction) limits the angular resolution to about 1 minute of arc.

3.1.2.3 Pre-collimator

The pre-collimator, which blocks off stray light that otherwise would enter the detector at a larger angle than intended, consists of concentrically nested aluminum foils similar to that of the reflector substrates. They are shorter, 22 mm in length, and thinner, 120 micrometers in thickness. They are positioned in a fashion similar to that of the reflectors, by 13 grooved aluminum plates at each circular edge of the pieces. They are installed on top of their respective primary reflectors along the axial direction. Due to their smaller thickness, they do not significantly reduce the entrance aperture in that direction more than the reflectors already do. Pre-collimator foils do not have reflective surfaces (neither front nor back). The relevant dimensions are listed in Table 3.4.

3.1.2.4 Thermal Shields

The *Suzaku* XRTs are designed to function in a thermal environment of 20$\pm$7.5°C. The reflectors, due to its composite nature and thus its mismatch in coefficients of thermal expansion, suffer from thermal distortion that degrades the angular resolution of the telescopes in temperature outside this range. Thermal gradient also distorts the telescope in a larger scale. Even though sun shields and other heating elements on the spacecraft help in maintaining a reasonable thermal environment, thermal shields are integrated on top of the pre-collimator stage to provide the needed thermal control.

3.1.2.5 XRT-I Performance in Orbit

The four XISs (cf. Fig. 3.12) are true imagers, with a large field of view ($\sim 18' \times 18'$), and moderate spectral resolution. Each of the co-aligned XRTs features an X–ray mirror with an angular resolution (expressed as Half-Power Diameter, or HPD) of $\sim 2'$. Figure 3.5 shows the total effective area of the XIS+XRT, which includes features due to the elemental

Figure 3.4: A thermal shield.

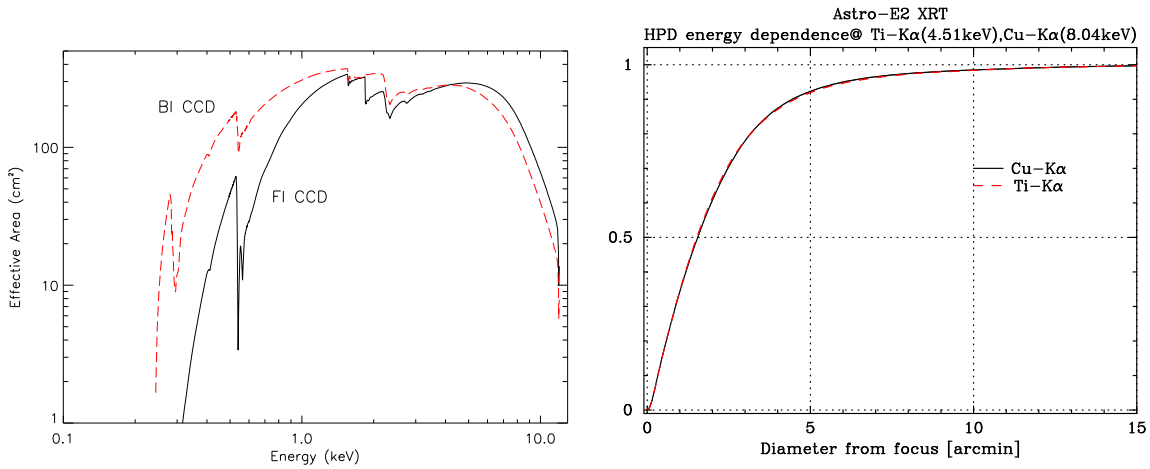

Figure 3.5: Left: XIS Effective area of one XRT + XIS system, for both the FI and BI chips. Right: The Encircled Energy Function (EEF) showing the fractional energy within a given radius for one quadrant of the XRT-I telescopes on *Suzaku* at 4.5 and 8.0 keV.

composition of the XIS and XRT. K-shell absorption edges from the oxygen (0.54 keV) and aluminum (1.56 keV) in the blocking filters are present, as well as a number of weak M-shell features between 2–3 keV arising from the gold in the XRT.

Fig. 3.6 shows the point spread functions (PSFs) of all the XRT-I+XIS modules, measured using a observation of a point-like source MCG−6−30-15. The preliminary HPD, with a typical statistical error of $\sim 0\farcm1$, ranges from $1\farcm8 \sim 2\farcm3$. Figure 3.7 shows the focal position of the XRT-Is, that the source is focused when the satellite points at the XIS aimpoint. The focal positions locate roughly within $0\farcm5$ from the detector center with an deviation of $\sim 0\farcm3$. This implies that the fields of view of the XIS coincides each other within $\sim 0\farcm3$.

A series of offset observations of the Crab observations were carried out in August and September at various off-axis angles of $0'$, $3\farcm5$, $7'$. The intensity of the Crab nebula is evaluated for each pointing and for each XIS module separately. By finding the maximum throughput angle, we also have obtained a direction of the optical axis of each telescope. The result is shown in Fig. 3.8. The optical axes locate roughly within $1'$ from the XIS aim

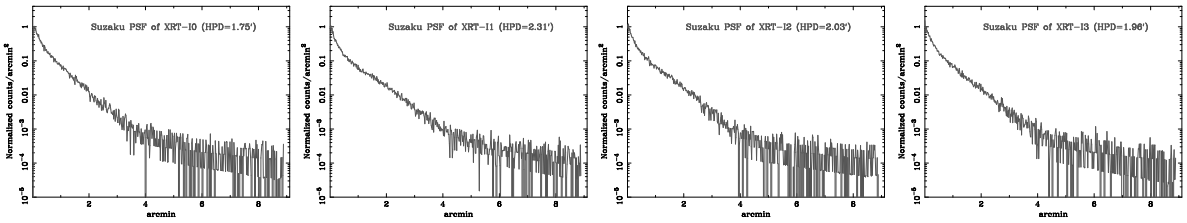

Figure 3.6: Point spread functions of the XRT–XIS modules for the XRT-I0 through XRT-I3 from left to right. Each PSF is normalized by the number of total photons collected over the entire XIS aperture.

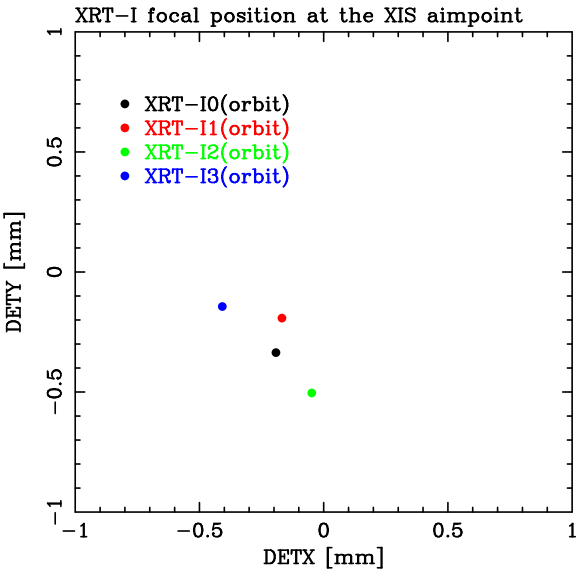

Figure 3.7: Focal positions at the XISs when the satellite points MCG−6−30-15 at the XIS aimpoint.

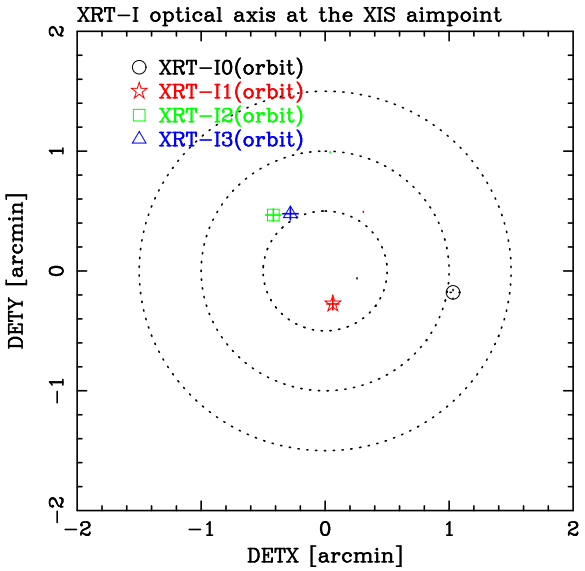

Figure 3.8: Optical axis directions of the XIS-S0 through S3. The optical axis of the XRT-I0 (XIS-S0), for example, locates at $(1\farcm0,\ -0\farcm2)$, which implies that the maximum throughput is achieved for XRT-I0 when the satellite points at the XIS aimpoint.

point. This implies that the efficiency of all the XRT-Is is more than 97 % even at 10 keV when we observe a point source on the XIS aimpoint. By assuming the detector efficiency is constant over the field of view, we determined the vignetting function as shown in Figure 3.9. The vignetting function is narrower in higher energy. The averaged effective area over the detector size of XIS (17.8′x17.8′) is 60%, 60% and 50% of the E.A on axis at 1.5, 4.5 and 8.0 keV, respectively.

In-flight stray-light observations were carried out with Crab at off-axis angles of 20′ (4 pointings), 50′ (4 pointing) and 120′ (4 pointing) in August and September. It was found that the pre-collimator works for reducing the stray light in orbit. Figure 3.10 shows angular responses of the XRT-I at 1.5 and 4.5 keV up to 2 degrees. The effective area is normalized at on-axis. The integration area is corresponding to the detector size of XIS ($17\farcm8 \times 17\farcm8$). The three solid lines in the plots correspond to different parameters of ray-tracing program

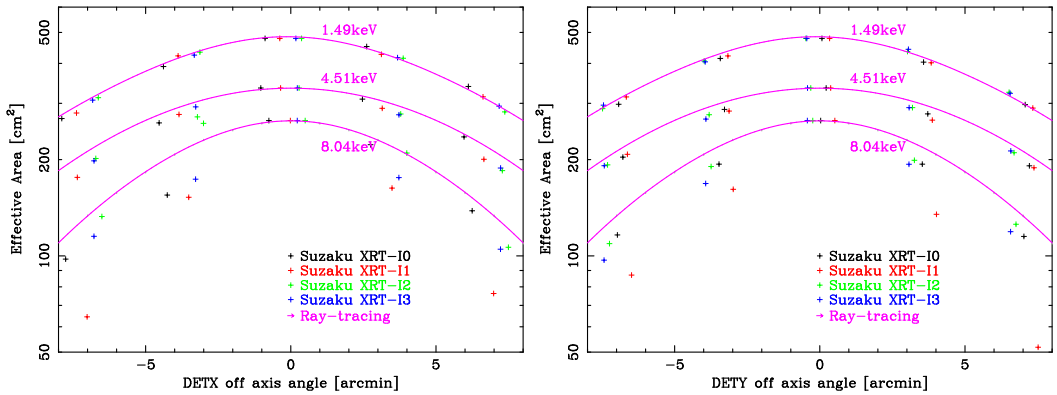

Figure 3.9: Vignetting curves of XRT-I at three different energies of 1.5, 4.5 and 8.0 keV. The three solid lines in the plots correspond to a parameter of ray-tracing program while the crosses are the preliminary XRT-I effective area "inferred" from the Crab pointings with some assumptions. The XRT-I effective area shown here does not includes either the quantum efficiency of the detector or transmissivity of the thermal shield and the optical blocking filter.

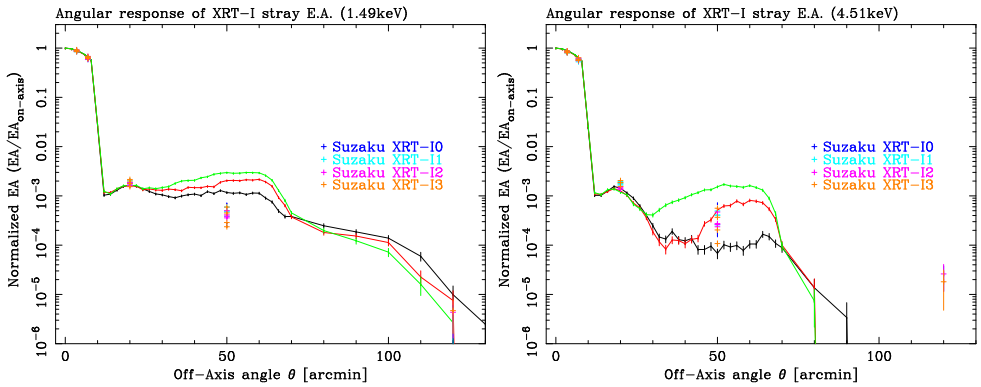

Figure 3.10: Angular responses of the XRT-I at 1.5 (left) and 4.5 keV (right) up to 2 degrees. The effective area is normalized at on-axis. The integration area is corresponding to the detector size of XIS ($17'.8 \times 17'.8$). The three solid lines in the plots correspond to different parameters of ray-tracing program while the crosses are the normalized effective area using the Crab pointings.

while the crosses are the normalized effective area using the Crab pointings. For example, the effective area of the stray lights at 1.5 keV is $\sim 10^{-3}$ at angles smaller than 70 arcmin off axis and $< 10^{-3}$ at angles larger than 70 arcmin off. The measured flux of stray lights are in good agreement with that of raytracing within an order.

3.1.3 X–ray Imaging Spectrometer (XIS)

3.1.3.1 Overview of the XIS

Suzaku has four X–ray Imaging Spectrometers (XISs), which are shown in Figure 3.11. These employ X–ray sensitive silicon charge-coupled devices (CCDs), which are operated in

Figure 3.11: The four XIS detectors before installation onto *Suzaku* .

a photon-counting mode, similar to that used in the ASCA SIS, *Chandra* ACIS, and *XMM-Newton* EPIC. The four *Suzaku* XISs are named XIS-S0, S1, S2 and S3, each located in the focal plane of an X–ray Telescope; those telescopes are known respectively as XRT-I0, XRT-I1, XRT-I2, and XRT-I3. Each CCD camera has a single CCD chip with an array of 1024×1024 picture elements ("pixels"), and covers an $18' \times 18'$ region on the sky. Each pixel is 24 μm square, and the size of the CCD is 25 mm $\times$ 25 mm. One of the XISs, XIS-S1, uses a back-side illuminated CCDs, while the other three use front-side illuminated CCDs.

A CCD has a gate structure on one surface to transfer the charge packets to the readout gate. The surface of the chip with the gate structure is called the "front side". A front-side illuminated CCD (FI CCD) detects X-ray photons that pass through its gate structures, i.e. from the front side. Because of the additional photo-electric absorption at the gate structure, the low-energy quantum detection efficiency (QDE) of the FI CCD is rather limited. Conversely, a back-side illuminated CCD (BI CCD) receives photons from "back," or the side without the gate structures. For this purpose, the undepleted layer of the CCD is completely removed in the BI CCD, and a thin layer to enhance the electron collection efficiency is added in the back surface. A BI CCD retains a high QDE even in sub-keV energy band because of the absence of gate structure on the photon-detection side. However, a BI CCD tends to have a slightly thinner depletion layer, and the QDE is therefore slightly lower in the high energy band. The decision to use only one BI CCD and three FI CCDs was made because of both the slight additional risk involved in the new technology BI CCDs and the need to balance the overall efficiency for both low and high energy photons. To minimize the thermal noise, the sensors need to be kept at ~ -90°C during observations.

To reduce contamination of the X–ray signal by optical and UV light, each XIS has an

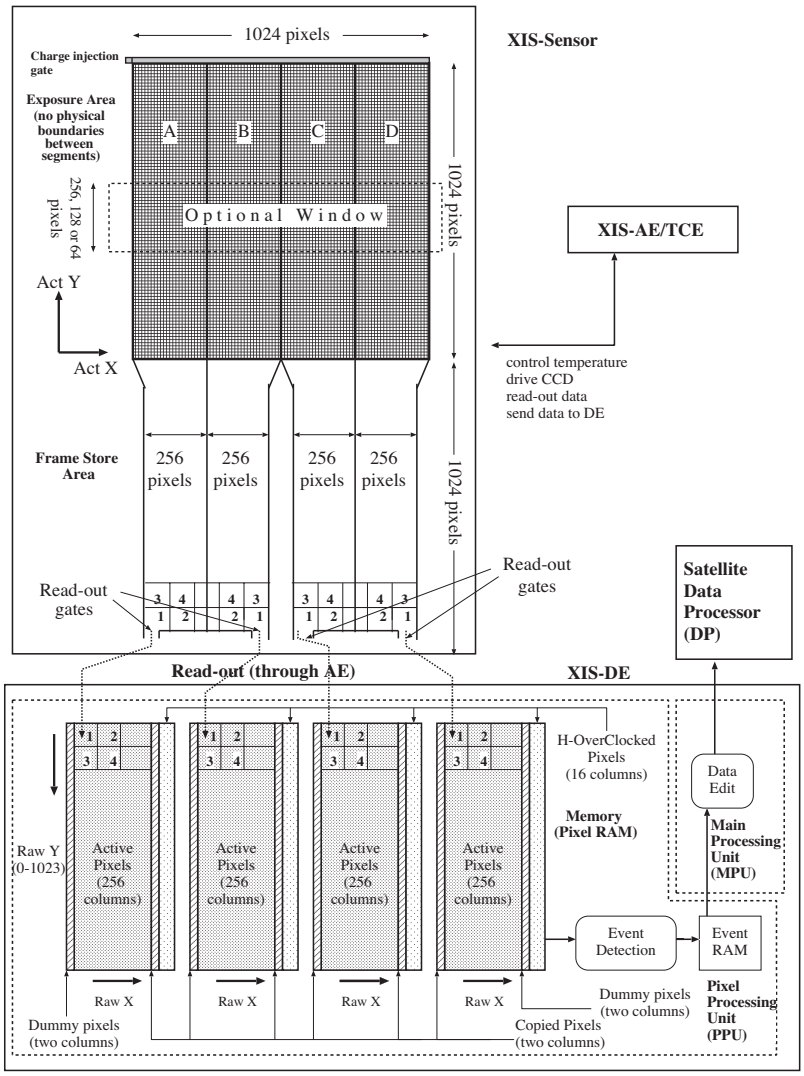

Figure 3.12: One XIS instrument. Each XIS consists of a single CCD chip with 1024×1024 X–ray sensitive cells, each 24 μm square. *Suzaku* contains four CCD sensors (XIS-S0 to S3), two AE/TCUs (AE/TCE01 and AE/TCE23), two PPUs (PPU01 and PPU23), and one MPU. AE/TCU01 and PPU01 service XIS-S0 and XIS-S1, while AE/TCE23 and PPU23 service XIS-S2 and XIS-S3. Three of the XIS CCDs are front-illuminated (FI) and one (XIS-S1) is back-illuminated (BI).

Optical Blocking Filter (OBF) located in front of it. The OBF is made of polyimide with a thickness of 1000 Å, coated with a total of 1200 Å of aluminum (400 Å on one side and 800 Å on the other side). To facilitate the in-flight calibration of the XISs, each CCD sensor has two ^{55}Fe calibration sources. One is installed on the door to illuminate the whole chip, while the other is located on the side wall of the housing and is collimated in order to illuminate two corners of the CCD. The door-mounted source will be used for initial calibration only; once the door is opened, it will not illuminate the CCD. The collimated source can easily be seen in two corners of each CCD. A small number of these X–rays scatter onto the entire CCD. In addition to the emission lines created by these sources, we can utilize a new feature of the XIS CCDs, "charge injection capability," to assist with calibration. This allows an

arbitrary amount of charge to be input to the pixels at the top row of the imaging region (exposure area), i.e. the far side from the frame-store region. The charge injection capability may be used to measure the CTI (charge transfer inefficiency) of each column, or even to reduce the CTI. The latter usage, so-called spaced-row CI, is successfully demonstrated in 2006.

Fig. 3.12 provides a schematic view of the XIS system. Charge clouds produced in the CCD by the X–rays focused by the XRT are accumulated on the exposure area for a certain exposure period (typically 8 s in the "normal" mode), and the data are transferred to the Frame Store Area (FSA) after each exposure. Data stored in the Frame Store Area are read-out sequentially by the AE, and sent to the PPU after the conversion to the digital data. The data are put into the memory in PPU named Pixel RAM. Subsequent data processing is done by accessing the Pixel RAM.

3.1.3.2 Pulse Height Determination, and Hot Pixels

When a CCD pixel absorbs an X–ray photon, the X–ray is converted to an electric charge, which in turn produces a voltage at the analog output of the CCD. This voltage ("pulse-height") is proportional to the energy of the incident X–ray. In order to determine the true pulse-height corresponding to the input X–ray energy, it is necessary to subtract *Dark Levels* and correct possible *optical Light Leaks*. XIS has capability to measure them on-board.

Hot pixels are pixels which always output over threshold pulse-heights even without input signals. Hot pixels are not usable for observation, and their output has to be disregarded during scientific analysis. In the case of XIS, hot pixels are detected on-board and their positions and pulse-heights are stored in the Hot-pixel RAM and sent to the telemetry. Thus, hot pixels can be recognized on-board, and they are excluded from the event detection processes. It is also possible to specify the hot pixels manually. There are, however, some pixels which output over threshold pulse-heights intermittently. Such pixels are called flickering pixels. It is difficult to identify and remove the flickering pixels on board; they are inevitably output to the telemetry and need to be removed during the ground processing. Flickering pixels sometimes cluster around specific columns, which makes it relatively easy to identify.

3.1.3.3 Pulse Height Distribution Function

Pulse hight distribution function for a monochromatic X-ray line can be represented by a Gaussian-like peak and low energy tail component. Energy resolution for Oxygen K_α line at 0.525 keV is about 50 eV (FWHM) for BI and 40 eV for FI (Koyama et al., 2007). The fraction of the low energy tail component of *Suzaku* XIS is very small in comparison with other X-ray CCDs used in X-ray satellite mission. Figure 3.13 shows energy spectra (pulse height distribution) for a monochromatic X-ray line emission at $E = 0.5$ keV, in comparison with X-ray CCDs on-board *XMM-Newton*. Clear peaks are shown by *Suzaku* FI/BI CCDs. Actual energy spectra of a SNR 1E0102-72 is shown in Figure 3.14. K_α lines of O VII (0.57 keV) and O VIII (0.65 keV) are clearly resolved with excellent energy resolution. Thus *Suzaku* is the most suitable to study diffuse hot plasma which can be characterized by emission lines.

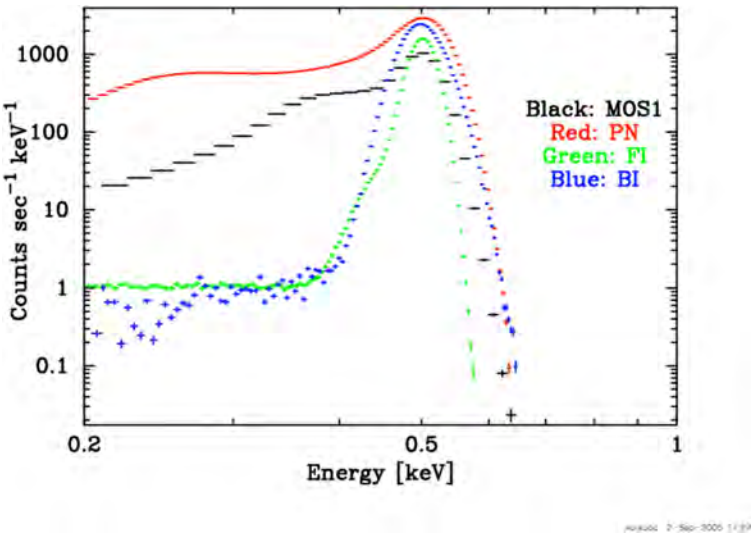

Figure 3.13: Energy spectra for monochromatic line by *Suzaku* FI/BI sensors and PN and MOS1 CCD onboard *XMM-Newton*.

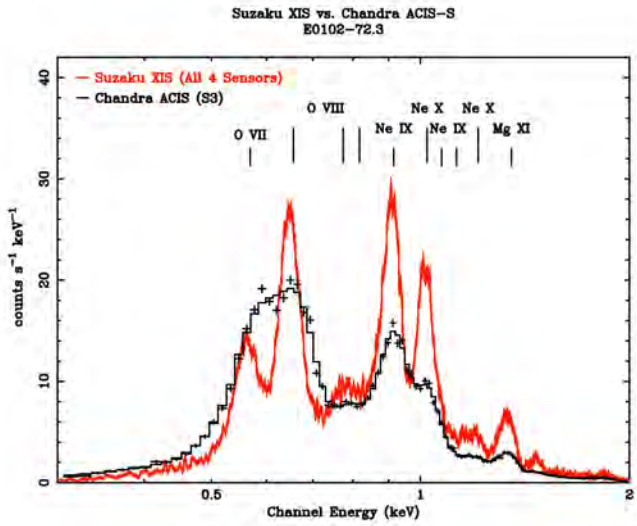

Figure 3.14: Energy spectra of SNR 1E0102-72 by a sum of 4 XIS of *Suzaku* and S3 CCD onboard *Chandra*. The O VII and O VIII lines are clearly resolved by *Suzaku* .

3.1.3.4 Photon pile-up

The XIS is essentially a position-sensitive integrating instrument, with the nominal interval between readouts of 8 s. If during the integration time one or more photons strike the same CCD pixel, or one of its immediate neighbors, these cannot be correctly detected as independent photons: this is the phenomenon of photon pile-up. Here, the modest angular resolution of the *Suzaku* XRT is an advantage: the central 3×3 pixel area receives 2% of the total counts of a point source, and $\sim$10% of the counts fall within $\sim$0.15 arcmin of the image center. The pile-up effect is negligible for the object studied in this thesis.

3.1.3.5 XIS background rate

All four XISs have low backgrounds, due to a combination of the *Suzaku* orbit and the instrumental design. Below 1 keV, the high sensitivity and energy resolution of the XIS-S1 combined with this low background means that *Suzaku* is the superior instrument for observing soft sources with low surface brightness.

In the XIS, the background originates from the cosmic X–ray background (CXB) combined with charged particles (the non-X–ray background, or NXB). When observing the dark earth (*i.e.* the NXB), the background rate between 1-12 keV in is 0.11 cts/s in the FI CCDs and 0.40 cts/s in the BI CCD; see Figure 3.15. Note that these are the fluxes after the grade selection is applied with only grade 0, 2, 3, 4 and 6 selected. There are also fluorescence features arising from the calibration source as well as material in the XIS and XRTs. The Mn lines are due to the scattered X-rays from the calibration sources. As shown in Table 3.5 the Mn lines are almost negligible except for XIS-S0. The O lines are mostly contamination from the day earth (3.1.3.5.2). The other lines are fluorescent lines from the material used for the sensor. Table 3.5 shows the current best estimates for the strength of these emission features, along with their 90% upper and lower limits.

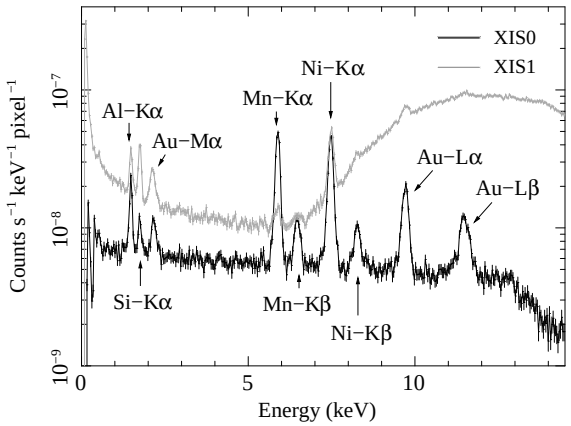

Figure 3.15: The night earth X-ray background (NXB) spectra for XIS-S0 and XIS-S1. The prominent fluorescent lines marked (See Table 3.5).

3.1.3.5.1 Out-of-time events X-ray photons detected during the frame-store transfer do not correspond to the true image, but instead appear as a streak or blur in the readout

Table 3.5: Energies and count rates of the line components in the NXB spectra.

Line	Energy	Count rate (10^{-9} cts s^{-1} pixel^{-1})			
	(keV)	XIS0	XIS1	XIS2	XIS3
Al-Kα	1.486	1.45 ± 0.11	1.84 ± 0.14	1.41 ± 0.10	1.41 ± 0.10
Si-Kα	1.740	0.479 ± 0.081	2.27 ± 0.15	0.476 ± 0.080	0.497 ± 0.082
Au-Mα	2.123	0.63 ± 0.093	1.10 ± 0.13	0.776 ± 0.097	0.619 ± 0.092
Mn-Kα	5.895	6.92 ± 0.19	0.43 ± 0.14	1.19 ± 0.13	0.76 ± 0.11
Mn-Kβ	6.490	1.10 ± 0.11	0.26 ± 0.13	0.40 ± 0.11	0.253 ± 0.094
Ni-Kα	7.470	7.12 ± 0.19	7.06 ± 0.37	8.01 ± 0.20	7.50 ± 0.20
Ni-Kβ	8.265	0.96 ± 0.10	0.75 ± 0.22	1.16 ± 0.11	1.18 ± 0.11
Au-Lα	9.671	3.42 ± 0.15	4.15 ± 0.49	3.45 ± 0.15	3.30 ± 0.15
Au-Lβ	11.51	2.04 ± 0.14	1.93 ± 0.48	1.97 ± 0.14	1.83 ± 0.14

The count rates are obtained from the whole CCD chip excluding the calibration source regions. Errors are 90 % confidence level.

Table 3.6: Origins of the fluorescence lines in the NXB spectra.

Line	Origin
Al-Kα	Optical blocking filter, housing, alumina substrate to mount CCD
Si-Kα	CCD (Si fluorescence line)
Au-Mα, Lα, Lβ	Housing, CCD substrate, heatsink
Mn-Kα, Kβ	Scattered X-rays from calibration sources
Ni-Kα, Kβ	Housing, heatsink

direction. These events are called out-of-time events., and they are an intrinsic feature of CCD detectors. Similar streaks are seen from bright sources observed with *Chandra* and *XMM-Newton* . Out-of-time events produce a tail in the image, which can be an obstacle to detecting a low surface brightness feature in an image around a bright source. Thus the out-of-time events reduce the dynamic range of the detector. Since XIS spends 25 ms in the frame-store transfer, about 0.3% ($= 0.025/8 \times 100$) of all events will be out-of-time events. However, because the orientation of the CCD chip is different among the sensors, one can in principle distinguish a true feature of low surface brightness and the artifact due to the out-of-time events by comparing the images from two or more XISs.

3.1.3.5.2 Day Earth Contamination When the XIS field of view is close to the day earth (i.e. Sun lit Earth), fluorescent lines from the atmosphere contaminate low-energy part of the XIS data, especially in the BI chip. Most prominent is the oxygen line, but the nitrogen line may be also noticed (see Fig. 3.15–right). These lines are mostly removed when we apply the standard data screening criteria (XIS FOV is at least 20 degree away from the day earth) during the ground processing. However, small amount of contamination can remain. This contamination may be further reduced if we subtract appropriate background. This subtraction, however, may be imperfect.

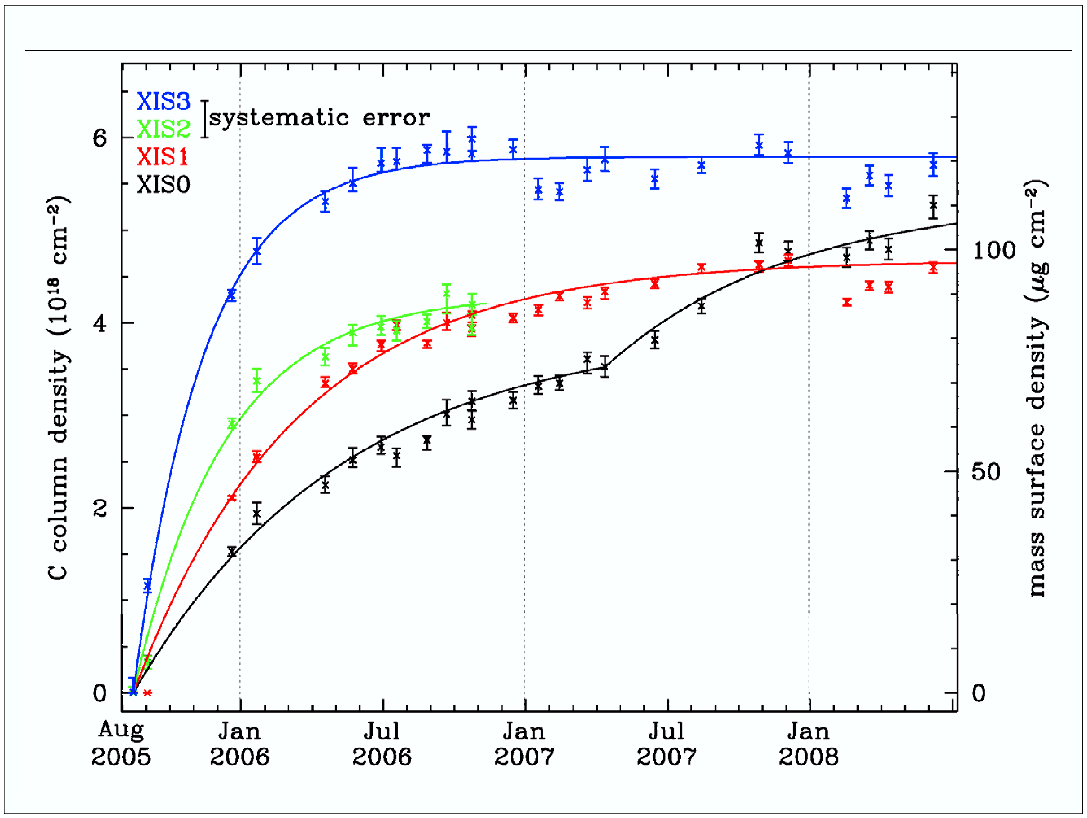

Figure 3.16: Trend plot of contamination column density (carbon) and mass surface density for each XIS sensor.

3.1.3.6 Radiation Damage and On-board Calibration of the XIS

The performance of X-ray CCDs gradually degrades in the space environment due to the radiation damage. This generally causes an increase in the dark current and a decrease of the charge transfer efficiency (CTE). In the case of XIS, the increase of the dark current is expected to be small due to the low (–90°C) operating temperature of the CCD. However, a decrease in CTE is unavoidable. Thus, continuous calibration of CCD on orbit is essential to the good performance of the XIS. This is calibrated using a radio isotope source and charge injection as explained below:
(i) Each XIS carries ^{55}Fe calibration sources near the two corners of the chip, which will be used to monitor the instrument gain.
(ii) Each XIS CCD is equipped with charge injection capability, which may be useful to measure and even suppress CTI.

3.1.3.7 Contamination on the OBFs

After the launch of *Suzaku*, a time and position dependent contamination of the XIS optical blocking filter (OBF) was found. The source is probably outgassing from the satellite. The level of contamination increases with time and is different from sensor to sensor. The *Suzaku* team investigated possible materials that caused the contamination and found DEHP

(a kind of rubber), which evaporates in high temperature is a candidate. The composition of DEHP is $C_{24}H_{38}O_4$, i.e., C/O=6. The time and position dependence of the contamination thickness has been empirically modeled by the XIS team as shown in Figure 3.16, assuming C/O=6. The uncertainties in composition, thickness and position dependence produce the largest systematic uncertainty on the effective area and response functions, in particular for diffuse emissions, at the time of this study.

3.1.3.8 On-ground event selection

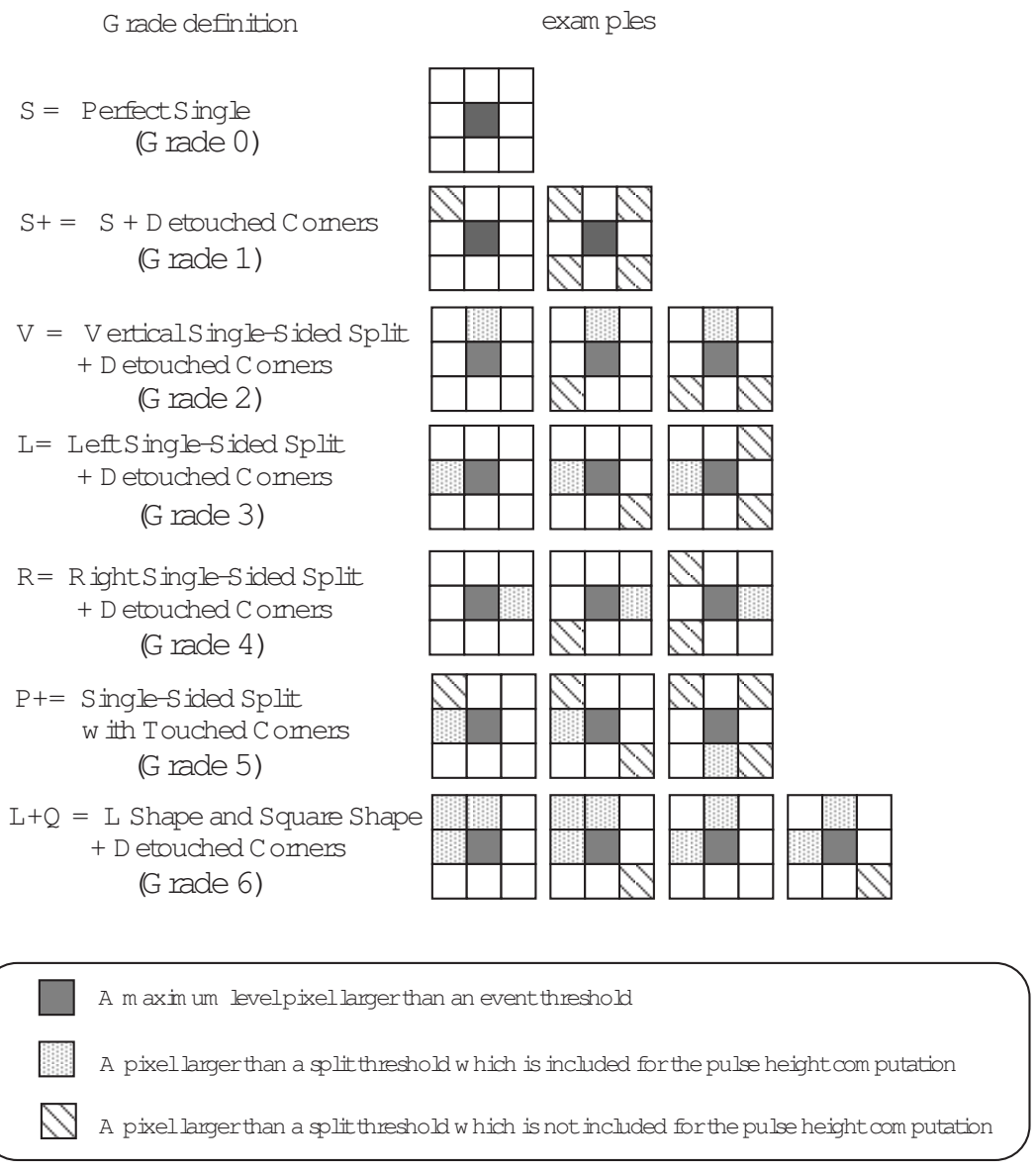

Figure 3.17: Definition of GRADE of CCD events.

Internal (non X-ray) background events can be effectively removed using the pattern on CCD pixels (GRADE), the position (STATUS) and time of an event. The definition of GRADE is shown in Figure 3.17. Most of X-ray events take GRADE = 0, 2, 3, 4, or 6. On

the other hand, most of the events of other GRADEs are dominated by non X-ray events, and should be excluded. STATUS parameter stores the information of pixel quality of an event. Known hot pixels, bad CTE columns, flickering pixels, and pixels on the segment boundaries can be removed by selecting the events with STATUS$<$ 131072. The parameters used in good time interval (GTI) selection are shown in Table 3.7. The signal to noise ratio can be improved with an appropreate GTI criteria, indicated in Table 3.7.

Table 3.7: Parameters used in GTI selection of *Suzaku*

Parameter	Definition	Recommended value to use
SAA	Whether the satellite was in the SAA[a] or not	eq.0
T_SAA	Time after the last SAA duration (s)	> 255
ELV	Elevetion angle from the Earth limb (degree)	> 5
DYE_ELV	Elevation angle from the day Earth limb (degree)	> 20
COR	Cut off rigidity of the cosmic ray (GeV/c/particle)	> 8

[a]: South Atlantic anomaly

3.2 The *Chandra* X-ray Observatory

3.2.1 Mission Description

Chandra (Figure 3.18) is placed highly elliptical orbit with an apogee of 132,200 km and a perigee of 16,700 km in December 2008. This elliptical orbit allows for high observing efficiency of $\sim$ 160 ksec long continuous observation.

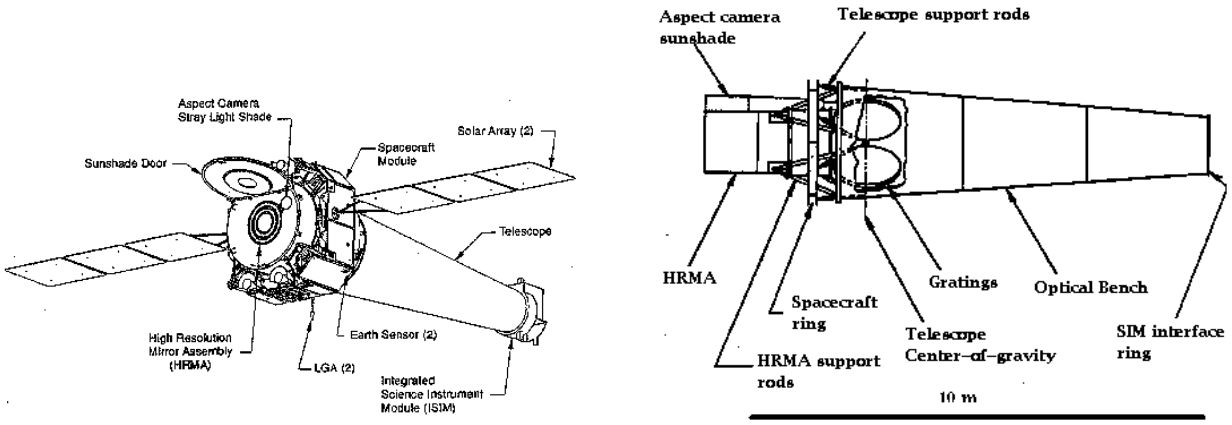

Figure 3.18: (left):The Chandra Observatory with certain subsystems labeled. LGA is an acronym for the Low Gain Antenna. (right): Major components of the telescope system. The grating assemblies are also shown.

High Resolution Mirror Assembly (HRMA) consists of a nested set of four paraboloid-hyperboloid (Wolter-1) grazing-incidence X-ray mirror pairs, with the largest having a diameter of 1.2 m. The focal length is 10 m. In the optical path just behind the HRMA, two gratings spectrometers can be placed. High-Energy Transmission Grating (HETG) achieves resolving power (E/ΔE) up to 1000 in the band between 0.4 keV and 10.0 keV when operated with ACIS-S. Low Energy Transmission Grating (LETG) provides the highest spectral resolution on Chandra at low (0.08 - 0.2 keV) energies when operated with HRC-S. The scientific payload on the focal plane consists of four distinct co-aligned instruments (Figure 3.19). There are two CCD arrays (Advanced CCD Imaging Spectrometer, or ACIS), ACIS-I and ACIS-S. ACIS-I is comprised of 4 chips of CCDs and was designed for CCD imaging and spectrometry. ACIS-S is comprised of 6 CCDs and can be used both for CCD imaging spectrometry and also for high-resolution spectroscopy in conjunction with the HETG grating. The second instruments are two microchannel plate (MCP) imaging detector (High Resolution Camera, or HRC), HRC-I and HRC-S. The HRC-I designed for wide-field imaging; and, HRC-S designed to serve as a readout for the LETG.

For combined analysis with high resolution X-ray spectra, we only used data obtained with grating detectors. The X-rays from the sky are gathered with mirror assembly (HRMA) and diffracted through grating assembly (HETG or LETG) and detected with focal plane detectors (ACIS-S or HRC-S). The detector sets are HETG + ACIS-S (HETGS), LETG + ACIS-S (LETGS) and LETG + HRC-S (LETGS). We only introduce the components which are indispensable to understand the properties of *Chandra* data used in this thesis.

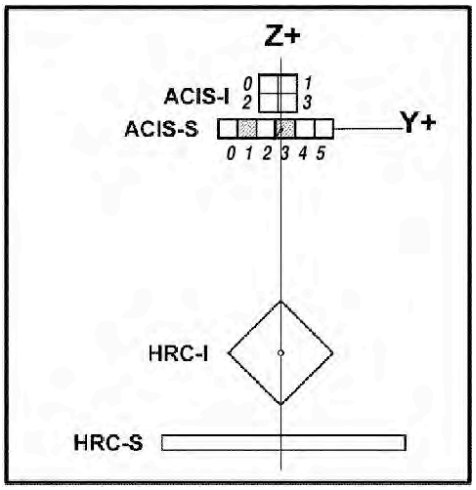

Figure 3.19: Arrangement of the ACIS and the HRC in the focal plane. The view is along the axis of the telescope from the direction of the mirrors. For reference, the two back-illuminated ACIS-S chips are shaded. Numbers indicate positions of chips I0-I3 and S0-S5. SIM motion can be used to place the aimpoint at any point on the vertical solid line.

3.2.1.1 Dithering

The spacecraft is dithered during all observations in a Lissajous figure. Dithering distributes photons over many detector elements (microchannel pores or CCD pixels) and serves several purposes: reduces uncertainty due to pixel to pixel variation in quantum efficiency (QE); allows sub-sampling of the image; and, in the case of the HRC, distributes the total exposure over many microchannel pores - useful since the QE of a pore degrades slowly with exposure to photons. And dithering smooth the gaps between detector segments, which produce edges in the grating spectrum. The effects of dither are removed during ground processing of the data.

3.2.2 High Resolution Mirror Assembly (HRMA)

The *Chandra* X-ray telescope consists of 4 pairs of concentric thin-walled, grazing-incidence Wolter Type-I mirrors called the High Resolution Mirror Assembly (HRMA). The front mirror of each pair is a paraboloid (P_n) and the back a hyperboloid (H_n). The eight mirrors were fabricated from Zerodur glass, polished, and coated with iridium on a binding layer of chromium.

3.2.2.1 Physical configuration

The HRMA, as shown in Figure 3.20, contains the nested mirrors, center, forward and aft aperture plates, baffles, inner and outer cylinders, mounts, pre- and post- collimators, fiducial light transfer components, mirror support sleeves, forward and aft contamination covers, flux contamination monitors, and thermal control hardware. The pair diameters range from about 0.65 to 1.23 meters. The distance from the center of the Central Aperture

Table 3.8: *Chandra* HRMA characteristics

Optics	Woter-Type-I
Mirror coating	Iridium (330Å, nominal)
Focal length	10.070 ± 0.003 m
PSF FWHM (with detector)	< 0.5”
Effective area:	@ 0.25 keV 800 cm^2
	@ 5.0 keV 400 cm^2
	@ 8.0 keV 100 cm^2

Plate (CAP) separating the paraboloid and hyperboloid mirrors to the HRMA focus is 10.0548 meters, with each mirror pair varying slightly about this value. An annular on-axis beam enters each mirror pair, is reflected from paraboloids and hyperboloids and exits to converge to a focus. The HRMA characteristics are listed in Table 3.8.

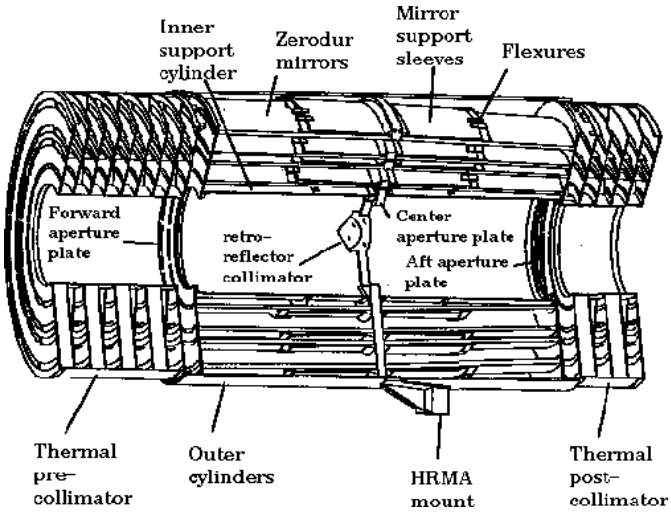

Figure 3.20: The four nested HRMA mirror pairs and associated structures.

3.2.2.2 Effective area

The unobstructed geometric aperture of the HRMA is 1145 cm^2 . The obstruction of the HRMA aperture by supporting struts is less than 10%. Since the reflectivity of the mirror optics depends on photon energy as well as grazing angle, the HRMA throughput varies with X-ray energy (Figure 3.2.2.2).

3.2.2.3 Contamination problem

There was an insignificant layer of molecular contamination on the mirrors. Subsequent in-flight gratings observations of blazers showed evidence for systematic effects near the Ir-M

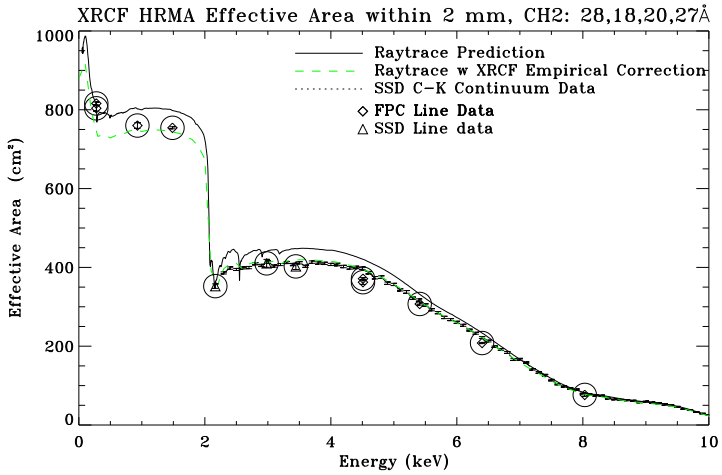

Figure 3.21: The HRMA Effective area from the raytrace prediction as a function of energy. The raytrace includes the effects of molecular contamination of variable thickness on the mirrors. The dotted line (to emphasize that these measurements were taken simultaneously) with error bars shows the data taken with a solid state detector (SSD) with a C-K continuum source. Data obtained from spectral line sources with a flow proportional counter (FPC) are shown as diamonds; obtained with a solid state detector (SSD) are shown as triangles. All the line measurements are circled for clarity. The dashed (green) line shows the absolute HRMA effective area with the X-Ray Calibration Facility (XRCF) empirical correction.

edges of the coating on the mirror and using these data and raytrace simulations, it was estimated that a 22Ålayer of hydrocarbon was present on the mirror optics.

Since the initial, ad-hoc, empirical correction of the HRMA model had already corrected for most of the effects of the molecular contamination, the addition of another 22Åof contamination in the raytrace model post-launch was an over-correction.

3.2.3 Advanced CCD Imaging Spectrometer (ACIS)

The Advanced CCD Imaging Spectrometer (ACIS) offers the capability to simultaneously acquire high-resolution images and moderate resolution spectra. The instrument can also be used in conjunction with the High Energy Transmission Grating (HETG) or Low Energy Transmission Grating (LETG) to obtain higher resolution spectra. ACIS contains 10 planar, 1024 × 1024 pixel CCDs (Figure 3.22); four arranged in a 2×2 array (ACIS-I) used for imaging, and six arranged in a 1×6 array (ACIS-S) used either for imaging or as a grating readout. We only use ACIS as a grating focal detector.

3.2.3.1 Energy Resolution

The ACIS FI CCDs originally approached the theoretical limit for the energy resolution at almost all energies, while the BI CCDs exhibited poorer resolution. The pre-launch energy resolution as a function of energy is shown in Figure 3.23. The loss of energy resolution is due to increased charge transfer inefficiency (CTI) caused by low energy protons encountered

Table 3.9: ACIS-S parameters

Focal Plane Arrays	6 CCDs in a linear array tangent to the grating Rowland circle
Spatial Resolution	0.4920 arcsec
Pixel size	23.985 μm
Spectral Resolution ($\Delta E/E$)	$\sim$100@1keV

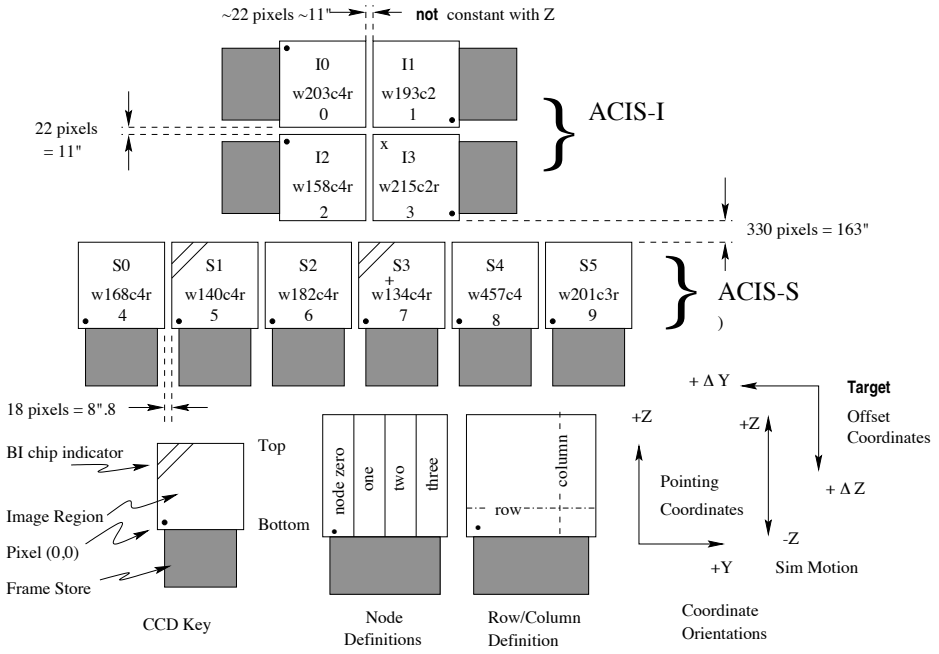

Figure 3.22: A schematic drawing of the ACIS focal plane; insight to the terminology is given in the lower left. Note the nominal aimpoints: on S3 (the'+')and on I3(the'x'). It is standard practice to add an offset to all observations on S3 to move the source away from the node 0-1 boundary (see Section 6.10). Note the differences in the orientation of the I and S chips, important when using Sub arrays (Section 6.12.1). Note also the(Y, Z) coordinate system and the target offset convention (see Chapter3) as well as the SIM motion(+/-Z). The view is along the optical axis, from the source toward the detectors, (-X). The numerous ways to refer to a particular CCD are indicated: chip letter+number, chip serial number, and ACIS chip number. The node numbering scheme is illustrated lower center.

during radiation belt passages and Rutherford scattering through the X-ray telescope onto the focal plane. Subsequent to the discovery of the degradation, operational procedures were changed, ACIS is not left at the focal position during radiation belt passages. Since this procedure was initiated, no further degradation in performance has been encountered beyond that predicted from pre-launch models. The BI CCDs were not impacted, which is consistent with the proton-damage scenario - it is far more difficult for low-energy protons from the direction of the HRMA to deposit their energy in the buried channels of the BI devices, since the channels are near the gates and the gates face in the direction opposite to

the HRMA. Thus the energy resolution for the two BI devices remains nearly at pre-launch values. The position-dependent energy resolution of the FI chips depends significantly on the ACIS operating temperature. Since

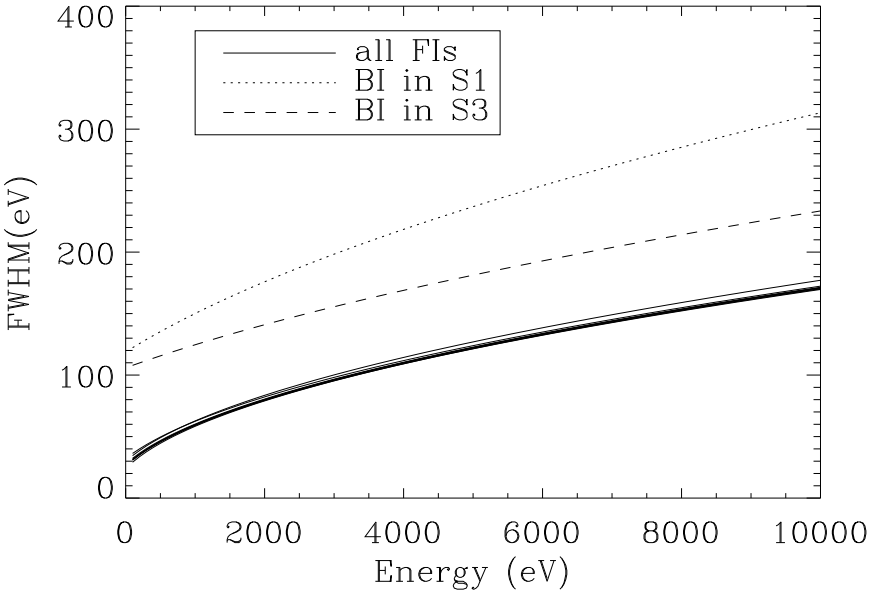

Figure 3.23: The ACIS pre-launch energy resolution as a function of energy.

3.2.4 High Resolution Camera (HRC)

The High Resolution Camera (HRC) is a microchannel plate (MCP) instrument comprised of two detectors, one optimized for imaging (HRC-I), and one (HRC-S) which serves as a readout for the Low Energy Transmission Grating (LETG) and here we only introduce the HRC-S.

Table 3.10: HRC-S parameters

Focal Plane Arrays	CsI-coated MCP pairs	100×20 mm × 3
Spatial Resolution	FWHM	∼20μm, ∼0.4 arcsec
	pore size	12.5 μm
	pore spacing	15 μm
	pixel size (electronic readout)	6.42938μm
Energy Range		0.08-10 keV
Spectral Resolusion	$\Delta E/E$	∼1@1keV

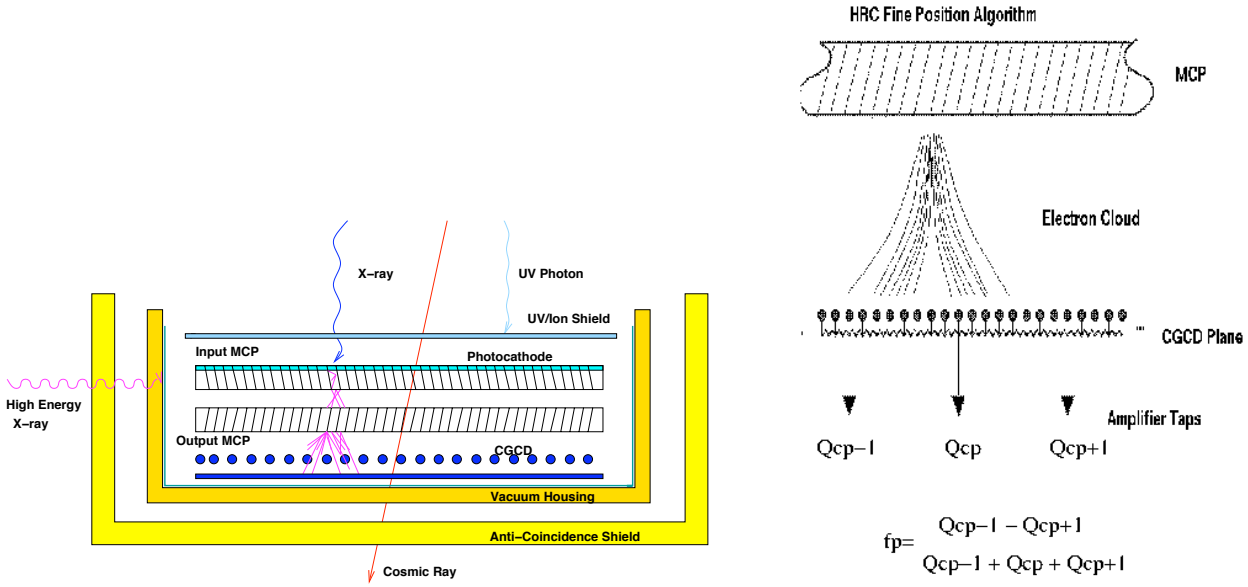

Figure 3.24: (left): A schematic of the HRC Micro-channel-Plate detector. (right): Schematic representation of event position determination for one axis of the crossed grid charge detector (CGCD). The electron cloud is divided between several amplifiers. The position of the event relative to the central coarse position is calculated from the difference between the signals on either side of the coarse position divided by the sum of the three signals.

3.2.4.1 Basic principles

Figure 3.24 illustrates the features of the HRC MCPs. X-rays enter through a UV/Ion shield, necessary in order to reduce/avoid signals from UV light, ions, and low energy electrons. Most of these X-rays are then absorbed in the CsI-coated walls of the first (input) of two consecutive MCPs. The axes of the millions of tubes that comprise the input and output MCPs are not parallel to the optical axis but are canted ("biased") at an angle of 6° in opposite directions as shown in Figure 3.24. This bias improves the probability of an interaction. The CsI coating enhances the photoemission over that from a bare MCP. The resulting photoelectrons are then accelerated by an applied electric field. The next interaction with the walls releases several secondary electrons and so on, until a cascade of electrons is produced.

One purpose of the second (output) MCP is to provide additional gain. In addition, reversing the direction of the second MCP's bias angle with respect to the first removes a clear path for positive ions, and hence reduces the possibility of (positive) ion feedback - where an accelerated ion moving in the opposite direction as that of the electrons ends up causing the release of electrons and starts the process all over again.

The electron cloud — typically about 2×10^7 electrons per photon — that emerges from the output MCP is accelerated towards a position-sensitive charge detector. The HRC-S uses a hybrid charge detectors where one axis is comprised of wires and the other has gold lines deposited on a ceramic substrate. Adjacent wires (or lines) are resistively connected

and every eighth wire is attached to a charge-sensitive amplifier, referred to as a "tap", as illustrated in Figure 3.24.

The X-ray position is determined by calculating the centroid of the charge cloud exiting the rear MCP via the "three tap algorithm". In short, the three tap algorithm determines the charge cloud centroid using a combination of digital and analog electronics and off-line processing.

3.2.4.2 Non-dispersive energy resolution

The intrinsic energy resolution of the HRC is poor. Even though the pulse- height amplitude (PHA) of each event is telemetered, spectral fitting cannot be usefully carried out for sources observed with the HRC .

3.2.4.3 Background

The anti-coincidence shield of the HRC-S does not work because of a timing error in the electronics. The error is not correctable. As a result the event rate is very high and exceeds the telemetry rate limit. To cope with this problem the HRC team has defined a "spectroscopy region" which is about 1/2 of the full width and extends along the full length of the HRC-S detector. The spectroscopy region ($\sim$10 mm) is implemented using the edge blanking feature of the electronics. With this change, the telemetered quiescent background rate is about 120 cts s^{-1} . The background can be further reduced in ground data processing by using pulse height filtering that preferentially selects X-rays over cosmic ray events. A reduction in background by a factor of about three is possible for dispersed spectra. Thus there are two relevant background rates for the HRC-S: a telemetry rate of 120 cts s^{-1} and a post-processing rate for calculating signal to noise.

3.2.5 High Energy Transmission Grating Spectrometer (HETGS)

HETG is the High-Energy Transmission Grating. In operation with the High Resolution Mirror Assembly (HRMA) and a focal plane imager, the complete instrument is referred to as the HETGS — the High-Energy Transmission Grating Spectrometer. The HETGS provides high resolution spectra (with $E/\Delta E$ up to 1000) between 0.4 keV and 10.0 keV for point and slightly extended (few arc seconds) sources.

The HETG itself consists of two sets of gratings, each with different period. One set, the Medium Energy Grating (MEG), intercepts rays from the outer HRMA shells and is optimized for medium energies. The second set, the High Energy Gratings (HEG), intercepts rays from the two inner shells and is optimized for high energies. Both gratings are mounted on a single support structure and therefore are used concurrently. The two sets of gratings are mounted with their rulings at different angles so that the dispersed images from the HEG and MEG will form a shallow X centered at the undispersed (zeroth order) position; one leg of the X is from the HEG, and the other from the MEG. The HETG is designed for use with the spectroscopic array of the Chandra CCD Advanced Imaging Spectrometer (ACIS-S) although other detectors may be used for particular applications. A summary of characteristics is given in Table 3.11.

Detector image and extracted LETGS spectrum are shown in Figure 3.25.

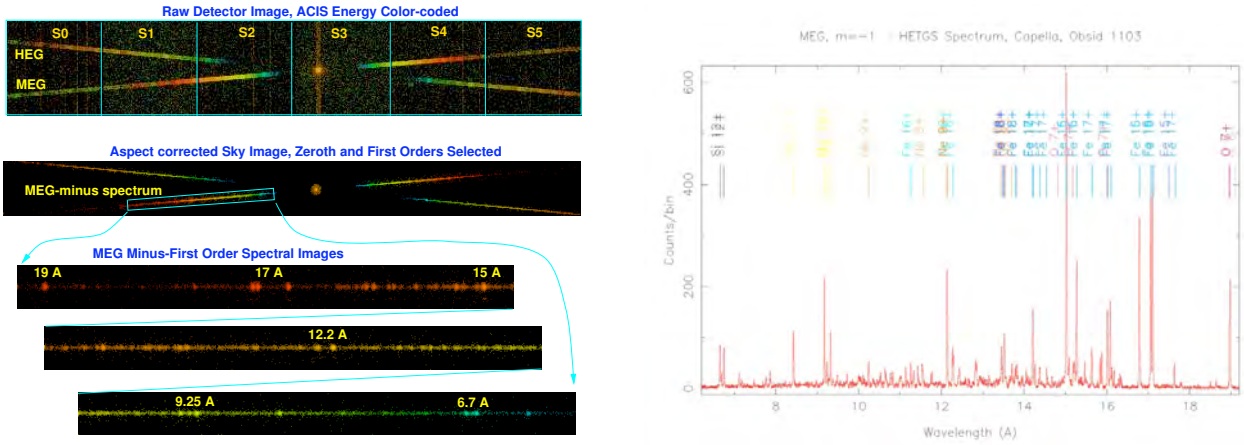

Figure 3.25: (left): HETGS observation of Capella. The top panel shows an image of detected events on the ACIS-S detector with the image color indicating the ACIS- determined X-ray energy. The bright zeroth-order image is visible on CCD S3 and includes at railed image(the vertical frame-transfer streak). Diffracted photons are visible forming a shallow "X" pattern; the HEG and MEG spectra are indicated. The images are broad due to dither of the spacecraft. The middle panel shows an image after the data have been aspect corrected and selections applied to include only valid zeroth and first-order events. Finally, the lower panel shows an expanded view of the MEG minus-first-order spectrum with emission lines clearly visible. (right): HETGS Capella spectrum, MEG m = -1. The first-order events identified in the MEG minus-side "arm" of the HETG X pattern are assigned wavelengths by CXC pipeline software according to the grating equation and known instrument parameters. These values are then binned to produce a pulse height analysis spectrum (pha2.fits file) which is plotted here.

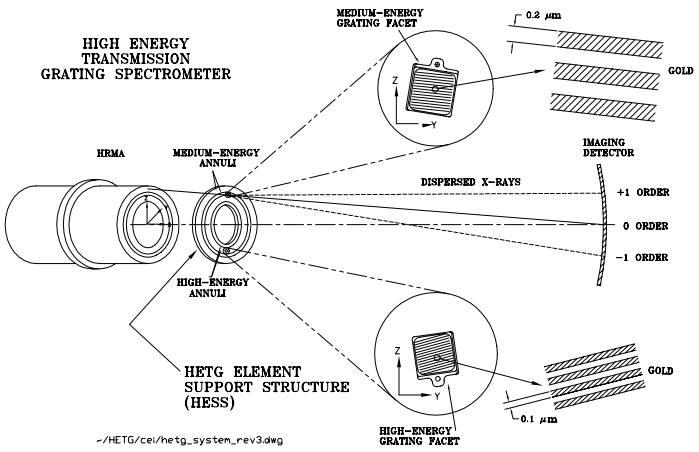

Figure 3.26: A schematic layout of the High Energy Transmission Grating Spectrometer, not the LETG. (Dimensions shown are approximate.)

Table 3.11: HETGS parameters with ACIS-S

Wavelength range	1.2 - 31 Å
- HEG	1.2-15 Å
- MEG	2.5-31 Å
Energy range	0.4 keV-10 keV
- HEG	0.8-10 keV
- MEG	0.4-5.0 keV
Resolution ($\Delta\lambda$, FWHM)	
- HEG	0.012 Å
- MEG	0.023 Å
Resolving power (E/ΔE)	
- HEG	1070-65 (1000 @ 1 kev)
- MEG	970-80 (660 @ 0.826 keV)
Wavelength Scale	
- HEG	0.0055595 Å/ ACIS pixel
- MEG	0.0111200 Å/ ACIS pixel
Effective area (1st order)	7-28 cm^2
HETGS Rowland spacing	8632.65 mm

3.2.5.1 Physical Configuration

The HETG is mounted, and can be inserted, just aft of the HRMA as shown in the schematic of the HRMA-HETG-detector system, Figure 3.26. The HETG provides spectral separation through diffraction. X-rays from the HRMA strike the transmission gratings and are diffracted (in one dimension) by an angle β given according to the grating equation,

$$\sin\beta = m\lambda/p, \tag{3.1}$$

where m is the integer order number, λ is the photon wavelength in angstroms, p is the spatial period of the grating lines, and β is the dispersion angle. A "normal" undispersed image is formed by the zeroth-order events, $m = 0$, and dispersed images are formed by the higher orders, primarily the first-order, $m = 1$. The HETGS-faceted Rowland design is shown in Figure 3.27 . The "Rowland circle" is a circle whose diameter is simply the distance from the grating that would lie on the optical axis to the point in the focal plane, where the zeroth order image is placed. The "Rowland torus" is formed by rotating the circle about the line in the dispersion direction going through the on-axis focus. Individual grating facets are mounted such that their centers lie on the torus. In the figure, the axis of the torus is perpendicular to the page for the side view and lies in the plane of the top view. Ideally, the detector is shaped to follow the counterpart Rowland torus in the image plane. The result is that the telescope focal properties in the dispersion direction are maintained for a large range of diffraction angles, β , thereby minimizing any grating-added optical aberrations.

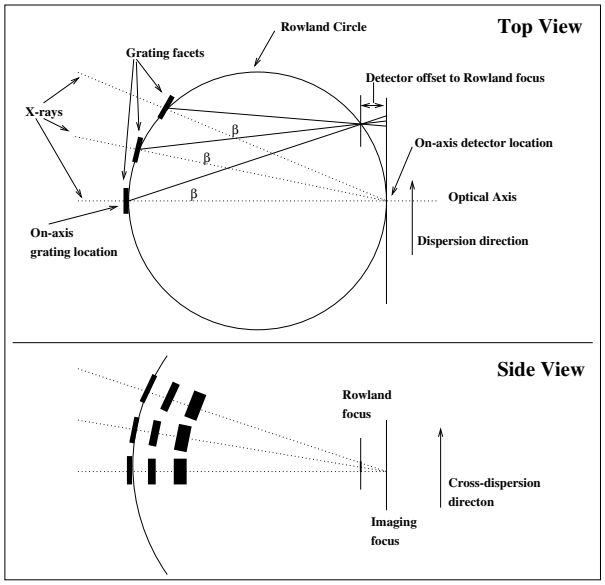

Figure 3.27: The Rowland geometry is shown schematically. In the Top view, we are looking across the dispersion direction. The diffraction angle is β. The geometry is such that converging rays diffracted at a specific angle by the gratings (which are located on the Rowland circle) will converge to a point that is also on the Rowland circle. The dotted lines represent zeroth-order rays and the solid lines the grating first-order diffracted rays. The bottom panel looks along the dispersion direction at rays from a set of gratings arranged perpendicularly to those in the top view and schematically shows the astigmatic nature of the spectrally focused image; since the converging rays have not yet reached the imaging focus, they are extended across the dispersion (by less than 100 microns).

3.2.5.2 Effective Area

Combining the HETG diffraction efficiencies with the HRMA effective area and the ACIS-S detection efficiency produces the system effective area as a function of energy, de- scribed by an "ancillary response file" or ARF. Plots of HETGS ARF's are shown in Figure 3.28. The effective include the effect of molecular contamination on the ACIS filter.

3.2.5.3 Order sorting

One of the advantages of using the ACIS-S as the HETG readout detector is the ability of ACIS to determine the energy of detected X-rays. This crude (by HETGS standards) energy measure can be used to determine the diffraction order of the photon, i.e., perform "order sorting", as shown in the "banana plot" of Figure 3.2.5.3 During data analysis, this filtering is accomplished by utilizing two of the data columns supplied in the level 1.5 (or 2.0) FITS data file: the ACIS-determined energy, ENERGY, and the dispersion distance, $m\lambda$ = TG MLAM. Ideally this order sorting would have perfect efficiency, that is, all first-order events would be correctly identified.

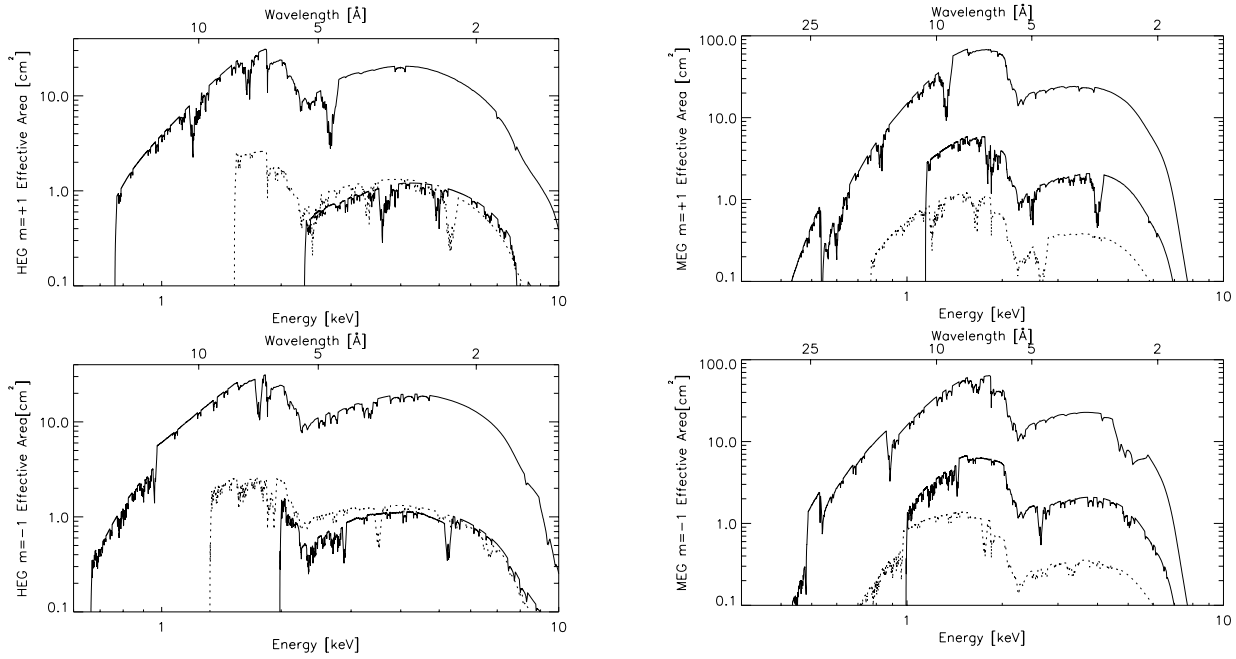

Figure 3.28: (left):The HETGS HEG effective area, integrated over the PSF is shown with energy and wavelength scales. The m = +1, +2, +3 orders (falling on ACIS chips S5, S4, S3; left to right) are displayed in the top panel and the m = -1, -2, -3 orders (falling on ACIS chips S0, S1, S2; left to right) are in the bottom panel. The thick solid lines are first order; the thin solid line is third order; and the dotted line is second order. (right): same as left panel for The HETGS MEG effective area.

3.2.5.4 Background

Since the HETG is always used in conjunction with a focal-plane detector, spectra from the HETGS have background events determined by the detector's intrinsic and environmental backgrounds. In addition to these detector-dependent backgrounds, there are additional grating-dependent effects such as scattering from the gratings which will produce extraneous photons in locations unexpected on the basis of the simple grating equation. Figure 3.2.5.3 shows the HEG and MEG spectra of the background for a long calibration observation of HR 1099 (observation ID 62538). The background was selected from regions 8-50 arcsec from the dispersion line in the HEG and 11-50 arcsec from the dispersion line in the MEG. The pulse height selection was simple, accepting events that satisfy the relation E_{ACIS}/E_{TG} < 0.30, where E_{ACIS} is the energy derived from the ACIS-S pulse height and E_{TG} is the energy based on the dispersion distance. The background was normalized to an aperture of $\pm$ 3 arcsec (full size of 6 arcsec) and averaged at 0.1 Åintervals.

Compared with the background, our observation target is very bright (> 10 counts ks^{-1} Å^{-1}) and the background effect is negligible.

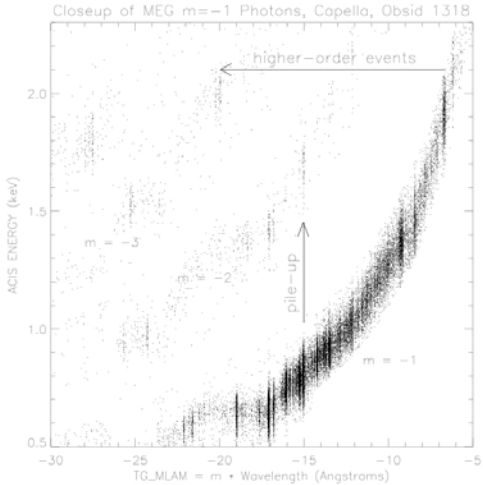

Figure 3.29: HETGS pile-up and higher-order events. Taking a close look at the MEG "banana plot" demonstrates how the ACIS ENERGY can be used to identify higher-order events and pileup in an HETGS spectrum. The 3rd order of the $\sim$ 6.7 Ålines are clearly visible; the lines are only weakly present in 2nd order because the MEG 2nd order is suppressed. In comparison, the 15 Åline (and others) are so bright in 1st order that a fraction of the events ($\sim$ 6% here) pile-up and produce events with twice the ACIS ENERGY.

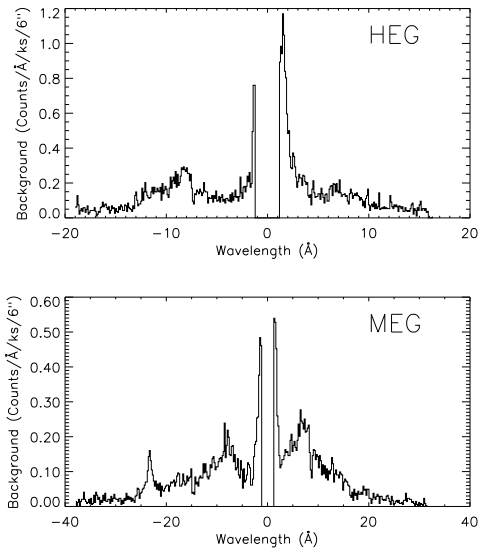

Figure 3.30: The background spectrum is plotted for the HEG (top) and MEG (bottom) for a long observation of the late-type star HR 1099. The background was normalized to a 6 arcsec wide aperture but determined from a substantially larger region out to 50 arcsec from the source dispersion line. The spectrum was binned to 0.1 Åto show details of structure that may be observed in a typical HETGS observation. The spikes near zeroth order are due to increased background included in the pulse height selection at high energies.

3.2.6 Low Energy Transmission Grating Spectrometer (LETGS)

The Low Energy Transmission Grating Spectrometer (LETGS) comprises the LETG, a focal plane imaging detector, and the High Resolution Mirror Assembly. The Chandra High Resolution Camera spectroscopic array (HRC-S) is the primary detector designed for use with the LETG. The spectroscopic array of the *Chandra* CCD Imaging Spectrometer (ACIS-S) can also be used, though with lower quantum efficiency below ∼0.6 keV and a smaller detectable wavelength range than with the HRC-S.

The LETGS provides high-resolution spectroscopy (E/ΔE > 1000) between 80 and 175 Å(0.07 - 0.15 keV) and moderate resolving power at shorter wavelengths. The nominal LETGS wavelength range accessible with the HRC-S is 1.2-175 Å(0.07-10 keV); useful ACIS-S coverage is 1.2 to roughly 60 Å(∼ 0.20-10 keV). A summary of LETGS characteristics is given in Table 3.12.

Detector image and extracted LETGS spectrum are shown in Figure 3.31.

3.2.6.1 Physical Configuration

When the LETG is used, the Grating Element Support Structure (GESS), an aluminum frame approximately 110 cm in diameter and 6 cm thick, is inserted ∼ 300 mm behind the exit aperture of the HRMA and 1.4 m behind the HRMA mid-plane. The GESS holds

Table 3.12: LETGS parameters

Wavelength range	
- HRC-S	1.2-175 Å
- ACIS-S	1.2-60 Å
Energy range	
- HRC-S	70 eV-10keV
- ACIS-S	200eV -10 keV
Resolution (Δλ, FWHM)	0.05Å
Resolving power (E/ΔE)	≥ 1000 (50-160Å)
	∼ 20 × λ (3-50Å)
Dispersion	1.148Å
Plate scale	48.80 μm/arcsec
Effective area (1st order)	
- HRC-S	1-25 cm^2
- ACIS-S	4-200 cm^2
Background(quiescent)	
- HRC-S	12-26 (at 50 and 175 Å) cts/0.07-Å/100-ksec
- ACIS-S	< 0.01 cts/pixel/100-ksec (ACIS-S, order sorted)
Pixel size	
- HRC-S	6.43 × 6.43 μm
- ACIS-S	24.0 × 24.0 μm
Rowland diameter	8637 mm

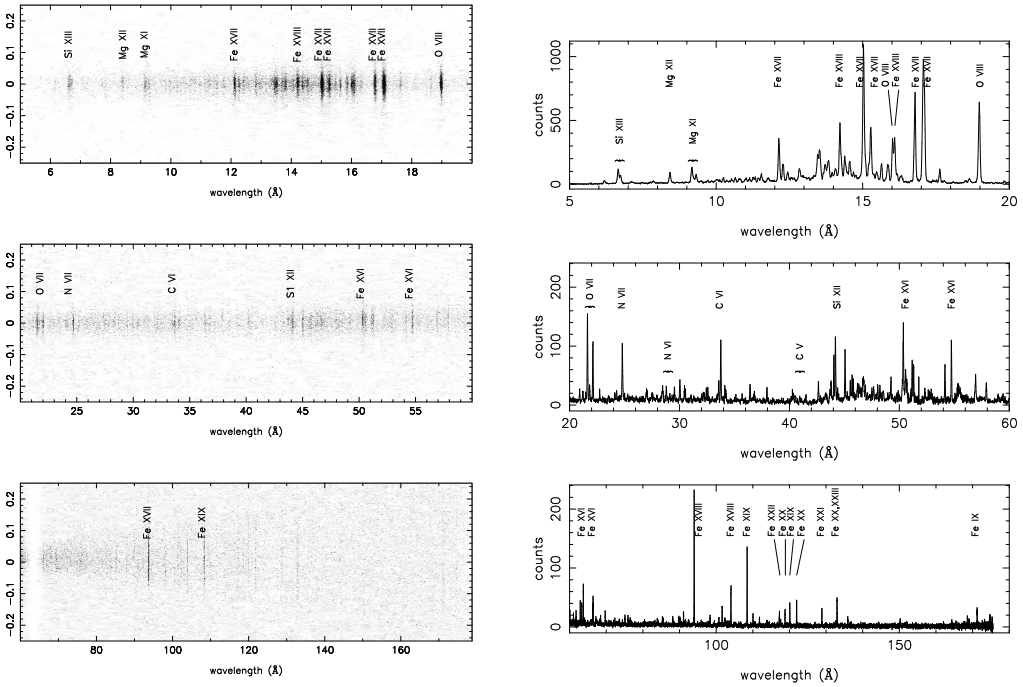

Figure 3.31: (left): HRC-S detector image of a Capella observation, showing positive order dis- persion. Both axes are in Åwith 1.148 Å/mm. The increasing cross-dispersion extent of lines at longer wavelengths is due to astigmatism in the HRMA/LETG system. The positive-order HRC-S plate gap is at *sim* 63 Å. (right): Extracted LETGS spectrum of Capella with some line identifications (from Brinkman et al. 2000, ApJ, 530, L111). Many of the lines visible between 40 and 60 Åare 3rd order dispersion of the strong features seen in 1st order in uppermost panel.

approximately 180 trapezoidal grating modules, which measure about 13×50 mm. A design drawing of the full GESS is shown in Figure 3.32. Each grating module holds three circular grating facets, each of which comprises approximately 80 of the triangular grating elements seen in Figure 3.32.

To reduce aberrations, the GESS is shaped to follow the Rowland torus. The basics of the Rowland geometry are shown in Figure 3.27. The primary readout detector (HRC-S) is made of three tilted array segments which also follow the Rowland circle in the image plane. Because the detector array elements are flat, the distance from the Rowland circle changes with position, and so the spectral resolution changes very slightly with wavelength.

The thickness of the gold of the grating bars on top of the support mesh determines the "phasing," or efficiency of redistribution of photons into each spectral order in wavelengths where the gold is partially transparent. The thickness is designed to optimize the 1st order response at energies of interest.

3.2.6.2 Effective area

The LETGS effective area for any diffraction order is equal to the product of the HRMA effective area, the net LETG efficiency for that order, and the overall detector efficiency (which

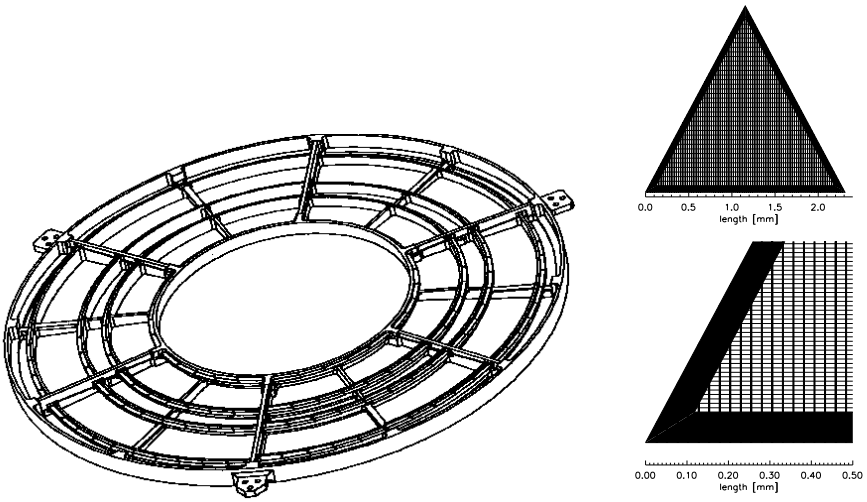

Figure 3.32: (left): LETG Grating Element Support Structure, a machined aluminum plate approximately 110 cm in diameter that holds grating modules on a Rowland torus behind the *Chandra* mirrors. (right): LETG facet structure schematic showing the basic shape of the individual grating elements and the relative sizes of the support structures. The upper view shows the complete grating element, which comprises the triangular coarse support, the vertical fine supporting bars, and the (horizontal) grating bars. The grating bars themselves are not shown to scale. In the upper view every 50th grating bar is drawn, in the lower view every 10th bar.

varies slightly depending on exactly where the diffracted spectrum falls on the detector). All these quantities vary with wavelength.

Of these three contributors, the HRMA is the best calibrated within the LETGS energy band. In-flight calibration, particularly of the net 1st order effective area, has provided the best and most extensive data, and the effective area is now believed to be accurate to a level of approximately 15% or better across the most of the bandpass. The effective area in the wavelength range 44-70 Å(0.28-0.17 keV) remains the least well-known, with uncertainties thought to be 20% or less. Effective areas for orders 2-7 have been calibrated relative to 1st order to an accuracy of $\sim$ 10% (5% for 3rd order). Uncertainties for orders beyond 7th may be larger but are generally unimportant.

In addition to fixed-position detector features (detector segment gaps) there are instrumental spectral features which occur at fixed energies because of absorption edges in the materials comprising the HRMA, LETG, and HRC-S or ACIS-S. Every effort has been made to adequately calibrate Chandra over its entire energy range, but it should be understood that effective areas near absorption edges are extremely difficult to quantify with complete accuracy and uncertainties in these regions are inevitably higher.

3.2.6.3 High-order diffraction

Although the LETG have been designed to reduce complications from higher-order diffraction by suppressing even orders, many grating spectra will have overlapping diffraction orders. When ACIS-S is used as the detector, its intrinsic energy resolution can be used to

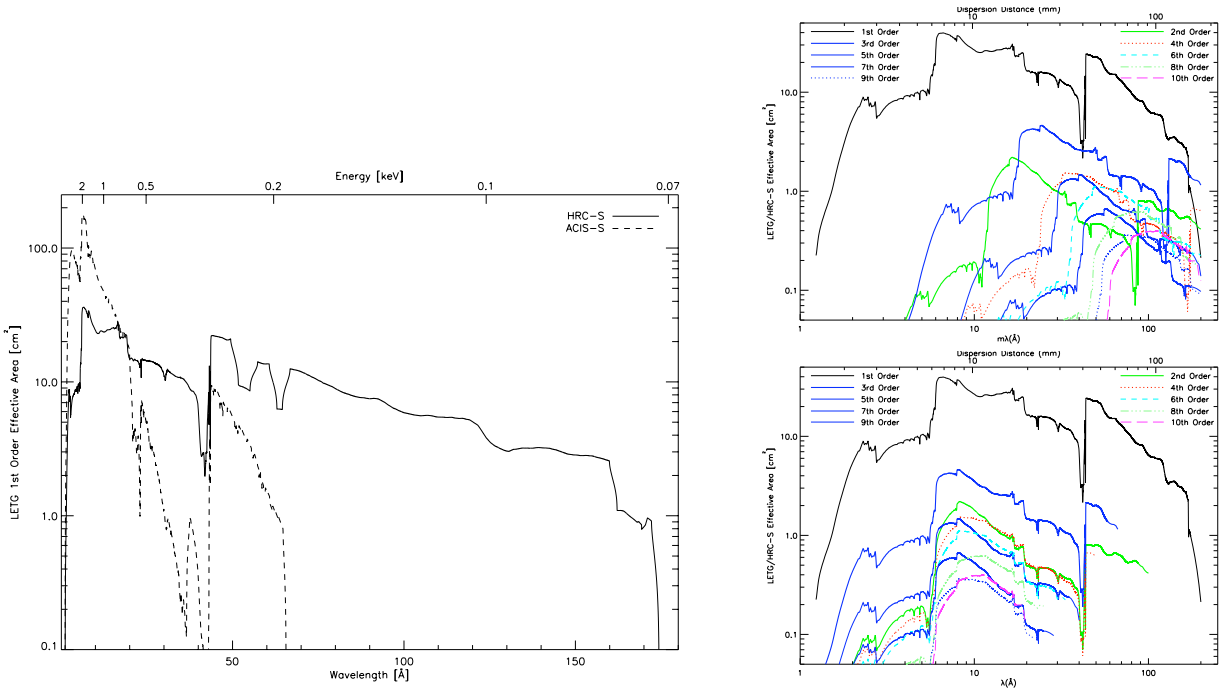

Figure 3.33: (left): LETGS 1st-order effective area for an on-axis point source, with HRC-S and ACIS-S detector configurations. Positive and negative orders are summed. LETG+ACIS-S areas were computed using an effective area model that included the effects of contamination build-up extrapolated to the level expected in mid-May 2009. (right): The combined HRMA/LETG/HRC-S effective area, illustrating the relative strengths of 1st and higher orders. Positive and negative orders are summed. In the label for the bottom axis of the top panel, m is the order number. See the text for an example of how to determine the relative strength of overlapping lines from different orders.

separate orders. The situation is more complicated, however, with HRC-S, which has very little energy resolution. The relative contribution of higher-order photons with different detector configurations can be estimated by inspection of Figure 3.33

3.2.6.4 Background

The LETG is always used in conjunction with a focal-plane detector, so the LETG spectra will exhibit that detector's intrinsic, environmental, and cosmic background. The quiescent background rate over the full detector is close to the 184 cts s^{-1} telemetry limit. Imposition of the HRC-S spectroscopy window reduces the rate to about 120 cts s^{-1}.

As of 2008, the quiescent background rate in HRC-S Level 2 data is $\sim 6.6 \times 10^{-5}$ cts s^{-1} $arcsec^{-2}$, or roughly 0.11 counts per pixel in 100 ks. Currently, default processing removes events with PHA=255, which reduces the rate above by 5-10%, though somewhat unevenly.

The extent of a dispersed line in the LETGS spectrum is roughly 0.07 Å(9.5 pixels) wide and the spectral extraction region is 25 to 85 pixels wide in the cross-dispersion direction, yielding roughly 25 to 90 background counts beneath the line in a 100 ks exposure. However, the HRC-S pulse height distribution is sufficiently narrow that a large fraction of pulse-height

space can be excluded from the data to further reduce the background, which has a relatively broad pulse-height distribution.

The mean of the pulse-height distribution increases weakly with photon energy, such that a factor of two difference in energy corresponds to a shift in the mean of ∼8%. The mean of 8th order will therefore be about 25% higher than 1st order; the new SPI filter removes 1.25% of 1st order at 160 Å, and about 11% of 8th order ($\lambda = 20\mathring{A}$, $m\lambda = 160\mathring{A}$). Extra filtering of higher orders will have negligible effect for nearly all analyses, but should be considered if deliberately studying wavelength ranges with very heavy higher order contamination.

Background rates in ACIS are somewhat higher than expected, but lower than in the HRC. Pulse-height filtering applied during order separation further reduces the effective ACIS-S background to extremely low levels when used with gratings.

Compared with the background, our observation target is very bright (> 10 counts ks^{-1} Å^{-1}) and the background effect is negligible.

Chapter 4

Observations and Data reduction

4.1 Observations

As mentioned in Chapter 2, combined analysis is a powerful method to constrain the physical properties of hot interstellar medium. In order to apply this method to hot ISMs, we had to find good point sources for absorption analysis which meet the following requirement as possible; 1) the source is bright enough in 0.4 - 1.2 keV energy range to obtain good statistic data (or time of observation is long enough), and 2) the distance is large enough (> few kpc) to know spatial distribution of the hot ISM.

PKS 2155-304 is a bright BL Lac object at z$\sim$ 0.116 ($\sim$ 0.5 Gpc) and fully meet the requirement to perform combined analysis. *Chandra* use PKS 2155-304 as a calibration target for grating detectors and high quality data of $\sim$ 1 Ms can be obtained. Many absorption lines including O VII and O VIII are detected in the spectrum (Williams et al. (2007)). And it is important that LMC X-3, the target of the first X-ray combined analysis, is located only 50 kpc away and we can not exclude the possibility that emission source exist beyond LMC X-3. While PKS 2155 located at $\sim$ 0.5 Gpc away and using the results of these direction, we can estimate the spatial extension of hot halo with more precision.

We observed the emission of the hot ISM toward two off-fields of the PKS 2155-304 sight line by *Suzaku* . To minimize confusion by stray lights from the PKS 2155-304 and to average out the possible spatial gradient of the diffuse emission intensity, the two fields were chosen to be $30'$ away from the PKS 2155–304 and in nearly opposite directions. With this configuration and the roll angle of the XIS field of view, we estimate that stray lights from PKS 2155-304 contribute no more than 10% to the observed X-ray emission in 0.3 - 1.0 keV energy range.

To understand physical properties of hot ISM toward the Galactic center direction, we had to select the absorption observation target in the direction. Extragalactic objects are the best for our purpose, however there is no one in which oxygen absorption lines are detected in this direction. Thus we searched for luminous X-ray objects in our galaxy and found four objects. Among them the low mass X-ray binary 4U 1820-303 is best for our analysis, because O VII and O VIII absorption lines are clearly detected and the distance is well determined. 4U 1820-303 is located in the globular cluster NGC 6624 at (l, b) = (2.8, 7.9) and the distance of NGC 6624 is determined from the optical reddening and the brightness of horizontal-branch and main-sequence turnoff stars (Richtler et al. 1994; Kuulkers et al. 2003). In this paper we adopt the value 7.6 $\pm$ 0.4 kpc from Kuulkers et al. (2003). *Chandra* observed 4U 1820-303

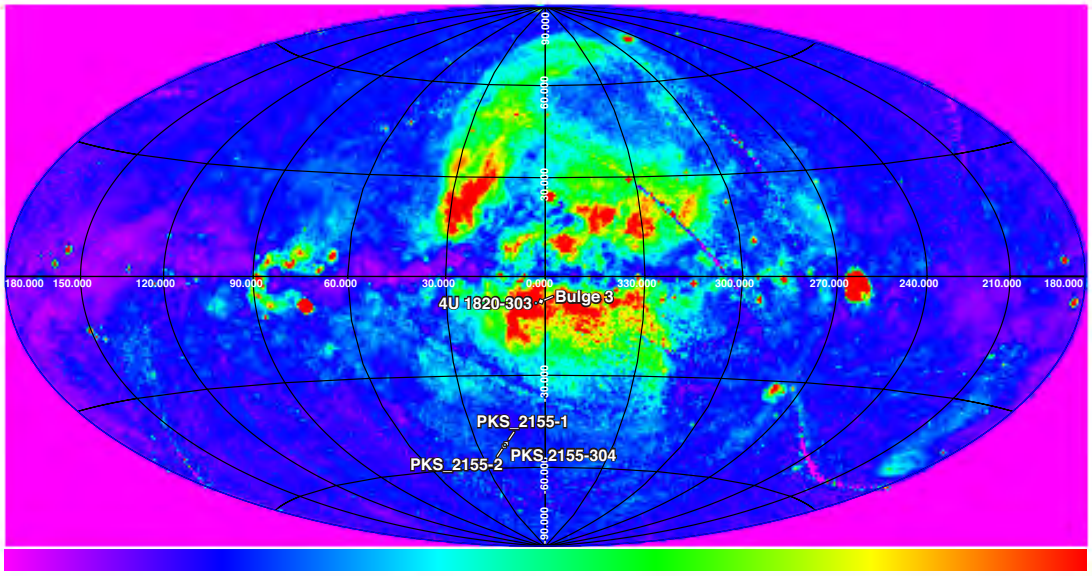

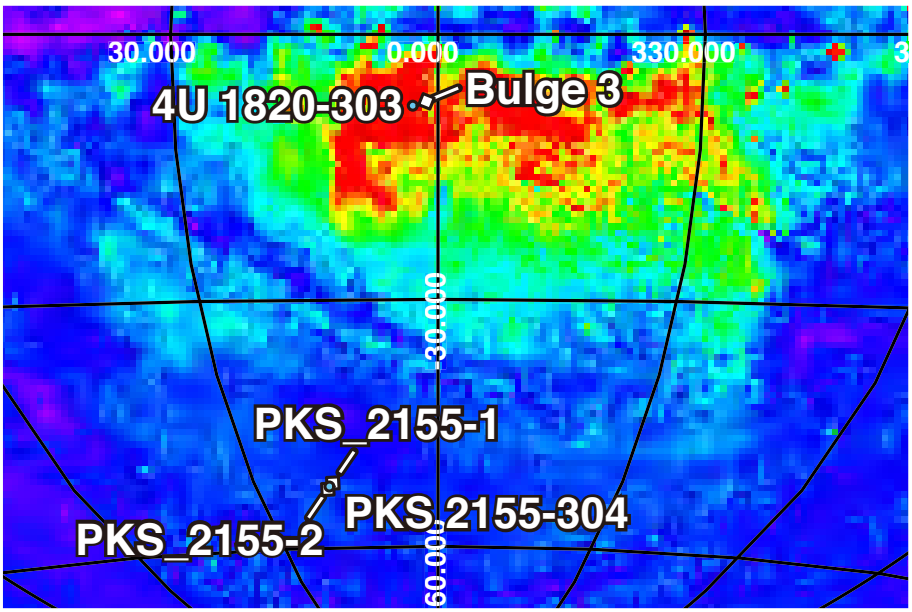

Figure 4.1: *Suzaku* and *Chandra* observation fields studied in this thesis are presented as squares and circles respectively, which are plotted in Aitoff projection of the sky with the Galactic center at the center of the figure and Galactic longitude increasing to the left. The backside color map is *ROSAT* R45 band image.

with HRC + LETG and O VII, O VIII and Ne IX absorption lines are detected by Futamoto et al. (2004). Serendipitously, *Suzaku* observed blank sky at (l,b)=(1.3, -7.5), which is 1° away from 4U 1820-303, and we can use this data as an offset observation.

The observation fields analyzed in this paper are shown in Figure 4.1 and observation

log and position are summarized in Tables 4.2, 4.1, 4.3, 4.4 and 4.5 respectively.

Table 4.1: *Chandra* Observation log of PKS 2155-304

Obs ID	Start Date	Exposure (ks)	Detector
337	1999-10-20 05:14:36	39.15	ACIS + HETG
1014	2001-03-28 19:32:50	27.13	ACIS + HETG
1705	2000-05-31 17:10:53	25.83	ACIS + HETG
3167	2001-11-30 19:45:43	30.14	ACIS + HETG
3706	2002-11-29 22:05:44	28.16	ACIS + HETG
3708	2002-11-29 14:15:17	26.96	ACIS + HETG
5173	2004-11-23 23:15:08	27.15	ACIS + HETG
6926	2006-07-06 10:30:52	14.04	ACIS + HETG
7291	2006-07-07 08:58:16	14.03	ACIS + HETG
8380	2007-07-14 00:35:42	15.54	ACIS + HETG
8436	2007-07-14 14:23:50	15.54	ACIS + HETG
9705	2008-07-02 06:44:08	15.17	ACIS + HETG
9712	2008-07-03 05:22:52	15.04	ACIS + HETG
1703	2000-05-31 02:08:03	26.18	ACIS + LETG
2335	2000-12-06 06:40:30	30.15	ACIS + LETG
3168	2001-11-30 10:54:02	30.48	ACIS + LETG
3668	2002-06-11 17:36:01	14.26	ACIS + LETG
3707	2002-11-30 06:25:53	28.51	ACIS + LETG
4416	2003-12-16 08:21:55	49.2	ACIS + LETG
6090	2005-05-25 18:43:22	29.14	ACIS + LETG
6091	2005-09-19 04:24:02	30.95	ACIS + LETG
6874	2006-07-29 21:39:09	30.12	ACIS + LETG
6924	2006-07-06 14:55:19	10.03	ACIS + LETG
6927	2006-04-02 21:01:07	28.56	ACIS + LETG
7293	2006-07-06 21:00:10	9.0	ACIS + LETG
8388	2007-07-14 05:18:01	31.06	ACIS + LETG
9704	2008-05-12 13:31:01	29.4	ACIS + LETG
9706	2008-07-02 11:16:33	10.06	ACIS + LETG
9708	2008-07-02 17:27:37	9.76	ACIS + LETG
9710	2008-07-02 23:25:14	9.74	ACIS + LETG
9713	2008-06-29 18:51:21	31.68	ACIS + LETG
331	1999-12-25 13:15:58	63.16	HRC + LETG
1013	2001-04-06 14:38:49	26.82	HRC + LETG
1704	2000-05-31 09:41:11	25.98	HRC + LETG
3166	2001-11-30 02:22:36	29.97	HRC + LETG
3709	2002-11-30 14:47:24	13.83	HRC + LETG
4406	2002-11-30 21:05:01	13.85	HRC + LETG
5172	2004-11-22 23:10:10	27.16	HRC + LETG
6922	2006-07-06 18:02:07	10.08	HRC + LETG
6923	2006-05-01 11:57:39	30.18	HRC + LETG
7294	2006-07-07 05:54:56	10.1	HRC + LETG
7295	2006-07-06 23:58:37	10.15	HRC + LETG
8379	2007-04-22 12:25:45	30.14	HRC + LETG
9707	2008-07-02 14:28:50	10.18	HRC + LETG
9709	2008-07-02 20:26:26	10.19	HRC + LETG
9711	2008-07-03 02:24:02	10.19	HRC + LETG

Table 4.2: *Chandra* Observation log of 4U 1820-30

Obs ID	Start Date	Exposure (ks)	Detector
98	2000-03-10 03:22:58	15.12	HRC-S + LETG

Table 4.3: *Suzaku* Observation log

Data set	Obs ID(phase[g])	Start Date	Exposure (ks)	
			Total	Filtered
PKS2155-1	503082010(AO3)	2008-04-29T18:32:39	90.2	46.9
PKS2155-2	503083010(AO3)	2008-05-02T08:31:41	87.3	58.2
Bulge 3	500001010(SWG)	2006-03-06T08:15:04	51.9	32.2

Table 4.4: Position of the *Chandra* Target Sources

Target Name	(RA, Dec)	(ℓ, b)	(Lon, Lati)	Distance
PKS 2155-304	(329.7, -30.2)	(17.7, -52.2)	(321.2, -16.8)	z$\sim$0.116
4U 1820-303	(275.9, -30.4)	(2.8, -7.9)	(275.1, -7.0)	7.6$\pm$0.4 kpc

Table 4.5: Position of the *Suzaku* Observations

Filed Name	(RA, Dec)	(ℓ, b)	(Lon, Lati)
PKS2155-1	(329.2 , -30.5)	(17.2 , -51.9)	(320.7 , -16.9)
PKS2155-2	(330.2 , -30.0)	(18.2 , -52.6)	(321.7 , -16.7)
Bulge 3	(274.7, -31.5)	(1.3, -7.5)	(274.1, -8.1)

4.2 Data Reduction: *Suzaku*

4.2.1 Data screening

In all the observations, the XIS was set to the normal clocking mode and the data format was either 3×3 or 5×5. The Spaced-raw Charge Injection (SCI) was used for the data PKS2155-2 and PKS2155-1. We used version 2.0 processed *Suzaku* data and the event files of 3×3 and 5×5 observation mode were merged. As described in Chapter 3, XIS-BI (xis 1) has a larger effective area than the sum of XIS-FIs (xis 0,2,3) below 1 keV. Since we were interested in energy band below 1 keV and in order to avoid increasing systematic errors by adding different CCD data, only XIS-BI was used for the later analysis.

Although no unpredicted background flare occurs to *Suzaku* observations, the count rate of non X-ray events of the XIS depends on the angle of the sight line against the Earth's rim. The contamination of the fluorescence lines of the atmosphere of the Earth is significant when the field of view (FOV) of the satellite is near the sunlit Earth. In addition, it is known that the background level becomes extremely high when the satellite is in South Atlantic Anomaly (SAA) or in regions where the cut-off rigidity (COR) of the cosmic ray is low. Therefore we first cleaned the data using the selection criteria: elevation from sunlit and dark earth rim > 20 deg, cut off rigidity > 8 GV.

4.2.2 Exclusion of the solar X-ray

Solar X-ray can scatter off the earth's atmosphere into the telescope, which is either by Thompson scattering or fluorescence, and could contaminate the spectrum. As *Suzaku* orbits the Earth with the fixed pointing, the column density of the atmosphere along the line of sight, which depends on the elevation of the satellite, varies rapidly and can affects the intensity of scattered X-ray (Figure 4.2). As we have great interest in O VII and O VIII emission lines, we checked the dependency of the 0.5 - 0.7 keV counting rate on the Oxygen column density of the sunlit atmosphere in the line of sight using the MSIS atmosphere model (see Fujimoto et al. (2007); Smith et al. (2007); Miller et al. (2008)). As shown in Figure 4.3, we found that the counting rate was constant as a function of the column density for the cleaned data. Thus there is no significant neutral O emission from Earth atmosphere in the filtered data.

4.2.3 Exclusion of the geocoronal SWCX

The spectrum below 1 keV could be contaminated by the emission induced from solar wind charge exchange (SWCX) occurred in the geocorona. During the observation of the blank field near the North Ecliptic Pole in September 2005, *Suzaku* detected a strong flare in 0.4-1 keV energy band. Fujimoto et al. (2007) divided observation period into two interval; in one period (flare) the solar wind is strong and the other (stable) the solar wind is weak. Comparing the flare and stable spectra (Figure 4.4), they found the intensities of the lines which characterize the emission induced from charge exchange. Thus they concluded that the increase of the X-ray flux during the flare is mostly due to emission lines from geocoronal SWCX.

For some data sets of soft X-ray diffuse emission observed with *Suzaku* XIS1, we extracted

the spectra sorted by proton flux of solar wind, and investigated the relation of the threshold of proton flux with O VII line intensity in the spectrum while proton flux is below the threshold. We found that O VII line intensity could be affected by geocoronal SWCX when the threshold of proton flux is larger than 4×10^8 protons s^{-1} cm^{-2} (see also Mitsuda et al. (2007)). Therefore, as the last stage of the data reduction, we removed time intervals in which the data is contaminated by the SWCX from the geocorona. We calculated the solar-wind proton flux using ACE SWEPAM data[1]. The ACE SWEPAM data is not available for certain time periods. In that cases we used WIND SWE data [2]. The proton flux and XIS-BI light curve in energy range of 0.3-2 keV in each observation period are shown in Figure 4.6.

The probability of a contamination by the SWCX from the geocorona increases if the shortest Earth-to-magnetopause (ETM) distance (Figure 4.5) is shorter than a few Earth radius ($R_{\rm E}$) (Fujimoto et al., 2007). Here, the magnetopause is defined to be the lowest position along the line of sight where geomagnetic field is open to interplanetary space. We calculated the ETM distance every 256 s of all the observation periods using the T96 magnetic field model (Tsyganenko & Sitnov, 2005). We obtained the interplanetary plasma parameters required for the calculations from the CDAWeb. Figure 4.7 shows the calculated ETM distance and position of magnetopause in GSM coordinates in the observation period.

Then we excluded those events meeting either of the following two criteria by Yoshino et al. (2009). The first one is solar wind flux. We removed the time intervals when the proton flux in the solar wind exceeds 4×10^8 s^{-1} cm^{-2} (Masui et al. (2008)). ACE and WIND is in L1 of the Solar-Earth system, 1.5×10^6 km away from the Earth and assuming average solar wind velocity as 300 km s^{-1}, we corrected traveling time of the solar wind from L1 to the Earth. The second criteria is the Earth-to-magnetopause (ETM) distance in the line sight of Suzaku (Fujimoto et al. (2007)), which is required to be $> 5R_E$.

For PKS 2155-304 observations, we found that about 20% and 5% of the exposure time of our 1st and 2nd observations meets the first criteria and no time meets the second criteria. For Bulge 3 observation, $\sim$ 40% of the exposure time meets the first criteria and no time meets the second criteria. Thus we exclude those times form observations and used the remaining time in further analysis.

[1]The data available at http://www.srl.caltech.edu/ACE/ACS/

[2]The data available at http://web.mit.edu/afs/athena/org/s/space/www/wind.html

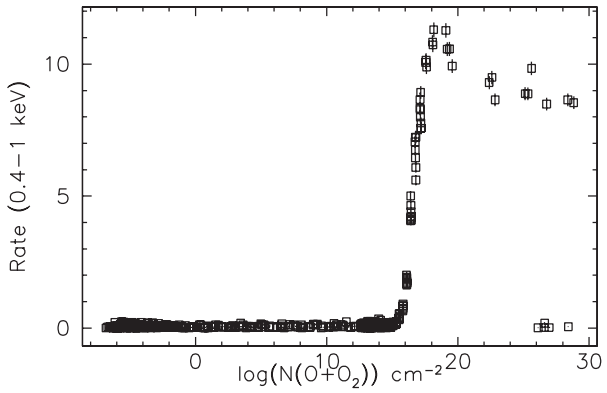

Figure 4.2: The raw count rate in the 0.4-1.0 keV band for the MBM12 on-cloud observation as a function of atmospheric column density of oxygen atoms and molecules. The scattered solar X-ray contribution rises sharply at low elevations, where the atmospheric column density of oxygen is larger than $\sim 10^{15}$ cm^{-2}. from Smith et al. (2007)

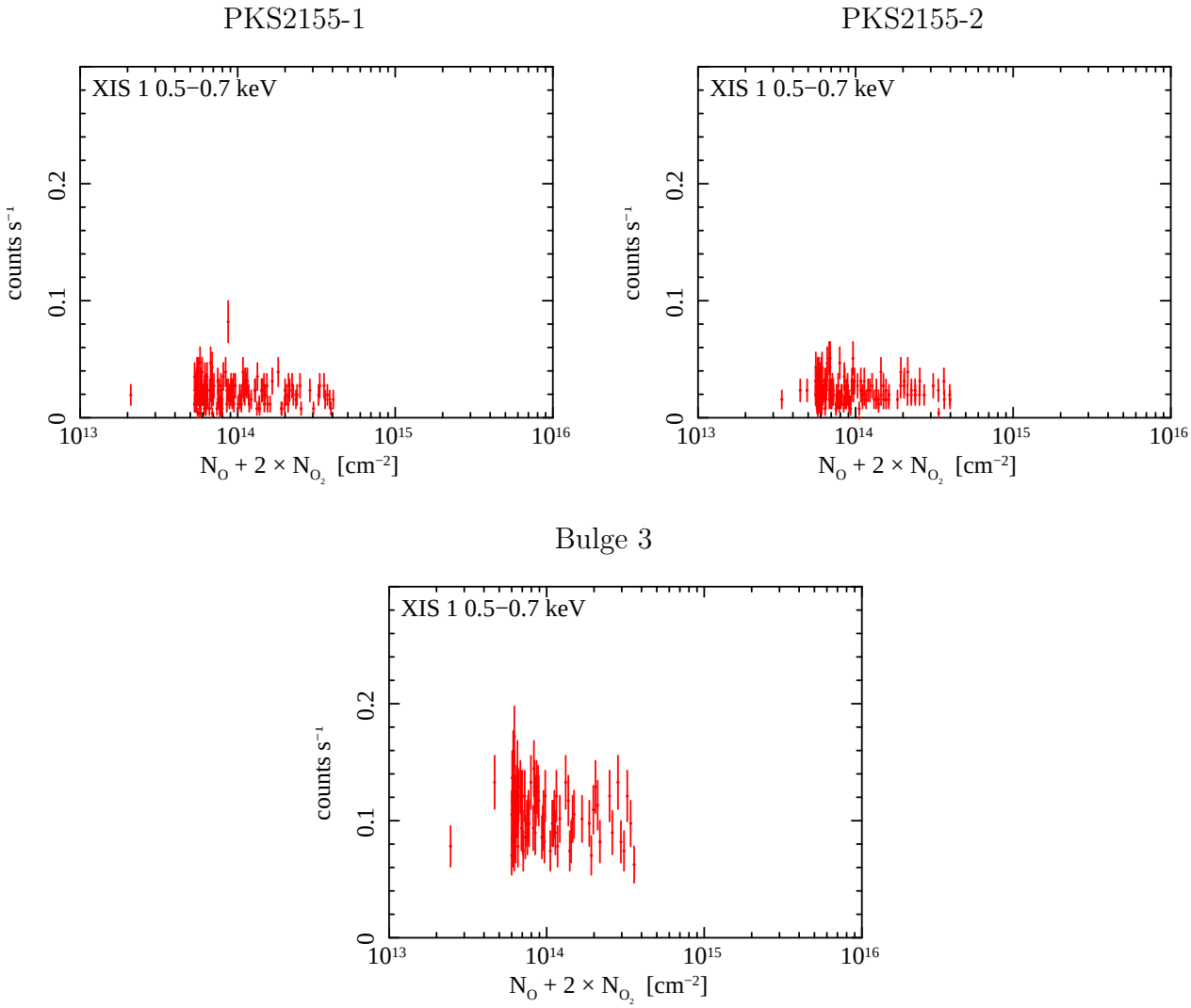

Figure 4.3: The 0.5-0.7 keV count rate of each observation in 256 sec bins as a function of Oxygen column density of the sunlit atmosphere in the line of sight using the MSIS atmosphere model.

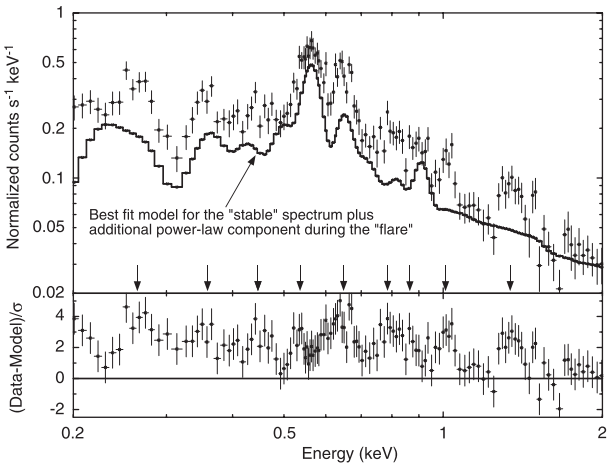

Figure 4.4: Comparison of the “flare” spectrum with the best-fit model for the “stable” spectrum plus additional power-law component during the “flare” in the 0.2–2 keV energy range. The vertical arrows indicate line-like structures in the residuals.

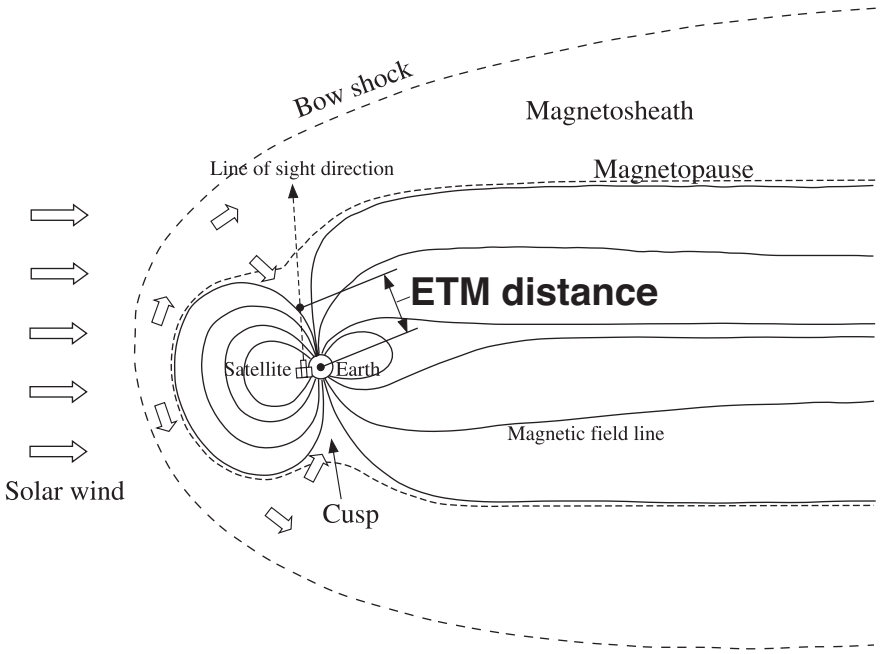

Figure 4.5: Schematic view of the magnetosphere and the definition of ETM distance.

PKS2155-1 PKS2155-2

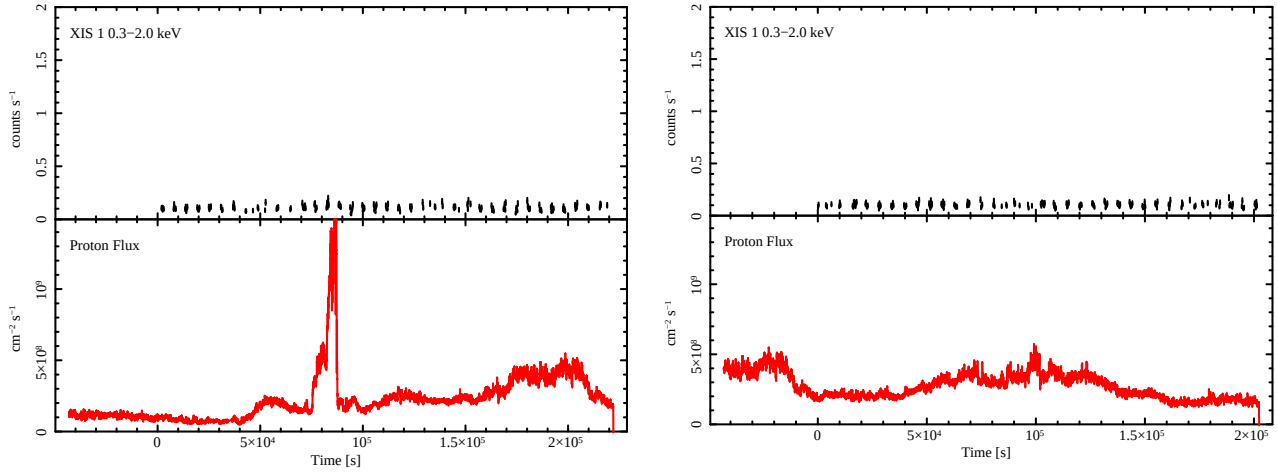

Bulge 3

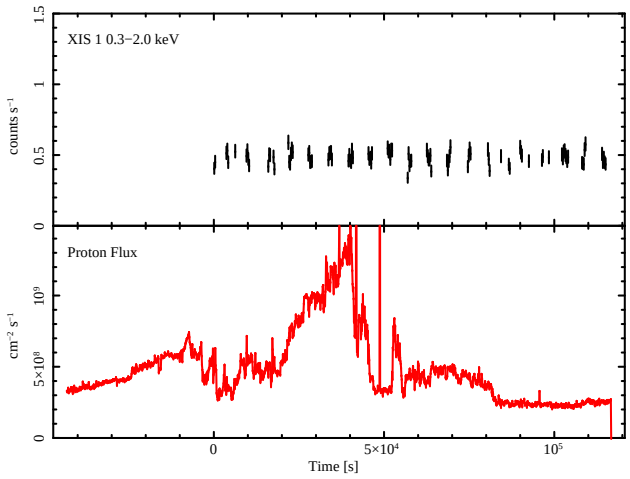

Figure 4.6: XIS-BI light curve in 0.3-2.0 keV (top panel) and solar wind proton flux (bottom panel) in each observation period calculated using the data of ACE SWEPAM (64 sec bin) or WIND SWE (64 sec bin). The origin is set to the beginning of each observation with *Suzaku* . For the data calculated from ACE and WIND, each bin was shifted in time to correct for the travel time of the solar wind from the satellites to the Earth (typically $\sim$ 5000 sec).

PKS2155-1

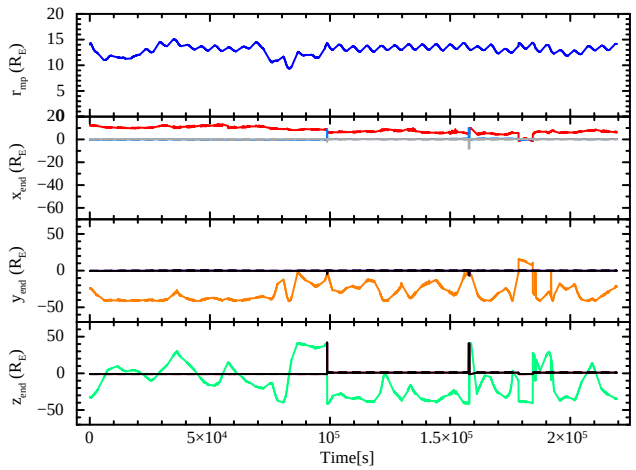

PKS2155-2

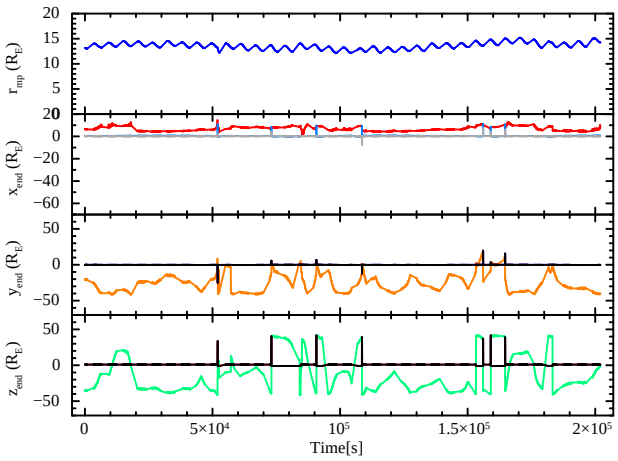

Bulge 3

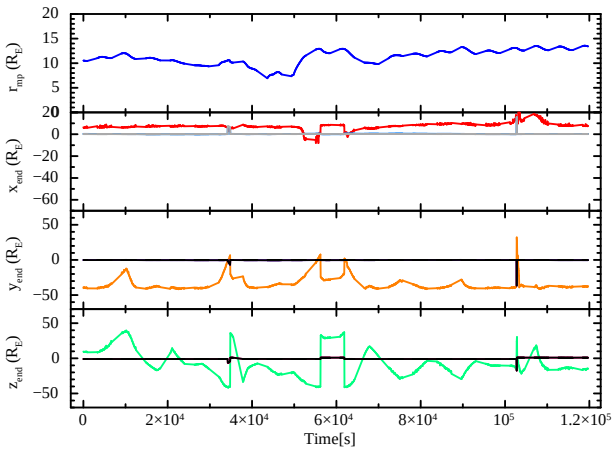

Figure 4.7: Magnetopause, which is defined to be the lowest position along the line of sight where geomagnetic field is open to the interplanetary space, in each observation period as a function of time calculated using T96 magnetic field model[a] (Tsyganenko & Sitnov (2005)). Top panel are earth-to-magnetopause distance, second, third and fourth panel are respectively the x, y, z value of the magnetopause in GSM (Geocentric Solar Magnetosheric[b]) coordinates every 256 sec in unit of earth radius R_E . [a] The parameters of this model are Geodipole tilt angle, Solar wind pressure, Dst index, Interplanetary magnetic filed and GSM position of the observation point. [b] The x-axis of the GSM coordinate system is defined along the line connecting the center of the Sun to the center of the earth. The origin is defined at the center of the earth, and ins positive towards the Sun. The y-axis is defined as the cross product of the GSM x-axis and the magnetic dipole axis; directed positive towards dusk. The z-axis is defined as the cross product of the x- and y-axis. The magnetic dipole axis lies within the xz plane.

4.2.4 Exclusion of the point source

We then constructed an X-ray image in 0.4 to 1 keV and in 1 to 5 keV energy range to remove point sources. In all analysis, we did not exclude the two corners of the image where the calibration sources ^{55}Fe illuminates, because it does not affect low energy spectra ($\lesssim 1$ keV)in which we are interested and the data can show better statistics.

For PKS 2155-304 observations, we found no obvious discrete X-ray sources in the fields (Figure 4.8, 4.9).

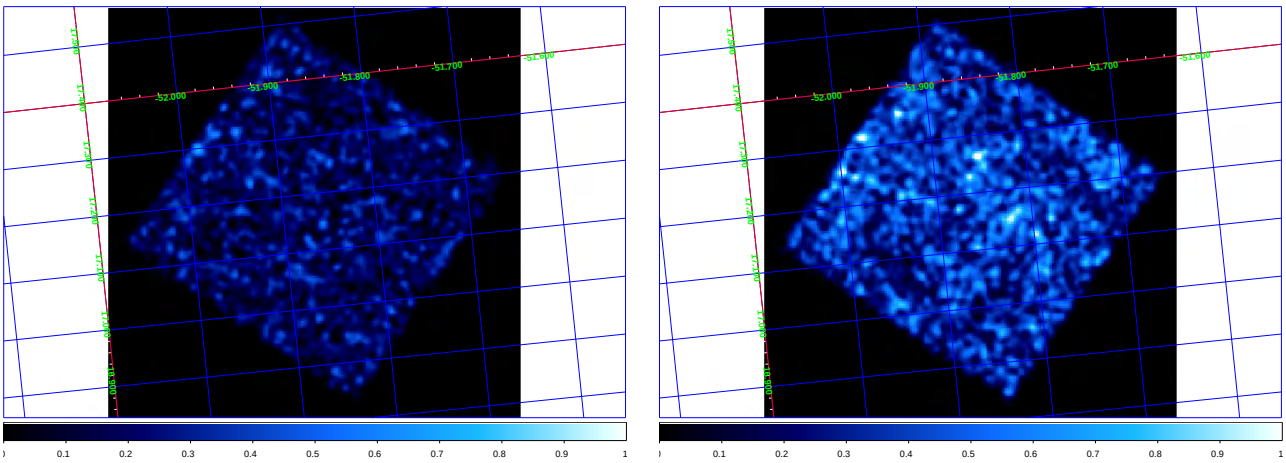

0.4keV-1keV 1keV-5keV

Figure 4.8: XIS 1 images in the 0.4 to 1 keV (left) and 1 to 5 keV (right) band of PKS2155-1.

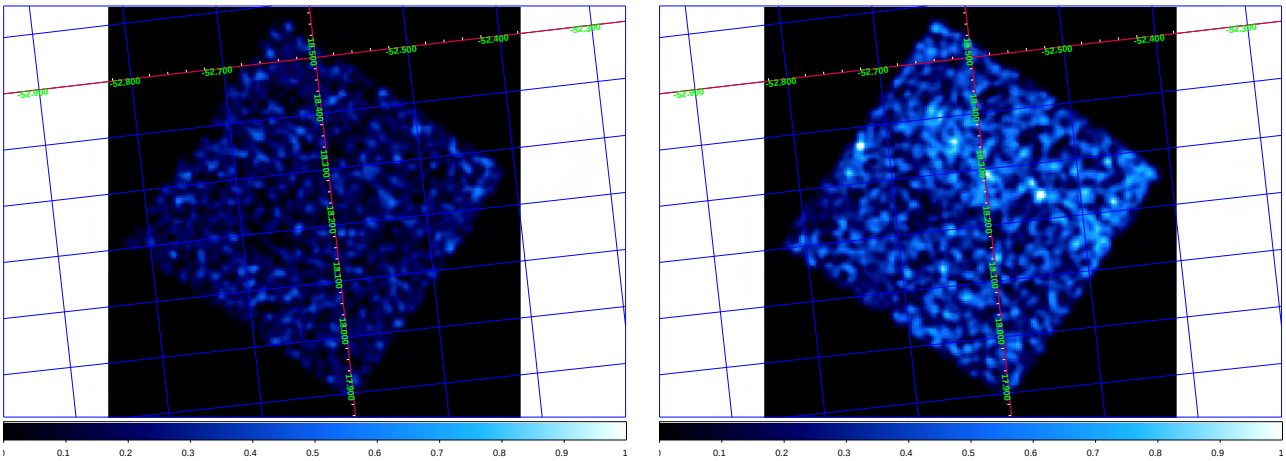

0.4keV-1keV 1keV-5keV

Figure 4.9: XIS 1 images in the 0.4 to 1 keV (left) and 1 to 5 keV (right) band of PKS2155-2.

For Bulge 3, we also found no discrete sources (Fig 4.10). However, there would be many low luminosity sources in this direction, thus we used wavelet analysis using CIAO: *wavdetect* to detect such point sources. We found 23 point source possibilities in the fields and removed a circular region with 1' radius centered at the source position from the data. These possibilities can be caused by statistical fluctuations and we have to check it. Then we

compared the spectrum including the point source possibilities and the spectrum excluding them and found there is no significant difference between these spectra. To increase the photon counts and reduce the statistical error, we decided to use data including the point source possibilities in further analysis.

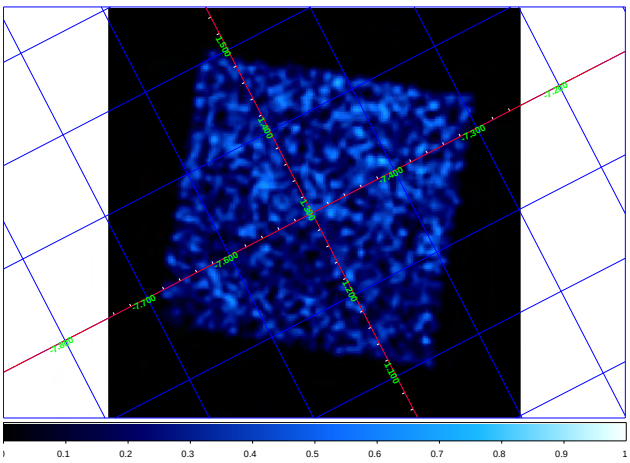

0.4keV-1keV (before exclusion)

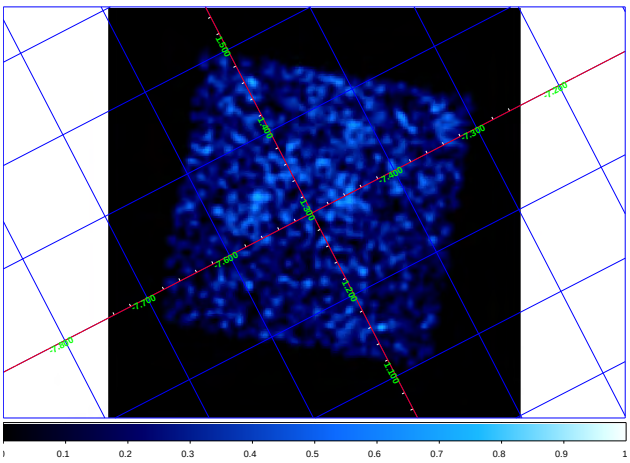

1keV-5keV (before exclusion)

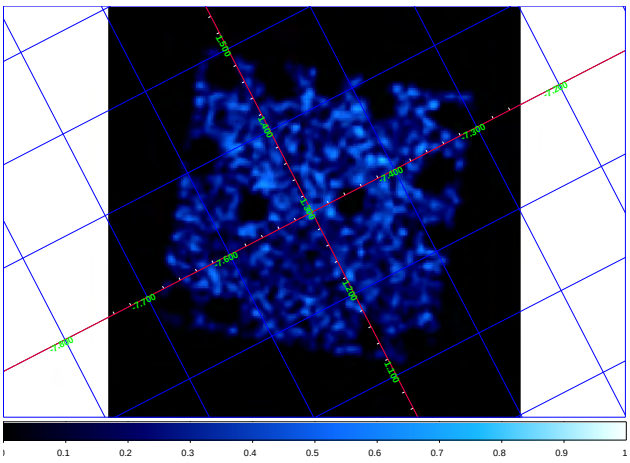

0.4keV-1keV (after exclusion)

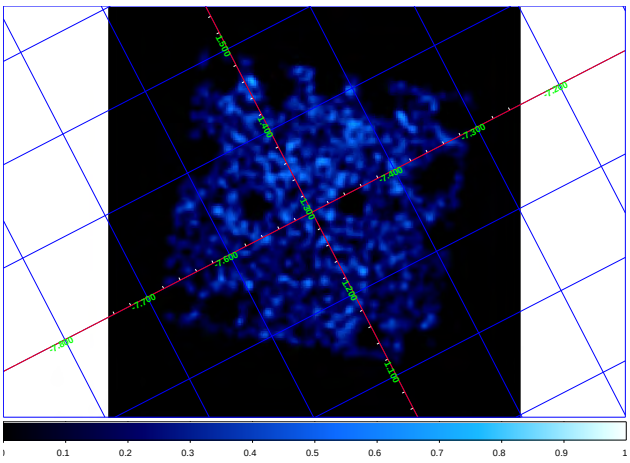

1keV-5keV (after exclusion)

Figure 4.10: XIS 1 images in the 0.4 to 1 keV (left) and 1 to 5 keV (right) band of Bulge 3 observation. In the top panel, point sources are included and in the bottom panel, they are removed.

4.2.5 Background and response

When the FOV of the XRT points at the night Earth where the atmosphere is not illuminated by the Sun, no X-rays from the source hits the detectors, i.e. all the events are due to charged particle or the noise of the circuit. The non X-ray background (NXB) spectrum based on this night Earth data is the background for our analysis. The NXB spectrum was created using the software of *Suzaku* FTOOLS **xisnxbgen** version 2008-03-08 (Tawa et al., 2008). The NXB spectrum was constructed from the dark Earth database using the standard method in

which the cut off rigidity distributions of the on-source and the background data were made identical.

We found 5 to 10 % discrepancy in the counting rates above 10 keV energy range between the non X-ray background and the observation data, suggesting background uncertainty of this level. However, since in the energy range below 1 keV, the non X-ray background is only about 10 % of the diffuse X-ray background, this level of the background uncertainty is negligible.

In order to perform spectrum fitting, we generated the efficiency file (so-called arf file) for a flat field, using *Suzaku* FTOOLS **xissimarfgen** version 2009-01-08 (Ishisaki et al., 2007) and the file for contamination thickness of ae_xi1_contami_20081023.fits, assuming a 20′-radius flat field as the input emission of the generator. The pulse height re-distribution matrix (so called rmf file) was created by *Suzaku* FTOOLS **xisrmfgen** version 2009-02-28.

4.3 Data Reduction: *Chandra*

4.3.1 Data screening

There are two grating spectrographs (the high and the low energy transmission grating spectrographs; LETG and HETG) and two sets of detectors (the advanced CCD imaging spectrometer and the high resolution camera; ACIS and HRC) aboard *Chandra* .

For PKS 2155-304, we used all observations available to the date of 2009 March, except for some observations made with non-standard configuration of ACIS (i.e., putting source outside the CCD-S3 chip) to avoid spectral resolution degradation. The data used in this work include 46 observations with an accumulated exposure time of 1.07 Ms (Table 4.1).

4U 1820-303 is observed three times by *Chandra* and we use all observations in analysis.. One observation used detector set of LETG + HRC and the accumulated exposure time is 15 ks.

4.3.2 Reprocessing

We reprocess the observations using CIAO 3.2.1[3] and the calibration database CALDB 3.1.0. When extracting the grating spectra and calculating the instrumental response files using CIAO thread, we used the same energy grid (0.0125 Å) for all observations with different grating instruments and/or with different detectors for ease of the co-adding process described in the following.

For those HETG + ACIS observations, we only use the medium energy grating (MEG), because the effective area of the MEG is $\sim$5 times larger than that of the High-Energy Grating (HEG) in the energy range in which our diagnostic absorption lines are exist ($<\sim$ 1keV). The effective area of the first orders is also at least one order of magnitude larger than that of the higher orders ($\geq$2). Therefor we only use the first-order MEG spectra in further analysis. As for the LETG + ACIS, also we only use the first-order spectra.

For the LETG + HRC observations, the HRC has little intrinsic energy resolution, and thus one needs to account for not only the local line spread but also the global spectral overlapping of different orders. Thus we followed method used in Wang et al. (2005). First

[3]http://cxc.harvard.edu/ciao/guides/

we calculate the RMFs and ARFs from the first to sixth grating orders assuming the higher than sixth order contribution is negligible below ∼1 keV. Then we added RMFs and ARFs to form order combined response file. To easily implement, we further followed the procedure presented in Yao et al. (2009) to extract the first order spectra. We first obtained a "global" best fit to the spectrum and then subtracted the spectral counts channel-by-channel by the difference of model-predicted counts based on the order-combined response file from those based on the first-order response file. In further analysis we used this first-order LETG+HRC spectrum.

4.3.3 Consistency check and co-adding

To improve counting statistics, we check the consistency and then co-added the first grating order spectra of all observations to obtain a single stacked spectrum and a corresponding instrumental response file.

In Figure 4.11 and Table 4.6, we show the results of consistency check. All the results are consistent each other.

Table 4.6: Consistency check of the PKS 2155-304 spectra

Detector Set	b	Centroid			Column Density		χ^2/dof
	km s^{-1}	keV			log cm^{-2}		
		O VIIKα	O VIIIKα	O VIIKβ	O VII	O VIII	
All combined	294^{+149}_{-220}	$0.5738^{+0.0001}_{-0.0002}$	$0.6531^{+0.0003}_{-0.0003}$	$0.6658^{+0.0006}_{-0.0006}$	$15.76^{+0.07}_{-0.08}$	$15.56^{+0.09}_{-0.12}$	489.82/474
ACIS+HETG	439^{+61}_{-176}	$0.5740^{+0.0003}_{-0.0003}$	$0.6538^{+0.0005}_{-0.0005}$	0.6659 (fixed)	$15.94^{+0.15}_{-0.19}$	$15.75^{+0.17}_{-0.25}$	522.62/517
ACIS+LETG	381^{+119}_{-361}	$0.5737^{+0.0003}_{-0.0003}$	$0.6532^{+0.0005}_{-0.0004}$	$0.6660^{+0.0007}_{-0.0007}$	$15.79^{+0.11}_{-0.13}$	$15.51^{+0.15}_{-0.20}$	486.95/516
HRC+LETG	59^{+375}_{-27}	$0.5738^{+0.0002}_{-0.0002}$	$0.6528^{+0.0004}_{-0.0004}$	$0.6652^{+0.0027}_{-0.0010}$	$16.05^{+0.33}_{-0.42}$	$15.85^{+0.99}_{-0.38}$	650.54/474

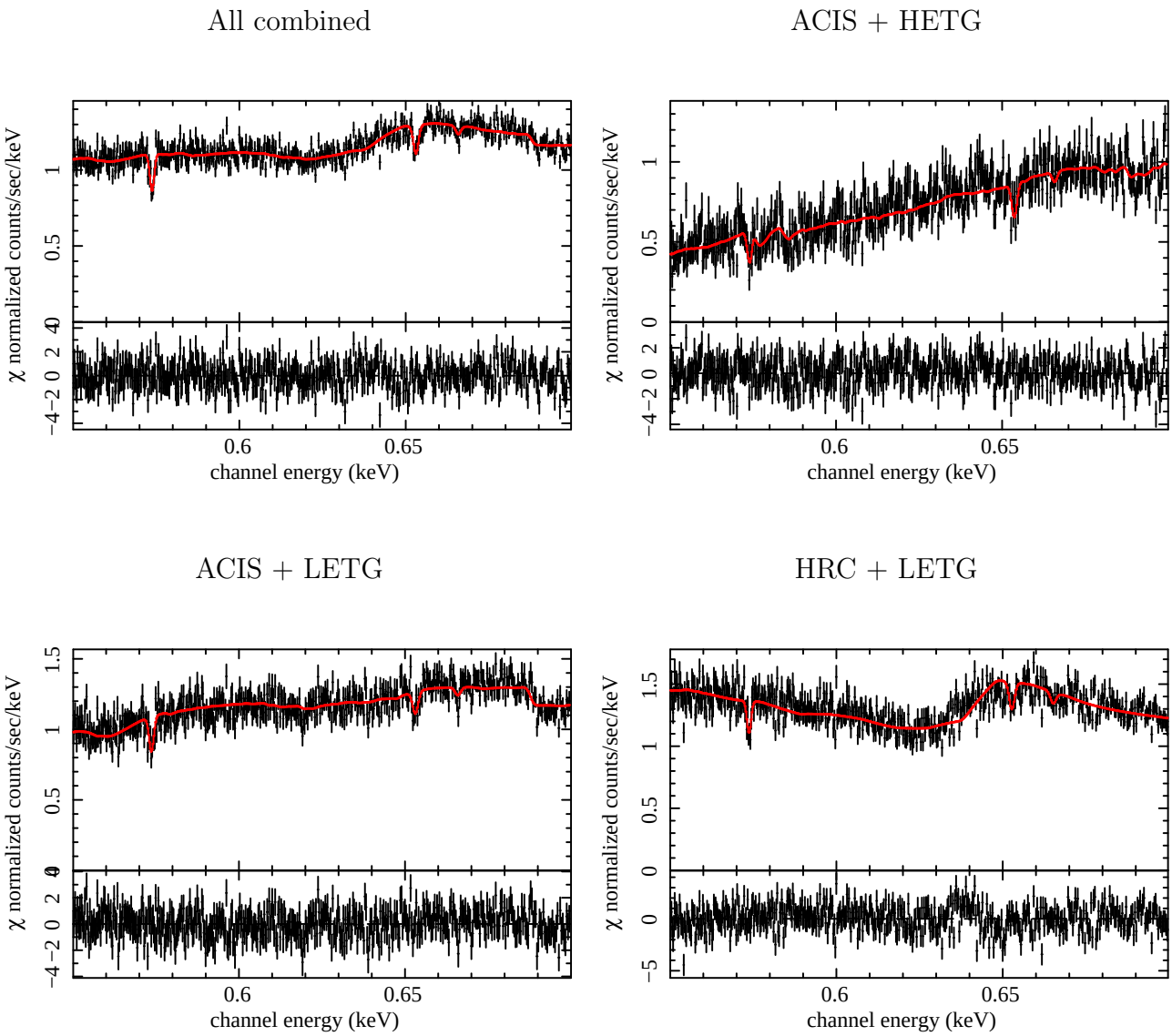

Figure 4.11: Spectra between 0.55 and 0.7 keV of combined all observation data (top-left), ACIS + HETG (top-right), ACIS + LETG (bottom-left) and HRC + LETG (bottom-right).

Chapter 5

Analysis and Results: High Galactic Latitude

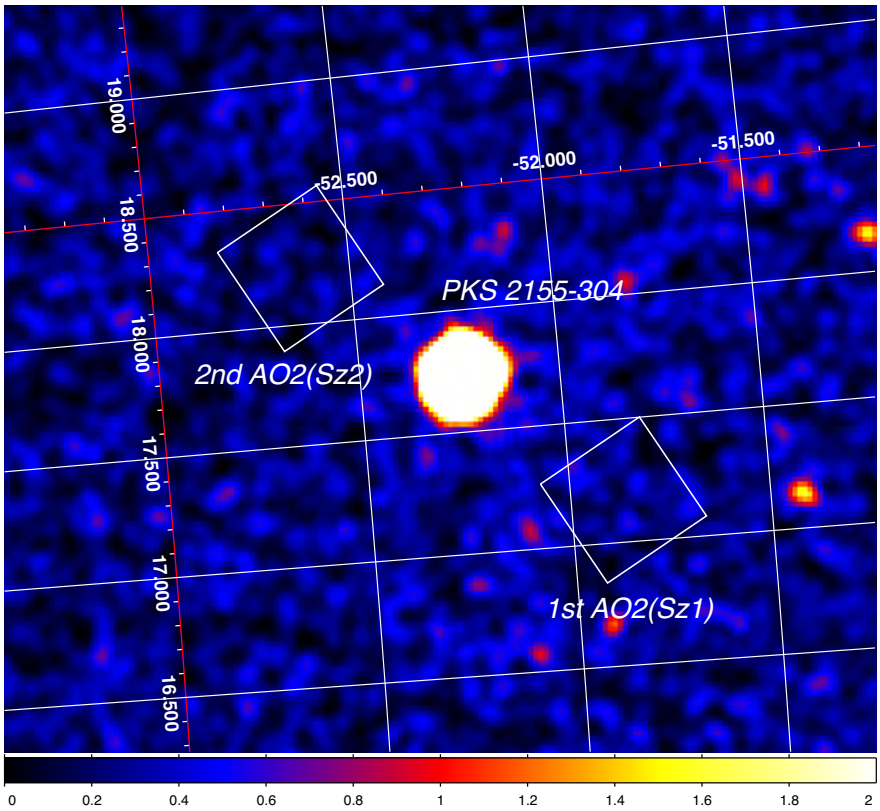

Figure 5.1: RASS 0.1 - 2.4 keV band X-ray map in the vicinity of PKS 2155-304 (the bright source at the center) and the XIS field of view of the two presented observations.

We observed the emission of the hot diffuse gas toward two off-fields of the PKS 2155-304 sight line during the AO2 program . To minimize confusion by stray lights from the PKS 2155-304 and to average out the possible spatial gradient of the diffuse emission intensity, the two fields were chosen to be 30′ away from the PKS 2155–304 and in nearly opposite directions (Figure 5.1). For convenience we call 1st *Suzaku* observation as Sz1 and second

observation as Sz2.

5.1 X-ray Absorption Line Analysis with *Chandra*

We first measure the equivalent widths (EWs) of the absorption lines of the highly ionized oxygen ions. Since the measurement of the narrow absorption lines is only relevant to the local continuum spectrum, we fit the final PKS 2155-304 spectrum between 0.55 and 0.7 keV using a power-law model modified with absorption by neutral ISM(*wabs*). The column density of neutral hydrogen is fixed to 1.47×10^{20} cm^{-2} that is obtained by LAB Survey of Galactic HI in this direction (Kalberla et al. (2005)). We use three Gaussian functions to model the O VII K_α, O VIII K_α, and O VII K_β absorption lines (model A1). The measured EWs are summarized in Table 5.1 and these values are consistent with those reported by Williams et al. (2007).

We then use an absorption line model, *absem* to replace the Gaussian functions to probe the properties of the absorbing gas. The *absem* model, adopting the voigt function in fitting the line profile, can be used to fit a individual line and jointly analyze multiple absorption lines at a same time (Yao et al. (2005), Yao & Wang (2007)). The diagnostic procedure of the absorbing gas can be summarized in the following: (1) A joint analysis of O VII K_α and O VII K_β directly constrains the O VII column density and the Doppler dispersion velocity ($v_{\rm b}$). With the constrained $v_{\rm b}$, adding O VIII K_α line in the analysis also yield the column density of O VIII (model A2). (2) Since the column density ratio of O VII and O VIII is sensitive to the gas temperature , a joint analysis of O VII and O VIII lines will naturally constrain the gas temperature (model A3). (3) Assuming solar abundance of oxygen, for the constrained gas temperature, the O VII (or O VIII) column density can be converted to the corresponding hot phase hydrogen column density (model A4). Our fitting results are presented in Table 5.2. The constrained O VIIcolumn density, 5.9 (+1.2, -0.9) $\times10^{15}$ cm^{-2} is comparable to the typical value $\sim 10^{16}$ cm^{-2} obtained by AGN observations from two systematical studies by Fang et al. (2006) and Bregman & Lloyd-Davies (2007).

Table 5.1: Spectral fitting results of absorption data with model A1

Model		O VII K_α	O VIII K_α	O VII K_β
A1	Centroid (eV)	$573.8^{+0.1}_{-0.2}$	$653.1^{+0.4}_{-0.4}$	$665.8^{+0.1}_{-0.4}$
	Sigma (eV)	$0.32^{+0.25}_{-0.32}$	$1.01^{+0.62}_{-0.54}$	$0.01^{+0.97}_{-0.01}$
	Equivalent Width (eV)	$0.354^{+0.075}_{-0.071}$	$0.377^{+0.116}_{-0.102}$	$0.119^{+0.058}_{-0.058}$

Model A1:*wabs*(*power-law*+3×*Gaussian*)

5.2 X-ray Emission Spectra with *Suzaku*

We analyzed the emission data to constrain emission measure and temperature of the hot ISM. For this purpose, first we modeled the SXDB by several components because the emission spectrum is a superposition of these components.

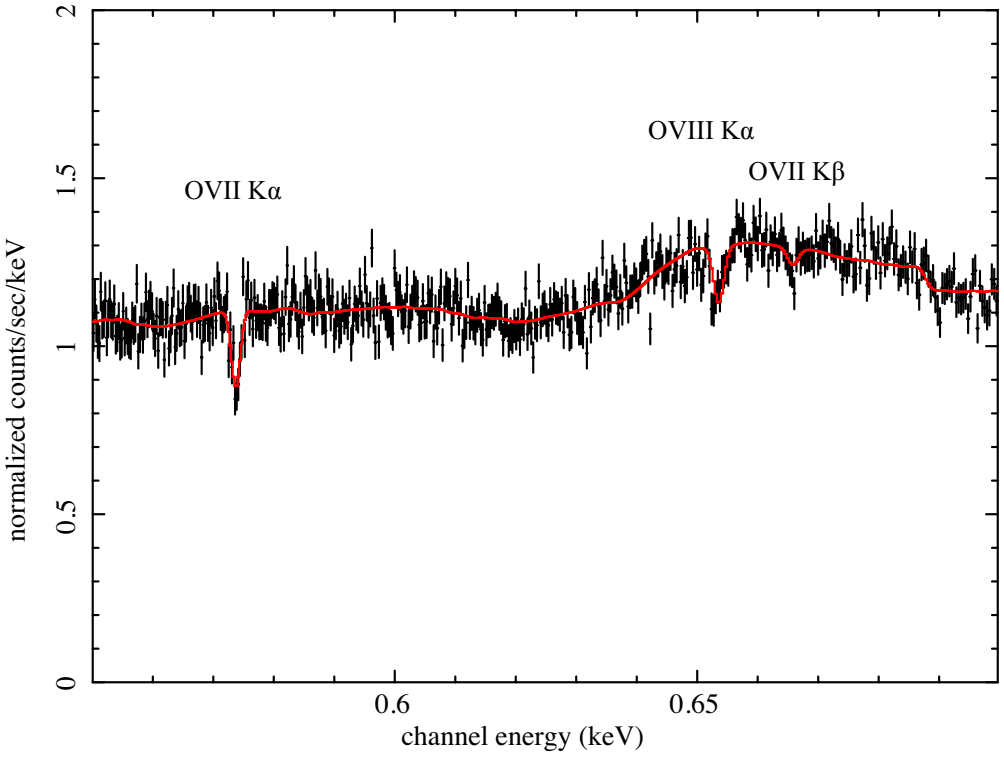

Figure 5.2: Chandra spectrum of PKS 2155-304 between 0.55 and 0.7 keV.

Table 5.2: Spectral fitting results of absorption data with model A2-A4

Model	v_b (km s^{-1})	log [Column Density] (cm^{-2})			log T (K)	χ^2/dof
		$N_{\rm O\ VII}$	$N_{\rm O\ VIII}$	$N_{\rm H_{Hot}}$		
A2	294^{+149}_{-220}	$15.76^{+0.07}_{-0.08}$	$15.56^{+0.09}_{-0.12}$	···	···	489.82/474
A3	375^{+124}_{-158}	$15.77^{+0.08}_{-0.07}$	···	···	$6.27^{+0.02}_{-0.03}$	498.01/474
A4	290^{+152}_{-220}	···	···	$19.08^{+0.06}_{-0.07}$	$6.28^{+0.02}_{-0.02}$	489.84/474

Model A2,A3,A4:*wabs*(*power-law*)×*absem*×*absem*×*absem*

5.2.1 Foreground and background emission

We assume here that the SXDB consists of four dominant components: 1) the Local Hot Bubble (LHB), 2) Solar Wind Charge eXchange in heliosphere (SWCX), 3) hot ISM, 4) the cosmic X-ray background emission (CXB; mainly from the unresolved extragalactic sources like AGNs). The contribution of unresolved Galactic sources is expected to be negligible at high galactic latitude ($|b| > 30°$) and we didn't consider it further in this work.

The parameters for the components are summarized in Table 5.3. The CXB spectrum can be well described by a *power-law*.

In study of 14 blank sky observations by *Suzaku*, Yoshino et al. (2009) found that there are at least 2 LU of OVII line emission even at the fov whose attenuation length for the line is less than 300 pc. This emission is considered to be come from the SWCX and LHB, though

Table 5.3: Parameters for the SXB components

Component	Model	$\log T$ (K)	Photo Index	Normalization[a,b]
CXB	power-law	-	1.4	~ 10
SWCX+LHB	thin thermal plasma	6.06	-	4.3

[a] in unit of photons cm^{-2} $s^{-1}str^{-1}$ eV^{-1} @1keV for the CXB

[b] Emission Measure $10^{-3} \int n_e n_p dl$: in unit of cm^{-6} pc for the SWCX+LHB

they are hard to be separated with the current CCD energy resolution. After Smith et al. (2007) and Henley et al. (2007), Yoshino et al. (2009) found that it can be well represented by an unabsorbed optically thin thermal emission from collisionally ionized plasma, and that the best-fit temperature is log T = 6.06. Therefor we use $\sim 10^6$ K plasma of 2 LU O VII surface brightness as SWCX+LHB component. The uncertainty of this estimation is discussed in section 5.4.

The observed emission has been absorbed by the foreground neutral ISM except for the SWCX+LHB component. In the following analysis, we also fix the column density of the neutral hydrogen to be 1.47×10^{20} cm^{-2} (Kalberla et al. (2005)).

5.2.2 Spectral fitting

To probe the hot ISM properties, we use the following model to fit our spectra (model E1): $wabs(power - law_{CXB} + vapec_{hotISM}) + apec_{LHB+SWCX}$, in which the photo index of the CXB is fixed at 1.4 and its normalization is a free parameter. The temperature and the corresponding emission measure (and thus the normalization) of the $apec_{LHB+SWCX}$ component are set to 1.2×10^6 K and 0.0043 pc cm^{-6}, respectively, which correspond to 2 LU of O VII K_α line emission. In the hot ISM component, we fix the abundance ratio of oxygen to hydrogen to the solar value, and let the abundances of nitrogen, neon, and iron free.

This model fitted spectra from both the two pointings consistently, except for apparently higher neon and iron abundance in Sz1 (Table 5.4) which would be caused by lower temperature of Sz1 hot ISM component. It is important to clarify whether this is caused by statistical effect or by true difference in plasma temperature. The surface brightness of each lines is a better indicator for this purpose.

Then we evaluate the surface brightness of O VII and O VIII lines by modifying the model E1 to a model E2. We set the oxygen abundance of the hot ISM and LHB+SWCX emission to be *zero* and use three *Gaussian* emission line to represent O VII K_α, O VII K_β, and O VIII K_α emission (Figure 5.3). This model fitted both spectra with χ^2/dof of 135.52/132 and 150.59/137 respectively. Assuming ratio between O VII K_β, and O VII $K_\alpha (= \mu)$ intensities as 0.07, we calculate the O VII, O VIII and Ne IX surface brightness as listed in Table 5.5. Intensities of these lines between the two fields are consistent within the 90% confidence level, and we assume that the temperature difference is not essential. We plot the O VII and O VIII surface brightness points over Yoshino et al. (2009) results (Figure 5.5, with 1 σ error) and found that O VII and O VIII surface brightness of PKS 2155-304 direction matches the trend of the other 14 field.

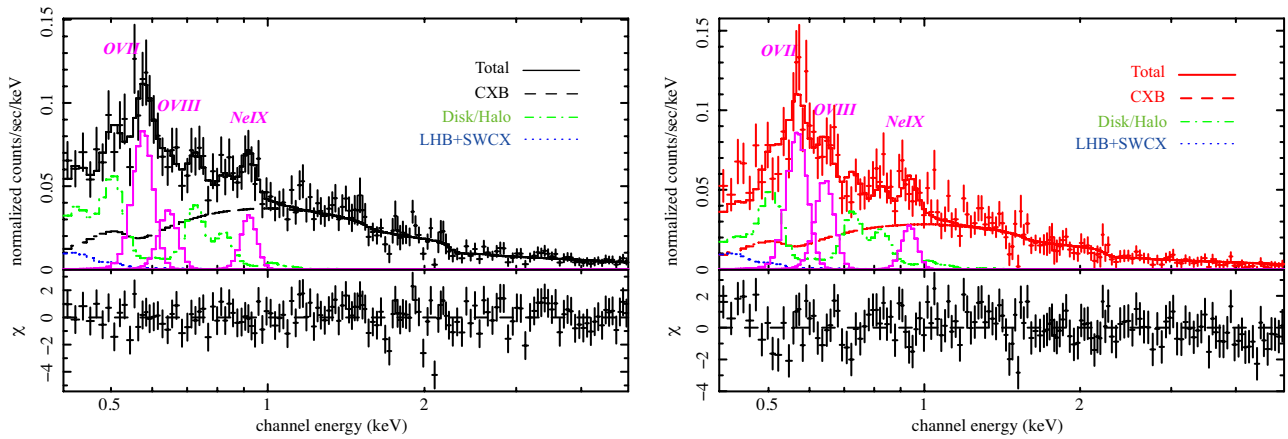

Figure 5.3: Suzaku spectra between 0.4 and 5.0 keV of Sz1 (left) and Sz2 (right) are plotted. Fitted model is E2.

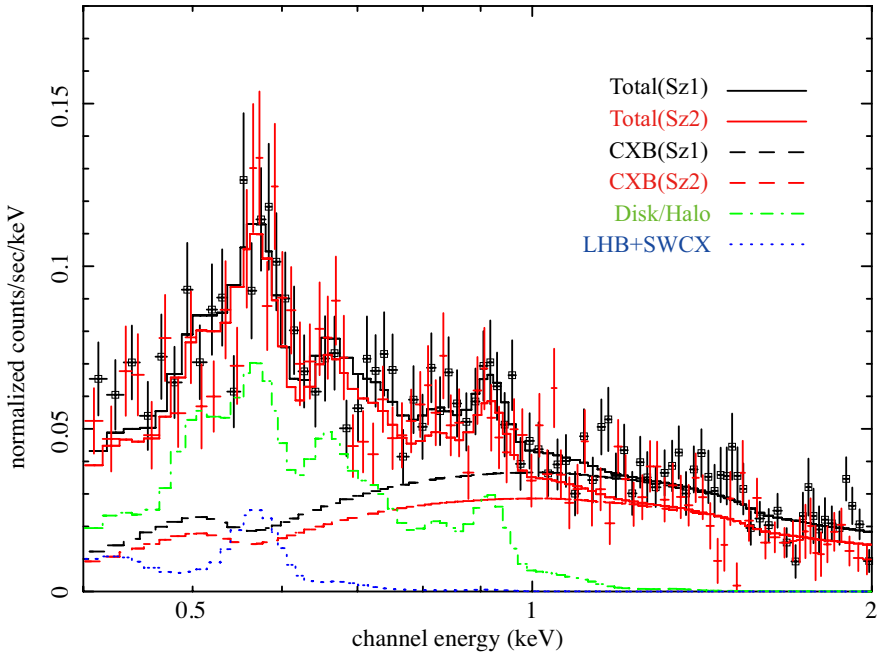

Figure 5.4: Suzaku spectra between 0.4 and 2.0 keV. Sz1 and Sz2 observations are both plotted. Fitted model is E1 ($wabs(power\text{-}law{+}vmekal_{\ hotISM}) + mekal_{LHB+SWCX}$) and parameters of the hot ISM components are linked in both spectra.

We then fitted both data simultaneously with model E1 by linking parameters of the hot ISM component in both observations. The results are shown in Table 5. This model fitted the both spectra simultaneously (figure 5.4). The emission measure is 3.0 (+0.3, -0.3) $\times 10^{-3}$ cm^{-6} and the temperature is 2.1 (+0.1, -0.1) $\times 10^{6}$ K. McCammon et al. (2002) reported emission measure and temperature of the absorbed thermal component (=hot ISM) as 3.7 $\times 10^{-3}$ cm^{-6} pc and 2.6 $\times 10^{6}$ K which are comparable to our value.

Table 5.4: Spectral fitting results for emission data with the model E1

Model	Data	CXB	LHB+SWCX		hot ISM				χ^2/dof
		Norm [a]	$\log T$ (K)	Norm[b]	$\log T$ (K)	Norm[b]	N/O	Ne/O	Fe/O	
E1	Sz1	$8.40^{+0.38}_{-0.40}$	6.06(fixed)	4.3(fixed)	$6.26^{+0.06}_{-0.04}$	$3.3^{+1.0}_{-0.8}$	$6.0^{+2.5}_{-1.9}$	$6.5^{+3.7}_{-2.5}$	$7.4^{+13.8}_{-4.8}$	148.61/136
E1	Sz2	$6.45^{+0.36}_{-0.43}$	6.06(fixed)	4.3(fixed)	$6.35^{+0.03}_{-0.03}$	$3.2^{+0.5}_{-0.4}$	$4.7^{+2.0}_{-1.6}$	$2.4^{+1.2}_{-0.9}$	$1.0^{+0.8}_{-0.5}$	147.33/141
E1	Sz1+Sz2(Sz1)	$8.30^{+0.35}_{-0.39}$	6.06(fixed)	4.3(fixed)	$6.33^{+0.02}_{-0.02}$	$3.0^{+0.3}_{-0.3}$	$5.8^{+1.6}_{-1.3}$	$3.3^{+1.2}_{-0.9}$	$1.7^{+1.2}_{-0.7}$	306.82/282
	Sz1+Sz2(Sz2)	$6.50^{+0.36}_{-0.39}$	↑	↑	↑	↑	↑	↑	↑	
E1 †	Sz1+Sz2(Sz1)	$8.38^{+0.35}_{-0.36}$	6.06(fixed)	0.0(fixed)	$6.25^{+0.03}_{-0.02}$	$4.9^{+0.7}_{-0.6}$	$4.2^{+1.0}_{-0.8}$	$4.5^{+1.4}_{-1.2}$	$4.7^{+3.0}_{-1.6}$	313.48/282
	Sz1+Sz2(Sz2)	$6.59^{+0.34}_{-0.39}$	↑	↑	↑	↑	↑	↑	↑	
E1 ‡	Sz1+Sz2(Sz1)	$8.25^{+0.38}_{-0.37}$	6.06(fixed)	7.5(fixed)	$6.37^{+0.03}_{-0.03}$	$2.3^{+0.3}_{-0.3}$	$6.9^{+2.4}_{-1.9}$	$3.2^{+1.3}_{-1.0}$	$1.5^{+0.9}_{-0.5}$	299.45/282
	Sz1+Sz2(Sz2)	$6.47^{+0.36}_{-0.38}$	↑	↑	↑	↑	↑	↑	↑	

↑ indicates linked parameters
Sz1+Sz2: simultaneous fitting of the data Sz1 and Sz2
Model E1:*wabs*(*power-law*$_{CXB}$ + *vmekal*$_{hotISM}$) + *mekal*$_{LHB+SWCX}$
Emission measure of *mekal* $_{LHB+SWCX}$ is fixed to 0.0043cm^{-6} which corresponds to 2.0 LU of O VII K_α emission
† Emission measure of *mekal*$_{LHB+SWCX}$ is set to 0 as the lower limit
‡ Emission measure of *mekal*$_{LHB+SWCX}$ is set to the upper limit which corresponds to 3.5 LU of O VII K_α emission
[a] in unit of photons cm^{-2} s^{-1}str^{-1} eV^{-1} @1keV
[b] Emission measure $10^{-3}\int n_e n_p dl$: in unit of cm^{-6} pc

Table 5.5: Surface brightness of O VII, O VIII and Ne IX

Model	Data	CXB		hot ISM		O VII K_α[c]	O VII K_β+ O VIII K_α[c]	O VIII K_α[c]	Ne IX K_α[c]	χ^2/dof
		Norm [a]	Norm[b]	N/O	Fe/O					
E2	Sz1	$8.22^{+0.61}_{-0.28}$	$4.2^{+0.3}_{-0.8}$	6.0 (fixed)	$7.29^{+1.96}_{-1.57}$	$5.01^{+0.68}_{-0.81}$	$1.45^{+0.33}_{-0.51}$	$1.10^{+0.39}_{-0.56}$	$0.65^{+0.12}_{-0.26}$	135.52/132
E2	Sz2	$6.41^{+0.44}_{-0.33}$	$3.8^{+0.7}_{-0.4}$	4.7 (fixed)	$1.42^{+0.34}_{-0.30}$	$5.41^{+0.56}_{-1.05}$	$2.22^{+0.42}_{-0.50}$	$1.84^{+0.49}_{-0.54}$	$0.58^{+0.09}_{-0.31}$	150.59/137

model E2: *wabs*(*power-law*$_{CXB}$ + *vmekal*$_{hotISM}$) + *vmekal*$_{LHB+SWCX}$ + 3×*gaussians*, where Oxygen abundances of two *vmekal* are set to 0
[a] in unit of photons cm^{-2} s^{-1}str^{-1} eV^{-1} @1keV
[b] Emission Measure $10^{-3}\int n_e n_p dl$: in unit of cm^{-6} pc
[c] in unit of LU = photons s^{-1} cm^{-2} str^{-1}

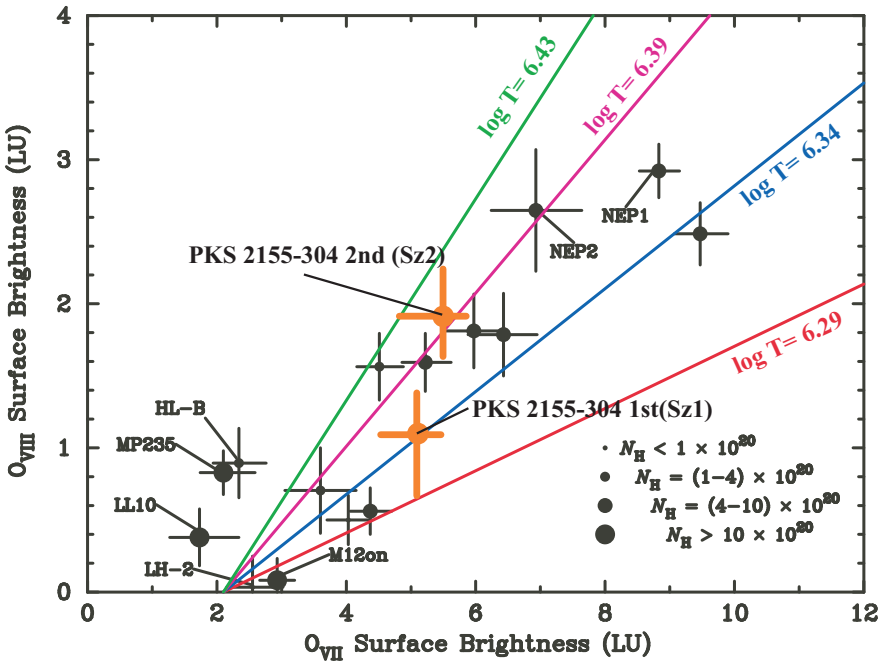

Figure 5.5: Relation between O VII and O VIII surface brightnesses for the 14 (Yoshino et al. (2009))+2 (this work) sky fields observed with *Suzaku*. The horizontal and vertical bars of data points show the 1 σ errors of the estimation. The contribution of O VII K_β emission is corrected for O VIII K_α. The diagonal lines show the relation between O VIIand O VIII , assuming an offset O VII emission of 2.1 LU and emission from a hot plasma of the temperature and the absorption column density shown in the figure. The Galactic absorption column density of the observation fields are indicated by the maker size of the data points.

5.3 Combined Analysis

Up to here, we analyzed the absorption and emission data separately and confirmed that the models including the hot ISM component fit both data with a temperature of 1.91(+0.09, -0.09) $\times 10^6$ K for the absorption and 2.14 (+0.15, -0.14) $\times 10^6$ K for the emission spectra.

Assuming that the both plasma is common and uniform, the plasma length and density can be simply calculated using the emission measure and the column density as 4.0 (+1.9, -1.4) kpc and 7.7 (+2.3, -1.7) $\times 10^{-4}$ cm^{-3}. However the errors of calculated values are over-estimated because errors can not be independent. Moreover important plasma parameters like temperature, velocity dispersion were not concerned in this simple calculation.

In this section, using combined analysis, we will try to obtain the physical condition of the hot ISM plasma, such as density, temperature and their distribution.

5.3.1 Uniform disk model

For the first step of our combined analysis, we try the simplest model: isothermal plasma model with uniform density extends up to h kpc above the disk (model C1).

To perform this combined analysis the emission measure and column density have to be linked with common parameter. We chose the equivalent hydrogen column density ($N_{\rm H_{Hot}}$) and scale height (h) as the control parameters and calculate the emission measure. The relation of the density n, scale height h, column density $N_{\rm H_{Hot}}$ and galactic latitude b is described as $N_{\rm H_{Hot}} = nh/{\rm sin}b$. Thus we can use the A4 model for absorption data directly, and revise the E1 model to use *vabmkl* instead of *mekal* model. The model *vabmkl*, an extension of the *mekal*, is constructed for the combined fit and use the column density and plasma length as the fitting parameters. (see Yao et al. (2009) for detailed model description). For the hot ISM components of the emission spectra, we fixed the abundance ratio of oxygen to hydrogen to the solar value and let the abundances of nitrogen, neon, and iron free again. All parameters but normalization of the CXB components are linked between two emission data. We put lower and upper limit (70-440 km s^{-1}) to the velocity dispersion (v_b) which are 90 % error range of the value obtained by absorption analysis.

The model C1 fits both data (χ^2/dof=802.78/754) and the results are shown in Table 5.6. The column density and temperature are consistent with the A4 model (Table 5.2), while the temperature and abundance of Ne and Fe are not consistent with the E1 model (Table 5.4). This is because that temperature is mostly constrained by absorption data and the lower temperature for the emission spectra preferred the higher abundance to describe the Ne and Fe lines. The plasma length is 4.2 (+1.5, -1.2) kpc and suggests that under isothermal assumption the hot ISM expands beyond the Galactic disk ($\sim$1 kpc).

Table 5.6: Combined spectral fitting results with the uniform disk model

Model	Data	CXB	hot ISM							χ^2/dof
		Norm[a]	$\log N_{\rm H_{Hot}}$ ($\rm cm^{-2}$)	h (kpc)	$\log T$ (K)	v_b⋆ (km $\rm s^{-1}$)	N/O	Ne/O	Fe/O	
C1	Emission:Sz1	$8.38^{+0.39}_{-0.38}$	$19.08^{+0.06}_{-0.07}$	$4.2^{+1.5}_{-1.2}$	$6.27^{+0.02}_{-0.02}$	···	$4.9^{+1.4}_{-1.0}$	$5.2^{+1.4}_{-1.5}$	$5.0^{+1.6}_{-1.7}$	802.78/754
	Emission:Sz2	$6.57^{+0.39}_{-0.38}$	↑	↑	↑	···	↑	↑	↑	
	Absorption	···	↑	···	↑	286^{+154}_{-206}	···	···	···	

↑ indicates linked parameters
model C1: *wabs*(*power-law*+*vmekal*)+*mekal* for the emission, *wabs*(*power*)×(*absem*)^3 for the absorption
⋆Parameter range is limited to 70-440 km $\rm s^{-1}$
[a]in unit of photons $\rm cm^{-2}$ $\rm s^{-1}$ $\rm str^{-1}$ $\rm eV^{-1}$ @1keV

5.3.2 Exponential disk model

Observations of the edge-on galaxies(ex. Wang et al. (2003), Li et al. (2008), Yamasaki et al. (2009)) have revealed that the intensities of X-ray emission from extending hot gas decrease exponentially as a function of height from the galactic plane. As a next step, we tried another simple model, an exponential distribution model (Yao et al. (2009)), to fit the data. In this model density n and temperature T of the hot gas distributed as following equation,

$$n = n_0 e^{-Z/h_n \xi}, \quad T = T_0 e^{-Z/h_T \xi}, \quad \gamma = h_T/h_n \tag{5.1}$$

where Z is the vertical distance from the Galactic plane, n_0 and T_0 are density and temperature at the plane, and h_n and h_T are the scale heights of the density and temperature, respectively, and ξ is the filling factor that is assumed to be 1 in this paper. Thus equivalent hydrongen column density of the hot gas ($N_{\mathrm{H_{Hot}}}$) is calculated as $N_{\mathrm{H_{Hot}}} = \int_0^\infty ndl = \int_0^\infty n_0 \exp(-Z/h_n) dZ/\sin b = n_0 h_n/\sin b$.

The model *vabmekl* and *absem* can also be used as exponential disk model using additional parameter γ (see Yao et al. (2009) for detailed description). So we used the same model as used in uniform model here (model C2). For fitting parameters, we used column density $N_{\mathrm{H_{Hot}}}$ instead n_0 for convenience.

We jointly fitted emission and absorption data using this exponential disk model (Figure 5.6). Fitting results are shown in Table 5.7. We then obtained the scale height for the temperature gradient as h_T = 2.2 (+13, -2.1) kpc and the gas density at the galactic plane as n_0 = 1.3 (+9.7, -0.7) $\times 10^{-3}$ cm^{-3}. This value is typical for mid-plane plasma density (Cox (2005)). The confidence contours of h_n, T_0 and $N_{\mathrm{H_{Hot}}}$ versus γ are plotted in Figure 5.7 over-laid on those of LMC X-3 direction (Yao et al. (2009)). As the high temperature plasma close to the Galactic plane can emit the Fe and Ne lines effectively, the spectrum can be fitted without higher abundance of heavy element than the solar value.

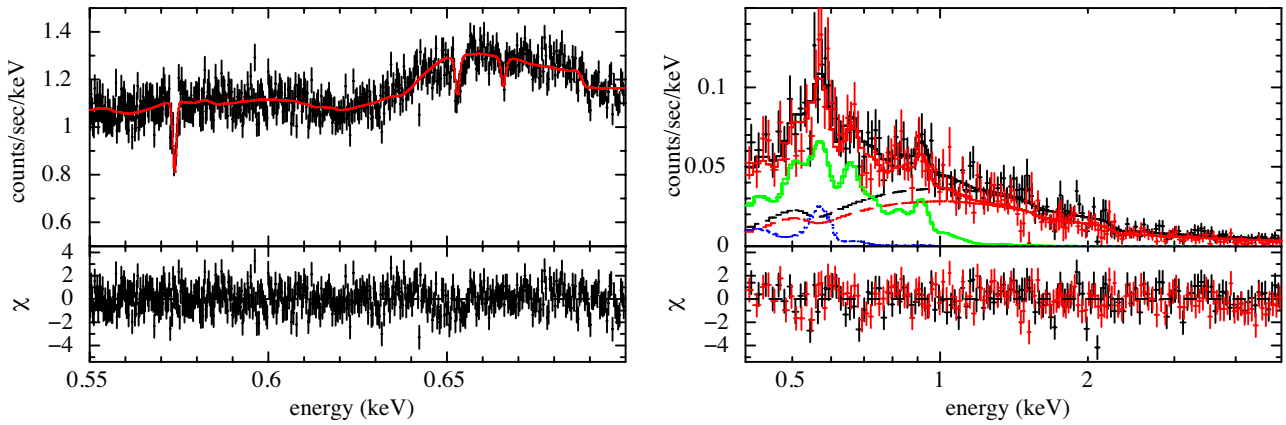

Figure 5.6: (left): *Chandra* spectrum and model C2, (right): *Suzaku* spectra and model C2.

Table 5.7: Combined spectral fitting results with the exponential disk model

Model	Data	CXB	hot ISM							χ^2/dof
		Norm[a]	$\log N_{\rm H_{Hot}}$ ($\rm cm^{-2}$)	h_n (kpc)	$\log T_0$ (K)	v_b[⋆] (km $\rm s^{-1}$)	γ	N/O	Ne/O	Fe/O	
C2	Emission:Sz1	$8.17^{+0.38}_{-0.39}$	$19.41^{+0.18}_{-0.20}$	$5.1^{+3.9}_{-4.7}$	$6.51^{+0.08}_{-0.10}$	···	$0.43^{+1.15}_{-0.23}$	$5.7^{+1.6}_{-1.3}$	$2.3^{+1.6}_{-0.5}$	$1.0^{+0.8}_{-0.5}$	
	Emission:Sz2	$6.37^{+0.38}_{-0.39}$	↑	↑	↑	···	↑	↑	↑	↑	
	Absorption	···	↑	···	↑	70^{+23}	↑	···	···	···	789.65/756
C2[†]	Emission:Sz1	$8.26^{+0.36}_{-0.35}$	$19.36^{+0.18}_{-0.18}$	$3.6^{+2.3}_{-3.2}$	$6.41^{+0.10}_{-0.06}$	···	$0.77^{+1.72}_{-0.06}$	$4.6^{+1.0}_{-0.8}$	$3.0^{+1.0}_{-0.8}$	$1.6^{+0.6}_{-0.8}$	
	Emission:Sz2	$6.46^{+0.39}_{-0.36}$	↑	↑	↑	···	↑	↑	↑	↑	
	Absorption	···	↑	···	↑	70^{+19}	↑	···	···	···	799.02/756
C2[‡]	Emission:Sz1	$8.04^{+0.39}_{-0.58}$	$19.45^{+0.21}_{-0.35}$	$7.5^{+6.4}_{-6.3}$	$6.63^{+0.44}_{-0.15}$	···	$0.35^{+1.02}_{-0.18}$	$6.7^{+2.3}_{-1.7}$	$1.6^{+1.3}_{-1.6}$	$0.6^{+0.7}_{-0.4}$	
	Emission:Sz2	$6.24^{+0.20}_{-0.38}$	↑	↑	↑	···	↑	↑	↑	↑	
	Absorption	···	↑	···	↑	70^{+207}	↑	···	···	···	781.84/756

↑ indicates linked parameters

model C2: *wabs*(*power-law*+*vabmekal*)+*mekal* fot the emission, *wabs*(*power*)×(*absem*)^3 for the absorption

[†]Emission measure of $mekal_{LHB+SWCX}$ is set to 0 as the lower limit.

[‡]Emission measure of $mekal_{LHB+SWCX}$ is set to upper limit which corresponds to 3.5 LU O VII $\rm K_\alpha$ emission

[⋆]Parameter range is limited to 70-440 km $\rm s^{-1}$

[a]in unit of photons $\rm cm^{-2}$ $\rm s^{-1}$ $\rm str^{-1}$ $\rm eV^{-1}$ @1keV

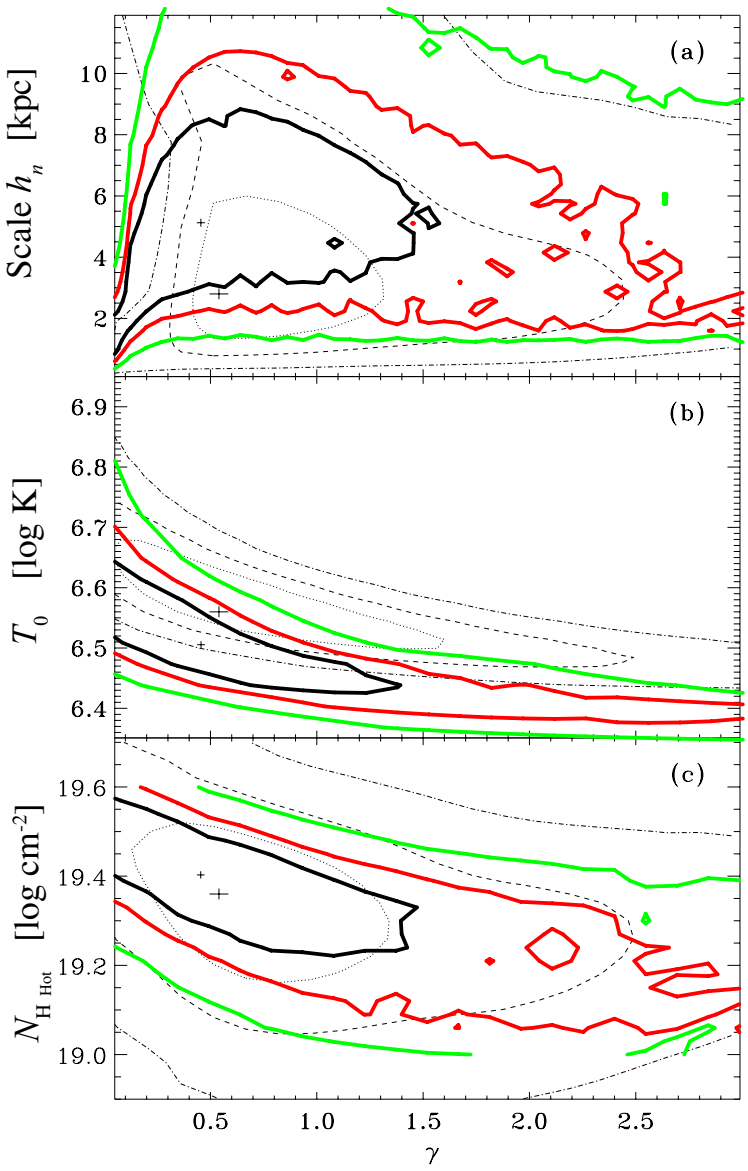

Figure 5.7: 68%, 90%, and 99% confidence contours of h_n, T_0, and $N_{\rm H_{Hot}}$ vs. γ, obtained in the combined fits to the X-ray absorption and emission data. Colored thick lines are for the PKS 2155-304 sight line, while the black thin lines are for the LMC X-3 sight lines (Yao et al. (2009)).

5.4 Uncertainty due to the LHB and the SWCX

Though our knowledge about the temporal and spatial variability of the SWCX and the LHB is limited, there could be uncertainty due to the assumption of their intensity, which could cause large uncertainties.

To assess this uncertainty, we estimated the lower and upper values of the LHB and SWCX contributions and evaluate the parameters of the hot ISM components again. The lower limit of the contribution is zero. As for the upper limit, we adopt 3.5 LU for the OVII emission, as obtained by the MBM 12 shadowing observation (Smith et al. (2007)). As the heliospheric SWCX is caused by the collision between the Solar wind and the neutral ISM, the estimated emissivity has a peak around the ecliptic plane (Koutroumpa et al. (2007) , Lallement (2004)). MBM 12 is located at (λ, β)=(47.4, 2.6) , while the PKS2155-304 is at (λ, β)=(321.2, -16.8). Thus we assume that the heliospheric SWCX contribution for the PKS 2155-304 direction could not be larger than that for the MBM12.

The results using these lower and upper limits are shown in Table 5.4 and Table 5.7. Though the best fit values are slightly changed, they are consistent with the previous analysis.

Chapter 6

Analysis and Results: Galactic Bulge Region

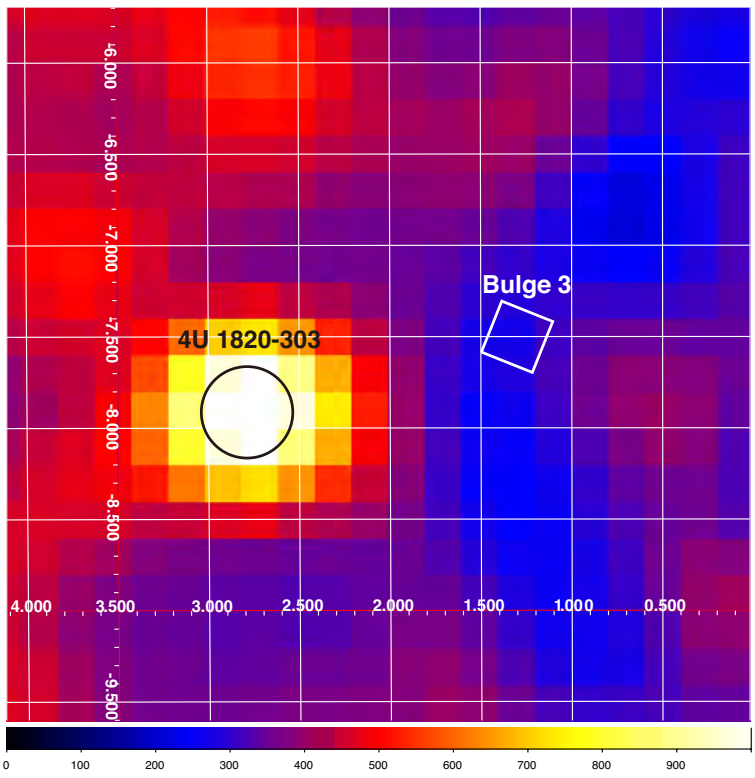

Figure 6.1: RASS R4 band X-ray map around 4U 1820−303 (the bright source at the center, enlarged apparently by the mirror PSF) and the XIS field of view of the observation used in this chapter.

6.1 X-Ray Absorption Line Analysis with *Chandra*

In this section, we analyzed the absorption data of 4U 1820−303 and obtained column density of O VII O VIII, Ne IX and Ne X.

6.1.1 Equivalent widths of lines

First, we evaluated the equivalent widths (EWs). We constructed a model with a power-law and a gaussian and fitted the spectra in narrow ranges shown in Table 6.1, and obtained EWs of each line using *eqwidth* command in Xspec. We put an upper limit of 1×10^{-3} ($\sim$ 200km/s) to the width of O VIII K_α to prevent artificial line broadening. The errors of equivalent widths are obtained as following; 1) we calculated the 90% error range of the normalization of the gaussian function. 2) Then we calculated the maximum error of the EW (EW_{max}) using normalization values of best fit (N_{best}) and maximum (N_{max}) as $EW_{max} = EW/N_{best} \times N_{max}$. The EWs are summarized in Table 6.1.

In Table 6.2, we summarized the EWs reported by previous studies. It is obvious that there are large fluctuations in those values. Cackett et al. (2008) examined four observations of 4U 1820−303 with HETG + ACIS and concluded that the fluctuations in the results between those four observations could due to statistical effect. However, they also conclude that intrinsic absorption in 4U 1820−303 is still possibility of those fluctuations.

In Futamoto et al. (2004) and Yao & Wang (2006b) , they evaluated the EW by the spectral fitting with wider energy range spectra including higher order diffraction photons. Due to the reproductivity of the continuum spectrum, their obtained values are different from ours, especially in O VII K_α . We used only the 1st order spectrum of the HRC observation, and modeled the continuum spectrum in narrow energy range, to obtain reliable values.

Table 6.1: Equivalent widths of absorption lines in 4U1820−303 spectrum

	O VII K_α	O VIII K_α	O VII K_β	Ne IX K_α	Ne X K_α
Centroid	0.5734	0.6537	0.6663	0.9223	1.022(fixed)
EW (eV)	$0.65^{+0.19}_{-0.14}$	$0.69^{+0.17}_{-0.20}$	$0.19^{+0.16}_{-0.16}$	$0.52^{+0.24}_{-0.22}$	< 0.16
EW (mÅ)	$24.4^{+7.1}_{-5.2}$	$19.9^{+4.9}_{-5.8}$	$5.3^{+4.4}_{-4.4}$	$7.5^{+3.4}_{-3.2}$	< 1.9
Fitting Range (Å)	20-22	18-20	18-20	12-14	11.5-12.5

6.1.2 Column density of ions

To obtain column density of ions and to estimate the total column density of the absorbing material, we had to fit all the line simultaneously . First we fitted the continuum between 0.54 and 1.1 keV with a continuum model of a blackbody and a broken power-law. Foreground absorption by the neutral ISM with the solar metal abundances is assumed. This model returned the minimum χ^2/dof = 858.0568/577 (left panel of Figure 6.2). The best-fit column density of the neutral ISM $N_{\rm H}$ is 1.9×10^{21} cm^{-2}. This value is consistent with $N_{\rm H}$ estimated by the 100 μm intensity (2.3×10^{21}cm^{-2}) and reported in Yao & Wang (2006b) (2.0×10^{21}cm^{-2}).

Table 6.2: Equivalent widths in 4U1820−303 spectra reported in various studies

Ref	*Chandra* Obs ID	O VII K_α	O VIII K_α	O VII K_β	Ne IX K_α
This analysis	98†	$0.65^{+0.19}_{-0.14}$	$0.69^{+0.17}_{-0.20}$	$0.19^{+0.16}_{-0.16}$	$0.52^{+0.24}_{-0.22}$
Futamoto et al. (2004) (eV)	98‡	$1.19^{+0.47}_{-0.30}$	$0.54^{+0.23}_{-0.25}$	< 0.48	$0.50^{+0.20}_{-0.20}$
Yao & Wang (2006a)	98⋆+1021+1022	$1.06^{+0.34}_{-0.27}$	$0.65^{+0.21}_{-0.21}$	< 0.36	$0.62^{+0.14}_{-0.14}$
Cackett et al. (2008)	1021	-	< 0.37	< 0.36	$0.50^{+0.12}_{-0.12}$
	1022	-	$0.78^{+0.22}_{-0.22}$	< 0.24	$0.44^{+0.15}_{-0.15}$
	6633	-	$0.22^{+0.10}_{-0.10}$	$0.35^{+0.11}_{-0.11}$	$0.27^{+0.06}_{-0.06}$
	6634	-	$0.63^{+0.15}_{-0.15}$	$0.25^{+0.09}_{-0.09}$	$0.40^{+0.05}_{-0.05}$

Note: marked observation used LETG + HRC. The non-marked used HETG + ACIS

† Only 1st order grating spectrum is used. Subtracting methods are shown in Yao et al. (2009)

‡ Only 1st order grating spectrum is used. Subtracting methods are shown in Takei et al. (2002)

⋆ 1st to 6th order spectra are used.

This poor fit might caused by residuals in the metal edge uncertainties due to the calibration of *Chandra*. Nicastro et al. (2005) set the metal abundance of the neutral absorption material to be free to deal with this problem. As we followed their method, it decrease the residuals (χ^2/dof=761.0619/560) with virtually absence of Ne and Na, and over-abundance of C, N and Mg with factors of 3, 3 and 26 respectively. These values are due to the uncertainties in calibration, rather than true ISM metallicity (Nicastro et al., 2005). Though the χ^2 is still not good, it is difficult to compensate the calibration uncertainties further and we use this model to describe the continuum.

Then we added two absorption lines representing O VII K_α and O VII K_β using *absem* model which is same as in PKS2155−304 analysis. The column density and velocity dispersion of these lines are linked because both lines are originate same ionization state of oxygen (model A1). The results are given in Table 6.3. O VII column density and velocity dispersion are consistent with the values reported by Futamoto et al. (2004) and Yao & Wang (2006b). Next, to check the consistency, we added absorption lines representing O VIII K_α and Ne IX K_α step by step (model A2, A3). In each step, the velocity dispersion of lines are linked together. The results maintain consistency, thus in further analysis the velocity dispersion is always linked together. For the next step, we evaluated the hot phase hydrogen column density assuming solar abundance of O and Ne (model A4). Then we let Ne abundance vary and fitted the spectrum (model A4'). Though the best fit hydrogen column density become smaller and the Ne abundance is $2.2(+1.8, -1.3)$, all the parameters are consistent with those of A4 model.

There might be intrinsic absorbing material around the 4U1820−303. Futamoto et al. (2004) discuss the possibility of intrinsic absorption using photo-ionization simulator and conclude that the size of binary system and luminosity can not explain the O VII ionization fraction estimated by the column density ratio. Thus we consider all of these absorption lines are originate hot ISM in further analysis.

Table 6.3: Parameters of the hot ISM absorbing the 4U1820−303 spectrum

Model	v_b (km s^{-1})	log [Column Density] (cm^{-2})				Abundance	log T (K)	χ^2/dof
		O VII	O VIII	Ne IX	$N_{\rm H_{Hot}}$	Ne/O	T_1	
A1	163^{+219}_{-77}	$16.17^{+0.33}_{-0.21}$						708.3744/573
A2	239^{+301}_{-102}	$16.10^{+0.37}_{-0.16}$	$15.90^{+0.37}_{-0.17}$					671.2156/571
A3	191^{+254}_{-101}	$16.14^{+0.35}_{-0.19}$	$15.92^{+0.42}_{-0.19}$	$15.87^{+0.30}_{-0.33}$				659.9174/569
A4	112^{+114}_{-26}				$19.66^{+0.16}_{-0.16}$		$6.27^{+0.13}_{-0.07}$	662.1264/570
A4'	187^{+254}_{-98}				$19.46^{+0.34}_{-0.15}$	$2.2^{+1.8}_{-1.3}$	$6.28^{+0.06}_{-0.06}$	659.83/569

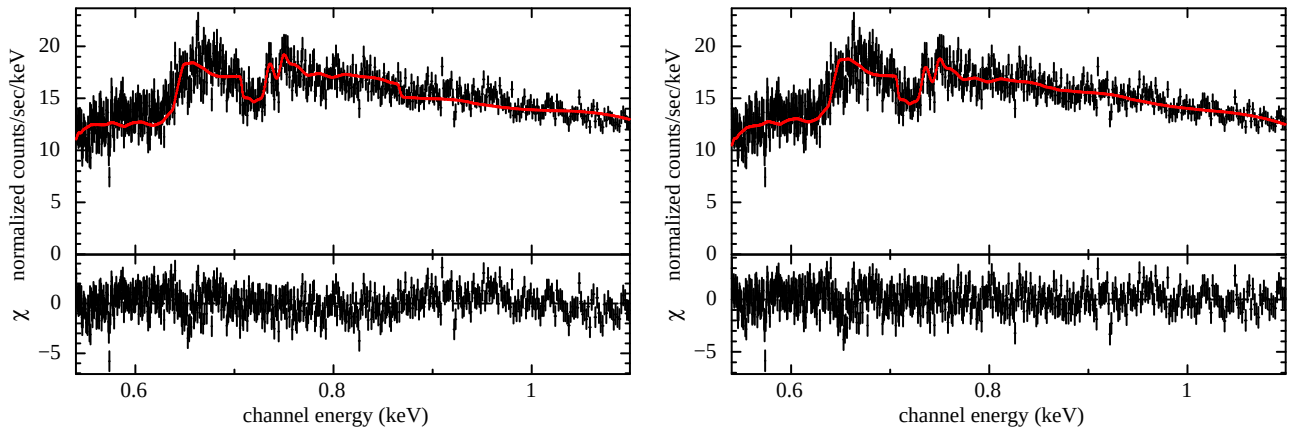

Figure 6.2: The energy spectrum of the continuum modeled by a blackbody + power-law absorbed by the neutral ISM of the solar abundance (left) and of variable metal abundance (right)

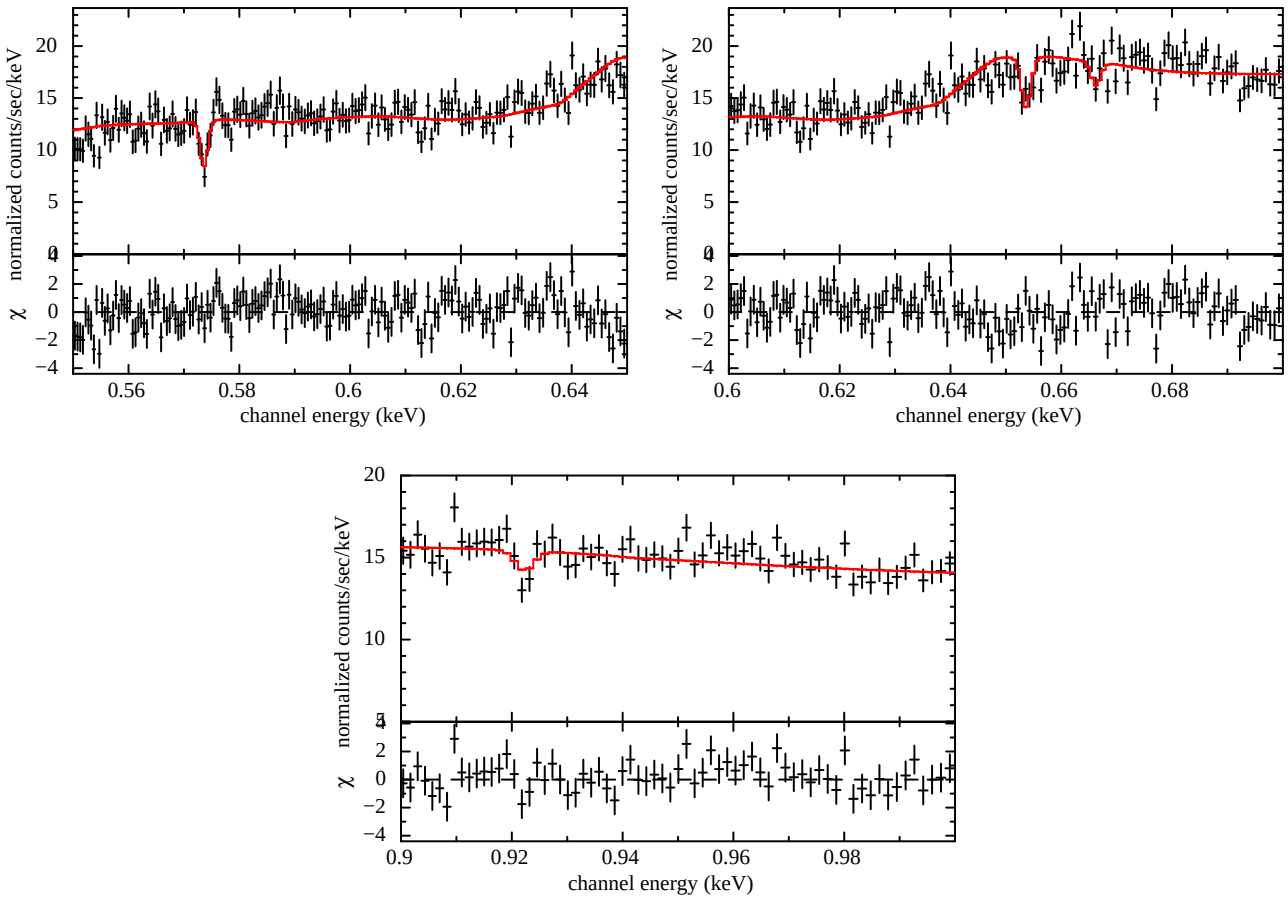

Figure 6.3: O and Ne absorption lines in the 4U 1820−303 spectrum. The solid lines are model A4.

6.2 X-Ray Emission Spectrum with *Suzaku*

First, we show the obtained energy spectra in this direction and PKS 2155−304 direction in Figure 6.4 for comparison. The intensity of the emission is significantly different and apparently high temperature component which shows the Ne K and Fe L complex exist in the galactic bulge direction. In this section we analyze emission data observed with *Suzaku* to constrain the emission component and hot ISM properties.

Before analyzing this complex spectrum, we roughly estimated the total surface brightness of O VII, O VIII, Ne IX and Ne X with a simple model consists of power-law + six gaussians. In this model power-law represents CXB emission and its photon index and normalization are fixed to 1.4 and 10 photons s^{-1} cm^{-2} str^{-1} at 1 keV respectively. Absorption by the neutral ISM is adopted to the CXB emission and the column density of the neutral medium is fixed to the values from 100μm IR intensity as 1.42×10^{21} cm^{-2}. The spectrum and the model parameters are shown in Figure 6.5 and Table 6.4. A thermal emission mainly consists of line emissions unless the temperature is higher than $10^{8.0}$ K, thus these maximum surface brightness can be used as a good indicator.

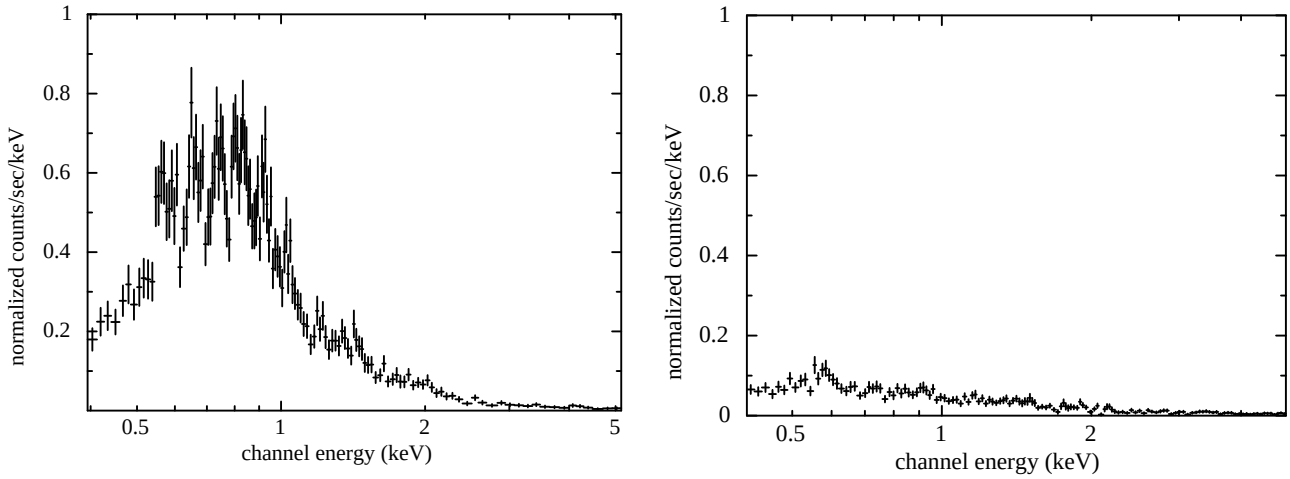

Figure 6.4: Spectrum obtained in the galactic bulge region (left) and the high galactic latitude, in vicinity of PKS 2155−304 (right).

Table 6.4: Apparent surface brightness of each line.

O VII (LU)	O VIII (LU)	Ne IX (LU)	Ne X (LU)
$23.45^{+3.21}_{-1.71}$	$18.96^{+0.87}_{-2.25}$	$10.49^{+0.49}_{-1.22}$	$5.99^{+0.76}_{-0.58}$

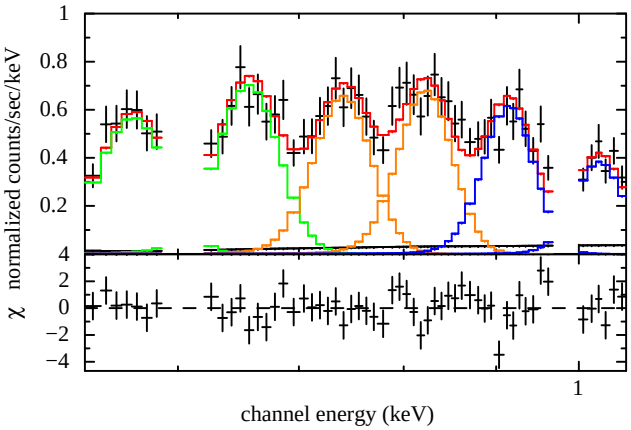

Figure 6.5: Emission line spectrum fitted by Gaussians. Green, yellow and blue represent O lines, Fe lines and Ne lines respectively

6.2.1 Absorption by the neutral ISM

The galactic latitude of this observation is only -7.5°, and it is important to estimate that how much neutral medium exist in front of the emission component. Ferriere (1998) made a global distribution model of the neutral hydrogen and we use this model for our estimation. In Figure 6.6 we show the horizontal and vertical distribution of the neutral hydrogen in our Galaxy given by this model. We calculated the density of the neutral hydrogen in the line of sight toward the 4U1820−303 vicinity direction and integrated the density to estimate the column density exist in the line of sight. The results are shown in Figure 6.7. It is clear that $\sim$ 80% of the hydrogen exist within 2 kpc from us. Also, we compare the column density estimated by radio (HI: 21cm) and IR (dust: 100μm) observations in Table 6.5. In the Ferriere (1998) model, local structure was not included and this cause the difference in calculated and observed column density. Thus we adapt the value of 1.42×10^{21} cm^{-2} obtained by the 100μm observation in later analysis, and assume that all of the absorbing material locates within 2 kpc from us.

Table 6.5: Column density of the neutral hydrogen estimated by different methods

	$N_{\rm H}$ [10^{20} cm^{-2}]		
	21 cm	100μm	Model
4U1820−303 vicinity	13.6	14.2	36.1

6.2.2 Estimation of the foreground emission

6.2.2.1 SWCX+LHB

As of Chapter 5, the SWCX and LHB component is represented by a thermal plasma of T=0.1 keV and its O VII line intensity of 2 LU. This is less than 10% of the observed emission

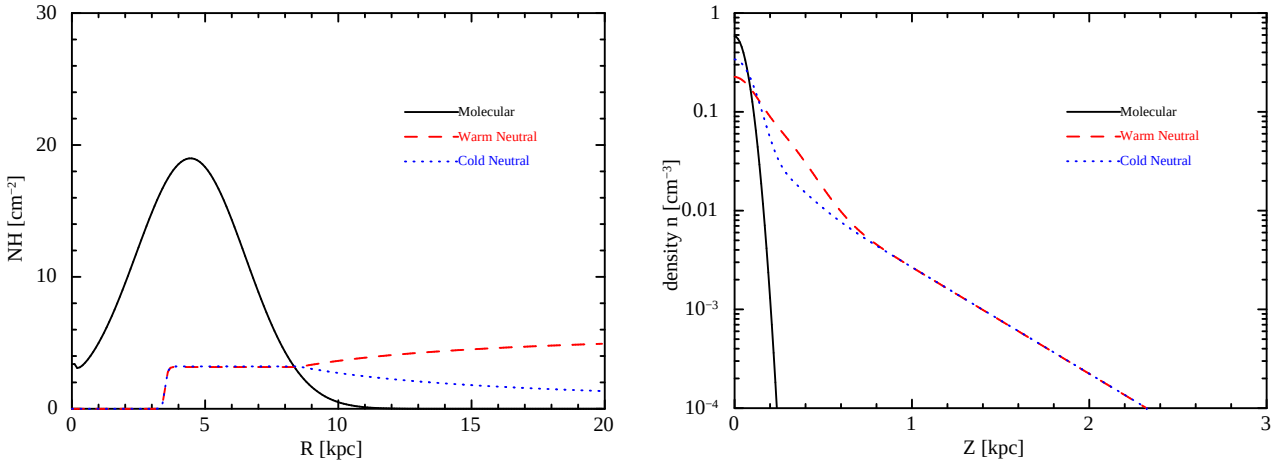

Figure 6.6: (left): Column density of interstellar neutral hydrogen, defined as the number of hydrogen nuclei contained in a vertical cylinder of unit cross section through the Galactic disk, as a function of Galactic radius R, for the different gas component. (right): Number density of interstellar hydrogen nuclei, as a function of Galactic height Z at the solar circle (R=$R_{\odot}$=8.5 kpc), for the different gas component.

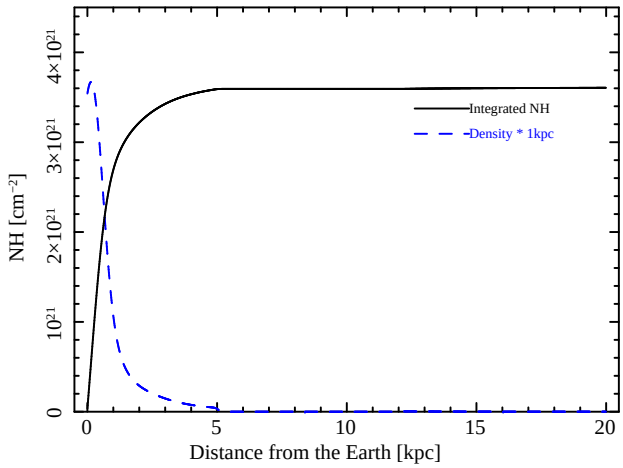

Figure 6.7: Integrated column density of the neutral ISM in the line of sight toward the 4U1820−303 vicinity.

line and the errors due to the uncertainty of this component is small. This temperature plasma emit almost no Ne IX and Ne X lines.

6.2.2.2 Loop I: an old SNR

The sight line would go through the Loop I, a large structure shown by the radio waveband, and considered to be a nearby SNR of 10^6 year old. For the first step, we estimate the size of the Loop I, assuming the origin of Loop I as Sco-Cen OB association, which locates 170 pc away from the Sun.

Table 6.6: Contribution of Loop I estimated from Egger & Aschenbach (1995) SNR shell model

Model	LoopI			Line Intensity (LU)				Column Density (log cm^{-2})			
	density (10^{-3} cm^{-3})	temperature (log K)	length of LOS (pc)	OVII	OVIII	NeIX	NeX	OVII	OVIII	NeIX	NeX
Loop I	2.5	6.66	300	1.83	2.10	0.31	0.04	14.3	14.8	14.3	13.8

Using expansion law for interstellar bubbles(Weaver, McCray & Castor 1977) and expansion speed of the HI shell of the Loop I($\sim$ 20 km s^{-1}), Egger & Aschenbach (1995) calculated the density and temperature in the cavity as 2.5×10^{-3} cm^{-3} and 4.6×10^{6} K (log T =6.66). We also calculated line intensity and column density using these parameter (Table 6.6). These results meet the observation results and we adopt the values in further analysis. The contribution of the Loop I to the absorption is small enough and this is why we neglect it in absorption analysis.

6.2.3 Emission from stars

Stars, in a precise sense its corona, emit X-rays. As shown in Figure 6.8, almost all type of star can be an X-ray source. Though X-ray luminosity of each star is not so high ($\sim 10^{29}$ erg^{-1} s^{-1} in 0.1–2.4 keV), their number density increase in lower latitude and contribution of stars can not be negligible in the bulge direction.

The stellar contribution to the SXDB is still very uncertain. Because luminosity of unresolved stars are very low and this makes it difficult to reveal their spectral distribution. Moreover there are uncertainties of their luminosity and energy spectra due to the stellar type and age. Rocks (2009) estimated the contribution of the stellar X-ray component from published models of stellar space densities, X-ray spectra and luminosities. In this thesis, we follow their method to estimate the contribution from stars in the diffuse emission toward the Galactic bulge (see Appendix A for details).

By evaluating the contribution of each spectral type star and binary, we include F, G, K, M spectral type stars and RS-CVn binaries to our stellar model. The spectral features of these stars are summarized in Table 6.7.

Table 6.7: Stellar type parameters summarized by Rocks (2009) after López-Santiago et al. (2007) and RS-CVn type binary parameters after Ottmann & Schmitt (1992)

Spectral type	Single temperature	Two temperature			Metal abundance
	(keV)	hotter (kev)	cooler (keV)	EMcool/ EMhot	
F	0.58	N/A	N/A	N/A	0.5
G	0.67	N/A	N/A	N/A	0.3
K	0.83	1.17	0.32	1.97	0.2
M	0.90	0.80	0.27	2.02	0.1
RS-CVn	N/A	2.59	0.17	0.22	1.0

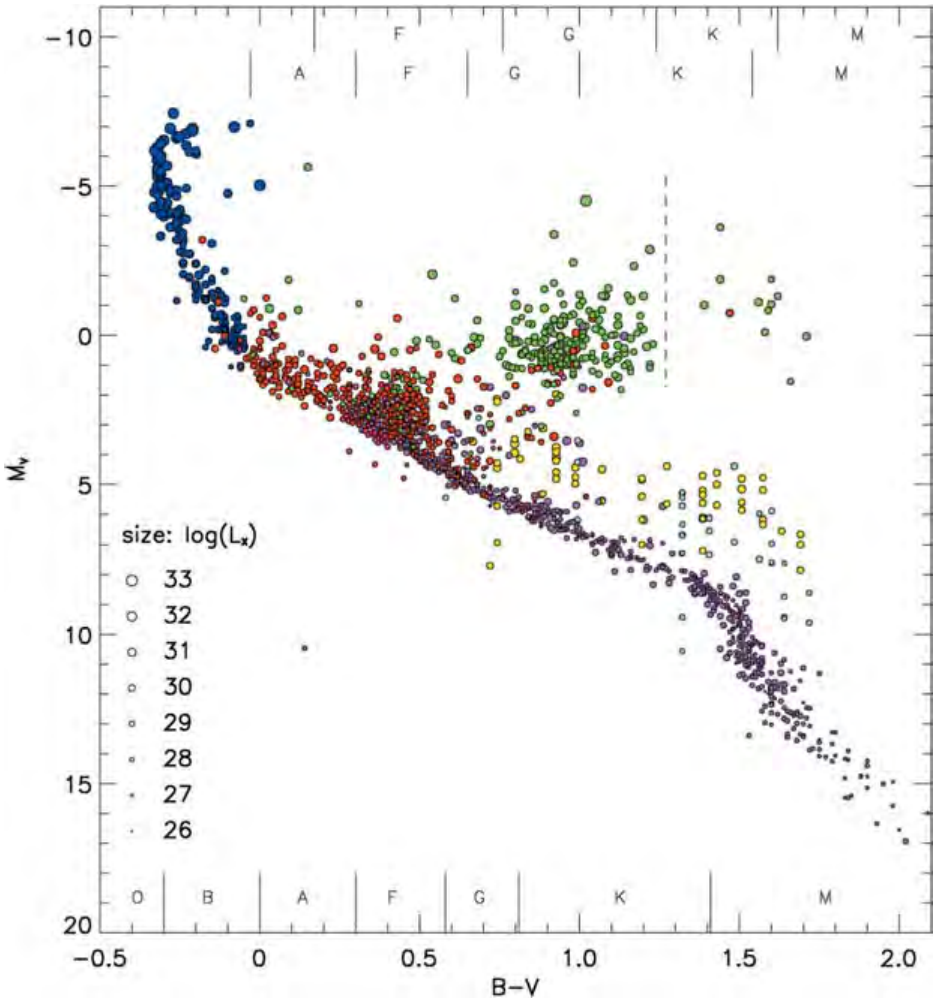

Figure 6.8: X-ray luminosity of normal stars taken from Güdel (2004). Hertzsprung-Russell diagram based on about 2000 X-ray detected stars extracted from the catalogs by Berghoefer et al. (1996) (blue), Hunsch et al. (1998a,b) (green and red, respectively), and Hunsch et al. (1999) (pink). Where missing, distances from the Hipparcos catalog (Perryman et al. 1997) were used to calculate the relevant parameters. The low-mass pre-main sequence stars are taken from studies of the Chamaeleon I dark cloud (Alcala et al. 1997; Lawson et al. 1996, yellow and cyan, respectively) and are representative of other star formation regions. The size of the circles characterizes log L_X as indicated in the panel at lower left. The ranges for the spectral classes are given at the top (upper row for supergiants, lower row for giants), and at the bottom of the figure (for main-sequence stars)

6.2.4 Spectral fitting

We summarized fitting components of the foreground and background emission in Table 6.8. As for the treatment of the absorption, the geometry of the emitting source and absorbing material should be assumed. As shown in Table 6.8 we did not adopt absorption by the neutral ISM to foreground components. As for stars and binaries, this can lead overestimate. However, most stars contributing the foreground emission located closer than 2 kpc and this approximation cause no significant difference.

6.2.4.1 Without hot ISM component

First, we tried to fit the spectrum without hot ISM component, i.e. to represent total spectrum by the foreground and background emission in Table 6.8. At first, we fixed the normalization of all components to the default (simulation based) values. Apparently this model failed to reproduce the whole spectrum because of lack of intensities of lines and continuum. Then we set the normalization of a spectral type star to be free step by step to estimate the maximum normalization of corresponding star components. The results are given in Table 6.9. These models are also far from reproducing the whole spectrum. Then all components representing background stars are set to be free (model S1). This model failed to fit the spectrum (Figure 6.9) due to the lack of O and Ne lines and the fitting results are also shown in Table 6.9.

In our one temperature stellar emission model, the temperature of the plasma is higher than ~ 0.6 keV. The emissivity of O and Ne lines become smaller at such high temperature and Fe complex lines located at ~ 0.9 keV dominate the emission instead. Therefore it is hard to reproduce O and Ne lines for one temperature stellar models. For two temperature models, lower temperature is ~ 0.3 keV and higher temperature is ~ 1 keV and the normalization of two components are linked together. Because the emission of the higher temperature component is strong and almost like continuum at ~ 1 keV, the upper limit of the normalization of the higher temperature component prevent the lower temperature component from reproduce O and Ne lines effectively. These spectral features are typical for the stellar coronal emission and thus it is hard to reproduce the whole spectrum only with varying the normalization of stellar components.

Table 6.8: Estimated contributions of the foreground and background emission

Component	Fitting model	Absorption[a]	Misc
SWCX+LHB	Thin thermal plasma	None	All parameters are fixed
Loop I	Thin thermal plasma	None	All parameters are fixed
Stars (Foreground)	Thin thermal plasma×8	None	Temperatures are fixed
Binaries (Foreground)	Thin thermal plasma×2	None	Temperatures are fixed
Stars (Background)	Thin thermal plasma×8	Full	Temperatures are fixed
Binaries (Background)	Thin thermal plasma×2	Full	Temperatures are fixed
Hot ISM	Thin thermal plasma×1–2	Full	
CXB	Power law	Full	Photo index is fixed to 1.4

[a] Full corresponds column density of neutral hydrogen of $1.42 \times 10^{21} \mathrm{cm}^{-2}$

Table 6.9: Ratio of the normalization of background star components to the default value.

Model	F	G	K	M	Binary	χ^2/dof
Max. Norm of each type	14.73	75.58	34.02	20.38	19.80	
All Free (S1)	4.54	< 0.01	< 0.01	13.13	2.77	567.06/130

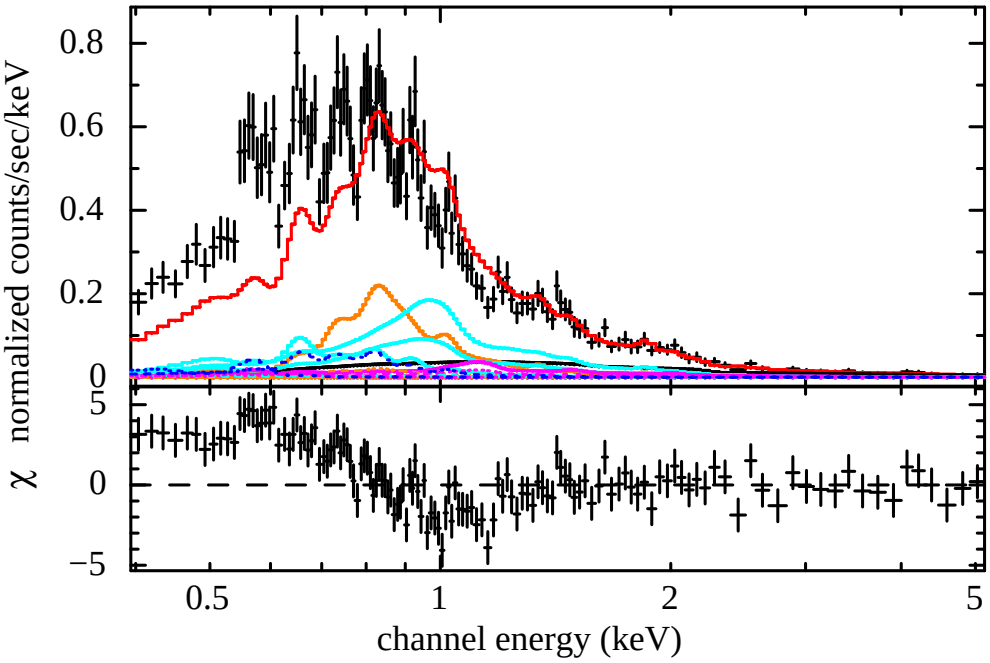

Figure 6.9: Energy spectrum fitting only by the foreground and background emissions with variable stellar components intensities.

6.2.4.2 Model E1: hot ISM and fixed stellar contribution

Next, we added hot ISM component to the model and tried to reproduce the spectrum. We fixed the normalization of stellar components to the simulated values. The normalization of CXB was fixed to the average value of 10 photons s^{-1} cm^{-2} str^{-1} at 1 keV (Hasinger et al. (1993)) and the normalization of stars and binaries are set to the simulated values described in previous sections. We tried one temperature hot ISM model with fixed and free (N, Ne and Fe) abundance and obtained poor χ^2/dof value of 578.62/133 and 366.20/130 respectively. This poor fit is caused by the spectrum where O VII and Ne X lines exist at the same time and it is difficult for single temperature plasma to produce these lines simultaneously. Then we gave up one temperature hot ISM model and tried two temperature model with fixed abundance (model E1). Though the χ^2 was improved to 358.17/131, there are still significant residuals between the model and spectrum (Figure 6.10). It is obvious that a continuum-like component is needed to reduce the residuals between 1 and 3 keV, thus we tried to free CXB parameters. Though this model reduced the residuals and improve the χ^2/dof to 121.85/129,

the best fit values of photon index is 2.4 (+0.1, -0.1) and the normalization is 41.5(+3.6, -7.6) photons s^{-1} cm^{-2} str^{-1} at 1 keV. These values are not reasonable for the CXB even though its fluctuation taken into account.

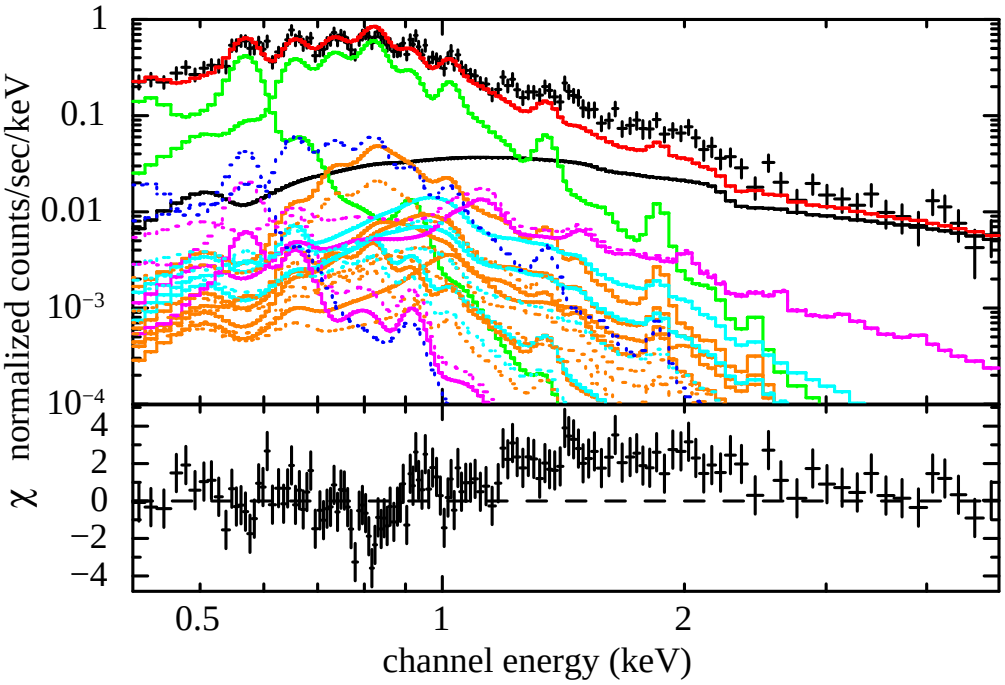

Figure 6.10: Spectrum and model (E1). The dotted lines indicate foreground (unabsorbed) components and the solid lines indicate background (fully absorbed) components. hot ISM (green), CXB (black), SWCX+LHB, and Loop I (blue) ,stars except for M stars (orange), M stars (light blue), and binaries(magenta).

As mentioned before, there are large uncertainties in the number densities, luminosities the energy spectrum of the background low luminosity stars and binaries. For this reason, we tried following two models.

- Model E2: Assuming underestimation of the stellar contribution, the normalization of background stars and binaries are set to be free.
- Model E3: Assuming unknown thermal component in the bulge, a one high temperature ($\sim$ 1.5 keV) thin thermal plasma emission model is added.

6.2.4.3 Model E2: hot ISM and variable stellar contribution

In E2 model, we set the normalization of stars to be free step by step and investigate the residuals and the normalization and estimate the effect of star contribution on the hot ISM properties.

To compensate the residuals exist around 2 keV, we need an additional $\sim$ 2keV component. One plausible component to produce such hard emission is RS CVn binaries of which we modeled spectrum with two temperature plasma of 2.59 keV and 0.17 keV. Moreover it

is not well understood how many stars make binaries and there is uncertainty in the distribution of the RS CVn binaries. Thus first we set the normalization of background binary components to be free (Model E2-b: Emission model with background binary normalization is set to be free). Though we found that this model certainly reduce the residuals around 2 keV, also found that this model cause another significant residuals around 1 keV and above 2.5 keV. Emission from plasma of kT= 2.59 keV is little bit too high to compensate the residual.

The M type stars have 0.9 keV temperature and its low luminosity could cause large uncertainties in number of stars exist in the FOV. For the next step, we fixed the binary normalization to the simulated value and set the normalization of the M type star to be free (Model E2-m: Emission model with background M type star normalization is set to be free). This model also could not explain whole spectrum. However, residuals caused by these two models (E2-b and E2-m) are complementary.

Thus we tried to free the normalization of binary and M stars simultaneously (model E2-mb). This model fit the data with χ^2/dof of 144.37/131. The normalization ratios to the simulated values are 6.57 (+1.17, -2.14) and 5.45 (+1.27, -2.20) for M stars and binaries respectively. It is difficult to confirm these values are correct or not and we accept this value at present, and it is beyond the scope of this thesis.

Then we set the normalization of K type star and F and G type star to be free sequentially (model E2-mkb, E2-mkfgb). This modify cause no significant changes to the fitting results and the contribution of K, F and G stars are vanished. Finally we linked the normalization of the all star components and set it to be free (model E2-(mkgf)b). The normalization ratios to the simulated values are 2.79 (+0.74, -0.78) and 6.22 (+1.35, -1.35) for all spectral type stars and binaries respectively. χ^2/dof is 151.29/129 and it is hard to explain the whole spectra with this model.

The normalizations and temperatures of the cooler and hotter hot ISM are consistent each other in three acceptable models (E2-mb, E2-mkb, E2-mkgfb). From these results we can know that the normalization of the stars are of little importance on the hot ISM parameters. As mentioned in Section 6.2.4.1, this is because the temperature range of the hot ISM and those of the star components are different.

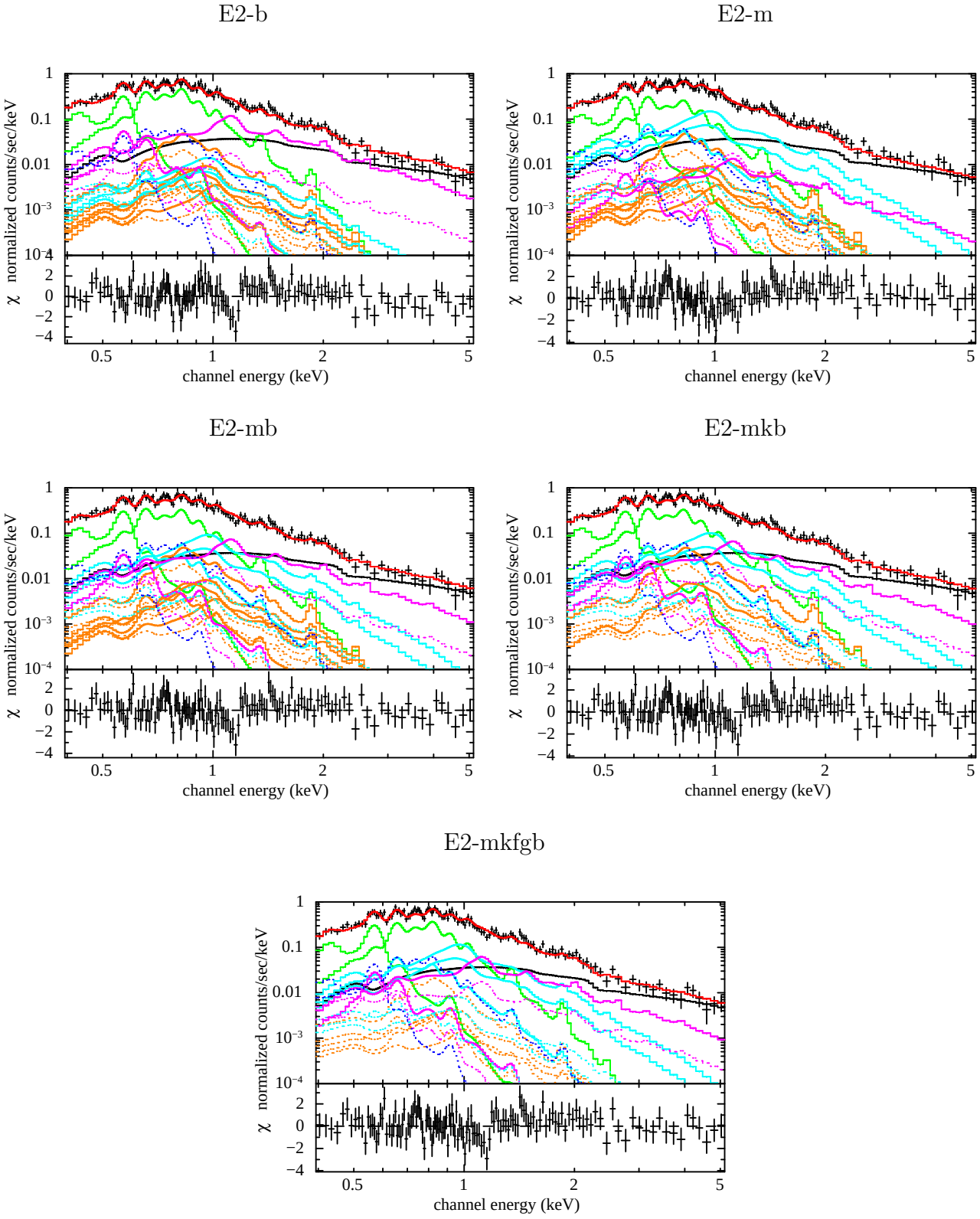

Figure 6.11: Spectrum and model (E2). The dotted lines indicate foreground (unabsorbed) components and the solid lines indicate background (fully absorbed) components. hot ISM (green), CXB (black), SWCX+LHB and Loop I (blue) ,stars except for M stars (orange), M stars (light blue), and binaries(magenta).

Table 6.10: Fitting results with model E2 (see text for details)

Model	Foreground†	hot ISM				Background†				χ^2/dof
		cooler		hotter		Stars		Binaries	CXB	
		log T [keV]	Norm[a]	log T [keV]	Norm[a]	Class[b]	Ratio[c]	Ratio[c]		
E2-b	fixed	$6.009^{+0.047}_{-0.083}$	$215.4^{+319.9}_{-87.6}$	$6.571^{+0.025}_{-0.022}$	$26.3^{+2.7}_{-2.6}$	-	fixed	$8.81^{+0.65}_{-1.28}$	fixed	167.78/132
		$[0.088^{+0.010}_{-0.015}]$		$[0.321^{+0.019}_{-0.016}]$						
E2-m	fixed	$6.019^{+0.067}_{-0.074}$	$179.6^{+212.9}_{-85.9}$	$6.524^{+0.035}_{-0.040}$	$18.6^{+2.9}_{-2.8}$	M	$10.61^{+1.13}_{-1.13}$	fixed	fixed	163.12/132
		$[0.090^{+0.015}_{-0.014}]$		$[0.288^{+0.024}_{-0.025}]$						
E2-mb	fixed	$6.012^{+0.065}_{-0.083}$	$195.3^{+288.8}_{-87.5}$	$6.542^{+0.036}_{-0.030}$	$21.5^{+3.0}_{-3.1}$	M	$6.57^{+1.17}_{-2.14}$	$5.45^{+1.27}_{-2.20}$	fixed	144.37/131
		$[0.089^{+0.014}_{-0.015}]$		$[0.300^{+0.026}_{-0.020}]$						
E2-mkb	fixed	$6.012^{+0.054}_{-0.080}$	$193.8^{+280.1}_{-84.2}$	$6.543^{+0.029}_{-0.029}$	$21.5^{+3.0}_{-3.0}$	M	$7.16^{+1.71}_{-2.34}$	$4.93^{+1.48}_{-1.43}$	fixed	142.54/130
		$[0.089^{+0.012}_{-0.015}]$		$[0.301^{+0.021}_{-0.020}]$		K	< 2.49			
E2-mkgfb	fixed	$6.016^{+0.060}_{-0.082}$	$183.4^{+264.3}_{-82.5}$	$6.558^{+0.029}_{-0.031}$	$22.1^{+3.4}_{-2.8}$	M	$8.21^{+1.67}_{-2.69}$	$4.60^{+1.63}_{-1.35}$	fixed	140.42/129
		$[0.090^{+0.013}_{-0.015}]$		$[0.312^{+0.021}_{-0.021}]$		K	< 3.38			
						FG	< 1.23			
E2-(mkgf)b	fixed	$6.007^{+0.037}_{-0.091}$	$204.2^{+292.6}_{-76.2}$	$6.519^{+0.027}_{-0.030}$	$21.0^{+3.9}_{-3.6}$	FGKM	$2.79^{+0.74}_{-0.78}$	$6.22^{+1.35}_{-1.35}$	fixed	151.92/129
		$[0.088^{+0.008}_{-0.016}]$		$[0.285^{+0.018}_{-0.019}]$						
E2-mb‡	fixed	$6.360^{+0.020}_{-0.021}$	$33.7^{+3.2}_{-3.2}$	···	···	M	$11.77^{+1.11}_{-1.00}$	$2.50^{+1.43}_{-1.33}$	fixed	214.09/133
		$[0.197^{+0.009}_{-0.009}]$								
E2-mkgfb‡	fixed	$6.334^{+0.023}_{-0.022}$	$35.8^{+3.3}_{-3.4}$	···	···	M	$7.01^{+2.64}_{-2.17}$	$4.34^{+1.52}_{-1.59}$	fixed	196.99/131
		$[0.186^{+0.010}_{-0.009}]$				K	< 2.55			
						FG	$4.29^{+1.31}_{-1.35}$			

† All parameters are fixed to referred or simulation based value without mentioned

‡ One hot ISM model.

[a] Emission Measure $10^{-3} \int n_e n_p dl$: in unit of cm^{-6} pc

[b] Spectral type of the stars whose normalization is set to be free

[c] Ratio of the normalization of stars of binaries to the simulation based value

6.2.4.4 Model E3: hot ISM with additional unknown continuum component

In this model, additional unknown component is assumed. Thus we fixed all the components to the simulated values other than hot ISM. First we added a thin thermal plasma to the model because contribution of the unknown star component would be highly possible (model E3). The abundance of the additional plasma is fixed to the solar value. However this model cause residual features like E2-b model and could not fit the data (χ^2/dof=165.37/131). The metal abundance of the stellar corona is not well understood and then we set the ratio of metal to hydrogen to be free (model E3-A). This model explain the whole spectrum very well (χ^2/dof=121.04/130). However the best fit abundance is ~ 0 and the additional component is quite close to thermal bremsstrahlung of kT=1.1 keV. Actually we can substitute thermal bremsstrahlung for the thin thermal plasma of E3-A model to found no changes in the fitting results (model E3-B). Then we set the abundance of the plasma of E3-A model to 0.1 solar value (E3-A'). This model also fit the data with χ^2/dof=133.34/131.

Some 1.5 keV thermal components are reported in the spectra of nearby dM stars (e.g. van den Besselaar et al. (2003)) and this could be origin of the unknown component. As shown in Table 6.7, the metallicity of the coronal spectra of the low luminosity stars are very low and this is consistent with the low metallicity of the unknown component. Flare of a star is another possibilities for the unknown component. In flare period, the high temperature ($>$ 1keV) component of the star corona become brighter. It is not plausible that this unknown component originate hot ISM because its metallicity is not high ($<\sim 0.1$) and temperature and induced pressure is too high to maintain such plasma.

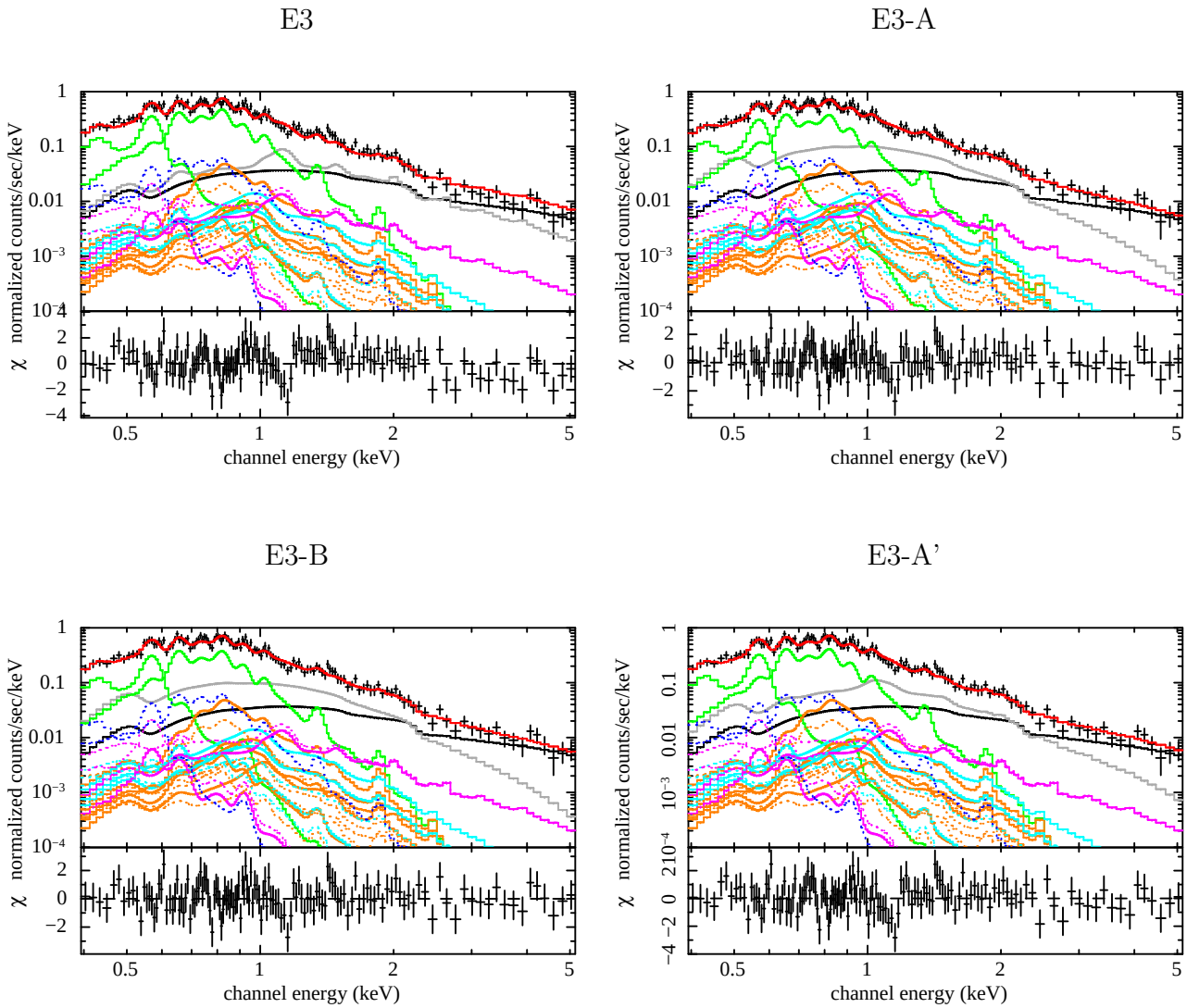

Figure 6.12: Spectrum and model (E3). The dotted lines indicate foreground (unabsorbed) components and the solid lines indicate background (fully absorbed) components. hot ISM (green), CXB (black), additional component (grey), SWCX+LHB and Loop I (blue) ,stars except for M stars (orange), M stars (light blue), and binaries(magenta).

Table 6.11: Fitting results of model E3

Model	Foreground†	hot ISM				Additional background			Background†	χ^2/dof
		cooler		hotter					CXB	
		log T (K)	Norm[a]	log T (K)	Norm[a]	log T (K)	Norm[a]	Abundance		
E3	fixed	$6.019^{+0.056}_{-0.062}$ [$0.090^{+0.012}_{-0.012}$]	$205.1^{+182.1}_{-87.3}$	$6.567^{+0.023}_{-0.021}$ [$0.318^{+0.017}_{-0.015}$]	$27.3^{+2.6}_{-2.6}$	$7.544^{+0.104}_{-0.082}$ [$3.017^{+0.816}_{-0.519}$]	$17.4^{+2.1}_{-2.0}$	1.0 (fixed)	fixed	165.37/131
E3-A	fixed	$6.022^{+0.078}_{-0.072}$ [$0.091^{+0.018}_{-0.014}$]	$171.0^{+190.7}_{-88.4}$	$6.546^{+0.027}_{-0.028}$ [$0.303^{+0.020}_{-0.019}$]	$24.0^{+2.8}_{-3.2}$	$7.109^{+0.105}_{-0.110}$ [$1.109^{+0.303}_{-0.248}$]	$64.3^{+27.3}_{-16.5}$	< 0.03	fixed	121.04/130
E3-B	fixed	$6.023^{+0.077}_{-0.071}$ [$0.091^{+0.018}_{-0.014}$]	$169.4^{+185.8}_{-86.9}$	$6.547^{+0.026}_{-0.025}$ [$0.304^{+0.019}_{-0.017}$]	$23.9^{+2.8}_{-2.9}$	$7.106^{+0.108}_{-0.098}$ [$1.101^{+0.311}_{-0.222}$]	$69.6^{+26.2}_{-18.4}$	···	fixed	120.94/131
E3-A'	fixed	$6.017^{+0.061}_{-0.073}$ [$0.090^{+0.013}_{-0.014}$]	$193.7^{+224.9}_{-87.5}$	$6.548^{+0.026}_{-0.022}$ [$0.305^{+0.019}_{-0.015}$]	$25.9^{+2.7}_{-2.6}$	$7.239^{+0.096}_{-0.077}$ [$1.495^{+0.372}_{-0.243}$]	$38.5^{+4.8}_{-5.8}$	0.1 (fixed)	fixed	133.34/131
E3-A'†	fixed	$6.440^{+0.015}_{-0.015}$ [$0.237^{+0.008}_{-0.008}$]	$37.3^{+2.3}_{-2.3}$	···	···	$7.151^{+0.038}_{-0.039}$ [$1.221^{+0.112}_{-0.104}$]	$49.8^{+4.7}_{-4.7}$	0.1 (fixed)	fixed	231.45/133

† All parameters are fixed to referred or simulation based value without mentioned

† One hot ISM model.

[a] Emission Measure $10^{-3} \int n_e n_p dl$: in unit of cm^{-6} pc

6.2.4.5 Comparison of the fitting results

From model E2 and model E3, we see that ~ 5 times normalization of stellar components or another thermal bremsstrahlung or a low abundance thin thermal plasma is needed to explain the whole spectrum. Though it is interesting to verify these models and check the cause of these components, the scope of this thesis is hot ISM and we should constrain their properties.

As shown in Table 6.10 and 6.11, there are at most 10% difference in hot ISM parameters between acceptable models. Our model assumes two extreme possibilities and it is reasonable to consider that the star contribution would change the hot ISM parameters at most 10% in any case. Thus we use model E2-mb and E3-A' to represent the bulge 3 direction emission model in further analysis.

We evaluated the line intensities corresponding the hot ISM component with model E2-mb and E3-A' as summarized in Table 6.12. The intensity and ratio of O lines are not affected by the foreground models, but the contribution of the Ne lines would change by the assumption of stellar components, especially of the high temperature stars.

Table 6.12: Surface brightness of the O and Ne lines.

Model	O VII (LU)	O VIII (LU)	Ne IX (LU)	Ne X (LU)
E2-mb	$14.72^{+2.74}_{-1.47}$	$9.80^{+-0.22}_{-3.15}$	$0.61^{+1.29}_{-0.47}$	< 0.19
E3-A'	$15.80^{+2.73}_{-1.51}$	$10.75^{+1.48}_{-1.32}$	$3.09^{+1.05}_{-0.54}$	$2.17^{+1.05}_{-1.24}$

6.3 Combined Analysis

Up to here we analyzed the absorption and emission data separately. The results are summarized in Table 6.13 and 6.14. It is clear that temperature range of the plasmas contributing to the emission and absorption are different from each other. It suggests that there are multi-temperature plasma toward the line of sight. In this section, we constrain the physical properties and spatial distribution of the hot ISM along the 4U 1820−303 sight line using combined analysis.

The positional relationship of the Sun, Galactic center and 4U 1820−303 is illustrated in Figure 6.13. The 4U 1820−303 located only 1 kpc above the Galactic plane. Thus we have to think about two possibilities. One is that the all plasmas contributing the emission exist in front of 4U 1820−303 (Figure 6.14: a). The other is that some plasmas exist beyond the 4U 1820−303 and contribute to the absorption partially (Figure 6.14: b). These two possibilities are complementary and we can not exclude either only by fitting as in the case of LMC X-3 direction. We examine models with combined fit and investigate the physical conditions of the plasmas.

Table 6.13: Results of the absorption line analysis

Model	v_b (km s^{-1})	log [Column Density] (cm^{-2}) $N_{\rm H_{Hot}}$	Abundance Ne/O	log T (K)	χ^2/dof
A4	112^{+114}_{-26}	$19.66^{+0.16}_{-0.16}$		$6.27^{+0.13}_{-0.07}$	662.1264/570
A4'	187^{+254}_{-98}	$19.46^{+0.34}_{-0.15}$	$2.2^{+1.8}_{-1.3}$	$6.28^{+0.06}_{-0.06}$	659.83/573

Table 6.14: Results of the emission spectrum analysis

Model	hot ISM				Background				χ^2/dof
	cooler		hotter		Stars	Binaries	Additional		
	log T (K)	Norm[a]	log T (K)	Norm[a]	Ratio[bc]	Ratio[c]	log T (K)	Norm[a]	
E2-mb	$6.012^{+0.065}_{-0.083}$	$195.3^{+288.8}_{-87.5}$	$6.542^{+0.036}_{-0.030}$	$21.5^{+3.0}_{-3.1}$	$6.57^{+1.17}_{-2.14}$	$5.45^{+1.27}_{-2.20}$			144.37/131
E3-A'	$6.017^{+0.061}_{-0.073}$	$193.7^{+224.9}_{-87.5}$	$6.548^{+0.026}_{-0.022}$	$25.9^{+2.7}_{-2.6}$			$7.239^{+0.096}_{-0.077}$	$38.5^{+4.8}_{-5.8}$	133.34/131

Note: All the parameters not written the Table is fixed to the simulation based values.
[a] Emission Measure $10^{-3} \int n_e n_p dl$: in unit of cm^{-6} pc
[b] Normalization of background M type star is set to be free
[c] Ratio of the normalization of the background stars or binaries to the simulation based value

6.3.1 Exponential disk model

First, we compare the data and the exponential disk model with the best fit value obtained by PKS 2155-304 direction. In this assumption, the scale height of the hot halo is ~ 5 kpc and 4U 1820−303 is located within the exponential disk. Thus the absorption was induced partially and it is hard to constrain the parameter of the exponential disk. For this reason we fixed those parameters to the best fit values of PKS 2155-304 analysis and try to estimate

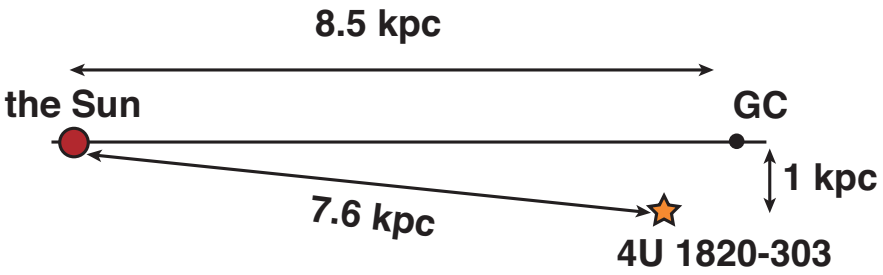

Figure 6.13: Geometry of the sight line toward 4U 1820−303 and the Galactic plane

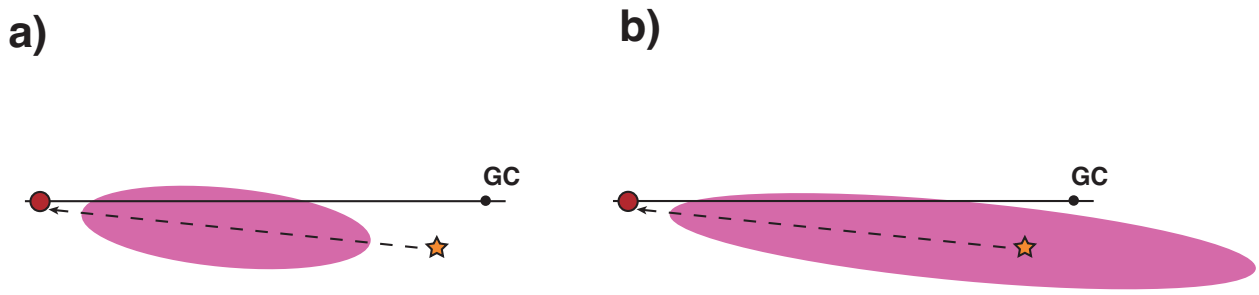

Figure 6.14: (a) all the plasma exist in front of 4U 1820−303. (b) some plasma exist in back of 4U 1820−303. This plasma only contribute emission spectra.

the contribution of the additional components (model C1). The density at the plane (n_0), the scale height of the density (h_n), the temperature at the plane (T_0) and the scale height of the temperature are 1.3×10^{-3} cm^{-3}, 5.1 kpc, $3.2 \times 10^6 = 10^{6.51}$ K and 2.2 kpc respectively. The corresponding γ is 0.43 and the velocity dispersion is set to 70 km s^{-1} (see Section 5.3.2 Table 5.7) The foreground and background emission model is based E2-mb and we substitute the exponential model for hot ISM. The normalization of the foreground and background components are fixed to the best fit value of E2-mb model in Table 6.10. Figure 6.15 shows the data, model and residuals.

It is obvious that the exponential disk model failed to explain the intensity of emission lines. It is important that not only high energy lines like Fe L lines and Ne lines, but O lines are not enough to describe the observed emission. On the other hand, the absorption spectrum is reproduced well.

These fact leads the assumption that additional components, which contribute little to the absorption, exist in back of 4U 1820−303. On the basis of this supposition, we added one uniform plasma to compensate the residuals in the emission spectrum. It returns the temperature of $T \sim 3.5 \times 10^6$ K. Though this certainly improve the χ^2, there still remain residuals around O VII Kα line. Thus we added another cooler plasma of T $\sim 1.2 \times 10^6$ K and tried to fit the spectrum. We constructed two models based on emission and absorption model sets of E2-mb + A4 (C1-1), in which normalization of the thin thermal plasma model representing M type stars and binaries are set to be free, and E3-A' + A4 (C1-2), to which a thin thermal plasma of $\sim$ 1.5 keV with 0.1 solar abundance is added. The fitting results are shown in Table 6.15. The temperature of the hotter component reaches $10^{6.6} = 4.0 \times 10^6$

K. If we assume that such high temperature plasma located in the Galactic bulge with symmetrical distribution of a radius of 1.4 kpc, the density and the pressure of the plasma become 2.5×10^{-3} cm^{-3} and 2.3×10^{4} cm^{-3} K.

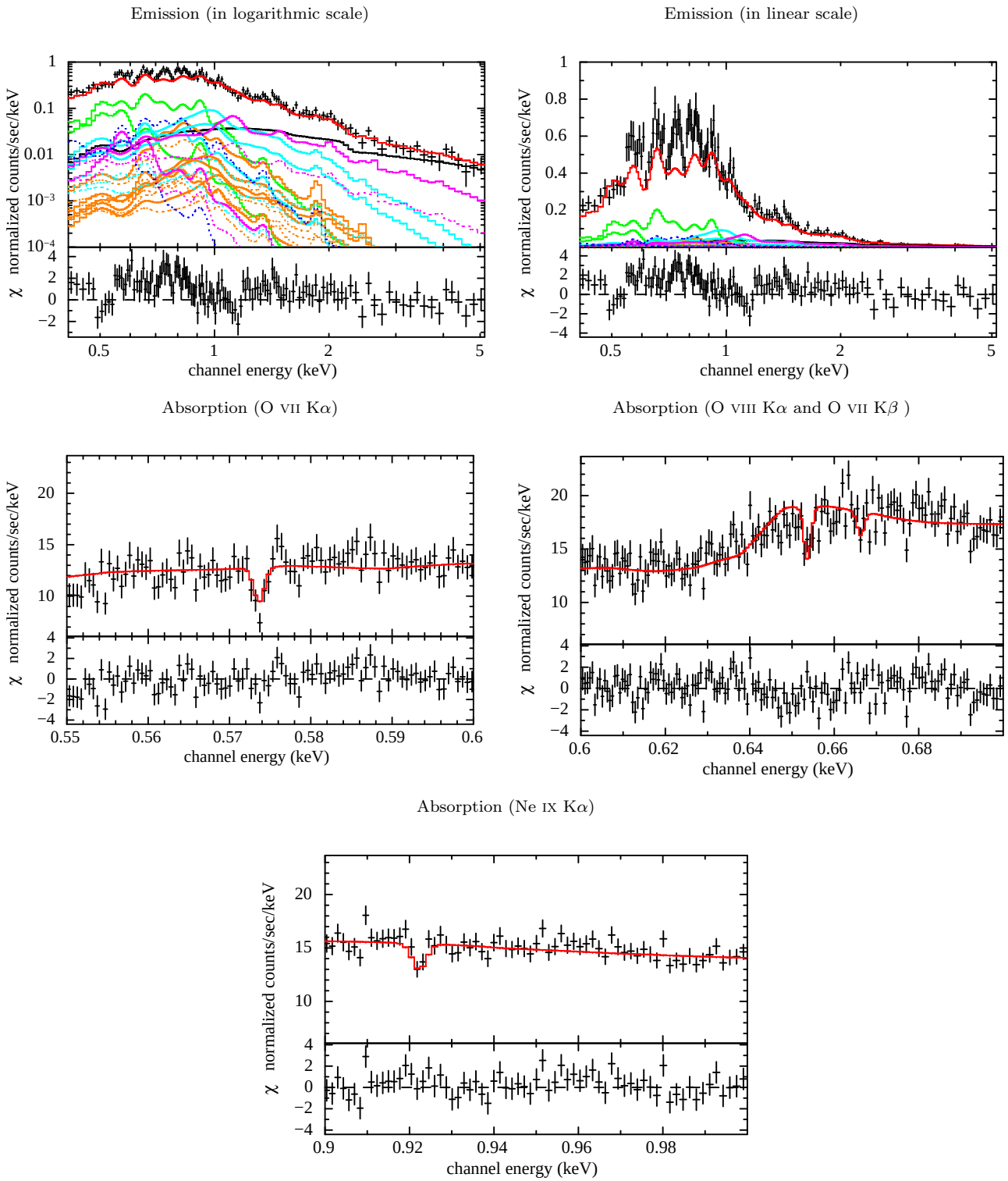

Figure 6.15: Observed data fitted by the exponential disk model for PKS 2155−304 without additional component

Table 6.15: Fitting results with the exponential disk model and additional emission components (C1)

Model		Back-Side component 1		Back-Side component 2		Stars	Binaries	Additional		χ^2/dof
		log T (K)	Norm[a]	log T (K)	Norm[a]	Ratio[bc]	Ratio[c]	log T (K)	Norm[a]	
C1-1	E2-mb	$6.610^{+0.069}_{-0.050}$	$10.3^{+1.1}_{-2.3}$	$6.001^{+0.240}_{-0.195}$	$71.4^{+354.6}_{-60.2}$	$4.34^{+1.58}_{-1.61}$	$6.27^{+1.17}_{-1.30}$			827.42/706
C1-2	E3-A'	$6.597^{+0.046}_{-0.044}$	$12.9^{+2.5}_{-1.8}$	$6.025^{+0.251}_{-0.183}$	$60.8^{+492.6}_{-50.1}$			$7.291^{+0.099}_{-0.071}$	$35.2^{+5.2}_{-5.5}$	809.78/706

Note: All the parameters not written the Table is fixed to the simulation based values.

[a] Emission Measure $10^{-3} \int n_e n_p dl$: in unit of cm^{-6} pc

[b] Normalization of background M type star is set to be free

[c] Ratio of the normalization of the background stars or binaries to the simulation based value

6.3.2 Uniform plasma model of two temperature component

In the previous section, we analyzed the emission spectra based on exponential disk model. In this section, we investigate the possibility of isothermal and uniform plasma. From emission analysis, it is obvious that at least two different temperature plasmas are needed and as shown in following sections, two plasmas are enough to reproduce the emission and absorption spectra simultaneously. Thus here we do not consider the case that three or more plasmas exist.

Assuming the geometry of the two temperature plasmas and the absorption observation target, there are only two possibilities for combined analysis. One is that both plasmas contribute the absorption and the other is that only one plasma contributes the absorption. Thus we consider these two cases in following sections.

6.3.2.1 Both plasmas contribute the absorption

For the first step, we assumed that both plasmas contribute the absorption (model C2) and all the plasma exist in front of 4U 1820−303 as illustrated in Figure 6.16. It is not determined that the two plasma components locate separately, or mixed together with filling factors.

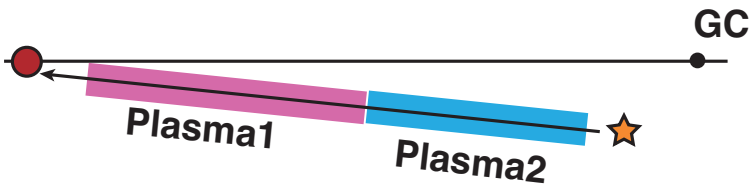

Figure 6.16: Schematic view of the model C2.

In the same way for PKS 2155-304 analysis, we constructed isothermal plasma model with a uniform density. We use plasma length L instead of the scale height for convenience. The abundance ratio of the hot ISM components are set to the solar value and we put an upper limit of 7.6 kpc on the length of the plasma to maintain consistency with the geometry. The velocity dispersions of the plasmas are linked together because this value was determined using the ratio of O VII Kα to O VII Kβ and once the temperature of one of two plasma become too low or high to produce sufficient O VII ions, the velocity dispersion of that plasma can not be determined.

We tried four sets of models, C2-1 and C2-2 is the combination of E2-mb and A4 model, and Ne/O abundance ratio are set to be free in C2-2. In C2-3 and C2-4 model, we adopt E3-A' model for the emission model. The fitting results are shown in Table 6.16. The results show that the length, column density and temperature of the hotter plasma and cooler plasma are 4.1–7.6 kpc, $\sim 2.5 \times 10^{19}$ cm^{-2}, $\sim 3.2 \times 10^{6}$K and 0.1–1.2 kpc, $\sim 1.5 \times 10^{19}$ cm^{-2}, $\sim 1.0 \times 10^{6}$ K as shown in Table 6.17. These values can be understood as following. First, as shown in the emission analysis, to reproduce the emission spectra two plasma is needed and their temperatures are $\sim 3.5 \times 10^{6}$ K and $\sim 1.0 \times 10^{6}$ K. The ionization fraction and emissivity of the plasma are fixed by these temperature and column density and emission measure to reproduce the both spectra are determined. We confirm this flow and found that the emission measures obtained here are about half of those obtained in emission analysis.

This is caused by the slight temperature decrease of hotter plasma induced by this combined analysis. Because in these temperature range of $logT \sim 6.5$, emissivity of O VII is almost proportional to T^{-3} and slight temperature decrease make the plasma to emit O VII lines much more efficiently.

The upper limit of the EW shown in Table 6.1, gives the upper limit for the column density of Ne X as $\log N_{\rm Nex} = 15.4$. With the model C2 results and assumption of the Ne abundance of the solar value, and the temperature dependence of the ionization fraction (Figure 6.18), the Ne X column density is at most 1×10^{15} cm^{-2}, thus we conclude that this result is consistent with the Ne X upper limit.

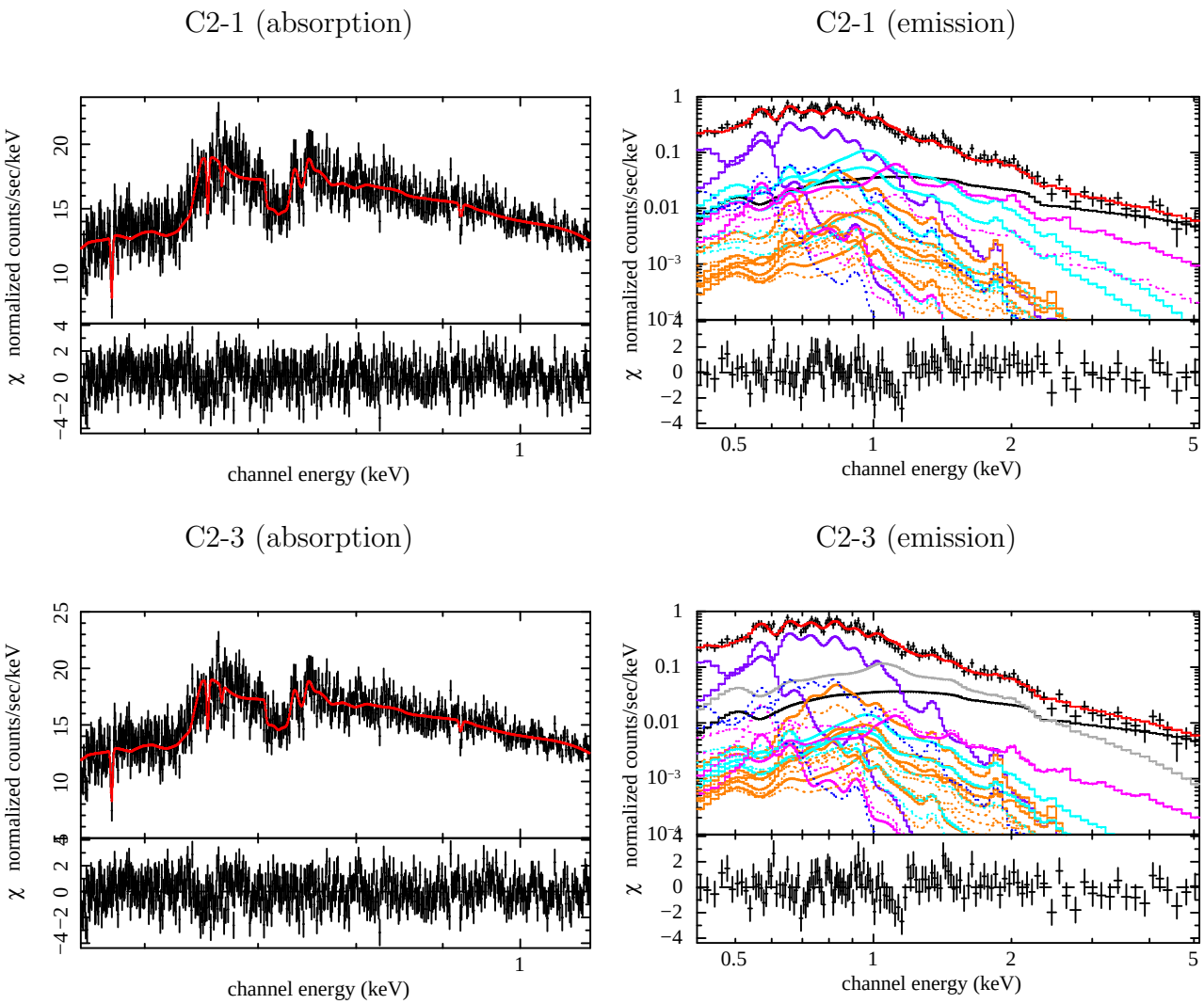

Figure 6.17: Spectra fitted by the model C2-1 and C2-3

Table 6.16: Fitting results with C2 model

Model		Uniform hot plasma 1					Uniform hot plasma 2			Stars	Binaries	Additional		χ^2/dof
		$N_{\rm H_{0t}}$ ($\rm cm^{-2}$)	Length (kpc)	log T (K)	Ne/O	v_b ($\rm km\ s^{-1}$)	$N_{\rm H_{0t}}$ ($\rm cm^{-2}$)	Length (kpc)	log T (K)	Ratio[a]	Ratio[b]	log T (K)	Norm[c]	
C2-1	E2-mb	$19.55^{+0.04}_{-0.24}$	$7.6^{+0.0}_{-5.2}$	$6.48^{+0.04}_{-0.04}$	...	...	$19.26^{+0.33}_{-0.32}$	$0.17^{+0.66}_{-0.15}$	$5.99^{+0.07}_{-0.15}$	$7.58^{+1.92}_{-1.81}$	$4.73^{+1.47}_{-1.46}$			805.65/703
	A4	↑	...	↑	...	139^{+286}_{-44}	↑	...	↑					
C2-2	E2-mb	$19.55^{+0.04}_{-0.22}$	$7.6^{+0.0}_{-5.1}$	$6.48^{+0.04}_{-0.04}$	$0.9^{+0.4}_{-0.4}$	...	$19.26^{+0.34}_{-0.31}$	$0.18^{+0.67}_{-0.16}$	$5.99^{+0.07}_{-0.15}$	$7.85^{+2.01}_{-2.09}$	$4.56^{+1.61}_{-1.62}$			805.49/702
	A4	↑	...	↑	...	140^{+282}_{-44}	↑	...	↑					
C2-3	E3-A'	$19.57^{+0.03}_{-0.22}$	$7.5^{+0.1}_{-4.9}$	$6.51^{+0.02}_{-0.03}$	...	...	$19.22^{+0.37}_{-0.25}$	$0.2^{+0.7}_{-0.1}$	$6.01^{+0.07}_{-0.10}$			$7.247^{+0.069}_{-0.094}$	$40.6^{+5.0}_{-4.7}$	800.67/703
	A4	↑	...	↑	...	156^{+269}_{-64}	↑	...	↑					
C2-4	E3-A'	$19.52^{+0.16}_{-0.21}$	$5.9^{+1.7}_{-3.7}$	$6.50^{+0.03}_{-0.04}$	$1.4^{+0.4}_{-0.3}$	...	$19.19^{+0.33}_{-0.25}$	$0.13^{+0.56}_{-0.11}$	$6.00^{+0.07}_{-0.11}$			$7.270^{+0.082}_{-0.069}$	$39.0^{+5.2}_{-5.3}$	796.36/702
	A4	↑	...	↑	↑	169^{+273}_{-76}	↑	...	↑					

Note: All the parameters not written the Table is fixed to the simulation based values.

[a] Normalization of background M type star is set to be free

[b] Ratio of the normalization of the background stars or binaries to the simulation based value

[c] Emission Measure $10^{-3} \int n_e n_p dl$: in unit of $\rm cm^{-6}$ pc

Table 6.17: Physical properties obtained by model C2

Model	Component	Length (kpc)	Density (10^{-3}cm^{-3})	Temperature (10^6 K)	Pressure (10^3cm^{-3} K)
C2-4	Plasma 1	$5.9^{+1.7}_{-3.7}$	$1.8^{+5.2}_{-0.9}$	$3.2^{+0.2}_{-0.3}$	$5.7^{+18.1}_{-3.2}$
	Plasma 2	$0.13^{+0.56}_{-0.11}$	$38.6^{+497.3}_{-34.5}$	$1.0^{+0.2}_{-0.2}$	$38.6^{+591.0}_{-35.4}$

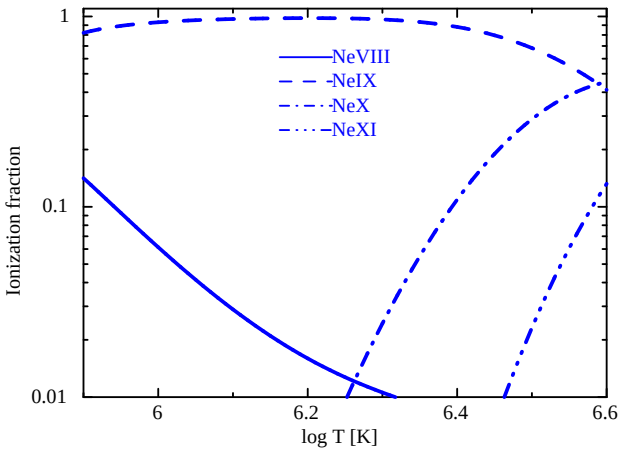

Figure 6.18: Enlarged display of Ne ionization fraction between $\log T$ =5.9 and 6.6.

The parameter of the plasma was determined as mentioned above, thus it is useful to consider what happen when a plasma of the same temperature exist beyond 7.6 kpc like Figure 6.14 (b) (case B). Under uniform assumption, emission measure (EM) and the column density (CD) obey following relations.

$$EM = n_e n_p \times length \tag{6.1}$$

$$CD = n_p \times length \tag{6.2}$$

$$length = CD^2/EM \tag{6.3}$$

Additional plasma, which do not contribute to the absorption, make the EM of the original plasma decrease to maintain the emission intensity, while CD is consistent. Thus the length become longer and the density become smaller assuming additional beyond plasma. As for the hotter plasma, the length is on the upper limit and there is no room for the additional component. While for the cooler component the length is only < 1.2kpc and its natural to assume additional component.

We summarized the induced physical properties of the plasma in Table 6.17. The density of the hotter plasma match to the mean density of the hot ISM in the disk and its pressure also meet the pressure equilibrium in the disk. While the density and pressure of the cooler plasma is far from reasonable. Certainly its lower limit meet the requirement of equilibrium, it is natural to consider that this plasma extend beyond the 4U 1820−303 and its density and pressure is reasonable. Using the equation 6.1, assuming the 90% of the emission originates beyond 4U 1820−303, the length of the plasma in front of 4U 1820-303 become 2.0 kpc

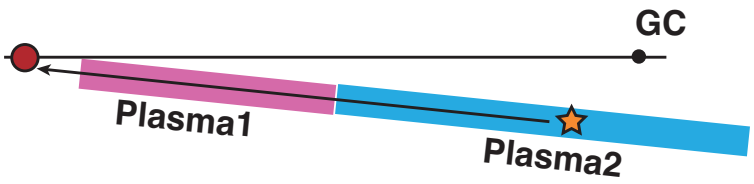

Figure 6.19: Schematic view of the model C2 case B.

and the length of the counterpart (in back of 4U 1820-303) become 20 kpc assuming same density. This assumption gives a scheme of thin hot and thick cold disk halo model.

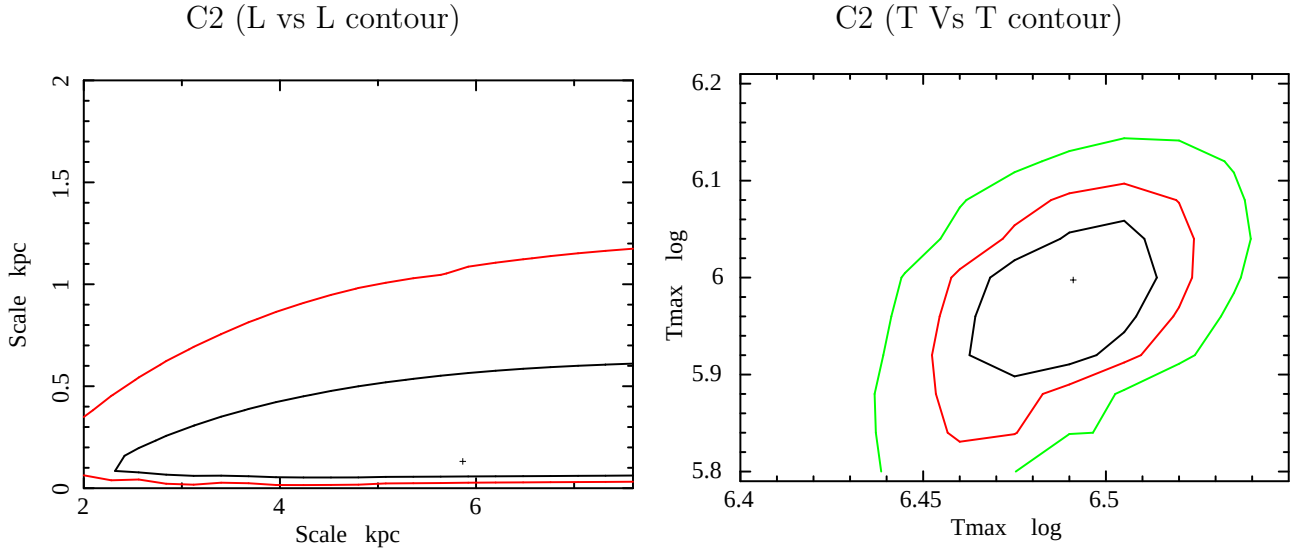

Figure 6.20: 68%, 90%, and 99% confidence contours of the length (left) and the temperature (right) of hotter vs cooler plasma with model C2-4.

6.3.3 Only one plasma contribute the absorption

For the next step, we assumed that only one plasma contribute the absorption (model C3). The geometry is as following; one uniform plasma (front-side plasma) exist in front of 4U 1820−303 and another uniform plasma (back-side plasma) exist in back of 4U 1820−303.

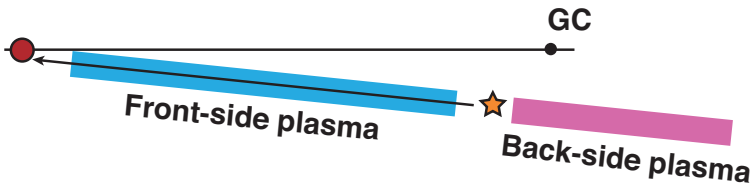

Figure 6.21: Schematic view of the model C3.

As same with the previous model C2, we constructed two models with model sets of E2-mb + A4 (C3-1, C3-2) and E3-A' + A4 (C3-3, C3-4). The abundance ratio of hot ISM components are set to the solar value for C3-1 and C3-3 model and Ne to O abundance is set to be free in C3-2 and C3-4 model. We put an upper limit of 7.6 kpc on the length of the front-side plasma.

The fitting results are shown in Table 6.19. The temperature of the front-side plasma (T$\sim 1.7 \times 10^6$ K) is determined mainly by the absorption spectra and is consistent with the temperature obtained by the absorption analysis (T$\sim 1.8 \times 10^6$ K). The temperature of the front- and back-side plasma (1.7×10^6 K and 3.9×10^6 K) are both higher than the those determined only by emission analysis (1.1×10^6 K and 3.6×10^6 K). A plasma of 1.7×10^6 K could emit O VII and O VIII lines three times and thirty times effectively than a plasma of 1.1×10^6 K. Though this makes the emission measure of the front-side plasma smaller to maintain the intensity of the O VII lines, O VIII lines are produced more effectively. Thus to suppress the O VIII intensity, the temperature of the back-side plasma become higher. Residuals caused by this adaptation could be compensated by the background components and this model also can reproduce the O, Fe and Ne emission lines. However in the energy range lower than 0.5 keV, there is a residuals caused by the deficit of N lines, because the lower temperature plasma (1.7×10^6 K) is too hot to emit N lines effectively. Though this deficit make the χ^2 larger (~ 10) than C2 model, the results are reasonable and we accepted them.

We summarized the physical properties of the plasma in Table 6.18. We assume the 1, 2 and 10 kpc of the length for the back-side plasma to estimate its density and pressure. There could be two schemes. Assuming the back-side plasma confined in the Galactic center region, its length is at most 2 kpc and this leads dens and high pressure plasma. Thus this leads a picture of that a hotter dens plasma exist Galactic center and warm thin plasma prevail the disk. Another is that assuming pressure equilibrium between front-side plasma and back-side plasma, the length of the back-side plasma become at least ~ 10 kpc. This means that a hotter disk exist over the warm thin disk.

Table 6.18: Physical properties obtained by the model C3

Model	Component	Length (kpc)	Density (10^{-3}cm^{-3})	Temperature (10^6 K)	Pressure (10^3cm^{-3} K)
C3-4	Front-Side plasma	$3.08^{+4.52}_{-1.81}$	$3.6^{+10.4}_{-2.6}$	$1.7^{+0.2}_{-0.2}$	$6.0^{+20.6}_{-4.6}$
	Back-Side plasma	1	$4.3^{+0.6}_{-0.4}$	$3.9^{+0.4}_{-0.3}$	$16.8^{+4.2}_{-2.9}$
		2	$3.1^{+0.6}_{-0.4}$	$3.9^{+0.4}_{-0.3}$	$12.1^{+3.7}_{-2.5}$
		10	$1.3^{+0.2}_{-0.2}$	$3.9^{+0.4}_{-0.3}$	$5.1^{+1.3}_{-1.2}$

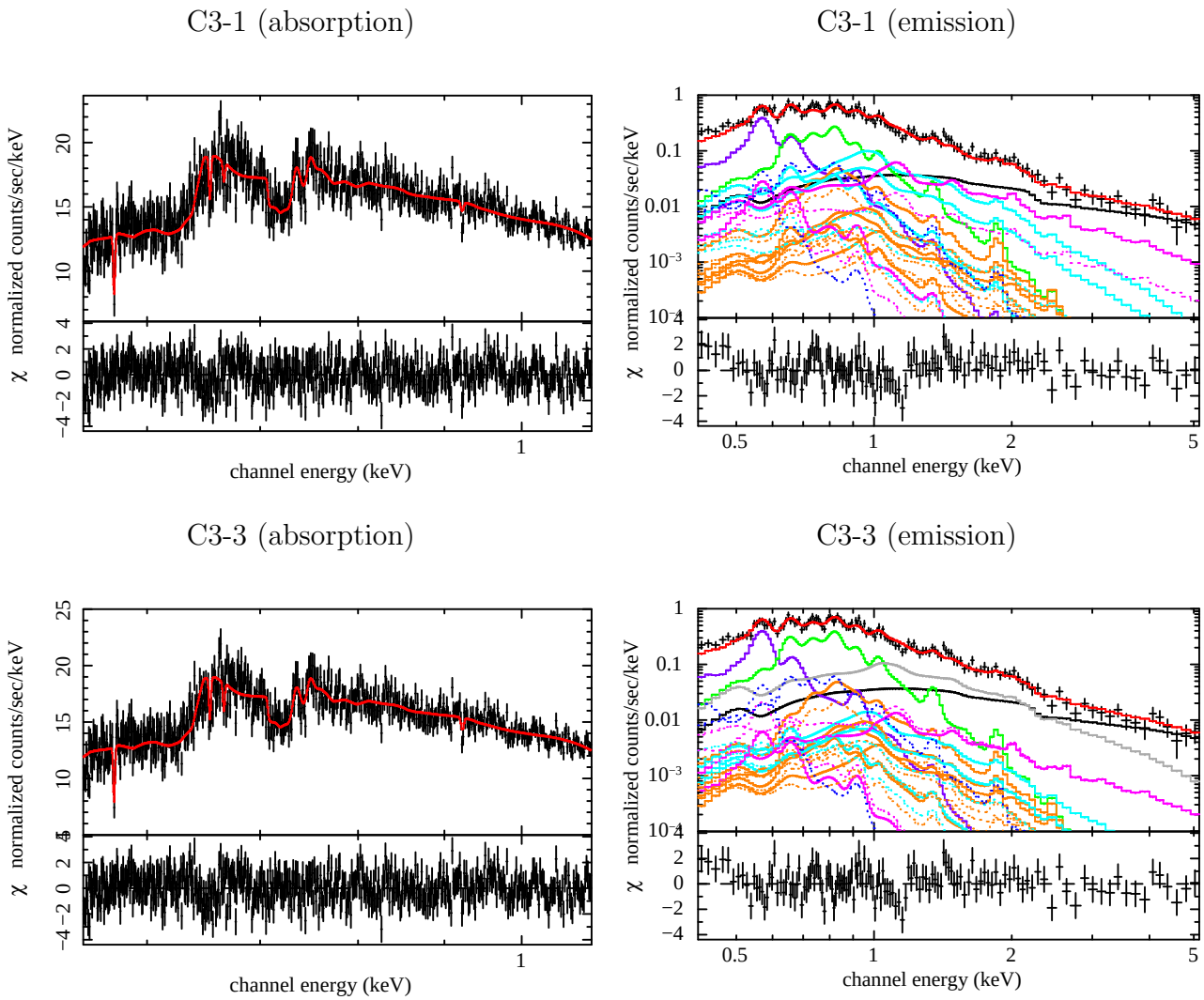

Figure 6.22: Spectrum fitted by the model C3-1 and C3-3

Table 6.19: Fitting results of C3 model

Model	Data	Front-Side plasma					Back-Side plasma		Stars	Binaries	Additional		χ^2/dof
		$N_{\rm H_{Hot}}$ ($\rm cm^{-2}$)	Length (kpc)	log T (K)	Ne/O	v_b (km $\rm s^{-1}$)	log T (K)	Norm[a]	Ratio[bc]	Ratio[c]	log T (K)	Norm	
C3-1	E2-mb	$19.71^{+0.09}_{-0.37}$	$7.60^{+0.00}_{-5.61}$	$6.22^{+0.05}_{-0.08}$	···	···	$6.583^{+0.055}_{-0.049}$	$15.5^{+5.1}_{-4.9}$	$7.00^{+1.90}_{-2.83}$	$4.66^{+1.56}_{-1.51}$			819.82/704
	A4	↑	···	↑	···	109^{+140}_{-29}							
C3-2	E2-mb	$19.60^{+0.18}_{-0.22}$	$4.67^{+2.93}_{-2.91}$	$6.22^{+0.05}_{-0.06}$	$1.4^{+1.2}_{-0.8}$	···	$6.588^{+0.047}_{-0.051}$	$15.3^{+5.2}_{-3.9}$	$6.67^{+1.98}_{-1.59}$	$4.86^{+1.48}_{-1.53}$			819.05/703
	A4	↑	···	↑	↑	126^{+164}_{-45}	···	···					
C3-3	E3-A'	$19.68^{+0.16}_{-0.11}$	$5.88^{+1.72}_{-3.66}$	$6.20^{+0.05}_{-0.04}$	···	···	$6.574^{+0.041}_{-0.029}$	$22.0^{+3.0}_{-5.2}$			$7.254^{+0.085}_{-0.086}$	$37.7^{+5.2}_{-5.3}$	810.11/704
	A4	↑	···	↑	···	111^{+84}_{-34}							
C3-4	E3-A'	$19.53^{+0.21}_{-0.19}$	$3.08^{+4.52}_{-1.81}$	$6.23^{+0.05}_{-0.05}$	$2.3^{+1.4}_{-1.1}$	···	$6.592^{+0.040}_{-0.040}$	$18.9^{+5.1}_{-4.0}$			$7.265^{+0.089}_{-0.073}$	$37.1^{+5.0}_{-5.5}$	805.94/703
	A4	↑	···	↑	↑	139^{+195}_{-55}							

Note: All the parameters not written the Table is fixed to the simulation based values.

[a] Emission Measure $10^{-3} \int n_e n_p dl$: in unit of $\rm cm^{-6}$ pc

[b] Normalization of background M type star is set to be free

[c] Ratio of the normalization of the background stars or binaries to the simulation based value

6.4 Uncertainty due to the Model Systematics

6.4.1 Absorption analysis

The energy resolution of the detectors ($\sim$ 0.05Å) corresponds $v_b \sim 400\mathrm{kms}^{-1}$ and is not enough to determine the v_b of the plasma only with the line shapes. The lower limit of the v_b can be determined from thermal limit. Thus, to determine velocity dispersion, we used the ratio of the absorption depth of O VII K_α and O VII K_β instead and assuming that the O VIII, Ne IX and Ne X originate same plasma, we linked the velocity dispersion of all lines. As shown in curve of growths (Figure 2.9), v_b and column density are coupled and if the plasma have temperature gradient and local structure, this assumption cause systematic errors.

6.4.2 Emission analysis

In Table 6.20 we summarized the systematic errors of the background and foreground models and their effect on the best fit values of the hot ISM parameters. Please see Appendix D.2 for the estimation of the systematic errors and details of the fitting results. Obtained hot ISM parameters are all within 90 % statistical error and cause no change to our results and conclusions.

Table 6.20: Estimated systematic errors of the models and their effect on the best fit values of the hot ISM parameters (all the parameters are within statistical error).

Component	Systematic Error	Affection to the best fit values of the Hot ISM			
		Cooler ($T < 1.3 \times 10^6$ K)		Hotter ($T > 2.5 \times 10^6$ K)	
		Temperature	Normalization	Temperature	Normalization
Foreground stars	+20%	$< 1\%(+)$	-3%	$< 1\%(-)$	$< 1\%(-)$
	-20%	$< 1\%(-)$	$+3\%$	$< 1\%(+)$	$< 1\%(+)$
Background stars	+50%	$< 1\%(-)$	$+2\%$	$< 1\%(-)$	-2%
	-50%	$< 1\%(+)$	-2%	$< 1\%(+)$	$+2\%$
CXB	+30%	$< 1\%(+)$	$\pm 3\%$	$< 1\%(-)$	$\pm 1\%$
	-30%	$< 1\%(-)$	$\pm 3\%$	$< 1\%(+)$	$\pm 1\%$
LHB+SWCX	+75%	$< 1\%(+)$	-15%	$< 1\%(+)$	$< 1\%(\pm)$
	-100%	$< 1\%(-)$	$+18\%$	$< 1\%(+)$	$< 1\%(\pm)$
Loop I	+50%	$< 1\%(+)$	-3%	$< 1\%(-)$	-10%
	-50%	$< 1\%(-)$	$+4\%$	$< 1\%(+)$	$+10\%$

6.4.3 Combined analysis

In addition to the systematic errors mentioned above, we have to consider systematics caused by combined analysis itself. Figure 6.23 shows contours of the temperatures of the hot ISM derived from emission analysis (E3-A') and combined analysis (C2-4, C3-4). As shown in

Figure 6.23, contours only lap over partially and those from combined analysis are shifted to each direction. The best fitted χ^2/dof value of C3 model is worse than those of the other models. These shifts would be caused by modeling multi-temperature plasma with two temperature plasmas. To check the contribution of the uncertainty of the star and unknown component, we fixed the parameters of the unknown component to the best fit value of E3-A' model (Table 6.11) and performed combined analysis with C2-4 and C3-4 model (Table 6.21, 6.22). The results are consistent with the those of C2-4 and C3-4 model. These two models (C2-4, C3-4) are representatives of the other combined analysis models and we concluded this systematics originate combined analysis. Using these contours, the temperature range of the two plasmas are determined as $2.8 - 4.3 \times 10^6$ K ($\pm 25\%$) and $0.68 - 1.9 \times 10^6$ K ($+80\%, -35\%$). These errors cause no change to our conclusions.

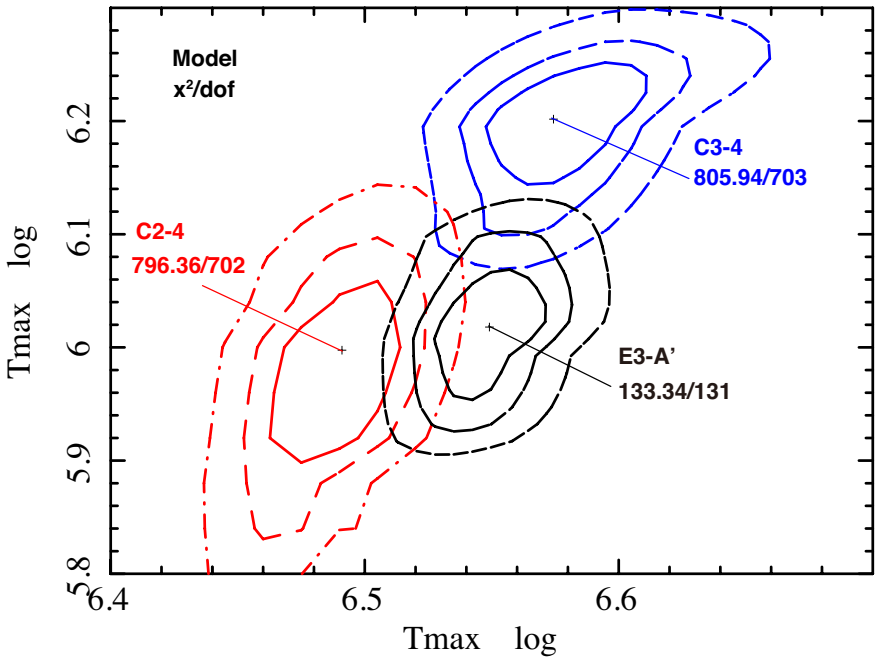

Figure 6.23: 68%, 90%, and 99% confidence contours of the temperature of hot ISM. Black, red and blue lines indicate the results of E3-A' model, C2-4 model and C3-4 model respectively. The best fitted χ^2/dof values are indicated.

Table 6.21: Fitting results with C2 model (fixed unknown component)

Model		Uniform hot plasma 1					Uniform hot plasma 2			Stars	Binaries	Additional		χ^2/dof
		$N_{H_{Hot}}$ (cm^{-2})	Length (kpc)	log T (K)	Ne/O	v_b (km s^{-1})	$N_{H_{Hot}}$ (cm^{-2})	Length (kpc)	log T (K)	Ratio[a]	Ratio[b]	log T (K)	Norm[c]	
C2-4	E3-A'	$19.52^{+0.16}_{-0.21}$	$5.9^{+1.7}_{-3.7}$	$6.50^{+0.03}_{-0.04}$	$1.4^{+0.4}_{-0.3}$	...	$19.19^{+0.33}_{-0.25}$	$0.13^{+0.56}_{-0.11}$	$6.00^{+0.07}_{-0.11}$			$7.270^{+0.082}_{-0.069}$	$39.0^{+5.2}_{-5.3}$	796.36/702
	A4	↑	...	↑	↑	169^{+273}_{-76}	↑	...	↑					
C2-4	E3-A'	$19.52^{+0.16}_{-0.21}$	$5.9^{+1.7}_{-3.7}$	$6.50^{+0.03}_{-0.03}$	$1.4^{+0.4}_{-0.3}$	...	$19.19^{+0.33}_{-0.25}$	$0.13^{+0.56}_{-0.11}$	$6.00^{+0.07}_{-0.11}$			7.239(fixed)	38.5(fixed)	797.18/704
	A4	↑	...	↑	↑	169^{+138}_{-75}	↑	...	↑					

Note: All the parameters not written the Table is fixed to the simulation based values.
[a] Normalization of background M type star is set to be free
[b] Ratio of the normalization of the background stars or binaries to the simulation based value
[c] Emission Measure $10^{-3} \int n_e n_p dl$: in unit of cm^{-6} pc

Table 6.22: Fitting results with C3 model (fixed unknown component)

Model	Data	Front-Side plasma					Back-Side plasma		Stars	Binaries	Additional		χ^2/dof
		$N_{H_{Hot}}$ (cm^{-2})	Length (kpc)	log T (K)	Ne/O	v_b (km s^{-1})	log T (K)	Norm[a]	Ratio[bc]	Ratio[c]	log T (K)	Norm	
C3-4	E3-A'	$19.53^{+0.21}_{-0.19}$	$3.08^{+4.52}_{-1.81}$	$6.23^{+0.05}_{-0.05}$	$2.3^{+1.4}_{-1.1}$	...	$6.592^{+0.040}_{-0.040}$	$18.9^{+5.1}_{-4.0}$			$7.265^{+0.089}_{-0.073}$	$37.1^{+5.0}_{-5.5}$	805.94/703
	A4	↑	...	↑	↑	139^{+195}_{-55}							
C3-4	E3-A'	$19.53^{+0.21}_{-0.19}$	$3.13^{+4.47}_{-1.84}$	$6.23^{+0.05}_{-0.05}$	$2.3^{+1.4}_{-1.1}$	...	$6.591^{+0.039}_{-0.039}$	$18.8^{+5.2}_{-4.0}$			7.239(fixed)	38.5(fixed)	806.10/705
	A4	↑	...	↑	↑	139^{+114}_{-55}							

Note: All the parameters not written the Table is fixed to the simulation based values.
[a] Emission Measure $10^{-3} \int n_e n_p dl$: in unit of cm^{-6} pc
[b] Normalization of background M type star is set to be free
[c] Ratio of the normalization of the background stars or binaries to the simulation based value

Chapter 7

Discussion

7.1 Summary of the Observational Results

We have investigated the hot ISM with combined analysis of unprecedented spectroscopic capability of *Suzaku* and *Chandra* . By analyzing the emission and absorption data in the high galactic latitude and the galactic bulge region, we have obtained new insights on the hot ISM.

1. In the high galactic latitude (PKS 2155-304) direction, absorption and emission data are explained by the exponential disk model.

2. In the galactic bulge (4U 1820-303) direction, the exponential model with the best fit parameter obtained in the high galactic latitude failed to explain emission data. Additional emission component of T$\sim 4 \times 10^6$ K and T$\sim 1 \times 10^6$ K is needed.

3. In the galactic bulge (4U 1820-303) direction, two single temperature uniform plasma can reproduce the absorption and emission spectra.

7.2 Global Structure of the Hot ISM

7.2.1 High galactic latitude

7.2.1.1 Pressure balance and the scale height of the exponential disk

The pressure P of a fully-ionized plasma is described as $P/k_{\rm B} = 2.3nT$ where $k_{\rm B}$, n and T are boltzmann constant, hydrogen (proton) density and temperature respectively, and 2.3 is the ratio of total particle density to hydrogen. The mid-plane pressure of the exponential model can be calculated using above equation as,

$$P_0/k_{\rm B} = 1.1 \times 10^4 \left(\frac{T_0}{10^{6.3}{\rm K}}\right) \left(\frac{n_0}{2.2 \times 10^{-3}{\rm cm}^{-3}}\right) \tag{7.1}$$

here T_0, n_0 are the temperature and density of the plasma at the plane respectively. The pressure due to the cold and warm ISM and the magnetic field at the mid-plane is estimated to be $1.1{\times}10^{-4}$K cm^{-3} at most (Cox (2005)). In figure 7.1, we plotted the contours of the column density and the mid-plane temperature as a function of the scale height. The

T_0=$10^{6.33}$ K line is drawn and it is clear that the mid-plane temperature exceeds $10^{6.3}$ K at any scale height. This means when n_0 exceeds 2.2×10^{-3}cm^{-3}, the pressure equilibrium is broken. The parameter region where n_0 exceeds the value is shadowed on the top panel. It is obvious that, to meet the equilibrium, the scale height of the density has to be greater than 1 kpc.

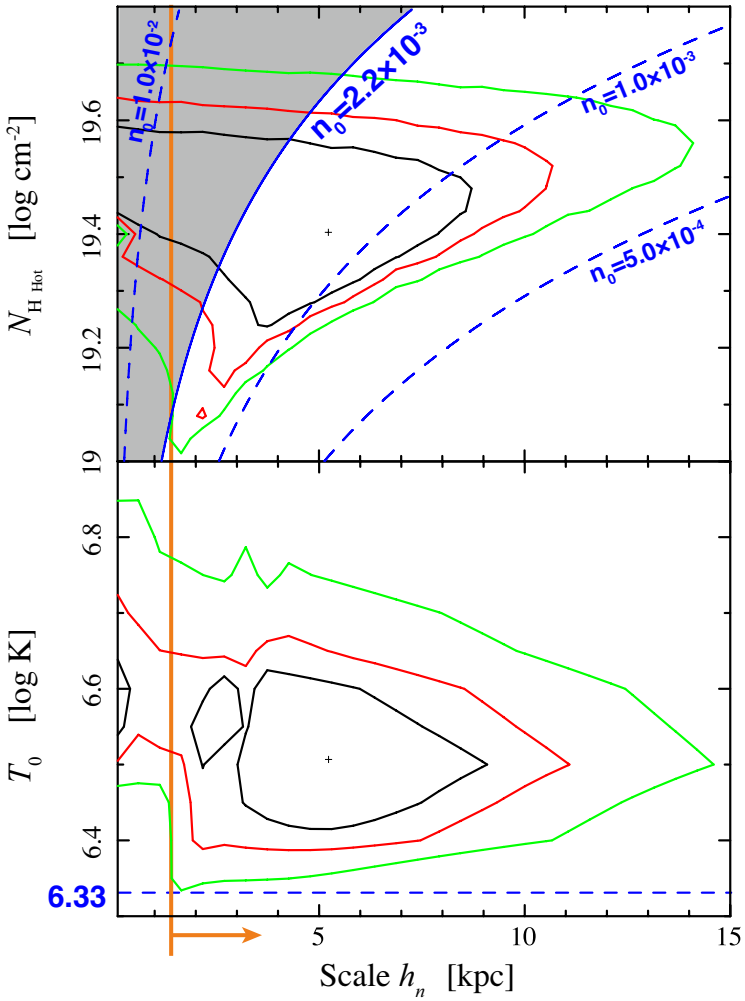

Figure 7.1: 68%, 90%, and 99% confidence contours of T_0 and $N_{\rm H_{Hot}}$ vs. scale height h_n obtained in the joint fit to the X-ray absorption and emission data. In the upper panel the density at the plane n_0 is constant along the solid and dashed lines. Dashed line in the lower panel shows critical temperature used in equation 7.1. The shadowed region is excluded by the pressure equilibrium assumption.

7.2.1.2 Comparison with the results for LMC X-3

We compared the results with that of the LMC X-3 (Table 7.1) direction. Directions of the LMC X-3 and PKS 2155-304 are (l,b) = (273.6,−32.1) and (17.7,−52.2). The fact that we obtained similar values for the two directions indicates that the hot ISM in the high galactic latitude is common in a big picture and can be explained with the exponential

model of the column density, scale height and temperature as $\sim 2 \times 10^{19}$ cm^{-2}, a few kpc and $\sim 2 \times 10^{6}$ K. As the distance to the targets are 50 kpc for LMC X-3 and 480 Mpc for PKS 2155-304. The consistency of the parameters of the exponential disk suggests that any significant contribution would be confined within a few 10 kpc around our Galaxy. We call this structure of the hot ISM "hot halo" hereafter.

Table 7.1: Disk model parameters for two sight lines

Direction	log $N_{\mathrm{H_{Hot}}}$ (cm^{-2})	h_n (kpc)	$logT_0$ (K)	γ	Ne/O	Fe/O
PKS 2155-304	$19.41^{+0.18}_{-0.20}$	$5.1^{+3.9}_{-4.7}$	$6.51^{+0.08}_{-0.10}$	$0.43^{+1.15}_{-0.23}$	$2.3^{+1.6}_{-0.5}$	$1.0^{+0.8}_{-0.5}$
LMC X-3†	$19.36^{+0.22}_{-0.21}$	$2.8^{+3.6}_{-1.8}$	$6.56^{+0.11}_{-0.10}$	$0.5^{+1.2}_{-0.4}$	$1.7^{+0.6}_{-0.4}$	$0.9^{+0.2}_{-0.2}$

† from Yao et al. (2009)

7.2.1.3 Expansion condition of the hot ISM

The parameter γ is defined as $\gamma = h_T/h_n$ where h_n and h_T is the scale height of the density and temperature respectively. Using the definition of the exponential disk model

$$T = T_0 \exp(-Z/h_T) \tag{7.2}$$
$$n = n_0 \exp(-Z/h_n) \tag{7.3}$$

the relation of the n and T can be redefined with γ as

$$n = n_0 \exp(-Z/h_n) = n_0 \exp(-Z\gamma/h_T) = n_0 \times \left(\frac{T}{T_0}\right)^{\gamma} \tag{7.4}$$

Though the error range of γ is large, best fit value is similar for PKS 2155-304 and LMC X-3 and it is useful to consider the physical meaning of the value. If $\gamma = 0.5$, the Equation 7.4 become

$$n = n_0 \times \left(\frac{T}{T_0}\right)^{0.5} \tag{7.5}$$
$$n^2 T^{-1} = Const \tag{7.6}$$
$$TV^2 = Const \tag{7.7}$$

in converting Equation 7.6 to 7.7, we used the relation $n \propto V^{-1}$. The relation of the volume and temperature for an adiabatic expanding plasma consists of ideal gas is

$$TV^{\frac{2}{3}} = Const \tag{7.8}$$

this means the plasma is cooled faster than adiabatic expansion. The radiative cooling time scale is $\sim 10^7$ year for the plasma of T $\sim 10^6$ K and n $\sim 10^{-3}$ cm^{-3}, and the traveling time of the plasma from inner disk to halo region would be order of 10^6 year (Shapiro & Marchant (1976)). Thus another mechanism such as energy convection through magnetic field would exist.

7.2.1.4 Comparing with the other observations

We tried to explain the results of Yoshino et al. (2009) with our exponential disk model. The best fit parameters are used for the calculation. We use 100μm IR data for the column density of the neutral medium. The foreground emission is assumed as 2 LU O VII and 0 LU O VIII emission. We plotted the simulated values vs the observed values in Figure 7.2.

As shown in the Figure 7.2, the exponential model well reproduce the data in general. It can be said that this model succeed to explain the global structure of the hot ISM. The discrepancy of the simulated values and observational value is at most 2 LU for O VII and 1 LU for O VIII. Fluctuations due to SWCX is estimated as 1 LU for O VII by Yoshino et al. (2009) and this suggest that there are fluctuations in plasma density and/or temperature corresponding to at least 1 LU of O VII and O VIII.

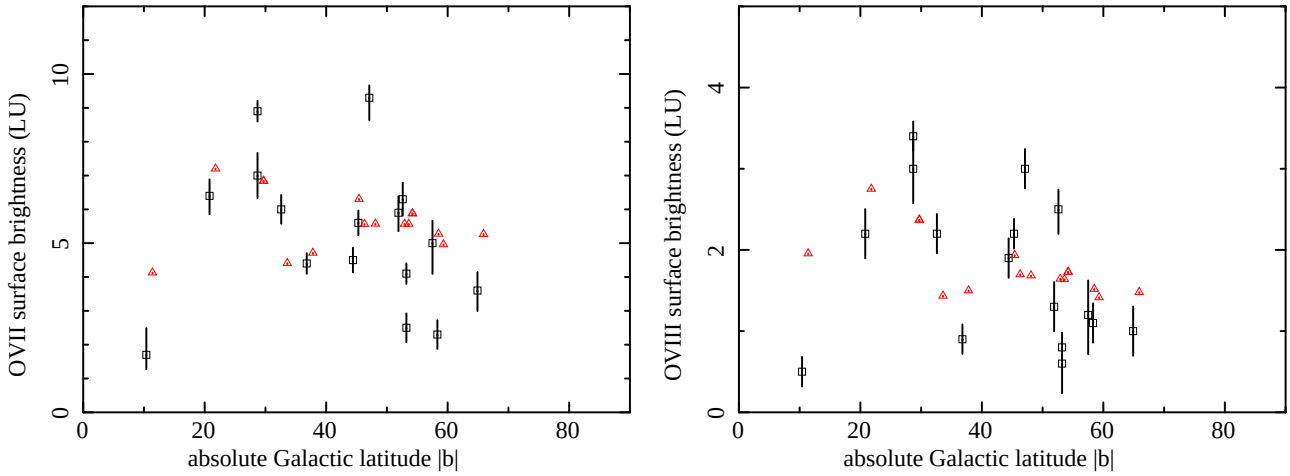

Figure 7.2: (left): O VII surface brightness of the simulated values vs absolute galactic latitude, (right): same as the left panel for O VIII surface brightness. The observational data are indicated with square and the vertical bars of the data points show the 1 σ errors. The simulated values with exponential disk model are indicated with red triangles.

7.2.2 Galactic bulge region

7.2.2.1 Verification of the hot ISM models

As shown in Chapter 6, there are three models to explain the emission and absorption data in the Galactic bulge direction. Though our knowledge is restricted to the sight line of the observation, it is useful to expand the results to global model and compare it with the results of the other sight lines. To clear the discussion, we only use the best fit values of the results here.

We summarized the results in Table 7.2. Only the emission measures are obtained for back-side component,because there are no absorption data. First we took notice of length of the front component. Except for Plasma 2 in C2 model, the error range include upper limit determined by the geometry. It is not likely that such fully filled component is confined only in a sight line and this implies that these components fill and prevail the disk. Thus we

consider that such long extended plasma is a part of the hot ISM disk. By the geometry of the 4U 1820-303, the height of this disk is 1 kpc.

First we check whether the hot ISM disk can produce consistent results in PKS 2155-304 direction. As for C2 model, the hot ISM disk induced from Plasma 1 produce too much O VIII and Fe L lines (Figure 7.3 left). Thus we exclude C2 model. The hot ISM disk induced from front plasma of C3 model produce less emission (Figure 7.3 right). However this could be compensated with abundance modification.

Then we realized that the temperature of the hot ISM disk of C3 model is similar to that determined with uniform disk model for PKS 2155-304 (Table 7.3). As discussed in Section 6.3.2, the length and the density of the front plasma have a freedom. In Figure 7.4, there are two plasma model. The circle indicate the observer and the star indicate the target of the absorption observation. Thus the plasma exist behind the star do not contribute the column density obtained by the absorption analysis. It is easy to confirm the column density and the emission measure in each situation is same as

$$a)\ EM = n^2 \times L \tag{7.9}$$
$$CD = n \times L \tag{7.10}$$
$$b)\ EM = (n/c)^2 \times cL + (n/c)^2 \times c(c-1)L = (n/c)^2 \times c^2 L = n^2 L \tag{7.11}$$
$$CD = n/c \times cL = nL \tag{7.12}$$

The length of the front plasma is 3.1 kpc. We use this equation and check the total length and total column density when the plasma become 7.6 kpc which corresponds $c = 7.6/3.1 = 2.5$ in above equation. The total length and the total column density are calculated as $(cL + c(c-1)L) = c^2 L = 19.4$ kpc and $nL + (c-1)nL = cnL = 10^{19.93}$ cm^{-2}. To compare these values with PKS 2155-304 results, we have to evaluate the height of the uniform disk as $19.4 \times \sin(b_{4\mathrm{U}}) = 2.7$ kpc and the column density in PKS 2155-304 direction as $10^{19.93} \times \sin(b_{4\mathrm{U}})/\sin(b_{\mathrm{PKS}}) = 10^{19.17}$ cm^{-2}, where $b_{4\mathrm{U}}$ is 7.9 for 4U 1820-303 direction and b_{PKS} is -52.2 for PKS 2155-304 direction. These values are comparable to the results of uniform disk assumption of PKS 2155-304 and we consider front plasma of C3 model is corresponds to the exponential disk. Then it is natural to think the back-side plasma is confined in the bulge region and this is also comparable to the C1 model.

Of course there are many possibilities not considered here, this roughly estimation suggest that the high temperature plasma is confined in the bulge region. We call this structure of the hot ISM "X-ray bulge" hereafter. Using the results of hotter component in C1 model and assuming spherical structure with 1.4 kpc radius (which corresponds 2 kpc of the length of the line of sight in the X-ray bulge), the density of the X-ray bulge is estimated as 2.5×10^{-3} cm^{-3}.

Table 7.2: Results of the analysis of the galactic bulge region.

Model	Component	Front-Side			Back-Side	
		log T (K)	log $N_{\mathrm{H_{Hot}}}$ ($\mathrm{cm^{-2}}$)	Length (kpc)	log T (K)	EM ($10^{-3}\mathrm{cm^{-6}pc}$)
C1	Exponential disk	Exponential disk			Exponential disk	
	Back-Side plasma 1		-		6.60	12.9
	Back-Side plasma 2		-		6.03	60.8
C2	Plasma 1	6.50	19.52	5.9		-
	Plasma 2	6.00	19.19	0.13		-
C3	Front-Side Plasma	6.23	19.53	3.1		-
	Back-Side Plasma		-		6.59	18.9

Table 7.3: The results of uniform disk model in PKS 2155-304 direction

Uniform disk		
log $N_{\mathrm{H_{Hot}}}$ ($\mathrm{cm^{-2}}$)	h (kpc)	log T (K)
$19.08^{+0.06}_{-0.07}$	$4.2^{+1.5}_{-1.2}$	$6.27^{+0.02}_{-0.02}$

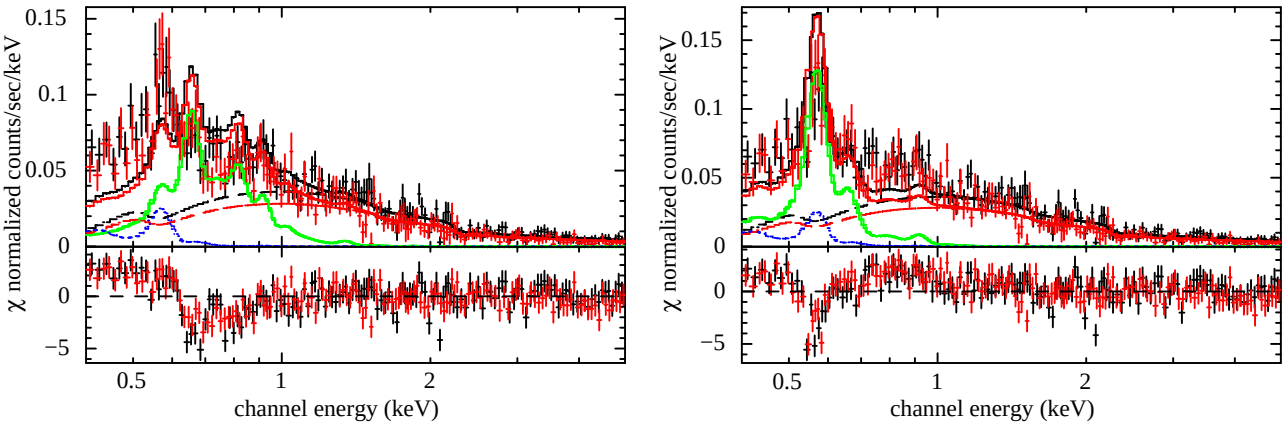

Figure 7.3: Spectrum of the high latitude observations and extrapolated model of galactic bulge region. The hot ISM model is indicated with green line. (left) model C-2, (right) model C-3.

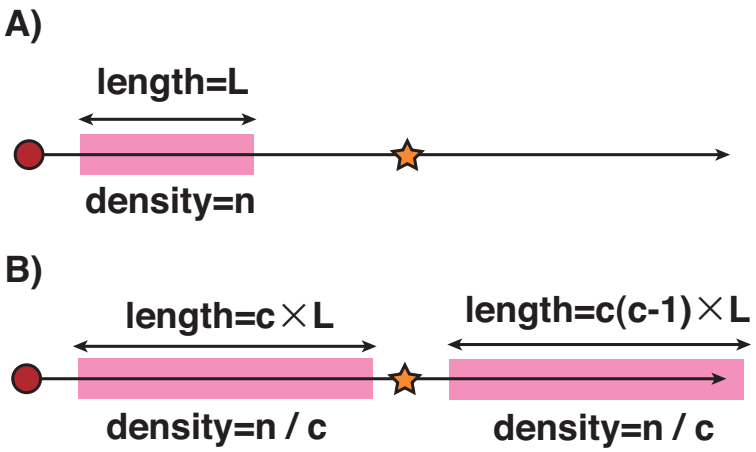

Figure 7.4: Spectrum of the high latitude observations and expanded model of galactic bulge region. (left) the hot ISM disk of C2 model, (right) the hot ISM disk of C3 model.

7.2.3 Distribution of the O VII and O VIII emitting/absorbing gas

We calculate the distribution of O VII and O VIII ions and their emissivities in the hot halo with the exponential disk model. The best fit parameters at $\gamma = 0.43$ and at $\gamma = 0.2$ and 1.5 are used for calculations (figure 7.5). It is clear that the O VII ions which contribute the absorption exist high above the disk, in contrast hot ISM which contribute the emission is confined within a few kpc above the disk. This cause the discrepancy of the temperature obtained with absorption analysis and emission analysis alone.

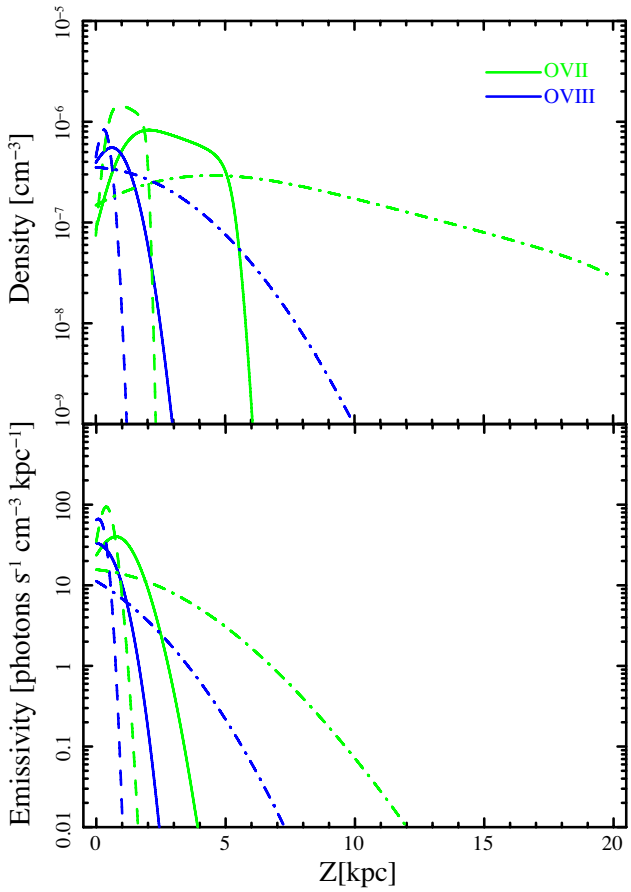

Figure 7.5: The density of O VII and O VIII ion(top) and the emissivity of O VII and O VIII lines (bottom) as a function of the height from the galactic plane under the best fit parameter of γ=0.43 (solid line), γ=0.2 (dashed line) and γ=1.5 (dash-dotted line).

7.2.4 Consistency with O VI absorbing gas

It is not clear that our model is consistent beyond $\sim$ 5 kpc where the temperature of the gas is below $\sim 10^{6.0}$ K and O VI ion becomes dominant.

Williams et al. (2007) found two local O VI absorption lines in PKS 2155-304 spectrum observed by *FUSE* , and we compared O VI column density given by our best fit model. The column densities reported in Williams et al. (2007) are $1.1(+0.1, -0.1) \times 10^{14}\mathrm{cm}^{-2}$ and

$8.7(+0.4, -0.4) \times 10^{13}\mathrm{cm}^{-2}$, while our exponential gives value of $4.6 \times 10^{14}\mathrm{cm}^{-2}$ with best fit parameters and $1.0 \times 10^{14}\mathrm{cm}^{-2}$ with best fit parameters when $\gamma = 1.5$.

However a plasma emitting O VI lines cools very rapidly and it would be difficult to maintain such plasma existing high above the Galactic plane. Radiative cooling is accelerated by the density fluctuations. Thus O VI absorbing gas can be patch or blob-like condensation. To discuss this problem, further analysis using UV observation data is needed and this is beyond the focus of this thesis.

7.3 Properties of the Hot ISM

We calculated the total mass, total energy, X-ray luminosity, bolometric luminosity and cooling time of hot halo and X-ray bulge. The results are summarized in Table 7.4.

For hot halo, assuming the solar abundance, best fit parameters and ionization faction and emissivity taken from SPEX, we obtained the energy loss rate as a function of the distance from the Galactic plane Z (Figure 7.6). Bump around 6 kpc in Figure 7.6 is due to O VI emission lines that make the cooling time significantly shorter. However it is dangerous to rely on our exponential model to much in the low temperature ($T < 10^{5.5}$) phase, because our results are obtained using X-ray measurement. When the temperature of the plasma is lower than $T \sim 10^{5.5}$, it becomes hard to detect only by the X-ray.

We integrated the energy loss rate until the temperature of the exponential disk become lower than $10^{5.5}$ K where is the limit of X-ray measurement and obtained total radiative energy loss rate as $3.6{\times}10^{37}$ erg s^{-1} kpc^{-2} in 0.001-40 keV and $2.9{\times}10^{36}$ erg s^{-1} kpc^{-2} in 0.3-8.0 keV. Assuming 15 kpc for the radius of the exponential disk, the luminosity is calculated as $2.0{\times}10^{39}$ erg s^{-1} in 0.3-8.0 keV. These values are comparable with X-ray luminosity of the other similar galaxies.

The metal abundance of the hot halo could be lower than 1 solar if it originate primordial gas. Thus we evaluated the hot halo properties assuming 0.1 solar abundance (see Appendix B) and calculated total mass and so on.

Assuming spherical X-ray bulge with 1.4 kpc radius and solar abundance, the luminosity is calculated as $6.1{\times}10^{37}$ erg s^{-1} in 0.3-8.0 keV. Here we used the best fit value of the Plasma 1 of the C1 model where the temperature is $10^{6.6}$ K and the emission measure is $12.9{\times}10^{-3}\mathrm{cm}^{-6}\mathrm{pc}$. This value is negligible to the luminosity of the exponential disk. The energy loss rate of the Plasma 2 (T= $10^{6.0}$ K) is order of magnitude less than that of the Plasma 1 and we neglect its contribution here.

7.4 Pressure balance

In section 7.2.1.1, we argued about pressure balance in the disk with other component such as the neutral ISM. Assuming solar abundance, the density in the mid plane is larger than 5.0×10^5 cm^{-3} from Figure 7.1. With the equation 7.1, it is obvious that the pressure of the hot ISM is at least quarter of the maximum pressure of the other component.

As for X-ray bulge, the density and the temperature are $\sim 2.5 \times 10^{-3}$ cm^{-3} and $10^{6.60} = 4 \times 10^6$ K. Almy et al. (2000) assumes polytrope plasma in which thermal pressure and gravitation are balanced. We compare our values with the best fit model of the this polytrope plasma in Almy et al. (2000). We calculated the density and the temperature of the polytrope

Table 7.4: Properties of the hot halo and X-ray bulge.

		Hot Halo (1 solar metallicity)	Hot Halo (0.1 solar metallicity)	X-ray Bulge
Total Mass	($M_\odot$)	1.1×10^8	6.0×10^8	7.5×10^5
X-ray luminosity†	(erg s^{-1})	2.0×10^{39}	1.8×10^{39}	6.1×10^{37}
Bolometoric luminosity‡	(erg s^{-1})	2.3×10^{40}	6.3×10^{40}	9.2×10^{37}
Total energy	(erg)	1.2×10^{56}	1.3×10^{57}	1.6×10^{54}
Cooling time	(year)	2×10^8	7×10^8	6×10^8

† in 0.3-8.0 keV
‡ in 0.001-40 keV

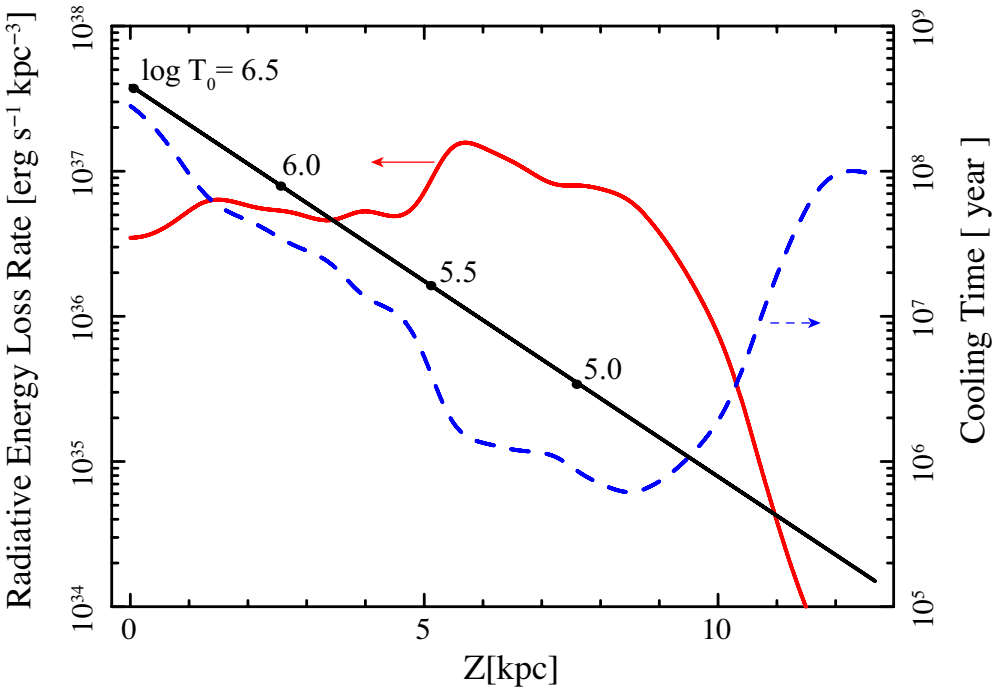

Figure 7.6: Radiative energy loss rate (red, solid) and cooling time (blue, dashed) as a function of the distance from the Galactic plane. The temperature is indicated with black solid line. The emissivity is calculated with *mekal* model and a scripts made by Sutherland. (http://proteus.pha.jhu.edu/∼dks/Code/Coolcurve_create/index.html)

model along the sight line of 4U 1820-303 and found that the density and the temperature between 7.6 kpc and 9.6 kpc from the Sun are distributed as $2.7 - 3.4 \times 10^{-3}$ cm^{-3} and $10^{6.55-6.61}$ K. These values are comparable to our values and this suggest that the pressure of the X-ray bulge balance with the gravitational force of the Galaxy.

7.5 Origin of the Hot ISM

There are three likely possibilities for the origin of the hot ISM; the accretion of the primordial gas from the intergalactic space, ejecta of the super novae and stellar wind in the galaxy. In this section we verify the origin of the hot ISM using physical properties estimated through this thesis.

7.5.1 Possibilities of the origin

First, we briefly summarized the properties of the possibilities.

7.5.1.1 The accretion of the primordial gas

White & Frenk (1991) showed that infall rate of the primordial gas to the galaxy with rotation velocity of 200 km s^{-1} is at most $\sim 1 M_\odot$/year using numerical and analytic methods.

The gravitational potential of the galaxy at the Sun radius can be roughly estimated using rotational velocity of $\sim 200 \mathrm{kms}^{-1}$. The released gravitational energy (E_G) is calculated with virial theorem as

$$E_\mathrm{G} \sim 1.3 \times 10^{40} \left(\frac{M_\mathrm{infall}/\mathrm{year}}{M_\odot} \right) \mathrm{erg\ s}^{-1} \tag{7.13}$$

where M_infall is infall rate of the primordial gas per year. Using this equation we can estimate the energy input rate of infalling primordial gas as 1.3×10^{40} ergs s^{-1}.

Though the metallicity and abundance pattern of the primordial gas is not well understood, explosion of the population III stars could be source of metals. Here we assume that the abundance pattern of the primordial gas resembles ejecta of SN II and its metallicity as 0.1 solar.

7.5.1.2 The SN ejecta

According to Ferriere (1998) SN rate near the sun is 19 and 2.6 Myr^{-1} kpc^{-2} for type II and type Ia respectively. Assuming each SN explosion release 1 $\times 10^{51}$ ergs, the total input energy is then 7 $\times 10^{38}$ ergs s^{-1} kpc^{-2}. Assuming 15 kpc radius for the Milky-Way galaxy, the total energy input rate is calculated as 5×10^{41} ergs s^{-1}.

The metallicity and abundance pattern of the ejecta are mixture of SN Ia and SN II and could be like solar values.

7.5.1.3 Stellar wind

Here we considered only stellar wind of OB type stars ($M > 3M_\odot$) and middle mass stars ($3M_\odot > M > 0.5M_\odot$). Though mass loss from AGB-type stars are very large, from the view point of the energy input, they play unimportant roles for the hot ISM.

We calculated the total number of main sequence stars in Milky-Way galaxy using initial mass function after Salpeter (1955) and Kroupa (2001) and life time of the stars from Hansen & Kawaler (1994). The calculated total number of OB type stars and middle mass stars are 3×10^7 and 1×10^{10}, respectively.

Then we evaluated energy output rate of stellar wind of each type star. The typical value of the stellar wind velocity of OB type stars is 1000 km s^{-1} and the mass loss rate

is $1 \times 10^{-7} M_{\odot}$ year^{-1} star^{-1} (Mokiem et al. (2007)). Then the total energy output rate is calculated as 1×10^{42}erg s^{-1}. The typical value of the stellar wind velocity of middle mass stars is 300 km s^{-1} and the mass loss rate is $2 \times 10^{-12} M_{\odot}$ year^{-1} star^{-1} (Willson (2000)). Then the total energy output rate is calculated as 6×10^{38}erg s^{-1}.

The metallicity and abundance pattern of the stellar wind could be like those of solar values.

7.5.2 Abundance pattern

We examined an abundance pattern for the hot ISM in the form of the number ratio to O as shown in Figure 7.7. Abundance ratio of Ne and Fe are $2.3^{+1.6}_{-0.5}$ and $1.0^{+0.8}_{-0.5}$ solar value. Figure 7.7 indicate that the origin of the metal in the hot ISM is the SN II or mixture of the SN Ia and SN II ejecta like solar neighbourhood.

As for bulge region, it is difficult to constrain the abundance ratio because of the contribution of the stars. Though we confirmed the error range include the solar value, further discussion is difficult.

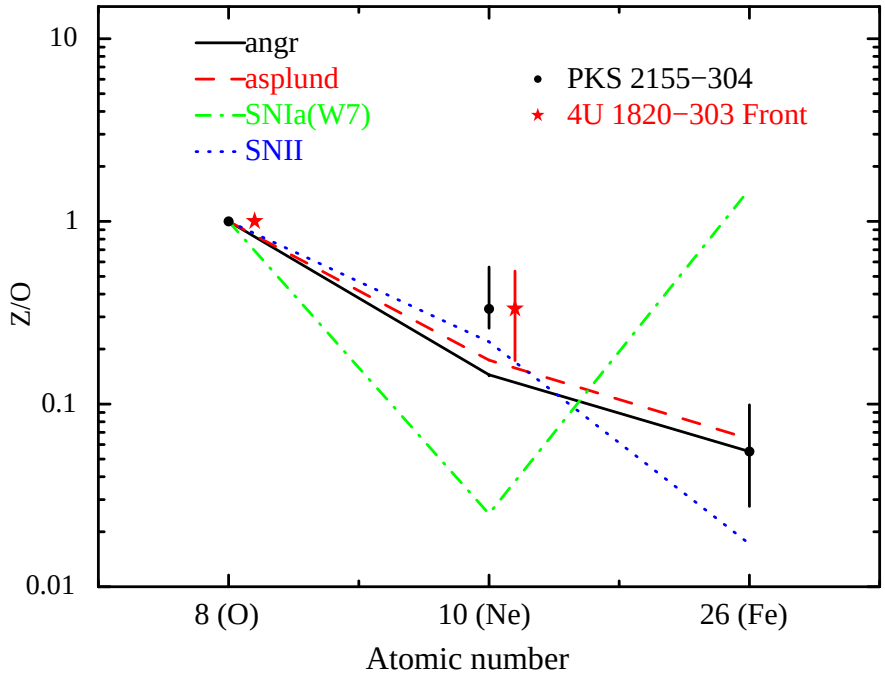

Figure 7.7: Number ratios of Ne and Fe to O for PKS 2155-304 direction and front-side plasma of 4U 1820-303 direction. Solid, dashed, dot-dashed and dotted lines correspond to the number ratios of metals to O for solar abundance by Anders & Grevesse (1989) (=angr) and Asplund et al. (2009) (=asplund), the abundance patterns of SNe Ia yield of Iwamoto et al. (1999) and SNe II yield of Nomoto et al. (2006) respectively.

7.5.3 Cooling time and supply of energy

Then we compared the energy loss rate with the energy input rate. If 5 % of the SN explosion energy is input to the hot halo, or 2 % of the stellar wind energy converted to the hot halo

the total energy loss can be compensated.

If the exponential disk originate primordial gas, its metal abundance is estimated as ~ 0.1. Here we use the values evaluated with 0.1 solar metallicity in Table 7.4. To compensate the total energy loss 500 % of the infalling primordial gas energy is needed thus it is hard to maintain the energy loss only by infall gas.

7.5.4 Possible origin of the hot ISM

We compare the origin of the hot ISM from the view point of abundance pattern and energy loss rate. Though it is difficult to choose one possibility only by the abundance pattern, the energy loss rate support the SN and stellar wind origin.

As for bulge region, the mass loss of the old stars and SN Ia is most likely origin. To clarify this possibility, more observations and detailed analysis is indispensable.

Chapter 8

Conclusion

We have analyzed high resolution X-ray absorption/emission data observed by *Chandra* and *Suzaku* to determine the physical properties of the hot ISM along the high galactic latitude (PKS 2155-304) direction and the galactic bulge (4U 1820-303) direction. By analyzing the emission and absorption data, we have obtained new insights on the hot ISM.

- PKS 2155-304 (high galactic latitude) direction

  1. Suzaku clearly detected O VII and O VIII lines. The surface brightnesses of O VII and O VIII in this direction can be understood in the same scheme as obtained by other 14 observations (Yoshino et al. (2009)).
  2. By the absorption analysis, column density is measured as 3.9 $(+0.6, -0.6)$ cm^{-3} pc and temperature is measured as 1.91 $(+0.09, -0.09)$ $\times 10^6$ K. By the emission analysis, emission measure is measured as 3.0 $(+0.3, -0.3)$ $\times 10^{-3}$ cm^{-6} pc and temperature is measured as 2.14 $(+0.15, -0.14)$ $\times 10^6$ K.
  3. The temperature determined by absorption and emission analysis are not consistent within 90 % statistical error and we tried simple multi-temperature hot ISM model, exponential disk model. In this model the density (n) and temperature (T) of the gas are functions of height from the Galactic plane (Z) and described as $n = n_0 \exp(-Z/h_n)$ and $T = T_0 \exp(-Z/h_T)$, where n_0 and T_0 are the density and temperature at the Galactic plane and h_n and h_T are the scale heights of the gas density and temperature. Combined analysis using the exponential disk model gives a good fit with χ^2/dof of 789.65/756 to both emission and absorption spectra. The n_0 and T_0 are determined to be $1.3(+9.7, -0.7) \times 10^{-3}$ cm^{-3} and $3.2(+0.7, -0.6) \times 10^6$ K and h_n and h_T are $5.1(+3.9, -4.7)$ kpc and $2.2(+13, -2.1)$ kpc respectively.
  4. The results obtained by the combined analysis are consistent with those for the LMC X-3 direction. This suggest that a global view that the hot ISM surrounding our Galaxy has common structure like a thick hot disk or a hot halo.

- 4U 1820-303 (galactic bulge region) direction

  5. The exponential model with the best fit parameters obtained in the high galactic latitude can not explain the emission spectrum in the galactic bulge region. Ad-

ditional plasma of $T = 4.0(+0.4, -0.4) \times 10^6$ K and $T = 1.0(+0.8, -0.5) \times 10^6$ K are needed behind 4U 1820-303.

6. Two single temperature model can reproduce the absorption and emission spectra. One model assumes that all the plasma exist in front of 4U 1820-303 and the determined temperature, column density and length of the plasmas are 3.2(+0.2,-0.2) $\times 10^6$ K, 3.3 (+1.5, -1.3)$\times 10^{19}$ cm^{-2} and 5.9 (+1.7,-3.7) kpc and 1.0 (+0.2,-0.2) $\times 10^6$ K, 1.5 (+1.8, -0.6)$\times 10^{19}$ cm^{-2} and 0.13 (+0.56,-0.11) kpc, respectively. The other model assumes one plasma exist in front of the 4U 1820-303 and another one behind. The temperature, column density and length of the front plasma are determined as 1.7 (+0.2,-0.2) $\times 10^6$ K, 3.4 (+2.1, -1.2)$\times 10^{19}$ cm^{-2} and 3.1 (+4.5,-1.8) kpc. The temperature and emission measure of the behind plasma are determined as 3.9 (+0.4,-0.3) $\times 10^6$ K and 18.9 (+5.1, -4.0) cm^{-6} pc.
7. Comparing with the results at the high galactic latitude, we conclude that high temperature ($\sim 4.0 \times 10^6$ K) component exist behind 4U 1820-303. It is not confirmed that this component is hot ISM or other origins like stars.

- Both directions

8. The metal abundance and energy loss rate of the hot ISM support the SN and the stellar wind origin of the hot ISM.

These insights are firstly revealed by this thesis with the combined analysis to constrain the length and density of the hot ISM quantitatively. We verified the global hot ISM structure and its origin using these quantities.

Appendix A

Emission from Stars

Initially we used TRILEGAL[1] (Girardi et al. (2005)) to estimate the main sequence stellar distribution in the observing cone. In the bulge direction, Vanhollebeke et al. (2009) used this simulator and compare the simulated data with Two Micron All Sky Survey (2MASS, Skrutskie et al. (2006)) and Optical Gravitational Lensing Experiment (OGLE, Udalski et al. (1997)) observational data in 11 directions. They tried several bulge star distribution model. To distinguish bulge stars from disk stars, they divided the color-magnitude diagram (CMD) into regions and excluded low magnitude stars from their analysis. Including interstellar extinction, this threshold is $K_s = 10.7$ for 2MASS and $I = 12.4$ for OGLE data. Assuming the distance to the bulge as 5 kpc, these values correspond the absolute magnitude of $K_{s_0} \sim -3$ and $I_0 \sim -1$ and spectral type of B0V and B5V for main sequence star (in converting magnitude to spectral type of star, we referred Cox & Pilachowski (2000) and use K value instead K_s). Thus there are large uncertainties in the distribution of low luminosity stars. Their best model explain the observational data within 20%, thus we assume 20% error in the simulation of the stellar type, age and spatial distribution with TRILEGAL.

We also have to keep it in mind that there are large uncertainties in the X-ray luminosity and spectrum of the stars and binaries used in the following section.

A.1 Normal isolated stars

In making stellar distribution by this simulator, we assume three components of thin disk and halo with the default value and bulge with best fit value of Vanhollebeke et al. (2009). This simulator output a list of simulated stars in the field of view following the assumed distribution. This list contains many information such as distance, B and V color and luminosity. Then we made the HR diagram from the list (Figure A.2) and classified the stars into O+B, A, F, G, K, M and giant using stellar color and luminosity correlation in Kuntz & Snowden (2001) as shown in the right panel of Figure A.2. The criteria and number of stars in the circle with 20 arcminutes radius, which corresponds to the assumed arf field of view in later *Suzaku* analysis, are given in Table A.1.

Then we assumed the X-ray luminosity and spectrum of each spectral type. Kuntz & Snowden (2001) estimated the log N – log S relation of A, F, G, K, M (early) and M (late) spectral type star grouped into 3 age classes (0-0.15, 0.15-1, 1-10 G year) as shown in

[1] http://stev.oapd.inaf.it/cgi-bin/trilegal_1.4

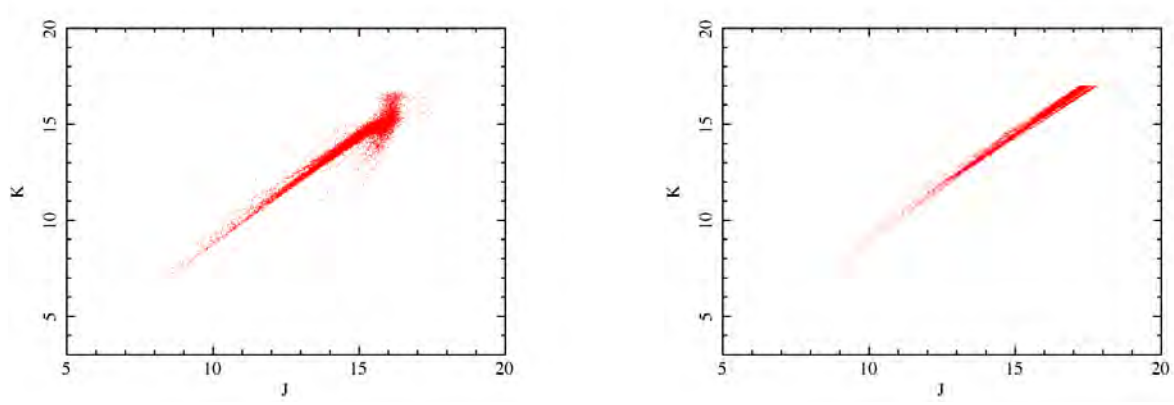

Figure A.1: Comparison with 2MASS catalogue (left): 2MASS, (right) :TRILEGAL. For comparison, we only use data K<17. Number of stars included in the figure, left=15623, right=16489

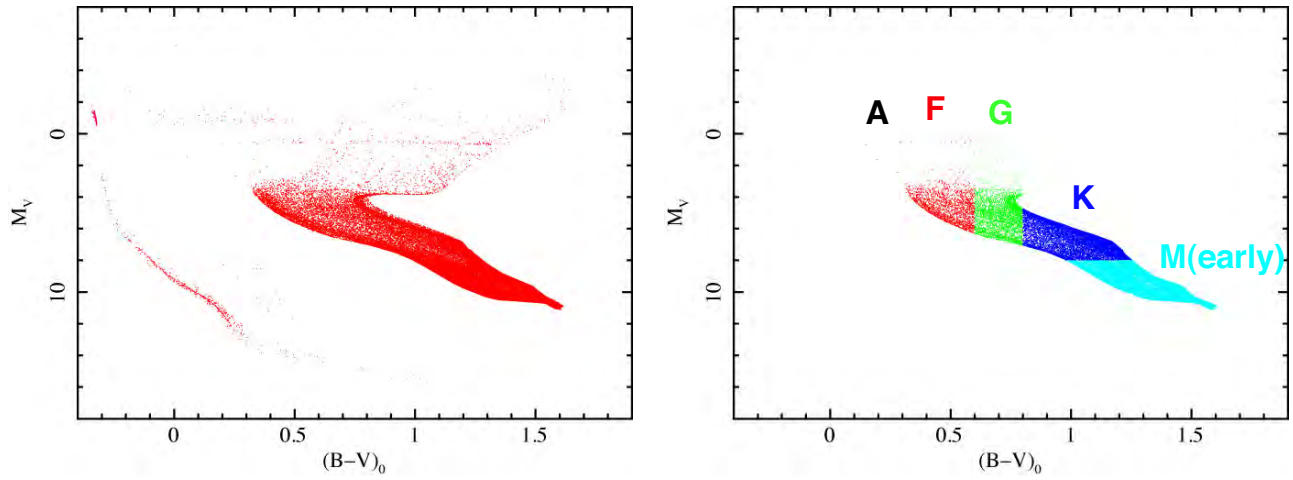

Figure A.2: (left):HR diagram construct by the TRILEGAL list in bulge 3 direction. (right):

Table A.1. We binned number of stars par 1 kpc from the sun until 15 kpc and integrated further stars in the last bin. We also estimated the flux distribution (Figure A.4) by each type as following; 1) when a star exist in a bin, we check its age and spectral type, 2) the luminosity of the star is determined with the luminosity table (Table A.1), 3) calculate the flux of the star observed from us using the distance. In this plot we can clearly see a division line around 4 kpc and it corresponds to the component border between disk and halo + bulge. Here after we call the stars located in front of this border as foreground stars and beyond this border as background stars.

It is known that the emission from stellar corona can be explained with thin thermal plasma model. Using *XMM-Newton* survey data, López-Santiago et al. (2007) fitted an X-ray spectrum models to identified stars and found one or two thin thermal plasma model with depleted abundance can well explain the emission. We use the typical values of coronal

Table A.1: Criteria and number of stars in the field of view for each spectral type and assumed X-ray luminosity from Kuntz & Snowden (2001)

spectral type	$(B-V)_0$	M_V	0-0.15 Gyr		0.15-1 Gyr		1-10 Gyr		>10 Gyr
			Number	log L_X[a]	Number	log L_X[a]	Number	log L_X[a]	Number
O+B	<-0.01	-	8	-	6	-	7	-	0
A	-0.01-0.3	-	6	$29.64^{+0.65}_{-0.60}$	58	$28.84^{+1.11}_{-0.91}$	12	-	90
F	0.3-0.6	2-8	12	$29.51^{+0.12}_{-0.11}$	78	$29.02^{+0.07}_{-0.07}$	35212	$29.06^{+0.47}_{-0.43}$	41152
G	0.6-0.8	2-10	6	$29.91^{+0.51}_{-0.44}$	58	$28.82^{+0.17}_{-0.16}$	97672	$28.13^{+0.43}_{-0.40}$	29270
K	>0.8	<8	41	$29.66^{+0.11}_{-0.11}$	240	$28.52^{+0.15}_{-0.14}$	454739	$27.89^{+0.32}_{-0.29}$	72546
M(early)	>0.8	8-15	133	$29.31^{+0.08}_{-0.08}$	1054	$28.49^{+0.36}_{-0.32}$	1851091	$27.54^{+0.29}_{-0.27}$	407848
M(late)	>0.8	>15	0	29.40	0	28.48	35	$27.50^{+0.56}_{-0.42}$	0
Giant			0	-	4	-	29170	-	1590

[a] Lx is the luminosity in units of erg s$^-$1 in the 0.1-2.4 keV band

Table A.2: Stellar type parameters summarized by Rocks (2009) after López-Santiago et al. (2007).

spectral type	single temperature	two temperature			metal abundance
	(keV)	hotter (kev)	cooler (keV)	EMcool/ EMhot	
F	0.58	N/A	N/A	N/A	0.5
G	0.67	N/A	N/A	N/A	0.3
K	0.83	1.17	0.32	1.97	0.2
M	0.90	0.80	0.27	2.02	0.1

temperature given in Table A.2 to describe the star spectrum. In López-Santiago et al. (2007) results, roughly half of K and M stars have two temperature coronas and in this model we assume just half of the K and M stars have one temperature corona and the other have two.

A.2 Giant stars

Recent observations revealed that the not only giants in AGB phase but several M giants is bright in X-ray. However, we think these rare M giants are only exceptional, because though there are a large number of giants potentially, X-ray bright giants are reported only few numbers. Thus we neglect the contribution of giants in further analysis.

A.3 RS CVn-type binaries

Though each star is not bright, once they construct a binary system it become a bright X-ray source. The most common and dominant binary systems are RS CVn-type systems

Table A.3: Binary star parameters and distribution

hotter temperature (keV)	cooler temperature (keV)	EMcool/ EMhot	0.4-4 keV $\log(L_X)$ erg s^{-1}	number of binaries in the FOV (circle with 20' radius)
2.586	0.172	0.22	30.75	980

that typically contain a G- or K-type giant or sub-giant with a late-type sub-giant or main sequence companion. RS CVn-type binary contribute dominantly in X-ray, rather than other type of binary, and we only think the contribution of this type. We used the model discussed by Ottmann & Schmitt (1992) for the distribution of RS CVn binaries,

$$n(r,z) = n_0 e^{-\frac{Z}{H}} e^{-\frac{(r-r_0)}{h}} \tag{A.1}$$

where r_0 is the distance of the Sun from the Galactic center (8.5 kpc), H is a vertical scale factor equal to 325 pc, h is a horizontal scale factor equal to 3500 pc, and n_0 is the local density of binaries. Here we use 6×10^{-5} pc^{-3} for the n_0. For the binaries, we used RS CVn binary spectral parameters reported in Ottmann & Schmitt (1992): two temperature components, one with of 2×10^6 K and the other at 3×10^7 K and solar metal abundances. We created the distribution plot for RS CVn binaries and they are also shown in Figure A.3 and Figure A.4.

A.4 LMXBs

Low mass X-ray binaries are very bright source and it is reported by observation of the bulge of M 31 (Irwin & Bregman (1999))that significant fraction of the X-ray emission would be originate them. However its number density is very low (only ~ 80 LMXBs are detected in M 31) to exist in the FOV accidentally. Moreover its luminosity is very high ($logL_x > 33$) and we could detect it as point source if one exist in the FOV. Thus we do not consider contribution of LMXB further.

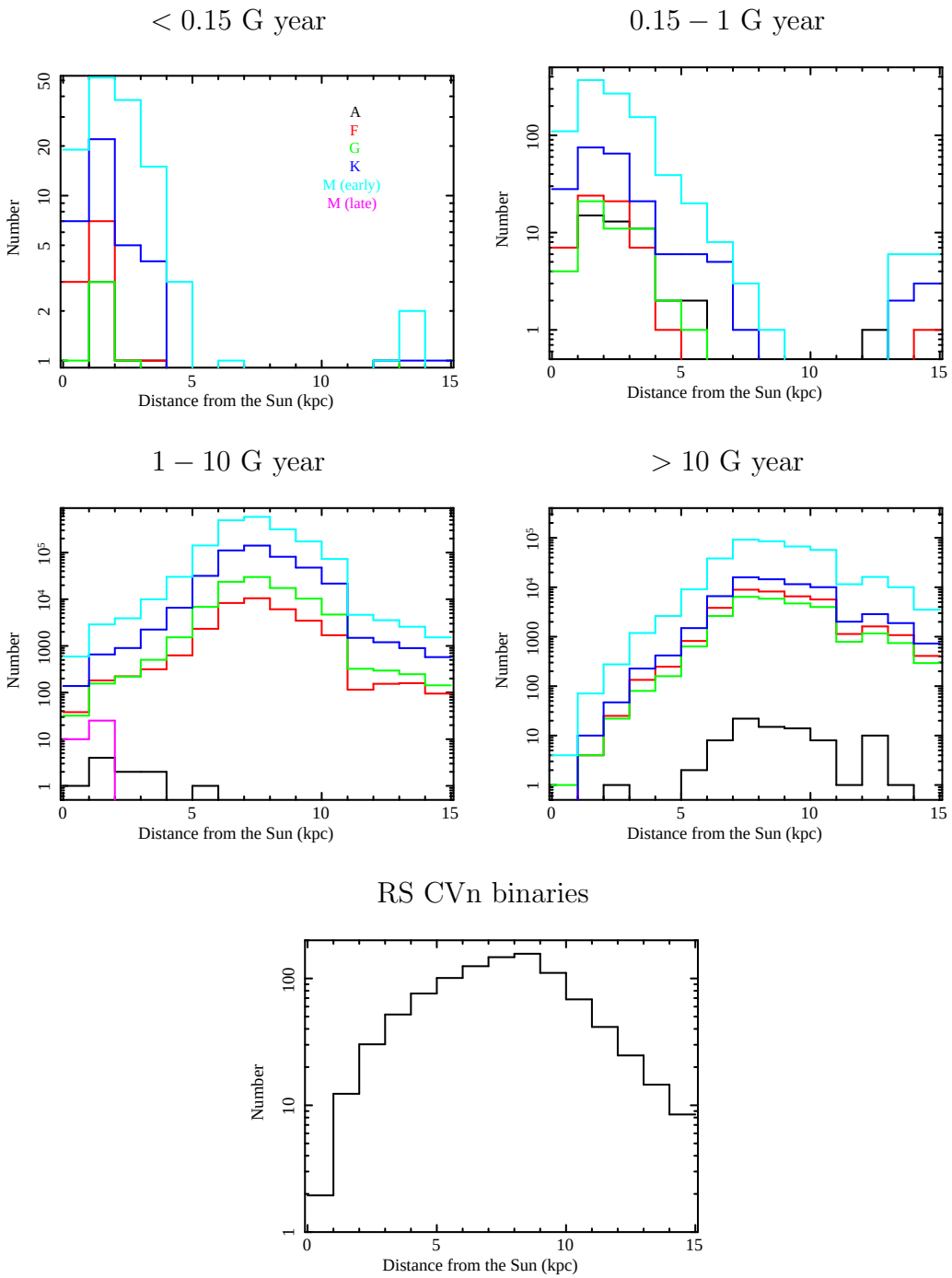

Figure A.3: Number of stars in each distance bin. The binning is every 1 kpc from the sun until 15 kpc and further are binned in the last one. The age class of each plot is shown in above the panel.

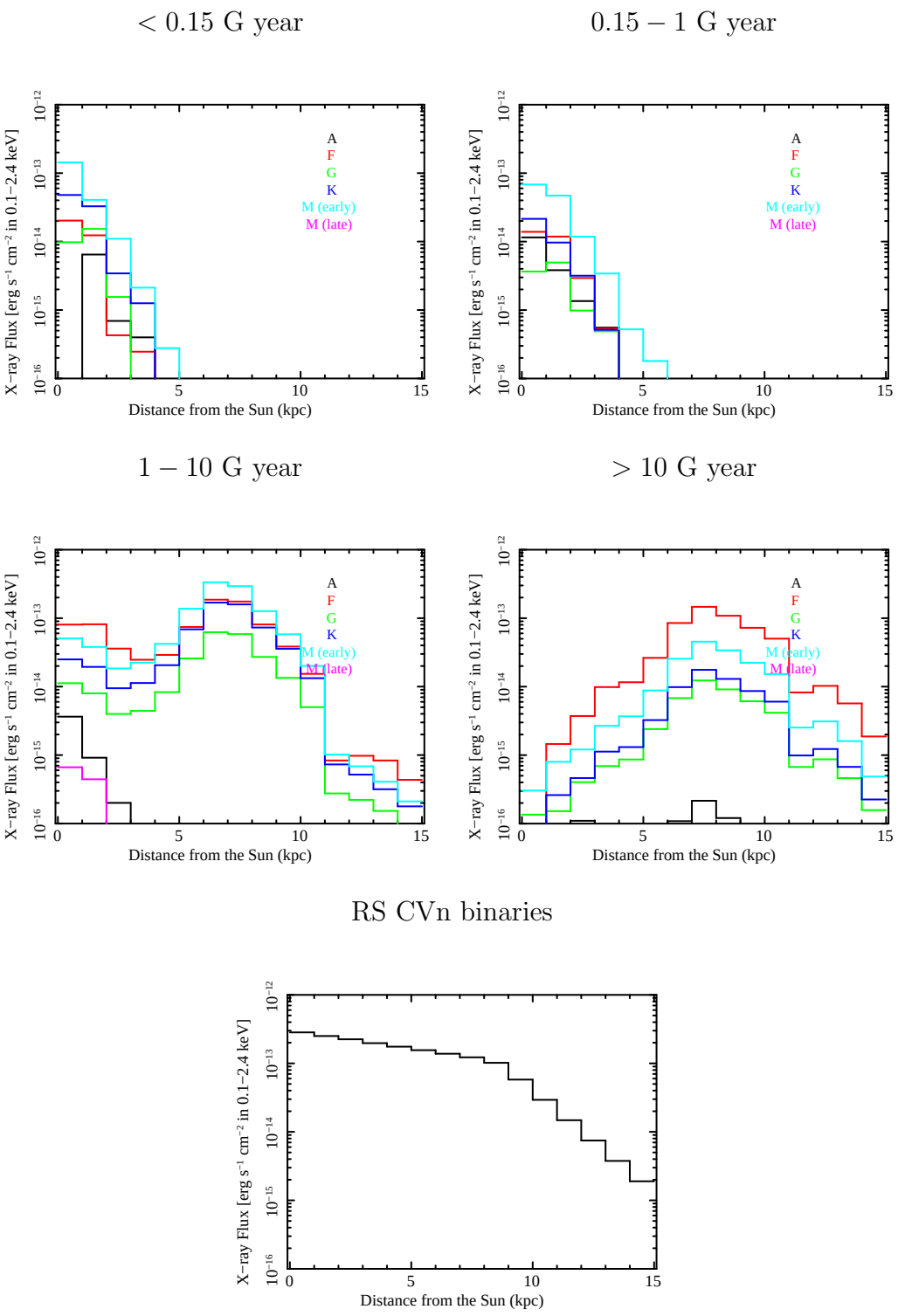

Figure A.4: X-ray flux from each distance bin. The binning is every 1 kpc from the sun until 15 kpc and further are binned in the last one. The age class of each plot is shown in above the panel.

Table A.4: Flux contribution of stars in the Galactic bulge direction

Spectral Type	X-ray Flux (10^{-13} erg s^{-1} in 0.1-2.4 keV)	
	$<$ 4kpc	4kpc $<$
A	0.30	$<$ 0.01
F	3.00	11.4
G	0.64	2.29
K	1.87	6.06
M (early)	4.62	11.8
M (late)	0.01	$<$ 0.01
RS CVn Binary[b]	9.56	8.11

[b] in 0.4-4.0 keV band

Appendix B

Exponential Disk Model with Low Metal Abundance

It is hard to restrict the metal abundance of the hot ISM only by fitting, because the temperature of hot ISM is not so high and continuum emission induced from bremsstrahlung is not well determined. Thus we can not constrain the number of hydrogen and the ratio of hydrogen to metals is not restricted.

To evaluate the effect of metal abundance uncertainty, we performed combined analysis fixing the metallicity of the hot ISM model to 0.1 solar. 0.1 solar is reasonable for primordial gas and if hot ISM originate such gas, its metallicity would be the value. The fitting results are shown in Table B.1.

Table B.1: Combined spectral fitting results with the exponential disk model with low metal abundance (O/H=0.1 solar)

Model	Data	CXB	hot ISM							χ^2/dof
		Norm[a]	$\log N_{\rm H_{Hot}}$ ($\rm cm^{-2}$)	h_n (kpc)	$\log T_0$ (K)	v_b* ($\rm km\ s^{-1}$)	γ	N/O	Ne/O	Fe/O	
C2	Emission:Sz1	$8.10^{+0.37}_{-0.35}$	$20.11^{+0.07}_{-0.07}$	$27.96^{+10.21}_{-5.11}$	$6.40^{+0.06}_{-0.05}$	...	$3.32^{+1.70}_{-1.52}$	$1.0^{+1.0}_{-0.0}$	$3.0^{+1.4}_{-0.9}$	$1.5^{+0.9}_{-0.4}$	
	Emission:Sz2	$6.29^{+0.37}_{-0.34}$	↑	↑	↑	...	↑	↑	↑	↑	
	Absorption	...	↑	...	↑	288^{+141}_{-164}	↑	...	...	...	774.01/756

↑ indicates linked parameters
model C2: *wabs(power-law+vabmekal)+mekal* fot the emission, *wabs(power)*×*(absem)*[3] for the absorption
Note: for models representing hot ISM, O/H is set to 0.1 solar value.
*Parameter range is limited to 70-440 $\rm km\ s^{-1}$
[a]in unit of photons $\rm cm^{-2}\ s^{-1}\ str^{-1}\ eV^{-1}$ @1keV

Appendix C

Systematic Errors of Fit (High Galactic Latitude)

C.1 Contamination on the optical blocking filter of *Suzaku* XIS

Table C.2 shows the results of spectral fits with in the case that the contaminants thickness on the optical blocking filter of *Suzaku* XIS is 10% thicker than nominal value used in the fit of Chapter 5. The contaminant is assumed to be DEHP $(C_{24}H_{38})_4$ which corresponds to the abundance ratio of C/H=1740 and O/H=124 to the solar values. The thickness of the contaminant in the observation is shown in Table C.1

Obtained parameters are all within the statistical error in the case of nominal contaminants thickness.

Table C.1: Thickness of the contaminant in each observation.

Observation	Thickness (10^{18} cm^{-2})	
	C	O
PKS 2155-304	4.6	0.76

Table C.2: Spectral fitting results for emission data with the model E1

Model	Data	CXB	LHB+SWCX		hot ISM					χ^2/dof
		Norm [a]	$\log T$ (K)	Norm[b]	$\log T$ (K)	Norm[b]	N/O	Ne/O	Fe/O	
E1	Sz1 (+10%)	$8.46^{+0.37}_{-0.43}$	6.06(fixed)	4.3(fixed)	$6.25^{+0.04}_{-0.04}$	$3.9^{+1.1}_{-0.9}$	$6.0^{+2.4}_{-1.1}$	$6.2^{+3.5}_{-2.3}$	$7.6^{+15.4}_{-3.4}$	150.06/136
E1	Sz1	$8.40^{+0.38}_{-0.40}$	6.06(fixed)	4.3(fixed)	$6.26^{+0.06}_{-0.04}$	$3.3^{+1.0}_{-0.8}$	$6.0^{+2.5}_{-1.9}$	$6.5^{+3.7}_{-2.5}$	$7.4^{+13.8}_{-4.8}$	148.61/136
E1	Sz1 (−10%)	$8.33^{+0.40}_{-0.38}$	6.06(fixed)	4.3(fixed)	$6.26^{+0.08}_{-0.05}$	$2.8^{+0.9}_{-0.8}$	$6.0^{+3.0}_{-2.0}$	$6.8^{+4.0}_{-2.7}$	$7.2^{+12.4}_{-5.2}$	147.27/136
E1	Sz2 (+10%)	$6.42^{+0.43}_{-0.37}$	6.06(fixed)	4.3(fixed)	$6.35^{+0.03}_{-0.03}$	$3.7^{+0.5}_{-0.5}$	$4.9^{+1.9}_{-1.5}$	$2.3^{+1.1}_{-0.9}$	$1.0^{+0.8}_{-0.5}$	150.43/141
E1	Sz2	$6.45^{+0.36}_{-0.43}$	6.06(fixed)	4.3(fixed)	$6.35^{+0.03}_{-0.03}$	$3.2^{+0.5}_{-0.4}$	$4.7^{+2.0}_{-1.6}$	$2.4^{+1.2}_{-0.9}$	$1.0^{+0.8}_{-0.5}$	147.33/141
E1	Sz2 (−10%)	$6.37^{+0.42}_{-0.37}$	6.06(fixed)	4.3(fixed)	$6.36^{+0.03}_{-0.03}$	$2.9^{+0.4}_{-0.4}$	$4.5^{+2.1}_{-1.6}$	$2.5^{+1.3}_{-1.0}$	$1.0^{+0.8}_{-0.5}$	144.23/141
E1	Sz1+Sz2(Sz1) (+10%)	$8.35^{+0.36}_{-0.39}$	6.06(fixed)	4.3(fixed)	$6.33^{+0.02}_{-0.02}$	$3.4^{+0.4}_{-0.3}$	$5.9^{+1.5}_{-1.3}$	$3.2^{+1.1}_{-0.9}$	$1.8^{+1.2}_{-0.7}$	312.43/282
	Sz1+Sz2(Sz2) (+10%)	$6.53^{+0.35}_{-0.40}$	↑	↑	↑	↑	↑	↑	↑	
E1	Sz1+Sz2(Sz1)	$8.30^{+0.35}_{-0.39}$	6.06(fixed)	4.3(fixed)	$6.33^{+0.02}_{-0.02}$	$3.0^{+0.3}_{-0.3}$	$5.8^{+1.6}_{-1.3}$	$3.3^{+1.2}_{-0.9}$	$1.7^{+1.2}_{-0.7}$	306.82/282
	Sz1+Sz2(Sz2)	$6.50^{+0.36}_{-0.39}$	↑	↑	↑	↑	↑	↑	↑	
E1	Sz1+Sz2(Sz1) (−10%)	$8.24^{+0.36}_{-0.38}$	6.06(fixed)	4.3(fixed)	$6.34^{+0.03}_{-0.02}$	$2.6^{+0.3}_{-0.3}$	$5.7^{+1.7}_{-1.4}$	$3.4^{+1.3}_{-1.0}$	$1.7^{+1.2}_{-0.6}$	301.49/282
	Sz1+Sz2(Sz2) (−10%)	$6.47^{+0.36}_{-0.38}$	↑	↑	↑	↑	↑	↑	↑	

↑ indicates linked parameters

Sz1+Sz2: simultaneous fitting of the data Sz1 and Sz2

Model E1:$wabs(power\text{-}law_{CXB} + vmekal_{hotISM}) + mekal_{LHB+SWCX}$

Emission measure of $mekal_{\ LHB+SWCX}$ is fixed to 0.0043cm^{-6} which corresponds to 2.0 LU of O VII K_α emission

[a] in unit of photons cm^{-2} s^{-1}str^{-1} eV^{-1} @1keV

[b] Emission measure $10^{-3}\int n_e n_p dl$: in unit of cm^{-6} pc

C.2 Consistency check with ACIS+LETG data

To estimate systematic error caused by co-adding of the spectra obtained with different detectors, we re-analyze the absorption data only with ACIS+LETG and perform combined analysis with the data. The results are shown in Table C.3 and Table C.4 which correspond Table 5.1 and Table 5.2 in section 5.1 respectively.

Obtained parameters are all within the statistical error.

Table C.3: Spectral fitting results of absorption data with model A1

Model	Equivalent Width (eV)		
	O VII K_α	O VII K_α	O VII K_β
A1	$0.354^{+0.076}_{-0.072}$	$0.343^{+0.136}_{-0.110}$	$0.148^{+0.063}_{-0.062}$
A1 (ACIS+LETG)	$0.442^{+0.136}_{-0.124}$	$0.291^{+0.125}_{-0.059}$	$0.215^{+0.092}_{-0.092}$

Model A1:*wabs*(*power-law*)+3×*Gaussian*

Table C.4: Spectral fitting results of absorption data with model A2-A4

Model	v_b (km s^{-1})	log [Column Density] (cm^{-2})			log T (K)	χ^2/dof
		$N_{\rm O\ VII}$	$N_{\rm O\ VIII}$	$N_{\rm H_{Hot}}$		
A2	294^{+149}_{-220}	$15.76^{+0.07}_{-0.08}$	$15.56^{+0.09}_{-0.12}$	···	···	489.82/474
A3	375^{+124}_{-158}	$15.77^{+0.08}_{-0.07}$	···	···	$6.27^{+0.02}_{-0.03}$	498.01/474
A4	290^{+152}_{-220}	···	···	$19.08^{+0.06}_{-0.07}$	$6.28^{+0.02}_{-0.02}$	489.84/474
A2 (ACIS+LETG)	380^{+120}_{-360}	$15.78^{+0.11}_{-0.13}$	$15.51^{+0.15}_{-0.20}$	···	···	464.69/474
A3 (ACIS+LETG)	374^{+126}_{-354}	$15.78^{+0.11}_{-0.12}$	···	···	$6.27^{+0.04}_{-0.04}$	464.59/474
A4 (ACIS+LETG)	414^{+86}_{-394}	···	···	$19.08^{+0.08}_{-0.11}$	$6.26^{+0.04}_{-0.04}$	465.60/474

Model A2,A3,A4:*wabs*(*power-law*)×*absem*×*absem*×*absem*

Appendix D

Systematic Errors of Fit (Galactic Bulge Region)

D.1 Contamination on the optical blocking filter of *Suzaku* XIS

As is in Chapter C.1, Table D.2 and Table D.3 shows the results of spectral fits with in the case that the contaminants thickness is 10% thicker and thinner than nominal value used in the fit of Chapter 6. The thickness of the contaminant in the observation is shown in Table D.1

Obtained parameters are all within the statistical error in the case of nominal contaminants thickness.

Table D.1: Thickness of the contaminant in each observation.

Observation	Thickness (10^{18} cm^{-2})	
	C	O
Bulge 3	2.8	0.46

Table D.2: Fitting results with model E2 with varied contamination thickness (corresponding is Table 6.10)

Model	Foreground†	hot ISM				Background†				χ^2/dof
		cooler		hotter		Stars		Binaries	CXB	
		log T [keV]	Norm[a]	log T [keV]	Norm[a]	Class[b]	Ratio[c]	Ratio[c]		
E2-mb (+10%)	fixed	$5.999^{+0.044}_{-0.075}$	$253.7^{+264.7}_{-118.4}$	$6.537^{+0.030}_{-0.027}$	$23.1^{+3.4}_{-3.4}$	M	$6.58^{+1.69}_{-0.84}$	$5.02^{+1.53}_{-1.57}$	fixed	144.33/131
E2-mb	fixed	$6.012^{+0.065}_{-0.083}$	$195.3^{+288.8}_{-87.5}$	$6.542^{+0.036}_{-0.030}$	$21.5^{+3.0}_{-3.1}$	M	$6.57^{+1.17}_{-2.14}$	$5.45^{+1.27}_{-2.20}$	fixed	144.37/131
E2-mb (−10%)	fixed	$6.018^{+0.049}_{-0.080}$	$165.8^{+150.9}_{-79.9}$	$6.545^{+0.030}_{-0.030}$	$20.3^{+2.7}_{-2.9}$	M	$6.55^{+1.70}_{-1.54}$	$4.84^{+1.63}_{-1.35}$	fixed	142.74/131

† All parameters are fixed to referred or simulation based value without mentioned

‡ One hot ISM model.

[a] Emission Measure $10^{-3} \int n_e n_p dl$: in unit of cm^{-6} pc

[b] Spectral type of the stars whose normalization is set to be free

[c] Ratio of the normalization of stars of binaries to the simulation based value

Table D.3: Fitting results of model E3 with varied contamination thickness (corresponding is Table 6.11)

Model	Foreground†	hot ISM				Additional background			Background†	χ^2/dof
		cooler		hotter					CXB	
		log T (K)	Norm[a]	log T (K)	Norm[a]	log T (K)	Norm[a]	Abundance		
E3-A'(+10%)	fixed	$6.012^{+0.049}_{-0.077}$	$225.4^{+290.8}_{-92.8}$	$6.547^{+0.025}_{-0.022}$	$27.2^{+2.7}_{-2.7}$	$7.249^{+0.085}_{-0.087}$	$38.1^{+5.3}_{-5.3}$	0.1 (fixed)	fixed	133.88/131
E3-A'	fixed	$6.017^{+0.061}_{-0.073}$	$193.7^{+224.9}_{-87.5}$	$6.548^{+0.026}_{-0.022}$	$25.9^{+2.7}_{-2.6}$	$7.239^{+0.096}_{-0.077}$	$38.5^{+4.8}_{-5.8}$	0.1 (fixed)	fixed	133.34/131
E3-A'(−10%)	fixed	$6.024^{+0.074}_{-0.065}$	$163.9^{+154.9}_{-79.7}$	$6.552^{+0.025}_{-0.024}$	$24.7^{+2.5}_{-2.5}$	$7.250^{+0.085}_{-0.087}$	$37.9^{+5.2}_{-5.2}$	0.1 (fixed)	fixed	132.72/131

Note: All the parameters not written the Table is fixed to the simulation based values.

† One hot ISM model.

[a] Emission Measure $10^{-3} \int n_e n_p dl$: in unit of cm^{-6} pc

D.2 Model dependant systematic errors

D.2.1 The Star component

D.2.1.1 The foreground stars

There are 20% uncertainties in the foreground star distribution from Girardi et al. (2005). To estimate the effect of uncertainty we varied the normalization of foreground stars ± 20%. The results are shown in Table D.4 and D.5.

D.2.1.2 The background stars

The number distribution of the background stars, especially low luminosity stars, strongly depend initial mass function (IMF), because this simulation only use bright stars for calibration and the low luminosity stars are deduced from IMF. We simulated using several type of IMF and found number distribution can vary $\sim 50\%$ at most.

This systematic error is dominant for the background stars and to estimate the effect of uncertainty we varied the normalization of background stars ± 50%. The results are shown in Table D.6 and Table D.7.

D.2.2 The CXB component

We adopted 10 photons s^{-1} cm^{-2} str^{-1} at 1keV for the normalization of the CXB component in Chapter 6. This value is nominal for the CXB, however it can vary 30% by the direction with *Suzaku* FOV.

In this analysis, it is difficult to decide the CXB normalization only by the fitting because the high temperature thermal components are coupled with the CXB. Thus, to estimate the effect of the uncertainty we varied the normalization ± 30%. The results are shown in Table D.8 and Table D.9.

D.2.3 The LHB+SWCX component

As mentioned in Section 5.4, there are uncertainties in the LHB+SWCX contribution. To check how much our results are affected by these uncertainties, we varied the normalization of the LHB+SWCX component using the same upper and lower limit adopted in Section 5.4. Table D.10 and Table D.11 show the results.

D.2.4 The Loop I component

The geometry of the Loop I is not well understood and this cause uncertainties. In this thesis, we adopted 300 pc for the length of the line sight in the Loop I, however this value can be changed.

To estimate the uncertainties, we varied the length of the line sight ±50% and fitted the spectra with the other components unchanged. The results are shown in Table D.12 and Table D.13.

Table D.4: Fitting results with model E2 with varied foreground star normalization.

Model	Foreground†	hot ISM				Background†				χ^2/dof
		cooler		hotter		Stars		Binaries	CXB	
		log T [keV]	Norm[a]	log T [keV]	Norm[a]	Class[b]	Ratio[c]	Ratio[c]		
E2-mb (foreground star +20%)	fixed	$6.013^{+0.053}_{-0.074}$	$189.4^{+210.7}_{-77.7}$	$6.541^{+0.032}_{-0.029}$	$21.2^{+2.9}_{-2.9}$	M	$6.35^{+1.47}_{-1.81}$	$5.04^{+1.31}_{-1.77}$	fixed	143.82/131
E2-mb	fixed	$6.012^{+0.065}_{-0.083}$	$195.3^{+288.8}_{-87.5}$	$6.542^{+0.036}_{-0.030}$	$21.5^{+3.0}_{-3.1}$	M	$6.57^{+1.17}_{-2.14}$	$5.45^{+1.27}_{-2.20}$	fixed	144.37/131
E2-mb (foreground star −20%)	fixed	$6.011^{+0.040}_{-0.079}$	$201.2^{+207.5}_{-83.0}$	$6.543^{+0.029}_{-0.028}$	$21.8^{+2.7}_{-2.9}$	M	$6.79^{+1.63}_{-1.47}$	$5.15^{+1.49}_{-1.46}$	fixed	143.10/131

† All parameters are fixed to referred or simulation based value without mentioned
[a] Emission Measure $10^{-3} \int n_e n_p dl$: in unit of cm^{-6} pc
[b] Spectral type of the stars whose normalization is set to be free
[c] Ratio of the normalization of stars of binaries to the simulation based value

Table D.5: Fitting results of model E3 with varied foreground star normalization.

Model	Foreground†	hot ISM				Additional background			Background†	χ^2/dof
		cooler		hotter					CXB	
		log T (K)	Norm[a]	log T (K)	Norm[a]	log T (K)	Norm[a]	Abundance		
E3-A' (foreground star +20%)	fixed	$6.018^{+0.063}_{-0.073}$	$188.3^{+215.1}_{-86.9}$	$6.549^{+0.026}_{-0.023}$	$25.4^{+2.6}_{-2.6}$	$7.254^{+0.091}_{-0.089}$	$36.4^{+5.2}_{-5.4}$	0.1 (fixed)	fixed	133.41/131
E3-A'	fixed	$6.017^{+0.061}_{-0.073}$	$193.7^{+224.9}_{-87.5}$	$6.548^{+0.026}_{-0.022}$	$25.9^{+2.7}_{-2.6}$	$7.239^{+0.096}_{-0.077}$	$38.5^{+4.8}_{-5.8}$	0.1 (fixed)	fixed	133.34/131
E3-A' (foreground star −20%)	fixed	$6.018^{+0.070}_{-0.078}$	$197.0^{+263.8}_{-98.0}$	$6.550^{+0.025}_{-0.023}$	$26.4^{+2.6}_{-2.6}$	$7.246^{+0.078}_{-0.085}$	$39.7^{+5.2}_{-5.2}$	0.1 (fixed)	fixed	133.18/131

† All parameters are fixed to referred or simulation based value without mentioned
[a] Emission Measure $10^{-3} \int n_e n_p dl$: in unit of cm^{-6} pc

Table D.6: Fitting results with model E2 with varied background star normalization.

Model	Foreground†	hot ISM				Background†				χ^2/dof
		cooler		hotter			Stars	Binaries	CXB	
		log T [keV]	Norm[a]	log T [keV]	Norm[a]	Class[b]	Ratio[c]	Ratio[c]		
E2-mb	fixed	$6.011^{+0.040}_{-0.079}$	$198.0^{+221.2}_{-81.0}$	$6.534^{+0.030}_{-0.029}$	$21.0^{+2.7}_{-2.8}$	M	$5.86^{+1.62}_{-1.51}$	$5.13^{+1.46}_{-1.49}$	fixed	145.09/131
(background star +50%)							$(3.91^{+1.08}_{-1.01}$	$3.42^{+0.97}_{-0.99})^{\star}$		
E2-mb	fixed	$6.012^{+0.065}_{-0.083}$	$195.3^{+288.8}_{-87.5}$	$6.542^{+0.036}_{-0.030}$	$21.5^{+3.0}_{-3.1}$	M	$6.57^{+1.17}_{-2.14}$	$5.45^{+1.27}_{-2.20}$	fixed	144.37/131
E2-mb	fixed	$6.013^{+0.046}_{-0.078}$	$192.0^{+185.5}_{-82.2}$	$6.550^{+0.029}_{-0.027}$	$21.9^{+2.4}_{-2.8}$	M	$7.28^{+1.58}_{-1.49}$	$4.89^{+1.45}_{-1.50}$	fixed	141.76/131
(background star −50%)							$(14.56^{+3.16}_{-2.98}$	$9.77^{+2.90}_{-3.00})^{\star}$		

† All parameters are fixed to referred or simulation based value without mentioned

$\star$ Calculated with varied normalization of stars

[a] Emission Measure $10^{-3} \int n_e n_p dl$: in unit of cm^{-6} pc

[b] Spectral type of the stars whose normalization is set to be free

[c] Ratio of the normalization of stars of binaries to the simulation based value

Table D.7: Fitting results of model E3 with varied background star normalization.

Model	Foreground[†]	hot ISM				Additional background			Background[†]	χ^2/dof
		cooler		hotter					CXB	
		log T (K)	Norm[a]	log T (K)	Norm[a]	log T (K)	Norm[a]	Abundance		
E3-A' (background star +50%)	fixed	$6.016^{+0.057}_{-0.075}$	$196.2^{+237.1}_{-86.8}$	$6.541^{+0.026}_{-0.024}$	$24.5^{+2.6}_{-2.6}$	$7.272^{+0.112}_{-0.088}$	$31.6^{+5.2}_{-5.5}$	0.1 (fixed)	fixed	133.24/131
E3-A'	fixed	$6.017^{+0.061}_{-0.073}$	$193.7^{+224.9}_{-87.5}$	$6.548^{+0.026}_{-0.022}$	$25.9^{+2.7}_{-2.6}$	$7.239^{+0.096}_{-0.077}$	$38.5^{+4.8}_{-5.8}$	0.1 (fixed)	fixed	133.34/131
E3-A' (background star −50%)	fixed	$6.019^{+0.061}_{-0.069}$	$190.9^{+201.9}_{-86.1}$	$6.556^{+0.024}_{-0.022}$	$27.3^{+2.6}_{-2.6}$	$7.233^{+0.061}_{-0.088}$	$44.5^{+7.6}_{-5.2}$	0.1 (fixed)	fixed	134.42/131

[†] All parameters are fixed to referred or simulation based value without mentioned

[a] Emission Measure $10^{-3} \int n_e n_p dl$: in unit of cm^{-6} pc

Table D.8: Fitting results with model E2 with varied CXB normalization.

Model	Foreground†	hot ISM				Background†				χ^2/dof
		cooler		hotter		Stars		Binaries	CXB	
		log T [keV]	Norm[a]	log T [keV]	Norm[a]	Class[b]	Ratio[c]	Ratio[c]		
E2-mb (CXB +30%)	fixed	$6.016^{+0.055}_{-0.075}$	$190.0^{+175.7}_{-83.2}$	$6.540^{+0.030}_{-0.028}$	$21.3^{+2.4}_{-2.9}$	M	$7.19^{+1.23}_{-1.49}$	$2.72^{+1.44}_{-1.52}$	fixed	141.52/131
E2-mb	fixed	$6.012^{+0.065}_{-0.083}$	$195.3^{+288.8}_{-87.5}$	$6.542^{+0.036}_{-0.030}$	$21.5^{+3.0}_{-3.1}$	M	$6.57^{+1.17}_{-2.14}$	$5.45^{+1.27}_{-2.20}$	fixed	144.37/131
E2-mb (CXB −30%)	fixed	$6.008^{+0.051}_{-0.086}$	$200.8^{+325.6}_{-87.2}$	$6.544^{+0.033}_{-0.029}$	$21.6^{+3.0}_{-3.0}$	M	$5.95^{+1.78}_{-2.05}$	$7.67^{+1.27}_{-2.02}$	fixed	152.47/131

† All parameters are fixed to referred or simulation based value without mentioned

[a] Emission Measure $10^{-3} \int n_e n_p dl$: in unit of cm^{-6} pc

[b] Spectral type of the stars whose normalization is set to be free

[c] Ratio of the normalization of stars of binaries to the simulation based value

Table D.9: Fitting results of model E3 with varied CXB normalization.

Model	Foreground†	hot ISM				Additional background			Background†	χ^2/dof
		cooler		hotter					CXB	
		log T (K)	Norm[a]	log T (K)	Norm[a]	log T (K)	Norm[a]	Abundance		
E3-A'(CXB +30%)	fixed	$6.016^{+0.057}_{-0.074}$	$196.7^{+232.6}_{-86.8}$	$6.544^{+0.025}_{-0.023}$	$25.7^{+2.6}_{-2.6}$	$7.149^{+0.070}_{-0.085}$	$33.8^{+5.2}_{-5.2}$	0.1 (fixed)	fixed	137.29/131
E3-A'	fixed	$6.017^{+0.061}_{-0.073}$	$193.7^{+224.9}_{-87.5}$	$6.548^{+0.026}_{-0.022}$	$25.9^{+2.7}_{-2.6}$	$7.239^{+0.096}_{-0.077}$	$38.5^{+4.8}_{-5.8}$	0.1 (fixed)	fixed	133.34/131
E3-A'(CXB −30%)	fixed	$6.018^{+0.061}_{-0.070}$	$192.4^{+208.9}_{-86.4}$	$6.553^{+0.025}_{-0.023}$	$25.9^{+2.6}_{-2.6}$	$7.345^{+0.085}_{-0.085}$	$41.7^{+6.1}_{-5.5}$	0.1 (fixed)	fixed	130.89/131

† All parameters are fixed to referred or simulation based value without mentioned

[a] Emission Measure $10^{-3} \int n_e n_p dl$: in unit of cm^{-6} pc

Table D.10: Fitting results with model E2 with varied LHB+SWCX normalization.

Model	Foreground†	hot ISM				Background†				χ^2/dof
		cooler		hotter		Stars		Binaries	CXB	
		log T [keV]	Norm[a]	log T [keV]	Norm[a]	Class[b]	Ratio[c]	Ratio[c]		
E2-mb (LHB+SWCX +75%)	fixed	$6.014^{+0.052}_{-0.089}$	$170.3^{+202.7}_{-87.4}$	$6.542^{+0.029}_{-0.029}$	$21.5^{+2.8}_{-2.9}$	M	$6.58^{+1.74}_{-1.54}$	$4.82^{+1.67}_{-1.34}$	fixed	143.64/131
E2-mb	fixed	$6.012^{+0.065}_{-0.083}$	$195.3^{+288.8}_{-87.5}$	$6.542^{+0.036}_{-0.030}$	$21.5^{+3.0}_{-3.1}$	M	$6.57^{+1.17}_{-2.14}$	$5.45^{+1.27}_{-2.20}$	fixed	144.37/131
E2-mb (LHB+SWCX −100%)	fixed	$6.010^{+0.048}_{-0.073}$	$229.3^{+271.6}_{-83.5}$	$6.542^{+0.035}_{-0.030}$	$21.5^{+2.9}_{-3.1}$	M	$6.56^{+1.69}_{-2.04}$	$5.40^{+1.27}_{-2.09}$	fixed	143.90/131

† All parameters are fixed to referred or simulation based value without mentioned
‡ One hot ISM model.
[a] Emission Measure $10^{-3} \int n_e n_p dl$: in unit of cm^{-6} pc
[b] Spectral type of the stars whose normalization is set to be free
[c] Ratio of the normalization of stars of binaries to the simulation based value

Table D.11: Fitting results of model E3 with varied LHB+SWCX normalization.

Model	Foreground†	hot ISM				Additional background			Background†	χ^2/dof
		cooler		hotter					CXB	
		log T (K)	Norm[a]	log T (K)	Norm[a]	log T (K)	Norm[a]	Abundance		
E3-A' (LHB+SWCX +75%)	fixed	$6.021^{+0.078}_{-0.078}$	$168.0^{+217.5}_{-85.8}$	$6.549^{+0.025}_{-0.023}$	$25.9^{+2.6}_{-2.6}$	$7.250^{+0.085}_{-0.087}$	$38.0^{+5.2}_{-5.2}$	0.1 (fixed)	fixed	133.45/131
E3-A'	fixed	$6.017^{+0.061}_{-0.073}$	$193.7^{+224.9}_{-87.5}$	$6.548^{+0.026}_{-0.022}$	$25.9^{+2.7}_{-2.6}$	$7.239^{+0.096}_{-0.077}$	$38.5^{+4.8}_{-5.8}$	0.1 (fixed)	fixed	133.34/131
E3-A' (LHB+SWCX −100%)	fixed	$6.015^{+0.044}_{-0.066}$	$227.5^{+223.2}_{-86.4}$	$6.549^{+0.025}_{-0.023}$	$25.9^{+2.6}_{-2.6}$	$7.250^{+0.085}_{-0.087}$	$38.0^{+5.2}_{-5.2}$	0.1 (fixed)	fixed	133.07/131

† All parameters are fixed to referred or simulation based value without mentioned
[a] Emission Measure $10^{-3} \int n_e n_p dl$: in unit of cm^{-6} pc

Table D.12: Fitting results with model E2 with varied Loop I normalization.

Model	Foreground†	hot ISM				Background†				χ^2/dof
		cooler		hotter		Stars		Binaries	CXB	
		log T [keV]	Norm[a]	log T [keV]	Norm[a]	Class[b]	Ratio[c]	Ratio[c]		
E2-mb (LoopI +50%)	fixed	$6.014^{+0.047}_{-0.083}$	$188.9^{+201.7}_{-90.0}$	$6.540^{+0.033}_{-0.033}$	$19.4^{+2.8}_{-3.0}$	M	$6.71^{+1.80}_{-1.32}$	$4.73^{+1.75}_{-1.31}$	fixed	142.39/131
E2-mb	fixed	$6.012^{+0.065}_{-0.083}$	$195.3^{+288.8}_{-87.5}$	$6.542^{+0.036}_{-0.030}$	$21.5^{+3.0}_{-3.1}$	M	$6.57^{+1.17}_{-2.14}$	$5.45^{+1.27}_{-2.20}$	fixed	144.37/131
E2-mb (LoopI −50%)	fixed	$6.010^{+0.044}_{-0.078}$	$202.3^{+227.4}_{-80.4}$	$6.544^{+0.027}_{-0.025}$	$23.6^{+2.8}_{-2.8}$	M	$6.43^{+1.38}_{-1.57}$	$5.13^{+1.39}_{-1.59}$	fixed	144.58/131

† All parameters are fixed to referred or simulation based value without mentioned
[a] Emission Measure $10^{-3} \int n_e n_p dl$: in unit of cm^{-6} pc
[b] Spectral type of the stars whose normalization is set to be free
[c] Ratio of the normalization of stars of binaries to the simulation based value

Table D.13: Fitting results of model E3 with varied Loop I normalization.

Model	Foreground†	hot ISM				Additional background			Background†	χ^2/dof
		cooler		hotter					CXB	
		log T (K)	Norm[a]	log T (K)	Norm[a]	log T (K)	Norm[a]	Abundance		
E3-A' (LoopI +50%)	fixed	$6.020^{+0.064}_{-0.070}$	$186.6^{+201.5}_{-86.3}$	$6.548^{+0.027}_{-0.025}$	$23.9^{+2.6}_{-2.6}$	$7.246^{+0.082}_{-0.089}$	$38.4^{+5.2}_{-5.2}$	0.1 (fixed)	fixed	132.78/131
E3-A'	fixed	$6.017^{+0.061}_{-0.073}$	$193.7^{+224.9}_{-87.5}$	$6.548^{+0.026}_{-0.022}$	$25.9^{+2.7}_{-2.6}$	$7.239^{+0.096}_{-0.077}$	$38.5^{+4.8}_{-5.8}$	0.1 (fixed)	fixed	133.34/131
E3-A' (LoopI −50%)	fixed	$6.016^{+0.055}_{-0.074}$	$201.3^{+237.2}_{-87.5}$	$6.550^{+0.023}_{-0.021}$	$27.9^{+2.6}_{-2.6}$	$7.253^{+0.087}_{-0.085}$	$37.6^{+5.2}_{-5.3}$	0.1 (fixed)	fixed	133.07/131

† All parameters are fixed to referred or simulation based value without mentioned
[a] Emission Measure $10^{-3} \int n_e n_p dl$: in unit of cm^{-6} pc

Bibliography

Almy, R. C., McCammon, D., Digel, S. W., Bronfman, L., & May, J. 2000, ApJ, 545, 290

Anders, E., & Grevesse, N. 1989, Geochim. Cosmochim. Acta , 53, 197

Asplund, M., Grevesse, N., Sauval, A. J., & Scott, P. 2009, Annual Rev. A&A, 47, 481

Berghoefer, T. W., Schmitt, J. H. M. M., & Cassinelli, J. P. 1996, A&AS, 118, 481

Berkhuijsen, E. M. 1971, A&A, 14, 359

Bregman, J. N., & Lloyd-Davies, E. J. 2007, ApJ, 669, 990

Cackett, E. M., Miller, J. M., Raymond, J., Homan, J., van der Klis, M., Méndez, M., Steeghs, D., & Wijnands, R. 2008, ApJ, 677, 1233

Cen, R., & Ostriker, J. P. 1999, ApJ, 514, 1

Cox, A. N., & Pilachowski, C. A. 2000, Physics Today, 53, 100000

Cox, D. P. 1998, "The Local Bubble and Beyond", proceedings of IAU Colloquium 166, 113, 271

—. 2005, Annual Rev. A&A, 43, 337

Cravens, T. E. 1997, GeoRL , 24, 105

—. 2000, ApJ, 532, L153

Egger, R. J., & Aschenbach, B. 1995, A&A, 294, L25

Fang, T., Mckee, C. F., Canizares, C. R., & Wolfire, M. 2006, ApJ, 644, 174

Ferriere, K. 1998, ApJ, 503, 700

Field, G. B., Goldsmith, D. W., & Habing, H. J. 1969, ApJ, 155, L149+

Fujimoto, R., Mitsuda, K., Mccammon, D., Takei, Y., Bauer, M., Ishisaki, Y., Porter, S. F., Yamaguchi, H., Hayashida, K., & Yamasaki, N. Y. 2007, PASJ, 59, 133

Futamoto, K., Mitsuda, K., Takei, Y., Fujimoto, R., & Yamasaki, N. Y. 2004, ApJ, 605, 793

Giacconi, R., Gursky, H., Paolini, F. R., & Rossi, B. B. 1962, Physical Review Letters, 9, 439

Girardi, L., Groenewegen, M. A. T., Hatziminaoglou, E., & da Costa, L. 2005, A&A, 436, 895

Güdel, M. 2004, The Astronomy and Astrophysics Review, 12, 71

Hansen, C. J., & Kawaler, S. D. 1994, Stellar Interiors. Physical Principles, Structure, and Evolution., ed. Hansen, C. J. & Kawaler, S. D.

Hasinger, G., Burg, R., Giacconi, R., Hartner, G., Schmidt, M., Trumper, J., & Zamorani, G. 1993, A&A, 275, 1

Henley, D. B., Shelton, R. L., & Kuntz, K. D. 2007, ApJ, 661, 304

Hurwitz, S., Mariner, R. H., Fehn, U., & Snyder, G. T. 2005, Earth and Planetary Science Letters, 235, 700

Irwin, J. A., & Bregman, J. N. 1999, ApJ, 527, 125

Ishisaki, Y., Maeda, Y., Fujimoto, R., Ozaki, M., Ebisawa, K., Takahashi, T., Ueda, Y., Ogasaka, Y., Ptak, A., Mukai, K., Hamaguchi, K., Hirayama, M., Kotani, T., Kubo, H., Shibata, R., Ebara, M., Furuzawa, A., Iizuka, R., Inoue, H., Mori, H., Okada, S., Yokoyama, Y., Matsumoto, H., Nakajima, H., Yamaguchi, H., Anabuki, N., Tawa, N., Nagai, M., Katsuda, S., Hayashida, K., Bamba, A., Miller, E. D., Sato, K., & Yamasaki, N. Y. 2007, PASJ, 59, 113

Iwamoto, K., Brachwitz, F., Nomoto, K., Kishimoto, N., Umeda, H., Hix, W. R., & Thielemann, F. 1999, ApJS, 125, 439

Jenkins, E. B. 1978, ApJ, 219, 845

Kalberla, P. M. W., Burton, W. B., Hartmann, D., Arnal, E. M., Bajaja, E., Morras, R., & Pöppel, W. G. L. 2005, A&A, 440, 775

Koutroumpa, D., Acero, F., Lallement, R., Ballet, J., & Kharchenko, V. 2007, A&A, 475, 901

Koyama, K., Tsunemi, H., Dotani, T., Bautz, M. W., Hayashida, K., Tsuru, T. G., Matsumoto, H., Ogawara, Y., Ricker, G. R., Doty, J., Kissel, S. E., Foster, R., Nakajima, H., Yamaguchi, H., Mori, H., Sakano, M., Hamaguchi, K., Nishiuchi, M., Miyata, E., Torii, K., Namiki, M., Katsuda, S., Matsuura, D., Miyauchi, T., Anabuki, N., Tawa, N., Ozaki, M., Murakami, H., Maeda, Y., Ichikawa, Y., Prigozhin, G. Y., Boughan, E. A., Lamarr, B., Miller, E. D., Burke, B. E., Gregory, J. A., Pillsbury, A., Bamba, A., Hiraga, J. S., Senda, A., Katayama, H., Kitamoto, S., Tsujimoto, M., Kohmura, T., Tsuboi, Y., & Awaki, H. 2007, PASJ, 59, 23

Kroupa, P. 2001, MNRAS, 322, 231

Kuntz, K. D., & Snowden, S. L. 2000, ApJ, 543, 195

—. 2001, ApJ, 554, 684

Kuntz, K. D., Snowden, S. L., & Verter, F. 1997, ApJ, 484, 245

Lallement, R. 2004, A&A, 422, 391

Lallement, R., Welsh, B. Y., Vergely, J. L., Crifo, F., & Sfeir, D. 2003, A&A, 411, 447

Li, J., Li, Z., Wang, Q. D., Irwin, J. A., & Rossa, J. 2008, MNRAS, 390, 59

Lisse, C. M., Dennerl, K., Englhauser, J., Harden, M., Marshall, F. E., Mumma, M. J., Petre, R., Pye, J. P., Ricketts, M. J., Schmitt, J., Trumper, J., & West, R. G. 1996, Science, 274, 205

López-Santiago, J., Micela, G., Sciortino, S., Favata, F., Caccianiga, A., Della Ceca, R., Severgnini, P., & Braito, V. 2007, A&A, 463, 165

Masui, K., Mitsuda, K., Yamasaki, N. Y., Takei, Y., Kimura, S., Yoshino, T., & McCammon, D. 2008, ArXiv e-prints 0810.2035

McCammon, D., Almy, R., Apodaca, E., Bergmann Tiest, W., Cui, W., Deiker, S., Galeazzi, M., Juda, M., Lesser, A., Mihara, T., Morgenthaler, J. P., Sanders, W. T., Zhang, J., Figueroa-Feliciano, E., Kelley, R. L., Moseley, S. H., Mushotzky, R. F., Porter, F. S., Stahle, C. K., & Szymkowiak, A. E. 2002, ApJ, 576, 188

McKee, C. F., & Ostriker, J. P. 1977, ApJ, 218, 148

Miller, E. D., Tsunemi, H., Bautz, M. W., McCammon, D., Fujimoto, R., Hughes, J. P., Katsuda, S., Kokubun, M., Mitsuda, K., Porter, F. S., Takei, Y., Tsuboi, Y., & Yamasaki, N. Y. 2008, PASJ, 60, 95

Mitsuda, K., Fujimoto, R., Yamasaki, N. Y., Yoshino, T., Hagihara, T., Masui, K., Bauer, M., Takei, Y., McCammon, D., Wang, Q. D., & Yao, Y. 2007, Progress of Theoretical Physics Supplement, 169, 79

Mokiem, M. R., de Koter, A., Vink, J. S., Puls, J., Evans, C. J., Smartt, S. J., Crowther, P. A., Herrero, A., Langer, N., Lennon, D. J., Najarro, F., & Villamariz, M. R. 2007, A&A, 473, 603

Nicastro, F., Mathur, S., Elvis, M., Drake, J., Fang, T., Fruscione, A., Krongold, Y., Marshall, H., Williams, R., & Zezas, A. 2005, Nature, 433, 495

Nomoto, K., Tominaga, N., Umeda, H., Kobayashi, C., & Maeda, K. 2006, Nuclear Physics A, 777, 424

Norman, C. A., & Ikeuchi, S. 1989, ApJ, 345, 372

Ottmann, R., & Schmitt, J. H. M. M. 1992, A&A, 256, 421

Park, S., Finley, J. P., Snowden, S. L., & Dame, T. M. 1997, ApJ, 476, L77+

Rocks, L. E. 2009, PhD thesis, University of Wisconsin

Salpeter, E. E. 1955, ApJ, 121, 161

Shapiro, S. L., & Marchant, A. B. 1976, ApJ, 210, 757

Shull, J. M., & Slavin, J. D. 1994, ApJ, 427, 784

Skrutskie, M. F., Cutri, R. M., Stiening, R., Weinberg, M. D., Schneider, S., Carpenter, J. M., Beichman, C., Capps, R., Chester, T., Elias, J., Huchra, J., Liebert, J., Lonsdale, C., Monet, D. G., Price, S., Seitzer, P., Jarrett, T., Kirkpatrick, J. D., Gizis, J. E., Howard, E., Evans, T., Fowler, J., Fullmer, L., Hurt, R., Light, R., Kopan, E. L., Marsh, K. A., McCallon, H. L., Tam, R., Van Dyk, S., & Wheelock, S. 2006, AJ, 131, 1163

Smith, R. K., Bautz, M. W., Edgar, R. J., Fujimoto, R., Hamaguchi, K., Hughes, J. P., Ishida, M., Kelley, R., Kilbourne, C. A., Kuntz, K. D., McCammon, D., Miller, E., Mitsuda, K., Mukai, K., Plucinsky, P. P., Porter, F. S., Snowden, S. L., Takei, Y., Terada, Y., Tsuboi, Y., & Yamasaki, N. Y. 2007, PASJ, 59, 141

Smith, R. K., Edgar, R. J., Plucinsky, P. P., Wargelin, B. J., Freeman, P. E., & Biller, B. A. 2005, ApJ, 623, 225

Snowden, S. L., Egger, R., Freyberg, M. J., McCammon, D., Plucinsky, P. P., Sanders, W. T., Schmitt, J. H. M. M., Truemper, J., & Voges, W. 1997, ApJ, 485, 125

Snowden, S. L., McCammon, D., & Verter, F. 1993, ApJ, 409, L21

Spitzer, Jr., L. 1968, Dynamics of Interstellar Matter and the Formation of Stars, ed. Middlehurst, B. M. & Aller, L. H. (the University of Chicago Press), 1–+

Strickland, D. 2002, in Astronomical Society of the Pacific Conference Series, Vol. 253, Chemical Enrichment of Intracluster and Intergalactic Medium, ed. R. Fusco-Femiano & F. Matteucci, 387–+

Strickland, D. K., Heckman, T. M., Colbert, E. J. M., Hoopes, C. G., & Weaver, K. A. 2004, ApJ, 606, 829

Takei, Y., Fujimoto, R., Mitsuda, K., & Onaka, T. 2002, ApJ, 581, 307

Tanaka, Y., & Bleeker, J. A. M. 1977, Space Science Reviews, 20, 815

Tawa, N., Hayashida, K., Nagai, M., Nakamoto, H., Tsunemi, H., Yamaguchi, H., Ishisaki, Y., Miller, E. D., Mizuno, T., Dotani, T., Ozaki, M., & Katayama, H. 2008, PASJ, 60, 11

Tsyganenko, N. A., & Sitnov, M. I. 2005, Journal of Geophysical Research (Space Physics), 110, 3208

Udalski, A., Szymanski, M., Kubiak, M., Pietrzynski, G., Wozniak, P., & Zebrun, K. 1997, Acta Astronomica, 47, 431

Urošević, D. 2003, Ap&SS, 283, 75

van den Besselaar, E. J. M., Raassen, A. J. J., Mewe, R., van der Meer, R. L. J., Güdel, M., & Audard, M. 2003, A&A, 411, 587

Vanhollebeke, E., Groenewegen, M. A. T., & Girardi, L. 2009, A&A, 498, 95

Wang, Q. D., Chaves, T., & Irwin, J. A. 2003, ApJ, 598, 969

Wang, Q. D., Yao, Y., Tripp, T. M., Fang, T.-T., Cui, W., Nicastro, F., Mathur, S., Williams, R. J., Song, L., & Croft, R. 2005, ApJ, 635, 386

Welsh, B. Y., & Shelton, R. L. 2009, Ap&SS, 323, 1

White, S. D. M., & Frenk, C. S. 1991, ApJ, 379, 52

Williams, R. J., Mathur, S., Nicastro, F., & Elvis, M. 2007, ApJ, 665, 247

Willson, L. A. 2000, Annual Rev. A&A, 38, 573

Yamasaki, N. Y., Sato, K., Mitsuishi, I., & Ohashi, T. 2009, PASJ, 61, 291

Yao, Y., & Wang, Q. D. 2006a, ApJ, 641, 930

—. 2006b, ApJ, 641, 930

—. 2007, ApJ, 658, 1088

Yao, Y., Wang, Q. D., Hagihara, T., Mitsuda, K., McCammon, D., & Yamasaki, N. Y. 2009, ApJ, 690, 143

Yao, Y., Wang, Q. D., & Nan Zhang, S. 2005, MNRAS, 362, 229

Yoshino, T., Mitsuda, K., Yamasaki, N. Y., Takei, Y., Hagihara, T., Masui, K., Bauer, M., McCammon, D., Fujimoto, R., Wang, Q. D., & Yao, Y. 2009, PASJ, 61, 805